Metal Oxide Based Catalysts for the Gas Phase Dehydrogenation of Representative Saturated and Unsaturated C_4 Hydrocarbons

Thesis Submitted to AcSIR for the Award of the Degree of

Doctor of Philosophy

in

Chemical Sciences

By

Aswathy T. V.

(AcSIR No: 10CC17J26021)

Under the guidance of

Dr. Thirumalaiswamy Raja

CSIR-National Chemical Laboratory

Pune-411 008, India

CERTIFICATE

This is to certify that the work incorporated in this Ph. D. thesis entitled **"Metal oxide based catalysts for the gas phase dehydrogenation of representative saturated and unsaturated C_4 hydrocarbons"** submitted by **Mrs. Aswathy T. V.** to Academy of Scientific and Innovative Research (AcSIR) in fulfillment of the requirements for the award of the ***Degree of Doctor of Philosophy,*** in ***Chemical Sciences***, embodies original research work under my supervision at the Catalysis and Inorganic Chemistry Division, CSIR-National Chemical Laboratory, Pune-411 008, India. I further certify that this work has not been submitted to any other University or Institution in part or full for the award of any degree or diploma. Research material obtained from other sources has been duly acknowledged in the thesis. Any text, illustration, table etc., used in the thesis from other sources, have been duly cited and acknowledged.

It is also certified that this work done by the student, under my supervision, is plagiarism free.

Mrs. Aswathy T. V.
(Research Student)
CSIR-NCL

Dr. Thirumalaiswamy Raja
(Research Supervisor)
CSIR-NCL

Date: 14.07.2020
Place: Pune

DECLARATION

I, *Aswathy T. V.* hereby declare that the work described in the thesis entitled **"Metal oxide based catalysts for the gas phase dehydrogenation of representative saturated and unsaturated C_4 hydrocarbons"** submitted for the degree of Doctor of Philosophy in Chemical Sciences to the Academy of Scientific and Innovative Research (AcSIR), Gaziabad, Uttar Pradesh, India, has been carried out by me at the Catalysis and Inorganic Chemistry Division, CSIR-National Chemical Laboratory, Pune-411 008, India, under the supervision of Dr. Thirumalaiswamy Raja. The material obtained from other sources has been duly acknowledged in this thesis. The work is original and has not been submitted in part or full by me for any other degree or diploma to this or any other university.

Mrs. Aswathy T. V.
(Research Student)
CSIR-NCL

Date: 14.07.2020

Place: Pune

Dedication

To my beloved family and friends…

…the reason of what I become today

"It always seems impossible until it's done."

Nelson Mandela

Acknowledgements…

The achievement of this Ph. D thesis symbolizes quite a pleasant journey of my life learning, gaining knowledge and gathering experiences in the research field. It, of course, gives me an opportunity to thank all those people with whom I have had interaction and their contribution in many ways in the final form of this work. Without their collective efforts and cooperation, this thesis could not have been completed as it stands. I feel privileged to convey my regards to all of them. This acknowledgement is just a mere reminder that they will never be forgotten and my apology to anyone whom I fail to mention.

Foremost, I would like to express my sincere gratitude to my advisor Dr. T. Raja for giving me an opportunity to work in his lab. I am grateful to thank him for the continuous support of my Ph.D study and related research, for his patience, motivation, and immense knowledge. His guidance helped me in all the time of research and writing of this thesis. Besides my supervisor, I am extremely honoured to thank my DAC committee: Dr. C. S. Gopinath, Dr. A. A. Kelkar, Dr. V. H. Rane, Dr. Vincent P. Swamy, and external expert Dr. Suresh B. Waghmode for their insightful comments and encouragement, but also for the hard question which assisted me to widen my research from various perspectives.

I wish to convey my genuine thanks to former directors, Dr. S. Pal, Dr. K. V. Pillai and the present director, Dr. A. K. Nangia for providing me with all the necessary facilities for the research. I place on record, my sincere thank you to Dr. A. P. Singh (former), Dr. D. Srinivas (former) and Dr. C. S. Gopinath, Chairman of Catalysis and Inorganic chemistry Division, for the continuous encouragement.

I take this opportunity to show my deepest gratefulness to Dr. C. P. Vinod, Dr. C. V. V. Satyanarayana, Dr. K. Krishnamoorthy and scientists of Catalysis and Inorganic chemistry Division for their valuable suggestions. I thank Ms. Violet Samuel, Dr. Tejas, Mr. Jha, Mr. Purushothaman, Mr. Madhu and non-scientific staffs of the division for their timely support in the technical matters. Sincere thanks to Ms. Rupali, Mr. Venketesh and all other instrumental operators for helping me to carry out sample analysis. Special regards are given to Ms. Edna Joseph for performing elemental analysis at the Venture Centre, CSIR-NCL.

Words fail me to thank Dr. Ashok Kumar V; my senior, M. Tech project co-guide, mentor because of whom I was able to do Ph. D and got motivation needed to successfully complete this degree. I would like to thank my ex-lab mate and the perfect partner Mr. Periyasamy K. for his endless love and encouragement throughout this entire journey. Thanks Maya, my forever friend for accompanying and motivating me in every turning points of my life. I am grateful to show thankfulness to my MSc project co-guide Dr. Kannan V for enlightening me the first glance of research.

I thank my former and present colleagues of lab No.223; K. Prabu, Pranjal, M. Prabu, Manikandan, Sumati, Sruthy, Divya, Fawaz, Fahima, Gayathri, Asamsa, Aditya, Athul, Sivaprasad, Vipul, Karthik Raja, Karthik G., Sampath, Amrin, Akash, Kiran, Snehal, Sheetal, Sana, Eeswar, Nikitra, Saravanan, Samridhi, Archana C. V., Archana, Abhijeet, Anshu, Aaron, Mayuri, Ganesh for the stimulating discussions and for creating a pleasant atmosphere in the lab for doing research.

I express my appreciation to the project trainees who worked with me; Prasad, Mudassir and Aswathy S. Kind regards to my collaborators Dr. A. K. Tyagi (BARC), Dr. Sanjay Negi and divisional scientists for giving me the chance to work with them.

I wish to acknowledge kind suggestions from my seniors (Drs.) Sreedala, Anju, Mohan, Lakshmiprasad, Anish, Sunil, Vysakh, Lenin, Sivaranjini, Edwin, Devaraji, Pradnya, Suman, Sreekanth, Hanmant and Kiran.

This research also benefited tremendously from many friends at my institute; Shibin, Sourik, Yogita, Preethi, Fayis, Sagar, Rajendraprasad, Rupa and Vibhavari. Special thanks to Seema, Sharad, Sudheesh, Sudhakar, Subrahmani, Satish, Vedikuyil, Maneesha, Pawan, Ananthan, Arunima, Sreejith, Kavya, Chaithanya, Kumar, Dr. CPV group, Dr. CSG group, Dr. NRD group, Dr. SU group, Dr. CVVS group, Dr. APS group, Dr. PLD group, Dr. PAJ group, Dr. BE group, Dr. SS group and well wishers in NCL for all the fun we have had together.

This was the first experience for me of being away from home and it has been a pleasure to have my affectionate roommates Anjali, Betsy, Athira K., Naina, Athira, Amritha, Meera, Prakriti during my NCL days. My first arrival to NCL was as a M. Tech. trainee and I thank my friends Ziyad, Silpa and Chitra for their assistance in the earlier days of my research.

Extra special thanks to Malayali, Tamil, Marathi and Telugu communities for the celebrations provided on the festival days which helped me to find myself relaxed throughout the tight schedule of my lab work.

I would also like to acknowledge and thank the entire hostel mates especially Vipin, Shabeeb, Ranjeesh, Rajith, Pranav, Aswini, Ajith, Zinoy, Vidyanand, Shailaja, Aarti, Aabha, Kavita for discussions on scientific and societal issues which led me to develop a critical sense of thinking and to evolve myself as a keen research student.

I am grateful to CSIR, New Delhi for awarding research fellowship. A very special gratitude goes out to all down at AcSIR, New Delhi for PhD registration; student academic office, NCL for the timely help; HR-II for safe accommodation; vendors for the technical facilities; NCL officials for their administration during my tenure as a Ph. D student. I would like to thank my M. Tech., M.Sc., B.Sc., and school friends for their encouragement. I also place on record, my sense of gratitude to one and all, who directly or indirectly, have lent their hand in this venture.

Words are not enough to express my love and appreciation to my family members. It gives me great pleasure to thank my parents Leela and Venugopalan for their love, unfailing support, tremendous patience, trust and encouragement that they have shown to me. No words would be sufficient in describing the affection and support of my in laws Vijayalakshmi and Kaliyappan. I am indebted to my sisters Anju and Pavitra; love to Kayal and Mahi; exceptional thanks to Raghupathy and Mahesh. I would extend my thanks to my cousins and their family for their affection and encouragement. I wouldn't have conquered all the hurdles to achieve any goal without their blessings, care and love. All the knowledge that I have acquired today is the result of their upbringing. It is to them that I dedicate this dissertation.

Last but not least, I am always grateful to the Almighty for His mercy for granting me the good health, knowledge and skill that were necessary to complete this thesis.

Aswathy T V

Contents

Figures

Schemes

Tables

Abbreviations

BD	1, 3-butadiene
BET	Brunauer-Emmet-Teller
BJH	Barret-Joyner-Halenda
C_n	'n' carbons where, n=1, 2, 3, 4 etc
CNT	Carbon nanotube
DH	Dehydrogenation
DHisoB	Dehydrogenation of isobutane
D_p	Pore diameter
DRS	Diffuse reflectance spectroscopy
DTA	Differential thermal analysis
EDX	Energy dispersive X-ray spectroscopy
EL	Explosive limit
FID	Flame ionization detector
FTIR	Fourier transform infrared spectroscopy
FWHM	Full width at half maximum
GC	Gas chromatography
GHSV	Gas hourly space velocity
h	Hour
HRTEM	High resolution transmission electron microscopy
ICP-MS	Inductively coupled plasma-mass spectroscopy
IUPAC	International Union of Pure and Applied Chemistry
JCPDS	Joint committee on Powder Diffraction Standards
LEL/UEL	Lower/upper explosive limit
MVK	Mars van Krevelen
ODH	Oxidative dehydrogenation
ODH1B	Oxidative dehydrogenation of 1-butene
ODHnB	Oxidative dehydrogenation of n-butane
OSC	Oxygen storage capacity
PXRD	Powder X-ray diffraction
SAED	Selected area electron diffraction
S_{BD}	Selectivity of 1, 3-butadiene

$\mathbf{S_{BET}}$	BET surface area
$\mathbf{S_{butenes}}$	Selectivity of butenes
SC	Steam cracking
SEM	Scanning electron microscopy
$\mathbf{S_{isobutene}}$	Selectivity of isobutene
$\mathbf{S_{TDP}}$	Selectivity of total dehydrogenated products
TCD	Thermal conductivity detector
TGA	Thermogravimetric analysis
$\mathbf{T_{max}}$	Temperature of the first maxima in the profile
TOS	Time on stream
TPD	Temperature programmed desorption
TPR	Temperature programmed reduction
UV	Ultra violet
$\mathbf{V_p}$	Pore volume
$\mathbf{X_{hydrocarbon}}$	Conversion of hydrocarbon
XPS	X-ray photoelectron spectroscopy

Abstract

Heterogeneous catalysis plays a vital role in the production of several bulk, fine and commodity chemicals. Numerous researches are enduring in this area to develop a better technology considering the economical and environmental aspects by changing the feedstock. An important challenge deals with the manufacture of C_4 olefins especially; 1, 3-butadiene (BD) and isobutene which are the key monomers in the polymer industry. They are mainly employed for the fabrication of synthetic rubber and organic chemicals that are the key precursors for so many materials used in our day to day life. Currently, C_4 olefins are obtained from the high temperature catalytic cracking of hydrocarbon feedstocks as well as catalytic dehydrogenation of the respective C_4 hydrocarbons both of which are energy consuming processes. Meanwhile the researchers have been searching for alternative efficient methods for C_4 olefins' synthesis to meet their increasing worldwide demand. In these regards, oxidative dehydrogenation (ODH) seeks more attention due to its exothermicity which makes the operation at low temperatures and thus making the process more economical. This thesis summarizes utilizing different metal oxide-based materials for the lab scale synthesis of C_4 olefins and the systematic study of their catalytic properties towards improving the productivity.

Oxidative dehydrogenation of n-butane is a promising process to produce economically important precursors like butenes and BD in the polymer industry. Various vanadia based catalysts are developed for this reaction. In the present work, a modified catalyst synthesis strategy is adopted by employing boron, a nonmetal for the active tetrahedral vanadia site isolation. A comprehensive investigation is carried over on the effect of material composition and reaction parameters in defining the C_4 olefins. A specific amount of boron and vanadium is the primary requisite for a superior catalyst at the optimized dehydrogenation conditions when molecular oxygen employed as an oxidant. This study provides an active and sturdy catalyst, unlike the previously reported vanadia containing catalysts.

Further, a systematic investigation of oxidative dehydrogenation of 1-butene is performed over various transition metal-doped bismuth ferrites. A considerable improvement in the conversion, as well as selectivity towards BD, is observed for Zn doped bismuth ferrite. PXRD study revealed the materials exist in a distorted rhombohedral perovskite structure. HRTEM also evidenced the perfect doping of Zn into the crystal lattice. The catalyst was sturdy without any transformation in the structural features and significant deactivation.

Steam can reduce the unwanted side reactions and lattice oxygen also can contribute remarkably for the activity under non-oxidative dehydrogenation conditions.

Low-temperature oxidative dehydrogenation (ODH) of alkanes to their alkenes is one of the challenging reactions in the polymer industry. Towards this a highly dispersed cerium iron oxide is synthesized by citrate gel combustion method and employed for the synthesis of butadiene (BD) from 1-butene. The reaction is carried out at low temperature under an oxygen-free atmosphere in a continuous flow fixed bed reactor. A decrease in the lattice parameters observed from PXRD and high-resolution TEM analysis proved that iron occupies cerium sites in the crystal lattice. XPS, TPR, and oxygen uptake studies quantified the nature and abundance of different oxygen species. ODH is observed through consuming lattice oxygens. The vacancies generated could be filled by reoxidation with an external supply of oxygen which will restore the catalytic activity demonstrating the Mars van Krevelen mechanism. The current work considerably brought down the reaction temperature which reduces the operating cost and makes BD synthesis more economical. Moreover, steam was not used in the present work which has added advantage over the existing methods.

Production of isobutene is commercially consequential and highly demanding from the end-use industries being a key platform molecule as well as an intermediate for a variety of chemicals. The catalytic non-oxidative dehydrogenation of isobutane over acidic, alkaline, and noble metal promoted mesoporous iron-doped catalysts was investigated. Iron doping has a significant function in controlling isobutene selectivity. The synthesis method is important to achieve successful metal doping in the mesoporous alumina matrix. Promoted catalysts exhibited a notable difference in isobutane conversion with a marginal change in dehydrogenation selectivity. Silver promoted catalyst exhibited the highest isobutene yield due to the optimal catalytic properties. The best catalyst was stable for an appreciable duration and coke deposition, as well as particle agglomeration, is observed to slightly inhibit the catalytic activity.

Chapter-1

Introduction

"Chemistry without catalysis would be a sword without a handle, a light without brilliance, a bell without sound" – Alwin Mittasch

1.1. Catalysis

An average person can tell about the catalyst as something which is there in the automobiles to clean the exhaust. However, catalysts and catalysis have a much broader scope than lessening pollution. Those are the basis of chemical transformations happening in the chemical industry for the manufacture of almost 90 % of products which we are using in our day to day life. According to the International Union of Pure and Applied Chemistry (IUPAC), a catalyst can be simply defined as a substance that accelerates the rate of a chemical reaction without altering the overall standard Gibbs free energy change of the reaction. The term 'catalyst' was first defined by Jöns Jakob Berzelius; a Swedish chemist in 1836 [1]. **Fig. 1.1.** illustrates the definition of an ideal catalyst which reduces the activation energy barrier between the reactants and products by providing an alternative pathway; and hence it increases the reaction rate. Generally, the catalyst participates in the slow process; which is the rate-determining step of a chemical reaction. Moreover, it does not influence the position of chemical equilibrium. Consequently, it enables the processes to be carried out under industrially realizing reaction conditions.

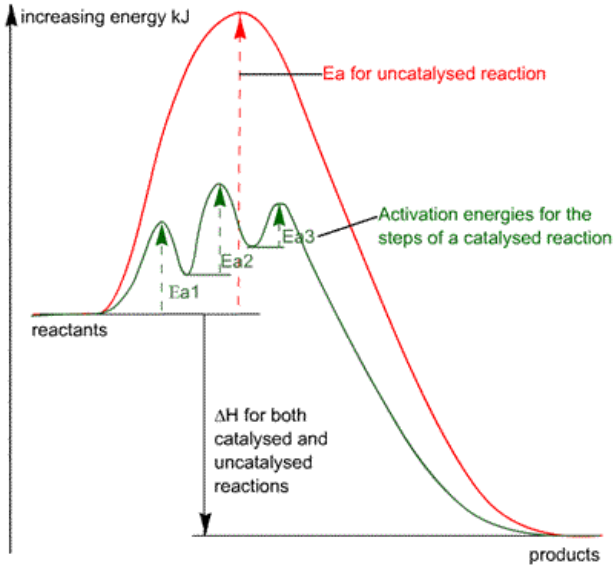

Fig. 1.1 Definition of a catalyst [2]

Catalysts can be atoms, molecules, solid surfaces or enzymes. Catalysis can be generally classified into three major types depending on the phases of reactant and catalyst such as homogeneous, heterogeneous and biocatalysis which are illustrated below with examples [3].

1.1.1. Homogeneous catalysis

In homogenous catalysis, the reactants and catalyst will be in the same phase. Thus, the system forms a single phase which makes separation and recycle of the catalyst from the product complex. The decomposition of ozone accelerates in the presence of chlorine where the reactant and catalyst are in the gaseous state is a typical homogeneously catalyzed reaction.

1.1.2. Heterogeneous catalysis

Heterogeneous catalysis involves the use of the catalyst in a different phase than the reactants. It allows for easy separation and recycling of the catalyst. Here, the rate-limiting step occurs on the surface of the solid, and so referred to as surface catalysis. Major processes occurring on the surface of the catalysts are diffusion, adsorption and desorption. Most of the industrially practised chemical transformations are the heterogeneous processes. Catalytic oxidation of CO in automobile exhaust is the most common heterogeneously catalyzed reaction wherein; noble metal on ceria is used as the catalyst.

1.1.3. Biocatalysis

Biocatalysts are also termed as enzymes; the naturally occurring catalysts. They are highly efficient and specific for a particular reaction. The decomposition of hydrogen peroxide to water and oxygen catalyzed by the enzyme catalase can best illustrate biocatalysis.

1.2. Selective conversion of alkanes

Catalysis plays an important role in the industrial sectors for the production of bulk, fine and commodity chemicals. Numerous researches are enduring in this area to develop a better technology considering the economical and environmental aspects by changing the feedstock. Meanwhile, light alkanes are widely available and generally environmentally friendly important raw material in the chemical industry [4]. Those are mainly used as fuels, but their derivatives can be used for the manufacture of a large number of value-added chemicals. An essential challenge deals with the synthesis of lower olefins; which are the basis of the petrochemical industry from the less expensive and readily available lower alkanes. Activation of light alkanes is a dynamic area of research from the origin of the petroleum

industry. Significant use of alkanes is the fabrication of alkenes, an indispensable starting component in the synthetic chemical industry which is currently produced in steam crackers. For the moment, the global demand for olefins is increasing in recent decades and expected to be amplified in the coming years as illustrated in **Fig. 1.2**. The boom in shale gas; which is enriched in lower alkanes reduced the price of industrial feedstock and improved supply levels. The cost of an alkane in the economy is half the price of the alkene. Accordingly, researchers have been put effort to encounter the future needs of unsaturated lower alkenes and functionalization methods.

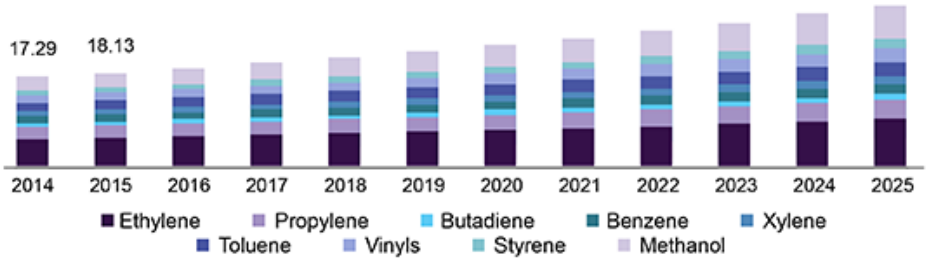

Fig. 1.2 Global olefins market revenue [5]

Olefins obtained after the selective oxidation of alkanes are potential precursors to many value-added chemicals with high economic importance in polymer and synthetic organic industry [6]. In fact, alkanes are made up of nonpolar C–C and C–H bonds and exhibit very low reactivity which makes the methods to operate at high temperatures. Steam cracking (SC) and dehydrogenation (DH) of lower alkanes (*Eq. 1.1*) are the existing processes for the synthesis of olefins [7]. **Fig. 1.3** demonstrates that in a typical endothermic DH process, to shift the equilibrium towards products, the reaction temperature should be increased. Also, any increase in the working pressure will change the equilibrium to an unfavorable direction. Therefore, SC and DH processes could operate at temperatures higher than 700 ºC [8] while they suffer from various disadvantages also [9]. It is very difficult to control the reaction at high temperatures which consecutively reduces the selectivity due to the formation of undesired products by hydrocarbon cracking. Followed with this, the coke deposition on the catalyst increases and hence; the activity of the catalyst decreases significantly [10]. To restore the catalytic activity for another cycle, coke must be removed from the surface. This can be achieved either by the regeneration step or by employing steam in the reactant feed. However, these processes demand an extra cost from an economic point of view.

$$C_nH_{2n+2} \leftrightarrow C_nH_{2n} + H_2 \qquad (Eq.\ 1.1)$$

In summary, stream cracking as well as dehydrogenation suffers from,

- Rapid catalyst deactivation due to coke deposition
- Low selectivity towards olefins
- Thermodynamic restriction on conversion
- High operational cost

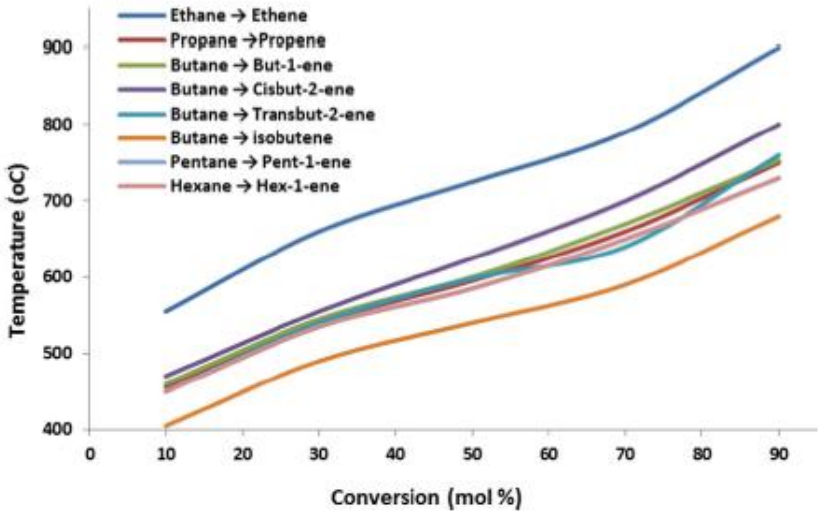

Fig. 1.3 DH conversion versus temperature of lower alkanes [11]

Commercially well-established methods of lower alkane DH are Catofin (Lummus), Olefex (UOP), Linde-BASF, Snamprogetti-Yarsintez, and Star (Philipps Petroleum) with chromia-alumina and fixed bed, supported Pt in moving bed, chromia-alumina and fixed bed, chromia-alumina and fluid bed and supported Pt and moving bed respectively [12]. However, the drawbacks as mentioned above of DH open the way for a more appealing process. Moreover, the production of olefins is not sufficient to meet the global requirement and the researchers put effort into developing new methods with economic effectiveness. Towards this, thermodynamic restrictions of the DH process may be omitted by the removal of liberated hydrogen as water in the presence of a suitable oxidant (*Eq. 1.2*). This method is known as oxidative dehydrogenation (ODH) represented in *Eq. 1.3* and is attracted to full attention which lessens the limitations of DH. This process is widely discussed in **Section 1.3.2**.

$$H_2 + {}^1/_2O_2 \rightarrow H_2O \qquad \textit{(Eq. 1.2)}$$

$$C_nH_{2n+2} + {}^1/_2O_2 \rightarrow C_nH_{2n} + H_2O \qquad \textit{(Eq. 1.3)}$$

Even though many catalysts are giving a considerable yield of olefins through ODH of lower alkanes, a better catalyst nullifying the drawbacks of existing processes has to be developed to convince the industries for commercial implementation.

1.3. Buta-1,3-diene

Butadiene generally exists in two isomeric forms viz., 1, 3-butadiene (BD) and the less stable 1, 2-butadiene. The French chemist E. Caventou has isolated BD a colourless gas for the first time through the pyrolysis of amyl alcohol [13]. In 1886, the presence of BD was identified in the cracking products of petroleum by Armstrong and Miller. Later, the structure was demonstrated in 1895 by Ciamician and Magnaghi [14]. After a decade, in 1910 when BD was recognized to form rubber-like polymers by Lebdev Germany and the United States started the large scale production for the Second World War. Researchers have developed different methods for the synthesis of BD followed by the production of high-quality rubber via the polymerization with organometallic catalysts by Ziegler and Natta [15]. Today, BD has acquired the most requisite monomer in the polymer industry for the manufacture of synthetic rubbers like polybutadiene (PB) rubber, styrene-butadiene rubber (SBR), acrylonitrile-butadiene-styrene (ABS) polymer, nitrile rubber, adiponitrile, etc [14]. Currently, it is the primary precursor of a large number of materials that are used in our everyday life (**Fig. 1.4**).

Fig. 1.4 BD as a precursor of synthetic rubber

The production of BD is mainly achieved by five different methods.

i. From acetylene
ii. From ethanol
iii. Catalytic cracking of naphtha
iv. DH of butane and butenes
v. ODH of butane and butenes

The first two methods are of historical importance and no longer used in the industry. The currently implemented processes are SC of naphtha and catalytic DH of n-butane and n-butenes.

1.3.1. Catalytic cracking

In the present day, the production of BD is mainly achieved via the catalytic SC of naphtha and fluid catalytic cracking of other high boiling hydrocarbon fractions. During this process, C_4 hydrocarbons are obtained along with C_1-C_3 fractions. Since the boiling points of C_4 fraction constituents are within a narrow limit, BD is isolated via extractive distillation with organic solvents or cuprous ammonium acetate (CAA) liquid-liquid extraction methods. However, ethylene is the preferred products in this process and the yield of BD is meager as given in **Table 1.1**.

1.3.2. Catalytic dehydrogenation

Catalytic DH of n-butane and butenes will provide a high yield of BD. The necessary basic information and the disadvantages of this method are already explained in **Section 1.2**. According to Le Chatelier's principle, the yield can be increased either by decreasing the partial pressure of the reaction products or by increasing the reaction temperature. Therefore, typically DH is an endothermic reaction with a positive enthalpy value as shown in *Eq. 1.4–1.7*.

Table 1.1 Comparison of steam cracking and dehydrogenation processes [16]

Process	**Steam cracking**	**Dehydrogenation**
Feedstock	Naphtha	Butane/Butenes
Operating conditions	750–900 °C, Moderate pressure	600–700 /400–500 °C
Advantages	Installed technology	Well established technology, on-purpose production
Disadvantages	Energy demanding, environmental concerns, finite resources, limited production	High endothermicity, catalyst deactivation
Yield to C_4H_6	4.5 %	70 %/71.8 %

$$\text{Butane} \leftrightarrow \text{1-butene} + H_2;\ \Delta H = +131\ \text{kJ/mol} \qquad \textit{(Eq. 1.4)}$$

$$\text{Butane} \leftrightarrow \text{cis-2-butene} + H_2;\ \Delta H = +118\ \text{kJ/mol} \qquad \textit{(Eq. 1.5)}$$

$$\text{Butane} \leftrightarrow \text{cis-2-butene} + H_2;\ \Delta H = +118\ \text{kJ/mol} \qquad \textit{(Eq. 1.6)}$$

$$\text{cis-2-butene} \leftrightarrow \text{Butadiene} + H_2;\ \Delta H = +126\ \text{kJ/mol} \qquad \textit{(Eq. 1.7)}$$

Table 1.1 represents the major differences between the cracking and DH methods. Later, in the last decade researchers have implemented a better and energy-efficient approach for the synthesis of unsaturated hydrocarbons; which is ODH.

1.3.3. Oxidative dehydrogenation

Recently, ODH of n-butane and butenes has been practised as a promising energy-efficient method in the presence of an oxidant which oxidizes the detached hydrogen to a stable water molecule (*Eq. 1.3*). A high BD yield can be achieved via this independent single unit method and has attracted remarkable attention. The exothermicity of the process (*Eq. 1.8, 1.9*) can perform subsequent coke removal and allows control over the existing equilibria. Moreover, the reaction can be operated at lower temperatures compared to naphtha SC and DH methods [17]. The oxidant will makes the process cost effective, reduces greenhouse gases emission and increases catalyst lifetime. Hence, ODH has acquired much more attention owing to its significant advantages over the other existing processes for BD production. Nevertheless, the reaction conditions have to be systematically optimized to avoid the loss of BD yield by controlling isomerization, cracking, and total oxidation processes which could occur along with the ODH reaction.

$$C_4H_8 \leftrightarrow C_4H_6 + H_2\ (\Delta H_r = +109.7\ \text{kJ/mol}) \qquad \textit{(Eq. 1.8)}$$

$$C_4H_8 + {}^1/_2O_2 \rightarrow C_4H_6 + H_2O\ (\Delta H_r = -132.1\ \text{kJ/mol}) \qquad \textit{(Eq. 1.9)}$$

1.4. ODH: General aspects

The fundamental scientific aspects of ODH including thermodynamics, kinetics, reaction mechanism etc are discussed in this section. A brief description of the parameters influencing this reaction is given with examples from the reported studies. Numerous catalysts are employed for the ODH of C_4 hydrocarbons and some selected systems are mentioned.

1.4.1. Type of oxidants

The presence of oxidant in the ODH process will reduce coke deposition on the active catalytic sites to some extent by converting coke to carbon oxides. In addition, the exothermic nature of the reaction can supply the needed heat to the reaction, and the operating temperature can be effectively brought down [18]. In earlier days, bromine, sulphur and

iodine were the common oxidants; where very good selectivity for DH products is achieved. Nevertheless, corrosive and hazardous nature prevented these gases from commercial execution [4]. Most of the studies have used O_2, CO_2, air, sulphur compounds, and N_2O as oxidants for ODH (**Fig. 1.5**); while C_4 hydrocarbons are well explored with molecular oxygen as oxidant (*Eq. 1.9*). Even though this process is eco-benign, the difficulty in controlling the over oxidation of hydrocarbons as well as the possibility of the explosion might be carefully considered while engaging O_2.

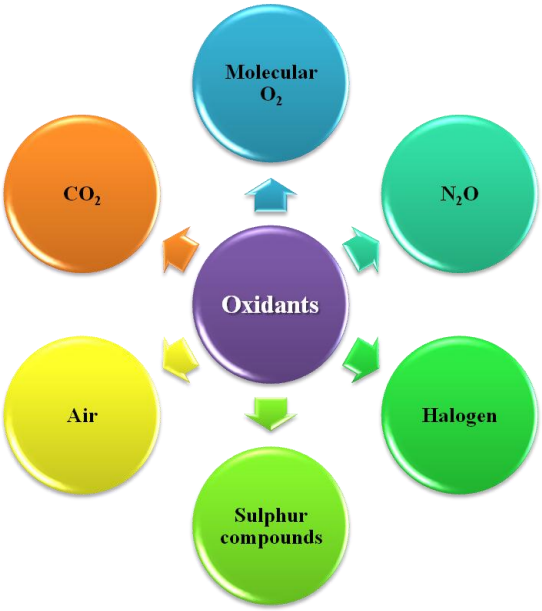

Fig. 1.5 Various oxidants employed in ODH

The use of CO_2 has also drawn attention for the ODH of alkanes (*Eq. 1.10*) as a non-traditional oxidant while; the endothermic nature of the reaction demands high working temperature to activate CO_2 molecule [11]. Since CO_2 is less aggressive than O_2; over oxidation may be limited which improves the selectivity towards olefins. It also nullifies the danger of explosion compared to the reaction feed mixture containing alkane and molecular oxygen.

$$C_nH_{2n+2} + CO_2 \rightarrow C_nH_{2n} + CO + H_2O \qquad (Eq.\ 1.10)$$

In many instances, a mixture of different oxidants is also utilized to enhance product yield. The addition of a small amount of oxygen reduces the energy load, and so ODH in the presence of CO_2/O_2 admixture is practised [19]. Air is the cheapest, widely available and so the perfect candidate for ODH. A few reports are available where N_2O has been employed as an oxidant [20–21]. However, the high cost of nitrogen oxides discourages from engaging in

ODH reaction even in the laboratory scale. Thus, it can be concluded that the utilization of oxidants is advantageous to obtain high selectivity for the dehydrogenated products. However, environmental problems have to be considered while engaging sulphur and halogen-containing molecules in ODH reactions.

1.4.2. Thermodynamics

A classic DH reaction is energy-intensive and hence, endothermic in nature which is an equilibrium controlled process. High temperature and low pressure will favour the complete conversion in DH; but, the selectivity of the desired product will be low due to the formation of undesired products. ODH can be contemplated as an exothermic reaction while considering *Eq. 1.1* and *Eq.1. 2* to a general thermodynamic summation to *Eq. 1.3*. Water, the by-product can be successively removed from the reaction mixture and the equilibrium constraints will be avoided making the reaction thermodynamically favorable [22]. Conversely, the presence of oxygen in the reaction medium may increase the formation of oxygenated side products which is more favourable in the thermodynamic point of view. This can increase the risk of the ODH process. However, a part of the energy required for the DH process could be supplied by exothermic hydrogen combustion (*Eq. 1.2*) and the burning of coke deposits. Consequently, ODH can be carried out at lower temperatures compared to conventional DH [4].

1.4.3. Kinetics

Table 1.2 Typical bond energies involved in hydrocarbons [23]

Bond type	**Energy (kJ mol^{-1})**
C–C	376
Primary C–H	420
Secondary C–H	401
Tertiary C–H	390
Allylic C–H	361
Vinylic C–H	445

Initial studies in the late 20th century illustrated the first step involved in ODH is the homolytic cleavage of the weakest C–C bond (**Table 1.2**) to form alkyl species. Later, the chain propagation proceeds with the reaction of alkane with radicals or atomic species. **Table 1.3** shows the activation energy and rate constants of various gas-phase reactions involved in the ODH of ethane. The evaluation of these data illustrates that the reactions of O atoms and

OH radicals with alkene are more rapid than that of an alkane which will consecutively limit the product yield [4].

Table 1.3 Activation energies and rate constants involved in ethane ODH [24]

Reaction	**E_a (Kcal Mole^{-1})**	**k(Sec^{-1} or cm^3 mol sec^{-1}) at 873 K**
$C_2H_6 \rightarrow CH_3 + CH_3$	88.31	2.4×10^{-3}
$C_2H_6 + O \rightarrow C_2H_5 + OH$	6.36	6.6×10^{11}
$C_2H_6 + OH \rightarrow C_2H_5 + H_2O$	1.81	3.1×10^{9}
$C_2H_4 + O \rightarrow CH_3 + HCO$	1.13	1×10^{12}
$C_2H_4 + OH \rightarrow C_2H_3 + H_2O$	1.23	2.4×10^{12}
$C_2H_4 + OH \rightarrow CH_3 + CH_2O$	0.96	1.2×10^{12}

Heterogeneous catalysis occurs on the active sites present in the catalyst surface. A gas-solid reaction is postulated to proceed through the following different steps.

1. Diffusion of the reactant to the catalyst surface
2. Adsorption of the reactant on the active sites
3. Reaction on the active sites
4. Desorption of products from the active sites
5. Diffusion of the products from the catalyst surface

Several factors depend on the rates of these steps are observed such as concentration gradients flow, diffusion characteristics of the fluid stream, the porosity of the catalyst, dimension of the pores and extent of interconnectivity. Various kinetic models used for the kinetic interpretation of ODH are; Eley-Rideal model, Rake model, Langmuir-Hinshelwood model, Redox or Mars van Krevelen model and power-law model [25].

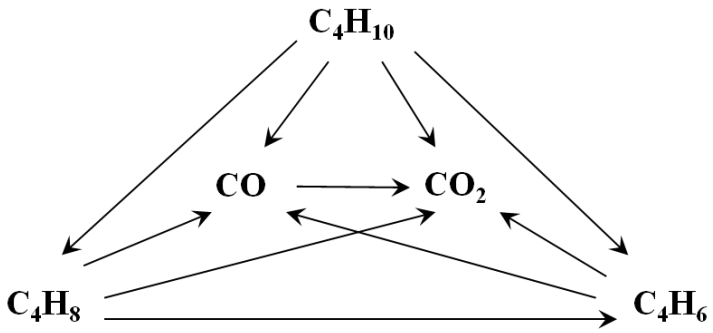

Scheme 1.1 Proposed reaction network for the ODH of butane [26]

The kinetics of ODH is described by the parallel-consecutive reaction networks wherein the formation of desired alkenes, consecutive oxidation and direct formation of carbon oxides are considered. For instance, the reaction network for the ODH of butane has been illustrated in

Scheme 1.1. Nonetheless, a part of these products is also produced by the consecutive DH and total oxidation of butenes. On the other hand, the experimental results proved that increase in butenes, BD and carbon monoxide partial pressures do not influence the rate of butane consumption [26]. As per the kinetic studies, CO_x was formed mainly by the consecutive oxidation of alkene. Therefore, the MVK model is mainly proposed for the kinetics explanation of ODH of lower alkanes.

1.4.4. Reaction mechanism

Different research groups have discussed multiple reaction mechanisms of the ODH reaction. The major steps included in the general ODH mechanism are the following [4].

1. Interaction of alkane with the catalyst
2. C–H bond of alkane will rupture to form alkyl species
3. The reaction of C–H bond with the surface oxygen to form an alkene
4. Regeneration of active species

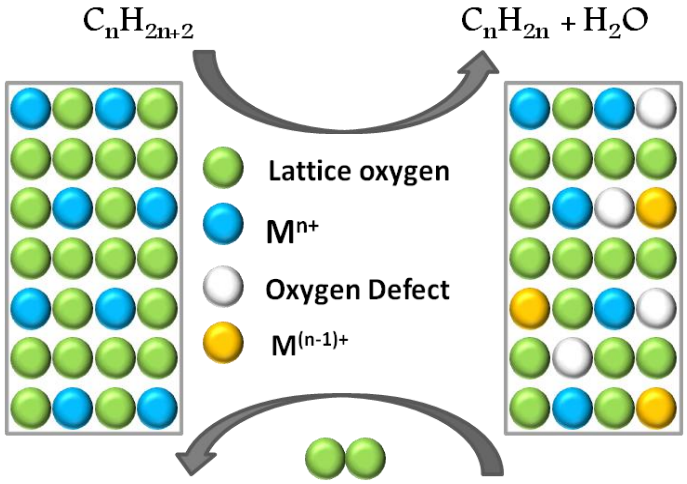

Fig. 1.6 The MVK redox model

The reactivity of surface oxygen, the reducibility of the metal ions and the environment of the active site will influence the reaction route [27]. ODH of C_4 hydrocarbons mainly proposed to follow Mars van Krevelen (MVK) mechanism or the redox model. A typical MVK mechanism consists of some elementary steps. Initially, an alkane adsorbed on the catalyst surface will cleave the weakest C–H bond which is the rate-limiting step [28] producing an allylic intermediate. Then, lattice oxygen from the catalyst will be inserted into the allyl intermediate forming the desired products. Ultimately, the external supply of oxygen will re-oxidize the catalyst surface to complete the redox cycle [29]. This cycle will be repeated and hence, the catalyst lifetime will improve. Accordingly, the nature, amount as well as the

mobility of oxygen species involved during the reaction is critical for MVK mechanism. The electrophilic peroxide O_2^{2-} and superoxide O_2^- species usually chemisorbed on the catalyst surface causes deep oxidation of hydrocarbons while the nucleophilic O^{2-} lattice oxygen anions are selective towards the required products [12]. A general representation of the metal oxide surface shown in **Fig. 1.6** simply explains the MVK mechanism.

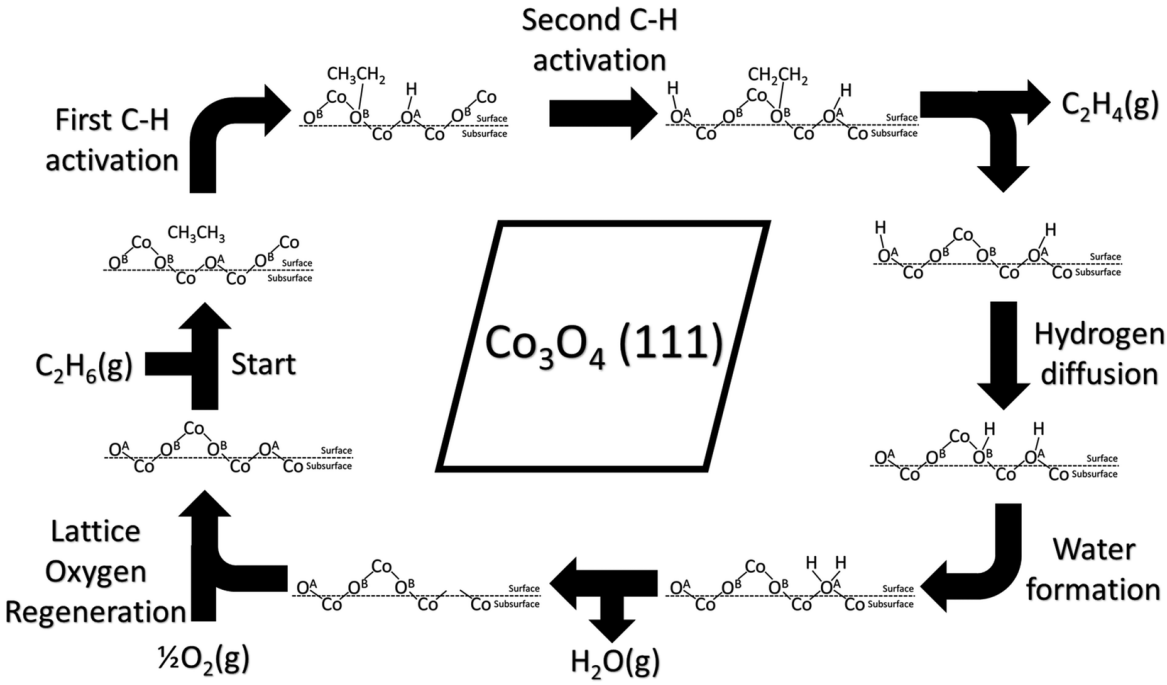

Scheme 1.2 The catalytic cyclic mechanism of ODH of ethane on Co_3O_4 [30]

Victor *et. al.* have been described the ODH of ethane over (111) plane of Co_3O_4 nanorods. Using the DFT method, the complete cycle for the MVK mechanism has been explained as illustrated in **Scheme 1.2** [30]. Because of that, C–H activation on the surface oxygen is the preliminary step. Hydrogen diffusion, water formation and lattice oxygen regeneration processes are taking place at the active sites followed with alkane activation. This example might best demonstrate the MVK mechanism which applies to many aliphatic as well as aromatic hydrocarbons. The participation of lattice oxygen in the formation of products will help to relate the catalytic activity with the thermodynamic parameters characterizing the catalyst lattice [31]. Downie *et. al.* have been developed a steady-state adsorption model (SSAM) influenced by the MVK model [32]. This method was postulated by making the assumptions that oxygen dissociation or oxygen desorption during the process is not negligible. Furthermore, a steady-state is assumed between the rate of adsorption of oxygen on the surface and the rate of removal of oxygen through the reaction with hydrocarbon from the gas phase. Understanding the proper mechanism will help to tune the catalyst to achieve better yield of olefins. The

design of a suitable catalyst with appropriate stable and active oxygen species for ODH is a pivotal challenge.

1.5. Factors affecting ODH

The reaction parameters involved in a catalytic process is critical to contribute towards the activity. Nature and composition of the catalyst has a primary role in defining the desired product. Other factors influencing ODH reaction are promoters, temperature, feed composition, and contact time. Proper tuning of these variables can considerably improve the product yield. Some important parameters affecting the ODH of lower alkanes have been discussed here.

1.5.1. Addition of promoters

Bromine, iodine and sulphur compounds can be used as promoter as well as dehydrogenating agent (oxidant). The addition of halogen can catalyze radical ODH of alkanes in the gas phase at relatively lower temperatures. Shell and Petro-Tex developed a process for the ODH of propane with high propene selectivity in the presence of iodine [33]. For butane, the Shell process with iodine is known as Idas process [34]. However, corrosion, product contamination and low space-time yield are the drawbacks of this process [35]. Besides, the environmental issues and the price of halogen compounds limit from the commercialization of this process. Several alkali metals like Li, Na, K, and Cs are exploited to improve the selectivity of olefins [36]. They reduce surface acidity of the catalyst and so increase product desorption from the catalyst. Increase in BD production is achieved by using alkaline earth metals as reported by Madeira *et. al.* using the $NiMoO_4$ catalyst [37]. **Table 1.5** represents some important catalysts consisting of alkali and alkaline earth metals for the ODH of C_4 hydrocarbons.

1.5.2. Catalyst composition

The composition of the catalytic system is a crucial factor in describing the activity of the catalyst. Multi-functionality in the material is mandatory to catalyze various steps involved in ODH. Mixed oxides containing two or more metals and carbon-based materials are the main categories of catalyst systems implemented by the researchers. In this regard, the precursor used, [4] nature of the support, [38] phase composition [38, 39] and calcination temperature [39] are observed to influence the activity trend in ODH reactions. Oxides of vanadium and molybdenum are widely exploited for this reaction, while the former is more preferred. For example, V-Mg-O system has MgO and magnesium orthovanadate ($Mg_3(VO_4)_2$) as major

phases. It can also form magnesium pyrovanadate ($Mg_2V_2O_7$) and magnesium metavanadate ($Mg_2V_2O_6$) by changing the synthesis method [16]. However, previous studies proved $Mg_3(VO_4)_2$ as the active phase for the ODH of n-butane and $Mg_2V_2O_7$ phase is non-selective towards butenes [18].

1.5.3. Operating conditions

Reaction conditions are important tools to alter the conversion and selectivity of a reaction. Amount of catalyst, reaction temperature, space velocity, reactor feed ratio etc., could be tuned to achieve optimum operating conditions for the highest activity. For example, Corma *et. al.* have observed an increase in the selectivity for DH products with the increase in reaction temperature while this relationship could not establish in the case of propane ODH [38, 40]. For the ODH of n-butane, a decrease in oxygen to butane ratio and reaction temperature has increased the selectivity of butanes and butadiene [39]. As a consequence, a low reactant to oxygen ratio is preferred for the studies to maintain feed flow out of explosive limit for safety considerations. Besides, the catalyst weight, as well as reactor feed, may be varied to achieve sufficient contact time. Optimizing the reaction parameters to improve the productivity of any catalyzed reaction is a regular practice.

1.5.4. Reducibility

Table 1.4 Effect of Cs in $NiMoO_4$ on rates of n-butane conversion [41]

Catalyst	**T_{onset}[a] (°C)**	**r_{butane}[b] $\times10^{-3}$ (mol/h g)**	**r_{butane}[b] $\times10^{-5}$ (mol/h m^2)**
$NiMoO_4$	300	8.9	20.1
1 % Cs–$NiMoO_4$	320	2.5	7.1
3 % Cs–$NiMoO_4$	335	1.4	5.0
6 % Cs–$NiMoO_4$	350	1.0	3.7

[a]Temperature of onset of reduction.
[b]Rates of butane conversion.
Operating conditions: T = 475 °C, butane:O_2:N_2 = 4:9:87, W/F = 12 g hr/mol_{butane}, W = 0.300 g.

Temperature programmed reduction analysis can furnish information about the reducibility of catalysts. As discussed in S**ection 1.4.4**, redox centres on the catalyst play a major role in ODH as they will participate in the MVK mechanism through which the reaction is proposed to occur. According to this mechanism, lattice oxygen will be removed which is accompanied by the reduction of the neighbouring cation. Hence, the ease of oxygen removal will depend on the reducibility of the cation in the lattice. Madeira *et. al.* have studied the ODH of n-butane over unpromoted and the Cs promoted α-$NiMoO_4$ catalysts. On addition of Cs (1–6

%), the reducibility of the catalysts has decreased which is observed as an increase in reduction temperature in the TPR profile. Corresponding to that, n-butane conversion is gradually reduced and the values are shown in **Table 1.4**. This may be considered as a proof for MVK mechanism [41].

1.5.5. Nature of oxygen species

Another factor that considerably affects ODH selectivity is the nature of oxygen species. Oxygen reactivity and availability will depend on the metal-oxygen bond strength and the atomic arrangement of the crystal lattice respectively; while the oxygen diffusivity through the lattice is also important for the ODH reaction mechanism [4]. Equilibria between the adsorbed and gaseous oxygen species will be established as given in *Eq. 1.11* from an electrophilic (O_2^-) to nucleophilic (O^{2-}) oxygen.

$$O_2\,(gas) \leftrightarrow O_2\,(ads) \leftrightarrow O_2^-\,(ads) \leftrightarrow O_2^{2-}\,(ads) \leftrightarrow 2O^-\,(ads) \leftrightarrow 2O^{2-}\,(lattice) \qquad \textit{(Eq. 1.11)}$$

The electron-deficient oxide (O^-), superoxide (O_2^-) and peroxide (O_2^{2-}) species will attack C=C which are electron-rich regions of hydrocarbons and lead to the combustion process. Conversely, the nucleophilic lattice oxygen (O^{2-}) with a high electron density will react with the electron-poor sites and helps in partial oxidation. Furthermore, the reactivity of oxygen depends on the strength of the metal-oxygen bond. The atomic arrangement within the material and the ease of oxygen diffusion through the crystal lattice are responsible for improving the reaction rate.

1.5.6. Acidic-basic sites

Acidic-basic properties are very crucial for the activation of C_4 hydrocarbons during the ODH process. Concepcion *et. al.* have studied vanadia loaded on different supports with varying acidity and basicity for the ODH of light alkanes [42]. **Fig. 1.7** shows the selectivity of olefins in the ODH of C_2-C_4 alkanes at 550 ºC (for propane and n-butane) and 600 ºC (for ethane) with an alkane conversion of 30 % over V-based catalysts. It was observed that ethylene selectivity is improved with the acidity of the catalyst support while; an opposite trend is detected with n-butane. In contrast, the behaviour of propane in ODH was difficult to correlate with the nature of the support as it was affected mainly by the nucleophilicity of surface oxygen species [43]. They have discovered that the selectivity must be optimized with the alkane feed. Butenes and BD consist of high electron densities at the bonds and are basic in nature. Hence, they will weakly adsorb on basic catalysts which make easy desorption of them from the active sites. Thus, the selectivity of these products will be

enhanced. In conclusion, acidic-basic properties will navigate the ODH reaction by quick desorption of alkenes which prevents over oxidation to form oxygenated products and carbon oxides.

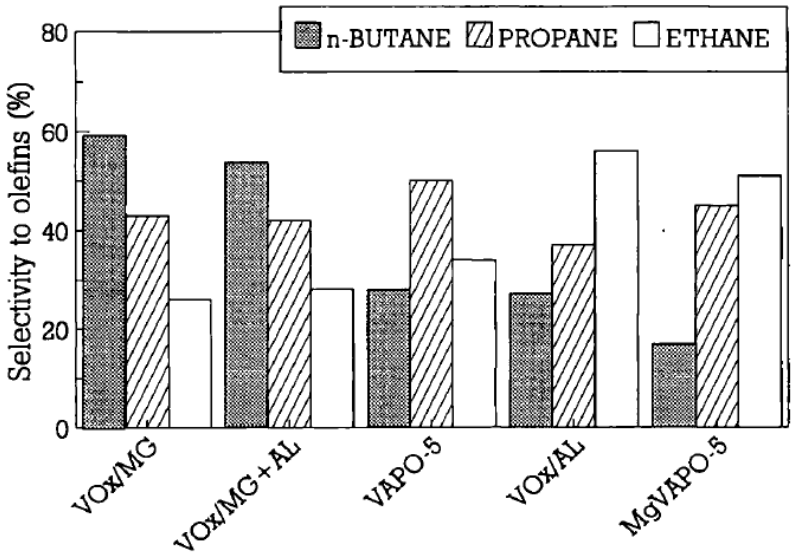

Fig. 1.7 Effect of acidic-basic supports. MG, AL, APO-5 are MgO, Al_2O_3 and aluminophosphate respectively. [42]

1.5.7. Reactor configurations

The type of reactor chosen for the process will largely affect the activity of the catalyst for alkane conversion. Various reactors so far engaged in ODH are summarized in **Fig. 1.8**. Usually, fixed bed reactors (FBR) were preferred for the reaction. However, the possibility of over oxidation of the products is a drawback while considering the size of the reactor tubes. In that context, fluidized bed reactors were developed for better activity. The kinetic studies for the ODH of C_4 hydrocarbons over 30VMgO catalyst illustrated the easy activation of n-butane in circulating fluid bed reactors for the future applications where; after the reaction zone the catalyst is re-oxidised by oxygen in a regeneration zone [26]. Hence, the lattice oxygen could be utilized for the ODH reaction to improve the BD selectivity followed by the periodical regeneration of lattice oxygen. This can be achieved by multiple or mobile or fluidized bed reactors. Meanwhile, separate hydrocarbon and oxygen feed could be supplied using two-zones fluidized bed reactor [44]. The safer operation and super performance compared to a conventional fluidized bed reactor are the added advantage of these types of reactors.

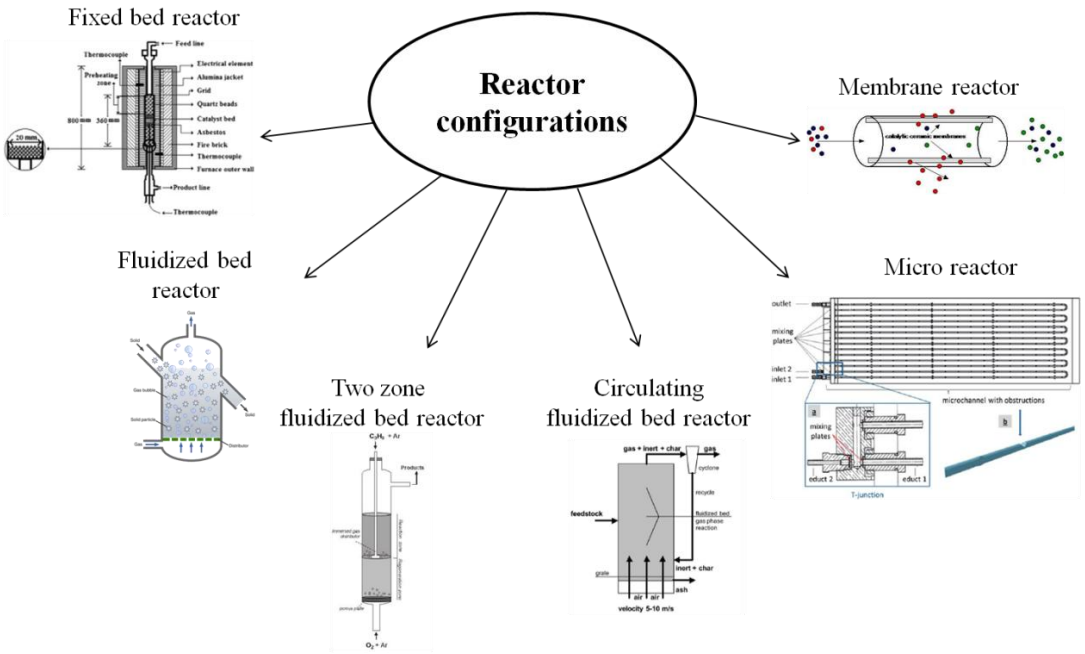

Fig. 1.8 Different types of reactors

Later, the emerging of microreactors allowed understanding the reaction mechanism and kinetic studies while the industrial implementation remains a challenge. The productivity can be improved if the feed of oxygen and alkane is controlled in a membrane reactor which was developed in the last two decades [45]. Here, one of the product can be successively removed which can shift the equilibrium and the membrane allow the fine control of oxygen distribution over the bed [45, 46]. A special kind of reactor is also available in which an electrochemical process is used for the extraction of oxygen from the gas mixture using a membrane and transferred to another zone containing hydrocarbon. Meanwhile, some simulation studies have been carried out with VMgO catalyst in a differential side stream catalytic membrane reactor [47]. A combination of different reactors may also be also utilized to improve catalyst performance.

1.6. Challenges involved in ODH

Researchers were concerned about developing a catalyst that can activate only the C–H bond of hydrocarbons. **Table 1.2** explains the difficulty of activating C–H bonds compared to the C–C bonds of hydrocarbons. Due to the nature of the chemical bonds involved, many side reactions are more favourable than the desired reaction. However, secondary products generally have no economic interest. The main challenge of the ODH process is to avoid total oxidation of desired products (olefins) by successfully desorbing it from the active sites so that the productivity can be improved. However, the more reactivity of products than the

reactants may easily lead to combustion or cracking which will reduce the catalytic activity. The rate of undesired side reactions is tabulated in **Table 1.3** and discussed in **Section 1.4.3**. To maintain the activity, the ODH process on metal oxides require high O_2 to butane ratio which may lead to total oxidation. Thus, inhibition of unwanted products and improving the selectivity of olefins are being the critical issues of this process. Low conversion level has to be maintained to improve the selectivities; but, the separation of an individual component from the product stream is the biggest task. Moreover, the deactivation of the catalyst by coke formation is very significant.

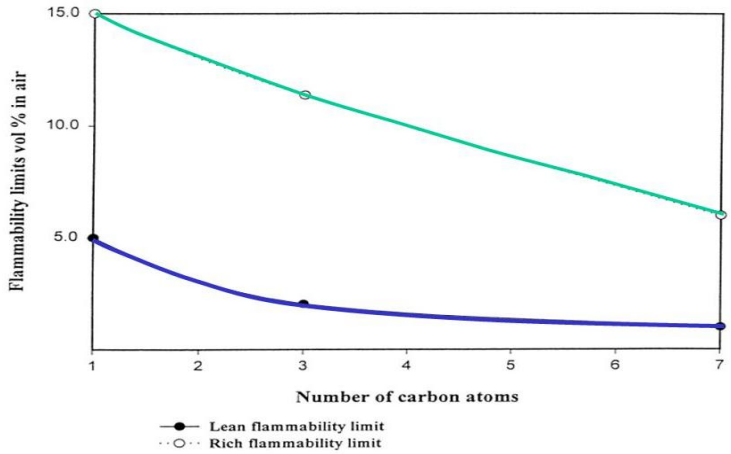

Fig. 1.9 Flammability limit of different hydrocarbons

For a gas mixture containing fuel and oxygen, there is a particular proportion of the components to avoid explosion which is determined by the explosive limit or flammability limit. The mixture should not be within this minimum (lower explosive limit, LEL) and maximum (upper explosive limit, UEL) concentration. Below LEL, the mixture will be too lean to explode and above UEL, it will be too rich and results in deflagration. These values will vary for different gases. **Fig. 1.9** represents the variation in ELs of hydrocarbons with diverse carbon atoms. The values differ even within the C_4 hydrocarbon family. Flammability ranges of n-butane, 1-butene and isobutane are 1.8–8.4, 1.6–10.0 and 1.8–8.4 respectively [48, 49]. The exothermic nature of the ODH reaction increases the risk factors and the feed composition should be taken into account to avoid the explosive nature. Thus, catalysis researchers have to meet numerous challenges to overcome the risks of this reaction.

1.7. Isobutene

Isobutene (2-methylpropene) is one of the important feedstock chemical, which is extensively used as a building block for the synthesis of a vast of intermediates in the chemical industry.

It is a vital precursor for the synthesis of various oxygenates like methyl *tert*-butyl ether (MTBE), ethyl *tert*-butyl ether (ETBE), and methacrylates which are used as an octane enhancing additives in gasoline [50]. Isobutene is also widely used in the polymer industry for the production of butyl rubber [51]. **Fig. 1.10** represents major applications of isobutene. The estimated increasing demand for isobutene soon insists on the need for alternative pathways other than conventional naphtha SC and crude oil fluid catalytic cracking methods. In this regard, catalytic DH of isobutane acquires much significance due to the available low-cost feedstock [52]. However, the endothermicity of this process requires elevated operational temperature (550–650 °C) to obtain a high yield of isobutene.

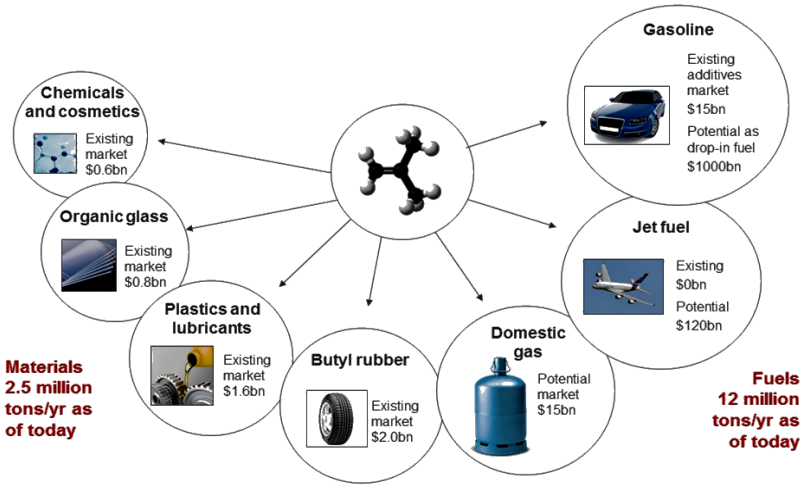

Fig. 1.10 Industrial importance of isobutene [53]

Chromium and platinum-based catalysts have been extensively studied for isobutane dehydrogenation (DHisoB). Pt-Sn/Al_2O_3 and CrO_x/Al_2O_3 systems are well explored and implemented in the industries, a few decades back. Even though these catalytic systems are giving satisfactory results; they are suffered from some disadvantages. A part of chromium ions exists in carcinogenic Cr^{6+} in alumina supported chromium catalyst causing severe environmental threats [54, 55]. Also, the possible sintering of Pt nanoparticles and high-cost limits Pt-based catalysts to some extent [56, 57]. Moreover, catalyst deactivation due to coke deposition is unpreventable at stringent reaction conditions. Hence, the development of an environmentally friendly and cost-effective promising catalyst for the non-oxidative dehydrogenation of isobutane becomes imperative.

1.8. Catalytic systems for C_4 activation

Supported and unsupported catalysts have been used for the activation of C_4 hydrocarbons. Multi-component materials are preferred for this purpose in order to catalyze various steps

involved. The catalytic systems used for C_4 activation could be categorized into three depending on the composition.

1.8.1. Alkali/alkaline earth metal-based catalysts

Several alkali (Li, Na, K and Cs) and alkaline earth (Be, Mg, Ca and Ba) metal-based catalysts are reported for the ODH of C_4 hydrocarbons **(Table 1.5)**. Among them, lithium-based catalysts are well exploited. However, the activity of these catalysts is generally low at lower temperatures. Halides can promote the selectivity of alkene and selectivities are observed to increase with temperature. The acidic sites of the material harmful for the reaction can be neutralized by the addition of alkali/alkaline earth ions [12]. The increased basicity can facilitate the easy desorption of the olefinic products. Thus, the formation of unwanted side products and carbon oxides may be prevented. However, the effect of these metals may vary with the catalyst system and the selected C_4 hydrocarbon [4].

1.8.2. Transition metal-based catalysts

Appropriate catalyst should be selected depending on the nature of the reactant alkane. Many transition metal-based materials are engaged in ODH taking advantage of their redox nature. Among all, molybdates, vanadates and nickel-based systems are well established for the ODH of n-butane. Several studies have shown that VMgO mixed oxide is the best catalyst for n-butane ODH. Group V and VI transition metal oxides have been explored as bulk or supported catalysts and among all, vanadium is the well-studied element. The acid-base nature of the supports is a crucial parameter for the catalytic activity and so alumina and silica-supported catalysts are selected by many research groups [58, 59]. Meanwhile, bismuth molybdates and metal ferrites have also been extensively explored as ODH catalysts for n-butenes [60]. For isobutane conversion, alumina-based materials are the most studied system [61–63]. A large number of transition metal-containing catalytic systems are reported in the literature and some of the selected catalysts are listed in **Table 1.5**.

1.8.3. Carbon-based catalysts

Carbon materials are terminated with functionalized oxygen groups (**Fig. 1.11**) such as the electron-rich ketonic as well as quinoidic species which can be utilized for the redox process occurs during the ODH of C_4 hydrocarbons [64, 65]. The Lewis basic sites on the surface of carbon can abstract hydrogen atoms from C–H bond and proceed to the formation of alkenes. Thus, different kinds of carbon will function as a metal-free catalyst centre. A few of the

reported carbon-based systems for the ODH of C_4 hydrocarbons are listed in **Table 1.5**. It is observed that the surface modification and the heteroatoms will increase the selectivity of corresponding olefins [66].

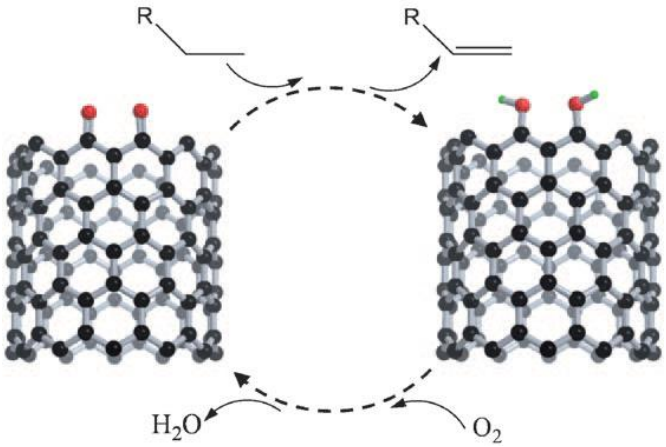

Fig. 1.11 ODH of alkane over functionalized CNTs [67]

According to the current understandings, nucleophilic ketonic carbonyl groups, and defect sites on graphene layers are the active species to play role in ODH reactions. Thus carbon is one of the promising catalysts in progressing material and sustainable chemistry. Even if the carbon materials can suppress the formation of non-selective oxygen species, the low overall activity for ODH is a drawback for these type of materials.

Table 1.5 Activation of C_4 hydrocarbons on different catalyst systems

Reaction system	**Catalyst**	**Yield (%)**	**Ref:**
n-butane to BD (ODH)	Mg-Dy-Li-Cl	50	[68]
	VO_x/Al_2O_3	6	[69]
	MoO_x/Al_2O_3	5	[70]
	CNT's	28	[71]
n-butane to butenes (ODH)	Modified CNT's	9.5	[72]
	Nano diamond	1	[73]
	Single-walled CNT's	0.5	[73]
	Gr-oCNT	10	[65]
1-butene to BD (ODH)	Sulfated $ZnFe_2O_4$	79	[74]
	$BiMoFe_x$ oxide	62	[75]
	PdM/SiO_2 (M=Bi, Fe, Ge, In, Sn, Zn)	12	[76]
	CNT's	28	[64]
Isobutane to isobutene (DH)	Pt/Sn/KL zeolite	56	[77]
	Transition metal sulfides	60	[78]

	Graphene oxide	3	[79]
	Activated carbon	10	[80]

Generally, unsupported metal oxide catalysts composed of multi-transition metals are used for C_4 hydrocarbons activation. A thorough study of the existing literature proves that multi-functionality is one of the central criteria to design suitable catalyst towards the selective oxidation of C_4 hydrocarbons.

1.9. Selection criteria of ODH catalyst and reaction parameters

An ideal ODH catalyst should be designed to conquer the disadvantages of existing materials. The first C–H bond activation is the rate-determining step of ODH reaction and hence, Lewis basic sites are compulsory for this purpose. Meanwhile, some amount of acidic sites can also contribute towards the selectivity of olefin by desorbing the formed olefins immediately after the reaction. The literature says that the reaction generally proceeds through MVK mechanism and so, metal cations which can show variable oxidation states are preferred with a higher oxidation state. Moreover, the material with a minimum amount of electrophilic oxygen may reduce the undesired reactions. The proper selection of the reactor configuration plays an indispensable role to increase the olefin yield. Likewise, membrane reactor would be a good candidate where the oxidant distribution over the catalyst can be controlled. The reaction parameters like temperature, feed flow ratio, space velocity etc can also be tuned in such a way to increase the product yield. In addition, the multi-functional centres of the catalysts have to be arranged to achieve the proper transformation of reactants and quick desorption of the products. These are some important factors that should be acknowledged during the catalyst design as well as ODH reaction towards attaining the best activity to compete with the industrial methods.

1.10. Industrial implementation

Selective conversion of C_4 hydrocarbons is a very significant technology with the increasing demands of olefins because the functionalizations of alkenes have extensive applications in the chemical industries. So far of now, selective oxidation of n-butane is the only reaction that has been commercialized [35]. Alkene necessity could be fulfilled by the industry utilizing the ODH process which hit the restrictions of conventional DH by reducing the operational energy and making it economically feasible. The trend in the activation of alkanes mainly follows the C–H bond strength. The bond energies for primary C–H, secondary C–H, tertiary C–H, allyl C–H and vinyl C–H groups are 420, 401, 390, 361 and 445 kJ/mol

respectively as shown in **Table 1.2.** Hence, lower alkanes will be activated at higher temperatures. From **Fig. 1.3**, it is evidenced that selectivity decreases with the increase in conversion due to the higher oxidising properties of olefins. These are major reasons why the ODH process has not been executed in industries [81].

Table 1.6 Commercial C_4 activation technologies [12, 82, 83]

Technology name	**Catalyst**	**C_4 olefin selectivity**	**Reactor type**	**Temperature (°C)**	**Development stage**
CATOFIN	CrO_x/Al_2O_3 with alkaline promoter	89–93	Adiabatic fixed bed	565–649	Commercial
UOP Oleflex	Pt-Sn/Al_2O_3 with alkaline promoter	91–93	Adiabatic moving bed	550–620	Commercial
FBD	CrO_x/Al_2O_3 with alkaline promoter	91	Fluidized bed	535–590	Commercial
FLOTU/Tsinghua	Pt-Sn/SAPO-34	81–86	Bimodal fluidized bed	570–610	Pilot plant
SABIC	Pt-Sn/K/SAPO-34	80–85	Adiabatic fixed bed and FBR	560–600	-

The potential advantages of ODH are not enough to convince the industries for commercialization. Instead, the best yields reported until now are still far from appealing for the industrial implementation [84]. Furthermore, the hazardous mixture of hydrocarbon and oxygen at high temperature will increase the hazard level of the explosion. Subsequently, the maximum yield of alkenes obtained from ODH is still less than that obtained from the DH process. In a while, an efficient catalyst with a promising reactor configuration might be discovered providing high conversion and selectivity for the ODH of light alkanes. Some of the industrially recognized DH technologies for C_4 up-gradation are listed in **Table 1.6**.

1.11. Objectives of the work

Olefins derived from the C_4 hydrocarbon family serve as vital precursors for the production of synthetic rubbers and organic chemicals. ODH overcomes many of the shortcomings of conventional SC as well as DH for the synthesis of C_4 alkenes. Previous studies have shown that ODH of C_4 hydrocarbons can be performed over multi-component metals and carbon-based catalytic systems. A thorough investigation of the available literature manifested that transitional metal-containing oxide can exhibit redox property preferably existing at a higher oxidation state and so will be a perfect candidate to perform the MVK mechanism through

which ODH reaction is proposed to proceed. The minimum amount of electrophilic oxygen species with optimum acidic-basic properties will reinforce the selectivity towards C_4 olefins. Considering all these aspects of different transition metal-based, mixed oxides were designed separately for the selective oxidation of n-butane, 1-butene and isobutane to butenes; BD and isobutene respectively. The reactions are performed in a continuous flow mode fixed bed reactor and the products are analyzed through gas chromatography. Reaction parameters like temperature, feed flow, C_4 hydrocarbon to oxidant ratio etc., were also varied over the best catalyst composition to attain maximum selectivity towards the desired olefin. Also, the catalytic activity is correlated to the physicochemical properties of the material with the help of various characterization techniques.

1.12. Thesis structure

The thesis is broadly divided into six chapters.

Chapter 1: Introduction

A general introduction on catalysis and selective activation of alkanes specifically the C_4 hydrocarbons are presented in this chapter. The importance of elected olefins such as BD and isobutene are stated along with the details of existing production methods. Further, the advantages and the scientific aspects of ODH are elaborated. A literature survey of the research problem is briefly explained with cited examples. Finally, the catalyst selection criteria and reaction parameters are summarized. A concise outlook of the work towards commercial implementation is also accomplished.

Chapter 2: Catalyst synthesis and characterization

The synthesis pathways adopted for the preparation of metal oxide systems are elaborately discussed. Different physicochemical characterization techniques employed for the investigation of the synthesized catalysts and the basic principles are thoroughly explained. The structural, textural, thermal properties as well as composition of these materials are studied with the help of diverse analysis methods like powder XRD, N_2 sorption, SEM, TEM, Raman spectroscopy, XPS, FT-IR, TGA, TPR, TPD, ICP-AES and DRUV-Visible spectroscopy. The basic principles of these techniques as well as the main characteristics of the fixed bed reactor and gas chromatograph are depicted. The details of instruments engaged for the thesis work are also given.

Chapter 3: Enhanced catalytic activity of boron-containing MgO on vanadium loading for the oxidative dehydrogenation of n-butane

In this first working chapter, ODH of n-butane to BD is investigated over vanadia loaded boron-containing MgO systems in the presence of oxygen. The best catalyst composition is screened, and the reaction conditions are varied to maximize the desired product yield. The role of active phase for the selective n-butane oxidation is elucidated with the help of proper analysis methods.

Chapter 4

Chapter 4 is discussed about the oxidative dehydrogenation of 1-butene and is successively divided into two parts depending on the catalyst system employed.

A. Influence of transition metal addition in bismuth ferrite on the oxidative dehydrogenation of 1-butene

Here, the synthesis of BD is achieved from a comparatively better activating starting molecule viz; 1-butene by the ODH process using molecular oxygen over different transition metals such as Ni, Cu, Cr, Mn, Zn and Co loaded bismuth ferrites existing in the distorted perovskite structure. The influence of Zn in boosting the product selectivity is analyzed with different physicochemical characterizations. The composition and reaction parameters are tuned for the highest BD yield.

B. Utilizing the oxygen carrier property of cerium iron oxide for the low-temperature synthesis of 1, 3-butadiene from 1-butene

The main aim of this chapter is to reduce the operating temperature for BD synthesis from 1-butene by employing a cerium-iron mixed oxide catalyst. The oxygen carrier property of this material is utilized for the dehydrogenation reaction in the absence of an external oxidant. The stability and recyclability of the material are being studied. The structural changes occurring on the catalyst surface after the reaction is investigated using appropriate analysis techniques.

Chapter 5: Selective dehydrogenation of isobutane to isobutene over promoted mesoporous Fe-alumina catalysts

In this final working chapter, the importance of isobutene as well as the shortcomings of existing materials and methods is discussed. Dehydrogenation of isobutane over *in-situ* Fe loaded mesoporous alumina catalyst after impregnating P, K and Ag are studied. Promoters

have appreciably improved isobutane conversion compared to the *ex-situ* synthesized catalyst. The difference in the catalytic activity is explained with the help of suitable material characterization. Major reasons for catalyst deactivation are well analyzed and interpreted.

Chapter 6: Summary and conclusions

This chapter summarizes the major results retrieved from the activation of C_4 hydrocarbons such as n-butane, 1-butene and isobutane over different metal oxide-based catalytic systems. The present work is concluded by suggesting several outlooks and future perspective for further research in this particular area. The probability of industrial realization is also analyzed.

References

[1] J. Berzelius, Ann. Chim. Phys. 61 (1836) 146–151.

[2] https://www.chemicool.com/definition/catalyst.html

[3] G. Ertl, H. Knözinger, J. Weitkamp (Eds.), Handbook of Heterogeneous Catalysis; VCH, Weinheim: 1997.

[4] H.H. Kung, Oxidative Dehydrogenation of Light (C_2 to C_4) Alkanes. Eley, D.D., Pines, H., Haag, W.O., In Advances in Catalysis; Eds.; Academic Press: New York, 1994; Vol. 40, 1–38.

[5] Alpha Olefin Market Analysis By Product, (1-Butene, 1-Hexene, 1-Octene, 1-Decene, 1-Dodecene), By Application (Polyethylene, Detergent Alcohol, Synthetic Lubricants), By Region, And Segment Forecasts, 2018–2025.

[6] F. Cavani, Catal. Today 157 (2010) 8–15.

[7] J.J.H.B. Sattler, J.R. Martinez, E.S. Jimenez, B.M. Weckhuysen, Chem. Rev. 114 (2014) 10613–10653.

[8] C.N. Satterfield, Heterogeneous Catalysis in Practice; McGraw-Hill: New York, 1980.

[9] F. Trifiro, F. Cavani, Oxidative dehydrogenation and alternative dehydrogenation processes. Catalytic Studies, No. 41920 D, 1993.

[10] M.A. Chaar, D. Patel, H.H. Kung, J. Catal. 109 (1988) 463–467.

[11] B.M. Weckhuysen, R.A. Schoonheydt, Catal. Today 51 (1999) 223–232.

[12] J.C. Vedrine, Catalysts 6 (2016) 22–48.

[13] E. Caventou, Justus Liebigs Annalen der Chemie 127 (1863) 93–97.

[14] M. Dahlmann, J. Grub, E. Loser, Germany Ullmann's encyclopedia of industrial chemistry. Wiley-VCH Verlag GmbH & Co. KGaA, Weinheim: 2013.

[15] G.S. Whitby, Synthetic Rubber, Chapter 2, John Wiley & Sons, New York: 1954.

[16] O.O. James, S. Mandal, N. Alele, B. Chowdhury, S. Maity, Fuel Process. Technol. 149 (2016) 239–255.

[17] L.M. Madeira, M.F. Portela, Catal. Rev. 44 (2002) 247–286.

[18] H.H. Kung, Transition Metal Oxides: Surface Chemistry and Catalysis; Studies in Surface Science and Catalysis; Vil. 45, Elsevier: Amsterdam: 1989.

[19] S. Ge, C. Liu, S. Zhang, Z. Li, Chem. Eng. 94 (2003) 121–126.

[20] J.P. Ramirez, A.G. Llamas, J. Catal. 223 (2004) 382–388.

[21] K. Nowinska, A. Waclaw, A. Izbinska, Appl. Catal. A Gen. 243 (2003) 225–236.

[22] M.M. Bhasin, J.H. McCain, B.V. Vora, T. Imai, P.R. Pujado, Appl. Catal. A Gen. 221 (2001) 397–419.

[23] D.R. Lide, Handbook of Chemistry and Physics, Ed. CRC press, 71st ed., 1990, 9–95.

[24] C.K. Westbrook, J.P. William, Cat. Sci. Technol. 37 (1984) I 17.

[25] R. Grabowski, Catalysis Reviews, 48 (2006) 199–268.

[26] A.A. Lemonidou, Appl. Catal. A Gen. 216 (2001) 277–284.

[27] M. Witko, R. Tokarz, J. Haber, Appl. Catal. A Gen. 157 (1997) 23–44.

[28] Z. Zhai, X. Wang, R. Licht, A.T. Bell, J. Catal. 325 (2015) 87–100.

[29] E. Grootendorst, Y. Verbeek, V. Ponec, J. Catal. 157 (1995) 706–712.

[30] V. Fung, F.F. Tao, De-en Jiang, Catal. Sci. Technol. 6 (2016) 6861–6869.

[31] C. Doornkamp, V. Ponec J. Mol. Catal. A Chem. 162 (2000) 19–32.

[32] J. Downie, K.A. Sheslstad, W.F. Graydon, Can. J. Chem. Eng. 69 (1965) 457.

[33] Y. Moro-oka, W. Ueda, Partial Oxidation and Ammoxidation of Propane: Catalysts and Processes. Catalysis; Specialist Periodical Report; Royal Society of Chemistry: Cambridge: 1994; Vol. 11, 223–245.

[34] M. Bohnet, M.; Eds. Ullmann's Encyclopedia of Industrial Chemistry, 6th Ed.; Wiley-VCH: Weinheim, Germany: 1999.

[35] S. Albonetti, F. Cavani, F. Trifiro, Catalysis Reviews, 38 (1996) 413–438.

[36] R.M. Martin-Aranda, M.F. Portela, L.M. Madeira, F. Freire, M. Oliveira, Appl. Catal. A-Gen. 127 (1995) 201–217.

[37] L.M. Madeira, R.M. Martın-Aranda, F.J. Maldonado-Hodar, J.L.G. Fierro, M.F. Portela, J. Catal. 169 (1997) 469–479.

[38] A. Corma, J.M.L. Nieto, N. Paredes, A. Dejoz, I. Vasquez, Oxidative Dehydrogenation of Propane and n-Butane on VMg-based Catalysts. In New Developments in Selective Oxidation II, Studies in Surface Science and Catalysis. Corberan, V.C., Bellon, S.V., Eds.; Elsevier: Amsterdam, 1994; Vol. 82, 113–123.

[39] M.A. Chaar, D. Patel, M.C. Kung, H.H. Kung, J. Catal. 105 (1987) 483–498.

[40] L. Smolakova, M. Kout, E. Koudelkova, L. Capekcan, Ind. Eng. Chem. Res. 54 (2015) 12730–12740.

[41] L.M. Madeira, M.F. Portela, C. Mazzocchia, A. Kaddouri, R. Anouchinsky, Catal. Today 40 (1998) 229–243.

[42] P. Concepcion, A. Galli, J.M.L. Nieto, A. Dejoz, M.I. Vazquez, Top. Catal. 1996, 3, 451–460.

[43] A. Corma, J.M.L. Nieto, N. Paredes, J. Catal. 144 (1993), 425–438.

[44] J. Soler, J.M.L. Nieto, J. Herguido, M. Menendez, J. Santamarıa, Ind. Eng. Chem. Res. 38 (1999) 90–97.

[45] M. Menendez, Membrane reactors as tools for improved catalytic oxidation process. In Handbook of Advanced Methods and Processes in Oxidation Catalysis. Duprez, D., Cavani, F., Eds.; Imperial College Press: London, UK, 2014; 921–942.

[46] C. Tellez, M. Menendez, J. Santamaria, AIChE J. 43 (1997) 777–784.

[47] D. Milne, T. Seodigeng, D. Glasser, D. Hildebrandt, B. Hausberger, Catal. Today 156 (2010) 237–245.

[48] Gas Data Book, 7th edition, copyright 2001 by Matheson Gas Products

[49] Bulletin 627, Flammability Characteristics of Combustible Gases and Vapors, copyright 1965 by U.S. Department of the Interior, Bureau of Mines.

[50] M.A. Centeno, M. Debois, P. Grange, J. Catal. 192 (2000) 296–306.

[51] H. Zhao, H. Song, L. Xu, L. Chou, Appl. Catal. A Gen. 456 (2013) 188–196.

[52] J.C. Serrano-Ruiz, A. Sepúlveda-Escribano, F. Rodríguez-Reinoso, J. Catal. 246 (2007) 158–165.

[53] https://www.global-bioenergies.com/

[54] F. Cavani, M. Koutyrev, F. Trifirò, A. Bartolini, D. Ghisletti, R. Iezzi, A. Santucci, G. Del Piero, J. Catal. 158 (1996) 236–250.

[55] V.Z. Fridman, R. Xing, Ind. Eng. Chem. Res. 56 (2017) 7937–7947.

[56] B.K. Vu, M.B. Song, I.Y. Ahn, Y.W. Suh, D.J. Suh, W.I. Kim, H.L. Koh, Y.G. Choi, E.W. Shin, Catal. Today 164 (2011) 214–220.

[57] H. Zhao, H. Song, L. Chou, J. Zhao, J. Yang, L. Yan, Catal. Sci. Technol. 7 (2017) 3258–3267.

[58] C.B. Murchison, G.E. Vrieland, Appl. Catal. A Gen. 134 (1996) 101–121.

[59] C.B. Murchison, G.E. Vrieland, B. Khazai, Appl. Catal. A Gen. 134 (1996) 123–145.

[60] E. Hong, J.H. Park, C.H. Shin, Catal. Surv. Asia 20 (2016) 23–33.

[61] G.J. Siri, M.L. Casella, G.F. Santori, O.A. Ferretti, Ind. Eng. Chem. Res. 36 (1997) 4821–4826.

[62] S. Kobayashi, S. Kaneko, M. Ohshima, H. Kurokawa, H. Miura, Appl. Catal. A Gen. 417–418 (2012) 306–312.

[63] U. Rodemerck, S. Sokolov, M. Stoyanova, U. Bentrup, D. Linke, E. V Kondratenko, J. Catal. 338 (2016) 174–183.

[64] X. Liu, D.S. Su, R. Schlogl, Carbon 46 (2008) 544 –561.

[65] J. Li, P. Yu, J. Xie, Y. Zhang, H. Liu, D. Su, J. Rong, J. Catal. 360 (2018) 51–56.

[66] B. Frank, J. Zhang, R. Blume, R. Schlogl, D.S. Su, Angew. Chem. Int. Ed. 48 (2009) 6913–6917.

[67] W. Qi, D. Su, ACS Catal. 4 (2014) 3212−3218.

[68] L. Leveles, S. Fuchs, K. Seshan, J.A. Lercher, L. Lefferts, Appl. Catal. A Gen. 227 (2002) 287–297.

[69] N. Madaan, R. Haufe, N.R. Shiju, G. Rothenberg, Top. Catal. 57 (2014) 1400–1406.

[70] B. Rman, K. David, S. Michal, T. Zdenek, Top. Catal. 58 (2015) 866–876.

[71] X. Liu, D. Su, R. Schlögl, Carbon 46 (2008) 547−549.

[72] J. Zhang, X. Liu, R. Blume, Z. Zhang, R. Schlögl, D. Su, Science 322 (2008) 73−77.

[73] X. Liu, B. Frank, W. Zhang, T.P. Cotter, R. Schlögl, D. Su, Angew. Chem., Int. Ed. 50 (2011) 3318−3322.

[74] H. Lee, J.C. Jung, I.K. Song, Catal. Lett. 133 (2009) 321–327.

[75] J.H. Park, H. Noh, J.W. Park, K. Row, K.D. Jung, C.H. Shin, Appl. Catal. A Gen. 431–432 (2012) 137–143.

[76] S. Furukawa, M. Endo, T. Komatsu, ACS Catal. 4 (2014) 3533−3542.

[77] R.D. Cortright, J.M. Hill, J.A. Dumesic, Catal. Today 55 (2000) 213–223.

[78] G. Wang, C. Li, H. Shan, ACS Catal. 4 (2014) 1139−1143.

[79] H. Xie, Z. Wu, S. Overbury, C. Liang, V. Schwartz, J. Catal. 267 (2009) 158−166.

[80] I. Gniot, P. Kirszensztejn, M. Kozłowski, Appl. Catal. A Gen. 267 (2009) 67−74.

[81] T. Blasco, J.M.L. Nieto, Appl. Catal. A Gen. 157 (1997) 117–142.

[82] Z. Nawaz, Rev. Chem. Eng. 2015 aop.

[83] K.J. Caspary, H. Gehrke, M. Heinritz-Adrian, M. Schwefer, Dehydrogenation of alkanes, in: G. Ertl, H. Knözinger, F. Schüth, J.Weitkamp (Eds.), Handbook of Heterogeneous Catalysis, second ed. Wiley 2008, 3206–3229.

[84] F. Cavani, N. Ballarini, A. Cericola Catal. Today 127 (2007) 113–131.

Chapter-2

Catalyst Synthesis and Characterization

2.1. Introduction

In this chapter, the experimental details involved during the systematic study of the thesis work are explained in brief. The synthesis strategies adopted for the preparation of various catalysts are clearly elaborated. All prepared materials are extensively analyzed for the crystallinity and porous nature with the help of powder X-ray diffraction and N_2 physisorption respectively. The microscopic analysis will provide the structure and morphology of the catalysts. Thermal properties are investigated through thermogravimetry as well as temperature-programmed studies employing H_2, NH_3 and CO_2 as probe molecules. Various spectroscopic techniques like XPS, UV-visible, Raman, FT-IR can reveal the surface features, composition and nature of the synthesized catalysts. The technical information of the instruments concerned with these analyses is given briefly. Furthermore, the reactor configuration involved in the activity measurement of the catalysts is specified. Qualitative and quantitative evaluation of the reaction products is done in gas chromatograph. The basic principle and instrumentation of the above-mentioned characterization methods are briefly discussed in this chapter.

2.2. Materials

The details of chemicals used in the catalyst synthesis for this study are represented in **Table 2.1**. All materials are employed as purchased without any further purification.

Table 2.1 Description of chemicals involved in catalyst synthesis

Name	Chemical formula	Purity (%)	Supplier
Magnesium nitrate	$Mg(NO_3)_2$	98.5	Merck
Aluminium isopropoxide	$C_9H_{21}AlO_3$	98.5	Aldrich
Bismuth nitrate	$Bi(NO_3)_3.5H_2O$	98	Alfa Aesar
Boric acid	H_3BO_3	99.5	Merck
Cerium nitrate	$Ce(NO_3)_3.\ 6H_2O$	99.5	Alfa Aesar
Chromium nitrate	$Cr(NO_3)_3.9H_2O$	99	Sigma Aldrich
Citric acid	$C_6H_8O_7$	99.5	Thomas baker
Cobalt nitrate	$Co(NO_3)_2.6H_2O$	98	Loba Chemie
Copper nitrate	$Cu(NO_3)_2.5H_2O$	99.9	Sigma Aldrich
Ethanol	C_2H_6O	99.9	CSS

Iron nitrate	$Fe(NO_3)_3.9H_2O$	99	Merck
Manganese nitrate	$Mn(NO_3)_2.4H_2O$	98	Alfa Aesar
Ammonium metavanadate	NH_4VO_3	99	Merck
Nickel nitrate	$Ni(NO_3)_2.6H_2O$	99	Merck
Nitric acid	HNO_3	69–70	Thomas Baker
Orthophosphoric acid	H_3PO_4	88	Merck
Oxalic acid	$C_2H_2O_4$	98	Thomas Baker
Potassium nitrate	KNO_3	99	Merck
Silver nitrate	$AgNO_3$	99.5	Alfa Aesar
Sodium hydroxide	NaOH	99	Merck
Zinc nitrate	$Zn(NO_3)_2.6H_2O$	99	Merck
Pluronic F-127	Triblock copolymer	-	Sigma Aldrich

Gases used for the DH of C_4 hydrocarbons are listed in **Table 2.2** given below. Pure gases and gas mixtures with purity ≥99.5 % are engaged during the product analysis and material characterization.

Table 2.2 List of gases and their application

Gas	**Supplier**	**Application**
n-butane	USA	Reaction
1-butene	USA	Reaction
Argon	Vadilal Chemicals Ltd, India	GC, Reaction
Helium	Vadilal Chemicals Ltd, India	GC, TPR, TPD, N_2 sorption
Hydrogen	Vadilal Chemicals Ltd, India	GC
Isobutane	USA	Reaction
Nitrogen	Vadilal Chemicals Ltd, India	GC, N_2 sorption
Oxygen	Vadilal Chemicals Ltd, India	Reaction
Zero air	Vadilal Chemicals Ltd, India	GC, TGA
5 % H_2/Ar	Vadilal Chemicals Ltd, India	TPR
10 % CO_2/He	Vadilal Chemicals Ltd, India	TPD
10 % NH_3/He	Vadilal Chemicals Ltd, India	TPD
10 % O_2/He	Vadilal Chemicals Ltd, India	TPR
Calibration gas mixture	Chemtron Science laboratories, India	GC calibration

2.3. Catalyst synthesis

A thorough study of the existing literature background of each kind of reaction is done prior catalyst selection. Following that, metal oxide based materials were elected for the DH of C_4 hydrocarbons. Different synthesis pathways like sol gel combustion, coprecipitation and impregnation are adopted for the material preparation. Boron–containing vanadium loaded MgO catalysts synthesized via combustion followed by wet impregnation are used for the ODH of n-butane. BD production from 1-butene is achieved by employing co-precipitated

bismuth ferrites and citrate gel combusted cerium iron mixed oxide as catalysts. Soft template based method is performed for Fe-alumina preparation followed by dry impregnation of the promoter for the isobutane DH. A more detailed explanation of each synthesis is given in the following.

2.3.1. Synthesis of vanadium loaded boron–containing MgO

a. Citrate gel combustion

Boron–containing MgO samples were prepared by the citrate gel combustion method reported elsewhere [1]. For a particular batch of material, $Mg(NO_3)_2$ and H_3BO_3 were employed as precursors. The calculated amount of these precursors was dissolved in deionized water to form different catalyst compositions. To this clear solution, 1.2 moles of citric acid per mol of the metal atom was added. Later, the solution was heated on a hot plate at 110 °C until the complete evaporation of water forming a gel. It was rapidly transferred into a furnace preheated to 550 °C and the gel were combusted to ashes. To eliminate the carbonaceous residues, these ashes were calcined at 550 °C for 12 h at 2 °C min^{-1} in a muffle furnace. The final solid was then ground well into a fine powder and labeled as xBMO where x = 0.1, 1, 5, 10, 25, and 50 according to the weight percentage loading of boron.

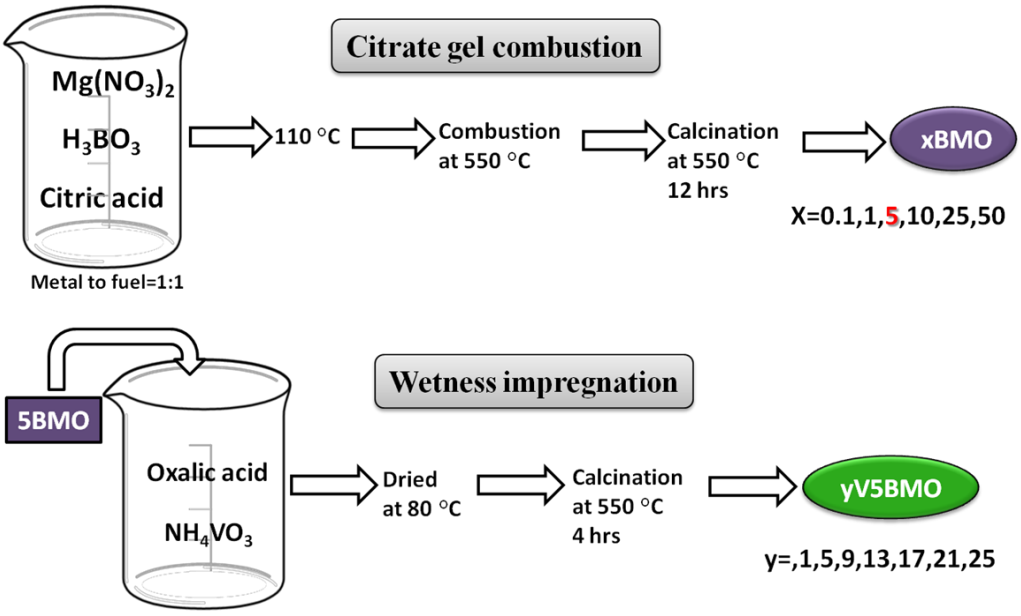

Scheme 2.1 Synthesis of vanadium loaded boron–containing catalysts

b. Wet impregnation of vanadium

Further, vanadium was wet impregnated to 5BMO in different amounts. For the synthesis of a single batch of vanadium loaded catalyst, a calculated quantity of NH_4VO_3 was dissolved in

minimum de-ionized water containing equal moles of oxalic acid. To this solution under stirring, a sufficient quantity of 5BMO was added and stirred at 80 °C. After drying, the solid was calcined at 550 °C at 2 °C min^{-1} for 4 h under static air. The final material was marked as y5BMO, where y stands for the loading of vanadium and y = 1, 5, 9, 13, 17, 21, 25. The schematic representation of the whole synthesis procedure is depicted in **Scheme 2.1**. The series of synthesized catalysts are listed in **Table 2.3**.

Table 2.3 Catalyst composition and codes of vanadia loaded boron–containing MgO

Sl. No.	Catalyst composition	Catalyst code
1	0.1 % B in MgO	0.1BMO
2	1 % B in MgO	1BMO
3	5 % B in MgO	5BMO
4	10 % B in MgO	10BMO
5	25 % B in MgO	25BMO
6	50 % B in MgO	50BMO
7	1 % V on 5BMO	1V5BMO
8	5 % V on 5BMO	5V5BMO
9	9%V on 5BMO	9V5BMO
10	13 % V on 5BMO	13V5BMO
11	17 % V on 5BMO	17V5BMO
12	21 % V on 5BMO	21V5BMO
13	25 % V on 5BMO	25V5BMO

2.3.2. Synthesis of bismuth ferrites

Coprecipitation method

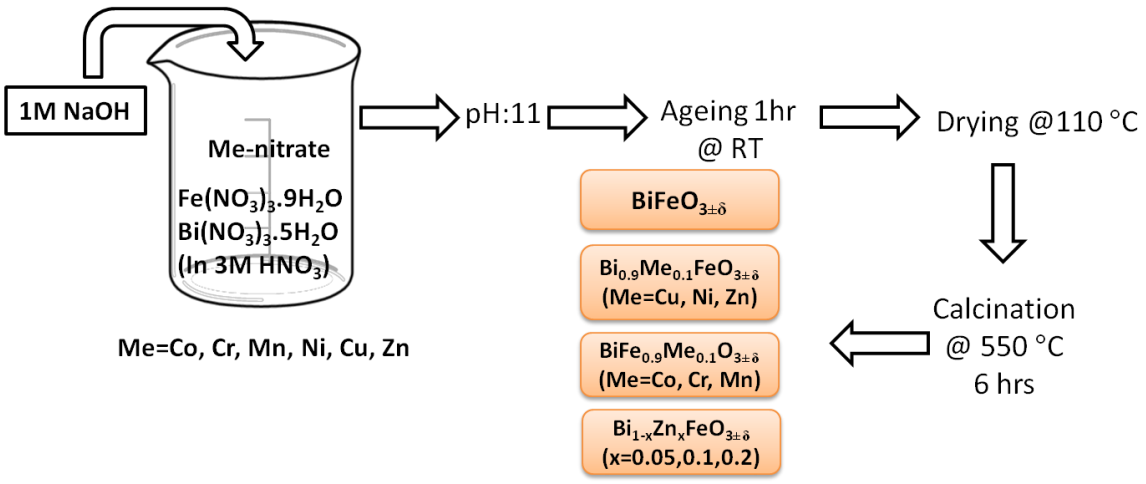

Scheme 2.2 Method of transition metal doped bismuth ferrite synthesis

The perovskite samples were prepared according to the following procedure [2]. For the synthesis of pristine $BiFeO_3$ (BF), $Fe(NO_3)_3.9H_2O$ was dissolved in 50 mL deionized water

followed by adding $Bi(NO_3)_3.5H_2O$ in 3M nitric acid. Later, 1M NaOH solution was added to this mixture under stirring until to reach pH 11. The suspension was stirred for another one hour and washed with 2 L deionized water to remove excess alkali and dried overnight at 80 °C. The powder was ground well and calcined for 6 h at 550 °C with 2 °C min^{-1} ramping under static air. Later, the transition metal doped bismuth ferrite viz; $M1_xBi_{1-x}FeO_3$ and $BiM2_xFe_{1-x}O_3$; where M1=Cu, Ni, Zn and M2=Co, Mn, Cr respectively were synthesized following the same procedure from the corresponding nitrate salts. $Cu(NO_3)_2.5H_2O$, $Ni(NO_3)_2.6H_2O$, $Zn(NO_3)_2.6H_2O$, $Co(NO_3)_2.6H_2O$, $Mn(NO_3)_2.4H_2O$ and $Cr(NO_3)_3.9H_2O$ were used as the metal precursors and the final solids were denoted as BCuF, BNiF, BZnF, BCoF, BMnF, and BCrF respectively. The synthesis procedure and catalyst composition are represented in **Scheme 2.2** and **Table 2.4**.

Table 2.4 Perovskite type bismuth ferrite catalysts' composition and codes

Sl. No.	Catalyst composition	Catalyst code
1	$BiFeO_{3\pm\delta}$	BF
2	$BiFe_{0.9}Co_{0.1}O_{3\pm\delta}$	BCoF
3	$BiFe_{0.9}Cr_{0.1}O_{3\pm\delta}$	BCrF
4	$BiFe_{0.9}Mn_{0.1}O_{3\pm\delta}$	BMnF
5	$Bi_{0.9}Cu_{0.1}FeO_{3\pm\delta}$	BCuF
6	$Bi_{0.9}Ni_{0.1}FeO_{3\pm\delta}$	BNiF
7	$Bi_{0.9}Zn_{0.1}FeO_{3\pm\delta}$	BZn0.1F
8	$Bi_{0.95}Zn_{0.05}FeO_{3\pm\delta}$	BZn0.05F
9	$Bi_{0.8}Zn_{0.2}FeO_{3\pm\delta}$	BZn0.2F

2.3.3. Synthesis of cerium iron mixed oxide

Citrate gel combustion

Cerium iron mixed oxide was synthesized by the citrate gel combustion method adopted from the reported literature [3]. An aqueous solution of $Ce(NO_3)_3.6H_2O$ and $Fe(NO_3)_3.9H_2O$ was taken in a 1:1 molar ratio with citric acid as fuel (metal ions: fuel=1:2) and made a homogenous solution. This solution was heated under stirring at 90 ºC to form a gel. Later, the gel was immediately transferred into an oven preheated at 180 ºC overnight to get a brown puffy solid mass. It was allowed to cool down to room temperature; ground well and calcined at 550 ºC at 2 °C min^{-1} in a muffle furnace for 6 h in air and labelled as CF. Pure CeO_2 and Fe_2O_3 were also prepared for the comparison studies by following the same procedure from the respective nitrate precursors. The material codes involved in cerium iron oxide system are specified in **Table 2.5** and the synthesis pathway is shown in **Scheme 2.3**.

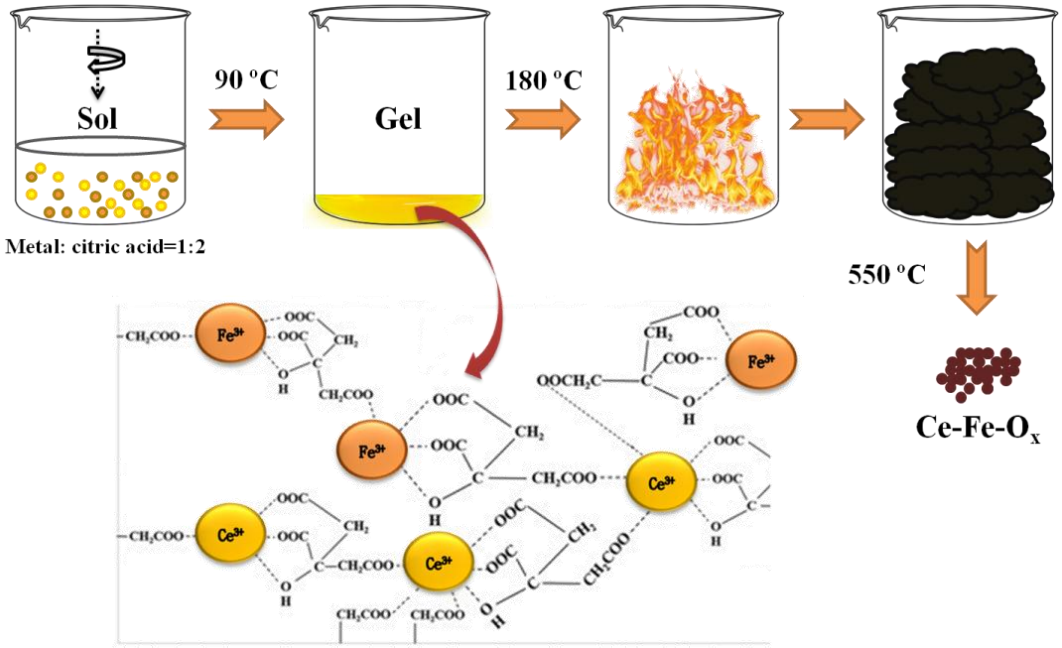

Scheme 2.3 Citrate gel combustion synthesis of CF

Table 2.5 Material codes in cerium iron mixed oxide

Sl. No.	Catalyst composition	Catalyst code
1	$CeFeO_x$ fresh	CF
2	CeO_2	CeO_2
3	Fe_2O_3	Fe_2O_3
4	$CeFeO_x$ after TOS	CFt
5	$CeFeO_x$ after regeneration	CFr

2.3.4. Synthesis of promoted iron-doped mesoporous alumina

a. Soft template-assisted synthesis

Mesoporous FeAl catalyst was prepared according to the method reported elsewhere [4]. For a typical synthesis, roughly 1.5 g of F-127 and 0.36 g $Fe(NO_3)_3.9H_2O$ was added to 20 mL anhydrous ethanol; vigorously stirred for 4 h and labeled as 'A'. Meanwhile, to a stirring mixture of 15 mL anhydrous ethanol and 1.6 mL concentrated nitric acid 12 mmol aluminium isopropoxide was dissolved and labeled 'B'. Further, A and B were combined using 3 mL ethanol to transfer the solution B. This final mixture was continuously stirred for another 8 h and dried in the oven at 60 °C for 48 h. Further, the residue was ground well and calcined at 700 °C for 5 h with a 1 °C min^{-1} ramping rate. The final powder was denoted as MesoFeAl.

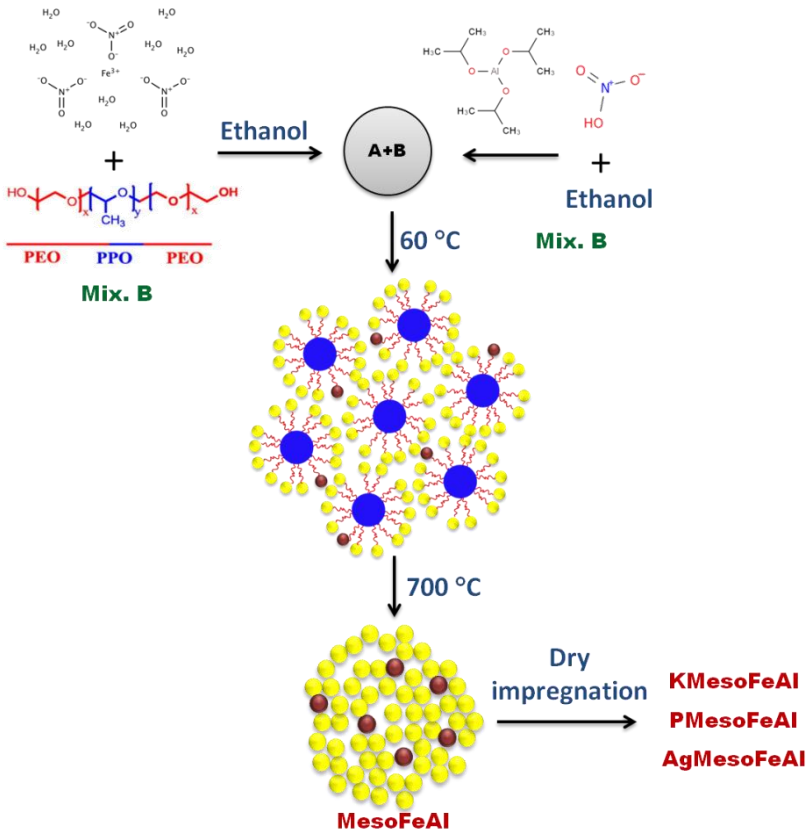

Scheme 2.4 Synthesis of promoted Fe-alumina catalysts

b. Dry impregnation

For the synthesis of promoted catalysts, 1 wt% of K, P and Ag were dry impregnated over 2 g MesoFeAl from a concentrated solution of the respective precursors KNO_3, phosphoric acid and $AgNO_3$. The solids were sintered at 550 °C for 2 h with at 1 °C min^{-1} and marked as KMesoFeAl, PMesoFeAl, and AgMesoFeAl. For the comparison study, the support MesoAl was also synthesized by following the above procedure without adding Fe precursor. Iron was dry impregnated from the nitrate precursor over mesoporous alumina and represented as FeMesoAl. Besides, pristine support MesoAl was also synthesized for further measurement [5]. The synthesis procedure is schematically represented in **Scheme 2.4**. The composition and codes of all mesoporous alumina catalysts are shown in **Table 2.6**.

Table 2.6 Composition and codes of mesoporous alumina catalysts

Sl. No.	Catalyst composition	Catalyst code
1	Mesoporous alumina support	MesoAl
2	5 wt% Fe in mesoporous alumina – *in situ*	MesoFeAl
3	1 wt% K on MesoFeAl	KMesoFeAl
4	1 wt% P on MesoFeAl	PMesoFeAl
5	1 wt% Ag on MesoFeAl	AgMesoFeAl
6	5 wt% Fe in mesoporous alumina – dry impregnation	FeMesoAl

2.4. Analysis methods

Catalyst characterization is crucial to establish the relationship between material properties and activity performance. A wide variety of analysis techniques are available in the research area for this purpose. However, proper recognition of the instrument characterization for a selected material is very significant in the systematic study of heterogeneous catalysis. The basic principle of the analysis methods practiced in the current study is illustrated briefly in this section.

2.4.1. Powder X-ray diffraction (PXRD)

Most of the available solid substances are crystalline in nature. When a parallel beam of monochromatic X-rays incident on a crystalline material, it interacts with the atoms in the periodic lattice. The diffracted beam is measured and the intensity will allow identifying the purity of the material. William. L. Bragg and William. H. Bragg assumed that the crystal planes of a solid behave perfect reflector for X-rays as schematically represented in **Fig. 2.1**. Thus, they derived Bragg's law which describes the conditions under which constructive interference could happen. The principle of X-ray diffraction lies in the Bragg's equation which is expressed as,

$$n\lambda = 2d\sin\theta \qquad (Eq.\ 2.1)$$

where, **n** is an integer called the order of diffraction which is equal to 0, ±1, ±2 etc., **λ** is the wavelength of the X-rays, **d** is referred as the interplanar distance, and **θ** is the diffraction angle which is the angle between the incident beam and scattering plane.

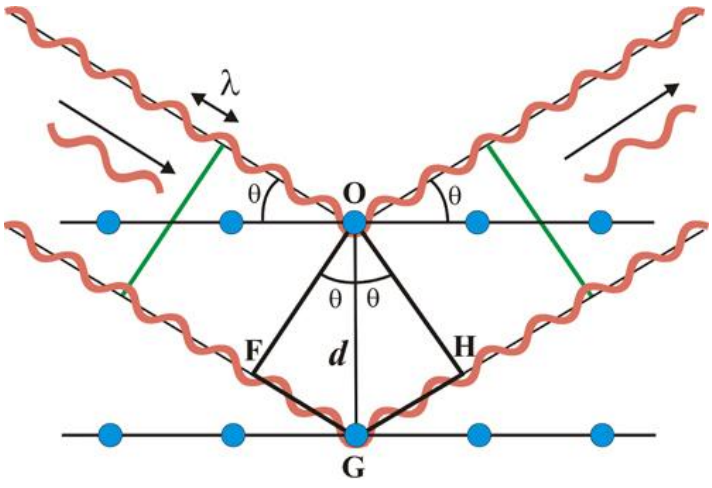

Fig 2.1 Principle of X-ray diffraction [6]

The d spacing derived from diffraction pattern can help to identify the material since this value is unique for each material. The collected data can be compared with the available standard reference patterns like the International Centre for Diffraction Data (ICDD) or the Joint Committee on Powder Diffraction Standards (JCPDS) [7]. Consequently, PXRD will provide complete information about the unit cell dimensions, lattice arrangement and phase identification of the sample. The line broadening occurs due to the phase lag between the crystal planes may be represented by the Debye-Scherrer formula,

$$D=k\lambda/\beta\cos\theta \qquad (Eq.\ 2.2)$$

Here, **D** is the average crystallite size, **k** is the dimensionless constant with a value 0.9, **λ** is the wavelength of X-ray source (Cu, 1.54178 Å), **θ** is Bragg's angle of the diffraction peak and **β** is the structural broadening. This expression is utilized to calculate the average crystallite size of a given material from the full width at half maxima (FWHM) obtained from the diffraction pattern.

2.4.2. N_2 physisorption

Heterogeneous catalysis occurs on the surface of the catalyst and so the surface area becomes crucial to illustrate the activity. N_2 physisorption analysis is the primary technique employed to study the porosity of catalysts. The measurement is based on BET theory developed by Stephen Brunauer, Paul H. Emmett and Edward Teller by extending the concepts of Irving Langmuir's monolayer adsorption of gas molecules in to multilayer adsorption. The specific surface area of a powder sample is determined by the physisorption of nitrogen gas on the surface and the adsorption-desorption isotherms are collected at 77 K. The information derived from isotherm is substituted in the BET equation given in *Eq. 2.3* to calculate the surface area.

$$\frac{1}{V[(P_0/P)-1]} = \frac{C-1}{V_m c}\left(\frac{P}{P_0}\right) + \frac{1}{V_m c} \qquad (Eq.\ 2.3)$$

where, **V** is the total amount of nitrogen adsorbed; $\mathbf{V_m}$ is the monolayer capacity; **P** and $\mathbf{P_0}$ are the pressure of adsorbate gas at equilibrium and saturation respectively; **c** is regarded as BET constant.

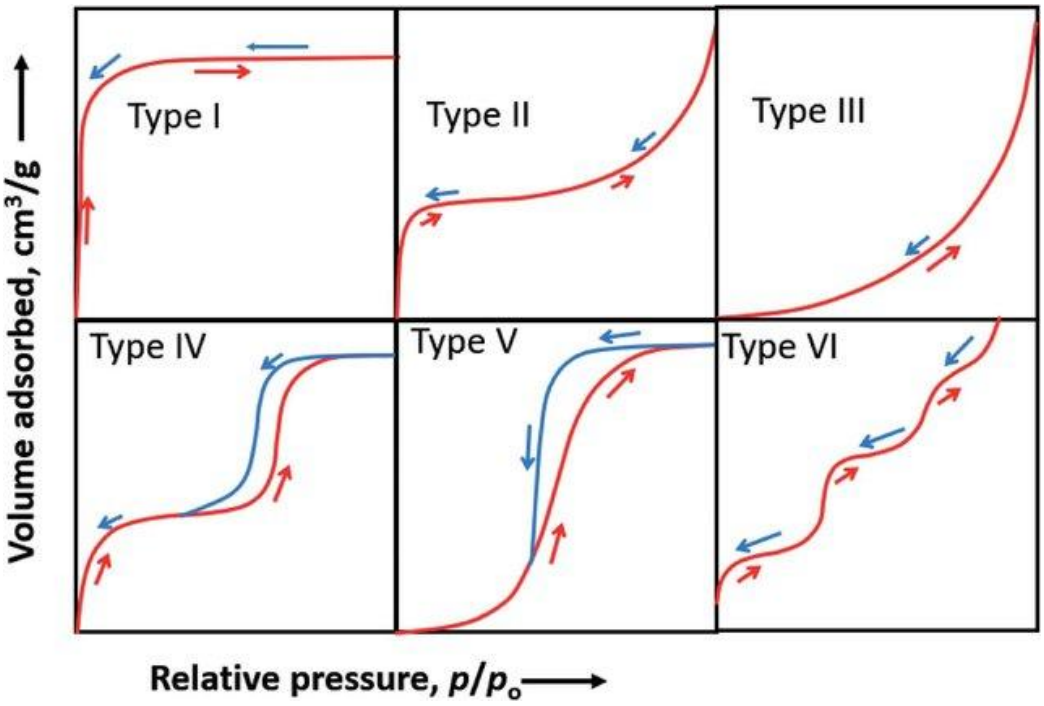

Fig. 2.2 IUPAC classification of BET isotherms [8]

International Union of Pure and Applied Chemistry (IUPAC) classified the adsorption isotherms in to six types and presented in **Fig. 2.2**. Accordingly, type I is shown by microporous solids while II and III are exhibiting multilayer adsorption in non porous solids. Type IV and V denote capillary condensation in mesoporous materials. However, type VI is very rare which is characteristic of stepped adsorption [9]. Furthermore, the Barret-Joyner-Halenda (BJH) method is applied to the nitrogen desorption data to establish the pore size distribution of mesoporous materials.

2.4.3. Scanning Electron Microscopy (SEM)

A scanning electron microscope uses a focused beam of high energy electrons (typically, 5-100 keV) to acquire the images of specimens in the nanometer scale. Images are monitored by scanning the sample and collecting the emitted secondary electrons by suitable detectors. Further, the signals are modulated to the image pixel. **Fig. 2.3** shows the complete instrumentation and working of SEM. This electron microscopy technique yields the size, distribution, particle aggregation as well as surface morphology of the catalyst. However, SEM is a surface analysis method and does not provide an internal structure.

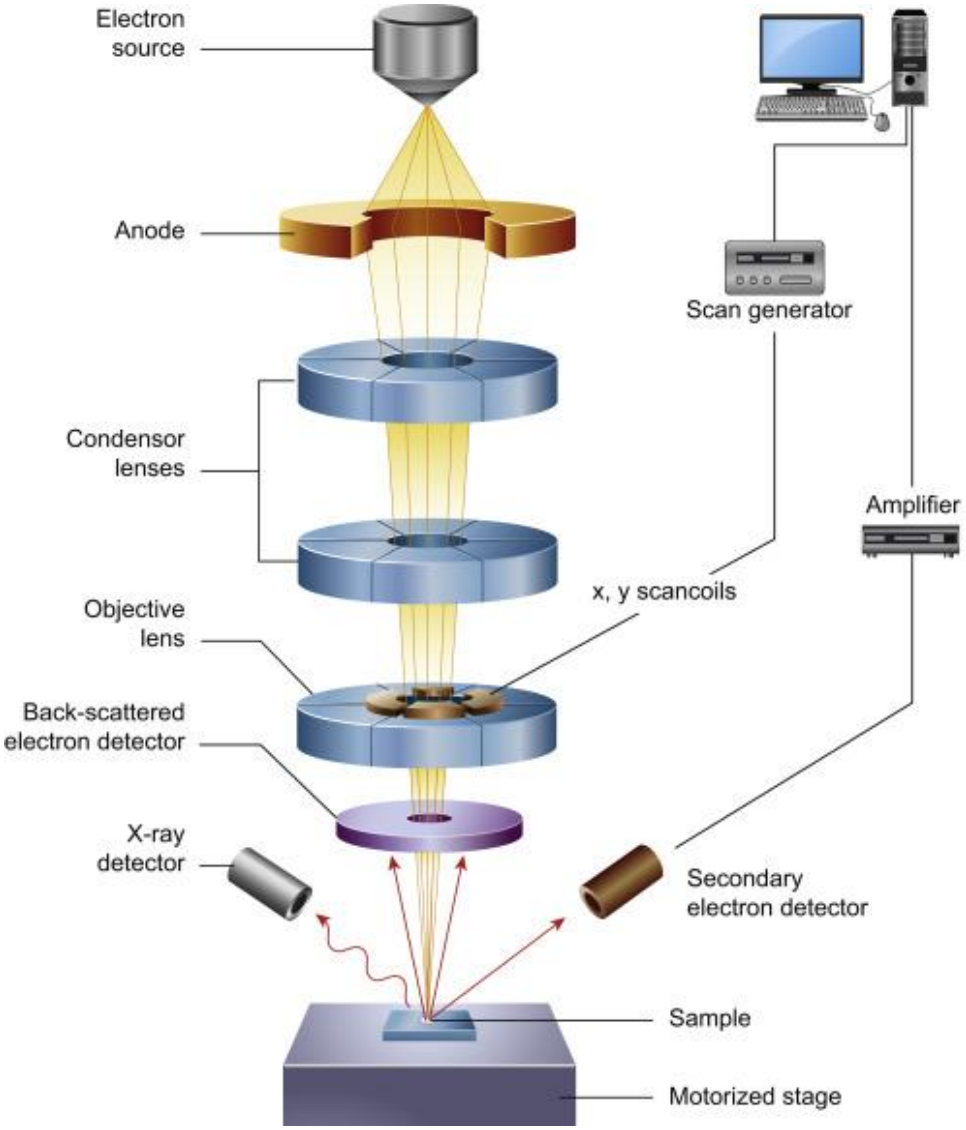

Fig. 2.3 Instrumentation of SEM [10]

Chemical composition, element concentration and sample purity can be studied with energy dispersive X-ray spectroscopy. When a primary electron beam interacts with an atom; an inner shell electron can be ejected. An outer high energy electron will compensate this electron loss by releasing its energy as X-rays (**Fig. 2.4**). This characteristic of X-rays can be used to identify the elements. It is a bulk analysis method and usually used together with microscopic techniques [11]. Besides, elemental mapping is studied with EDX which gives information about the spatial distribution of elements. This technique can be coupled with an electron microscope. The main disadvantage of elemental mapping is at low concentration; elements may not give a response.

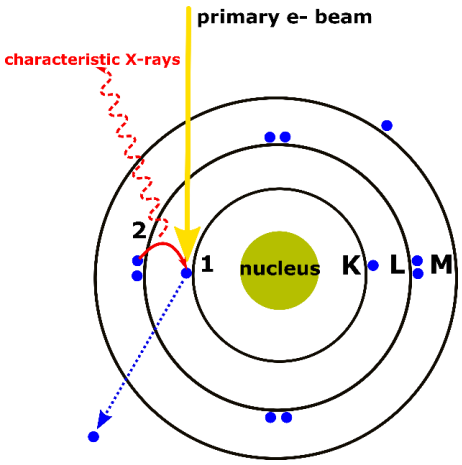

Fig. 2.4 Generation of X-rays during EDX analysis [12]

2.4.4. Transmission Electron Microscopy (TEM)

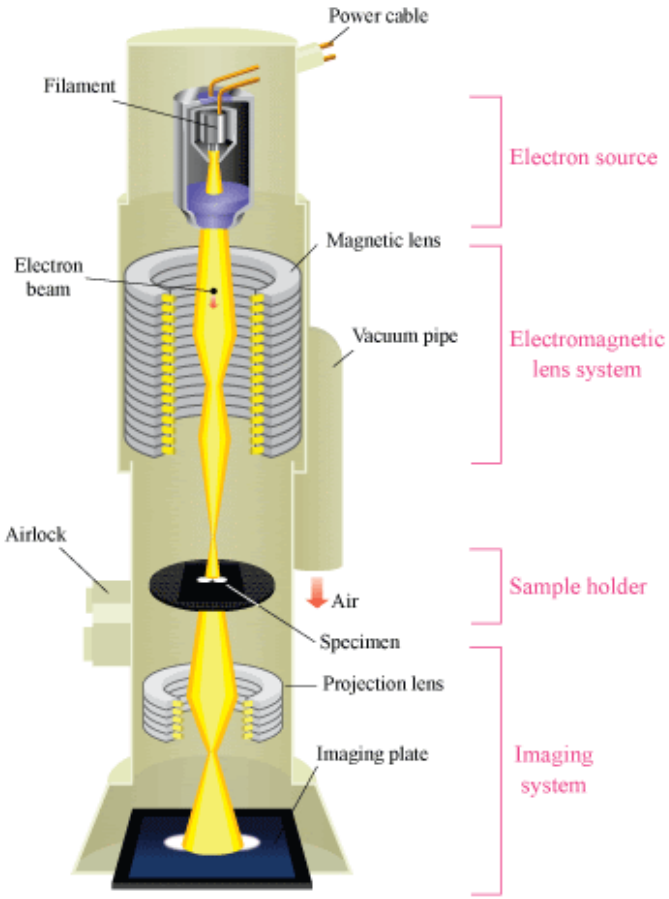

Fig. 2.5 Schematic outline of TEM [13]

Transmission electron microscopy is a popular microscopic technique to characterize the local structure and porosity of materials. The working principle of TEM is based on optical

microscopy while the order of magnitude is much superior. An accelerated high energy electron beam (60-350 keV) is employed to catch high resolution images above 1–2 nm visibility limits. The interaction between the electrons and sample will give the finest details of internal structure. In addition, precise particle size can be derived for the nanomaterials. The schematic of a transmission electron microscope is represented in **Fig. 2.5**. Compared to SEM, it can provide good quality images with powerful magnification. A TEM instrument can be used for imaging, EDX spectroscopy and selected area electron diffraction analysis [14]. Among this, SAED is a crystallographic technique that is performed in the transmission electron microscope. The diffraction pattern observed in this analysis indicates material crystallinity and helps in phase identification.

2.4.5. Thermogravimetric (TG) Analysis

Thermogravimetric analysis is a quantitative analysis method where the mass of a substance is monitored as the function of temperature or time under controlled heating and gaseous environment. Thus, it helps to study the thermal events associated with the material. The sample will be heated in a closed furnace in an inert or air atmosphere with programmed ramping. **Fig. 2.6** depicts the schematic diagram of the TG instrument. The resulting plot of weight loss as a function of temperature is called a thermogram. This curve will provide decomposition temperature and so illustrates the thermal stability of the material [15].

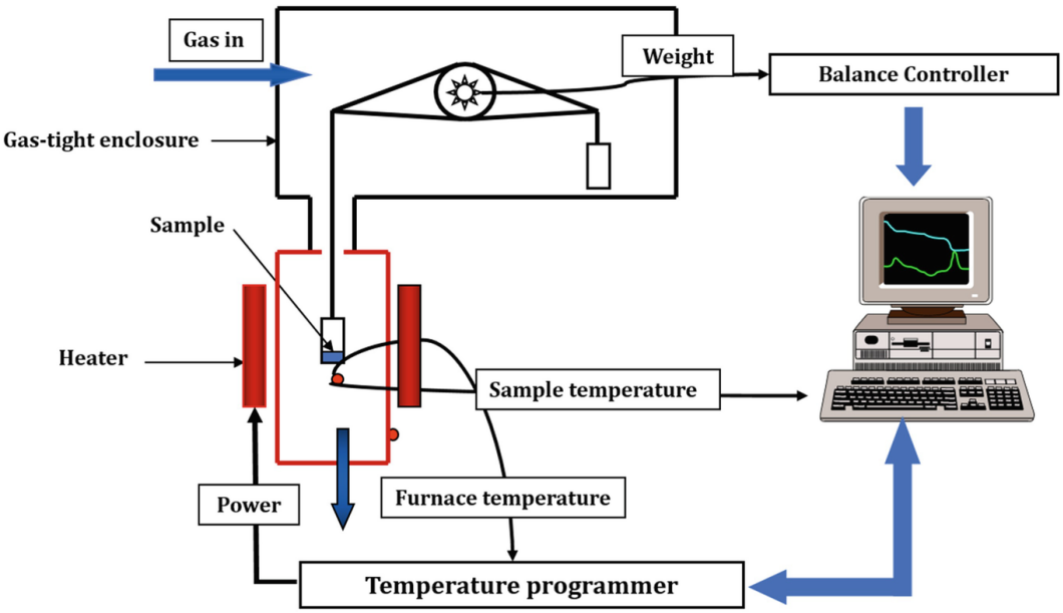

Fig. 2.6 Instrument set-up for TGA [16]

DTA involves monitoring the differential temperature between the sample and the reference material. This temperature difference is plotted against time or temperature and the analysis will help to identify and quantitatively analyze the chemical composition of the material. Generally DTA is coupled with TGA for the proper interpretation to study exothermic, endothermic events.

2.4.6. Temperature Programmed Reduction (TPR)

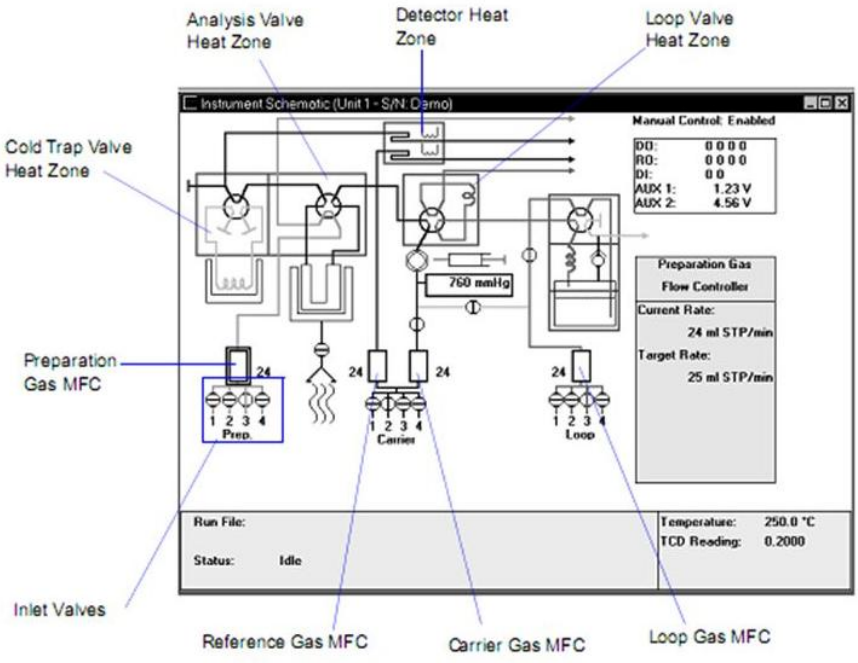

Fig. 2.7 Schematic diagram of TPR/TPD [17]

TPR is a vital aspect of heterogeneous catalysis which enables the study of metal oxide based materials upon varying thermal conditions. The instrument schematic shown in **Fig. 2.7** is common to TPR and TPD experiments. In a typical TPR analysis, the degassed sample is treated with a reducing gas mixture (usually H_2 in Ar/N_2) under programmed temperature. A thermal conductivity detector measures the effluent and H_2 gas consumed can be quantified as the function of temperature. The reaction may be represented in general as,

$$M_xO_y + yH_2 \rightarrow xM + yH_2O \qquad (Eq.\ 2.4)$$

Silver oxide is used for instrument calibration. Thus, TPR will provide the reducibility of oxides and treated as both quantitative and qualitative technique. This method yields bulk reduction of the oxide and is very sensitive to the metal support interactions [18]. The instrument diagram is given in **Fig. 2.8**.

2.4.7. Temperature Programmed Desorption (TPD)

The typical TPD analysis instrument scheme is shown in **Fig. 2.7** and the instrument is represented in **Fig. 2.8**. The experimental procedure is similar to TPR which is explained in the **Section 2.4.6**. TPD is carried out to investigate the interaction of the solid surface with gas molecules. Consequently, the active sites can be evaluated. This technique is crucial to understand the catalytic reaction mechanisms.

Fig. 2.8 AutoChem II 2920 instrument [17]

For example, probe molecules like NH_3 and CO_2 are employed respectively to study the acidic and basic properties of materials. After adsorbing these gas molecules at room temperature it is desorbed by applying programmed thermal environment. The nature, type and amount of acidity as well as basicity are evaluated by analyzing the TPD profiles [19].

2.4.8. Raman spectroscopy

Raman spectroscopy is a versatile analytical tool based on the Raman Effect [20]. Accordingly, when an incident light of wavelength 750–850 nm (usually Laser) falls on the specimen; the molecule excite to a different vibrational level. The inelastically scattered radiation is measured with the detector and converted to spectra as the function of the Raman shift. The basic principle of Raman scattering is schematically depicted in **Fig. 2.9**.

Consequently, if a molecule gains or losses energy; the corresponding processes result in Stokes and Anti-Stokes scattering respectively. Moreover, the elastic scattering too occurs which is called Rayleigh scattering.

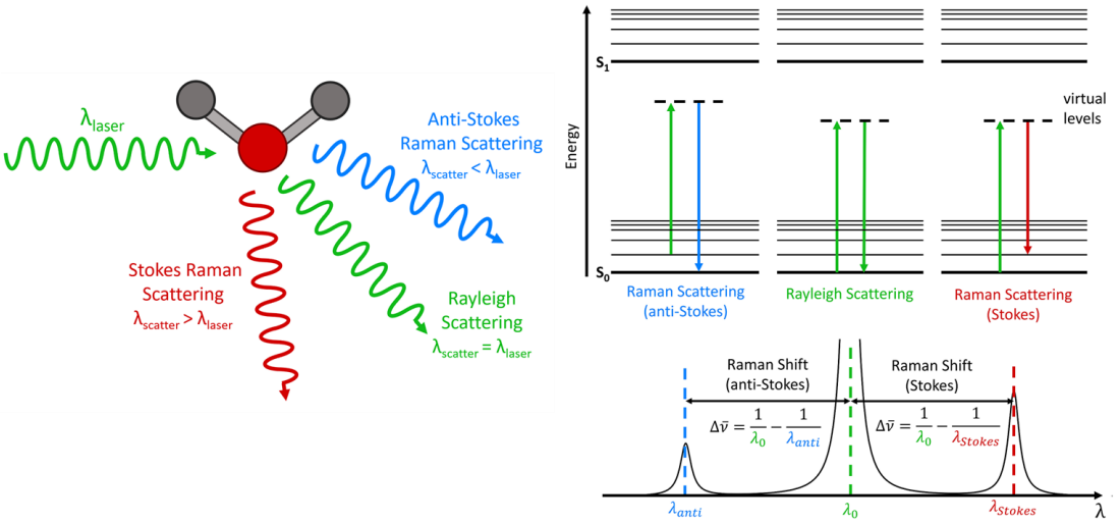

Fig. 2.9 Basics of Raman spectroscopy [21]

Raman shift may be calculated using the relation,

$$\Delta\bar{\upsilon}\ (\mathrm{cm^{-1}}) = \left(\frac{1}{\lambda_0\,(\mathrm{nm})} - \frac{1}{\lambda_1\,(\mathrm{nm})}\right) \times \frac{10^7\ \mathrm{nm}}{\mathrm{cm}} \qquad \textit{(Eq. 2.5)}$$

Here, $\Delta\bar{\upsilon}$ is the Raman shift in wave number (cm^{-1}), λ_0 and λ_0 are the excitation laser and Raman scatter wavelength in nm respectively.

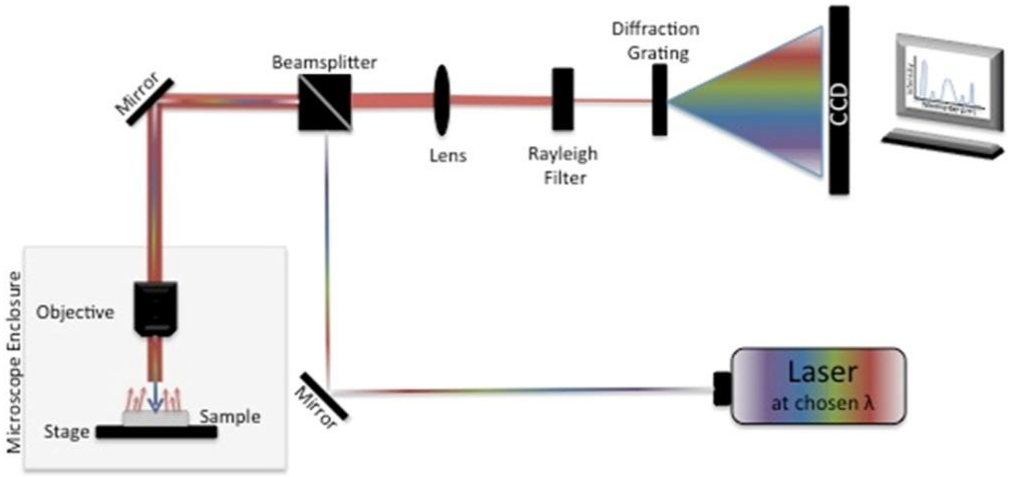

Fig. 2.10 Instrument scheme of Raman spectrophotometer [22]

As described above, this is a vibrational spectroscopic technique that measures the change in polarizability during molecular vibration; although complementary to infrared absorption spectroscopy. Thus, it provides the chemical and structural information about the sample. However, reduced sensitivity is the main drawback of this analysis method. **Fig. 2.10** shows the instrumental set up of a typical Raman spectrophotometer.

2.4.9. X-ray Photoelectron Spectroscopy (XPS)

Heterogeneous catalysis is a surface process and so the understanding of physical and chemical interactions occurring on the material surface becomes significant. XPS or electron spectroscopy for chemical analysis (ESCA) is the most widely used surface characterization technique based on the photoelectric effect. This phenomenon and the instrumentation are simply represented in **Fig. 2.11**. When a solid surface is irradiated with monochromatic X-rays, electrons are ejected and the detector records the kinetic energy (KE) of these electrons. The resulting spectra will be a function of binding energy (BE).

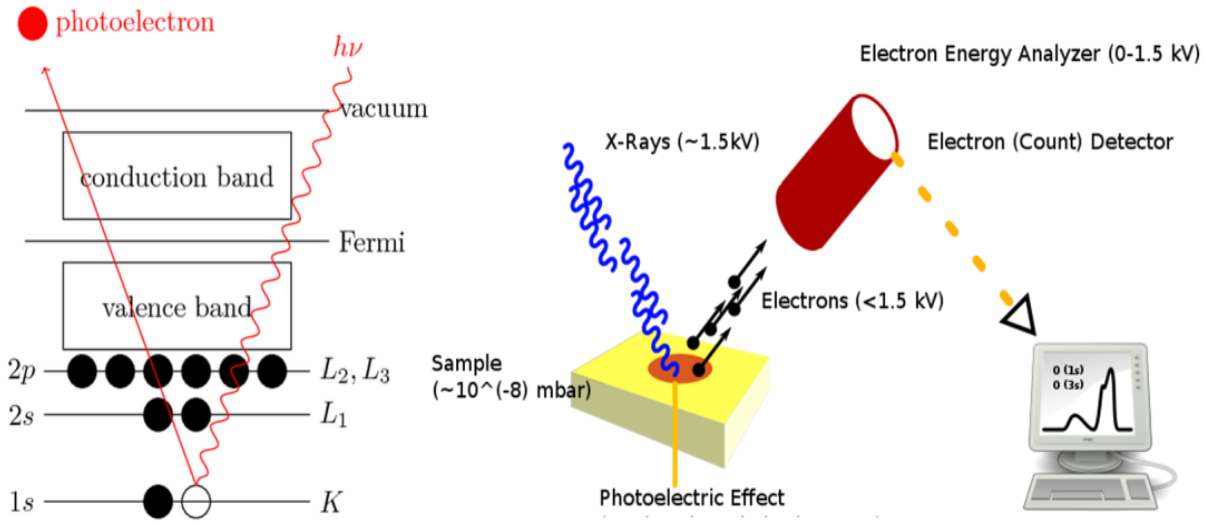

Fig. 2.11 Principle and instrumentation of XPS [23]

The basic principle of XPS may be mathematically represented as,

$$KE = h\upsilon - BE - \varphi - S \qquad (Eq.\ 2.6)$$

where, **hυ** is the photon energy; **φ** is called work function related to the specific surface area of a material and **S** is the eventual surface charge. This electron spectroscopic method gives information about the electronic environment of elements [24].

2.4.10. Fourier Transform Infrared Spectroscopy (FTIR)

The use of FTIR spectroscopy is considered as an effective analytical method to identify the functional groups in organic as well as inorganic materials. When IR radiation passes through the material, some of the radiation is absorbed by the material and excites to higher vibrational mode. The transmitted radiation is collected by the detector; digitalizes and finally Fourier transformed to the spectra which is considered as the molecular finger sprint of the sample. A simple schematic representation of this process is given in **Fig. 2.12**.

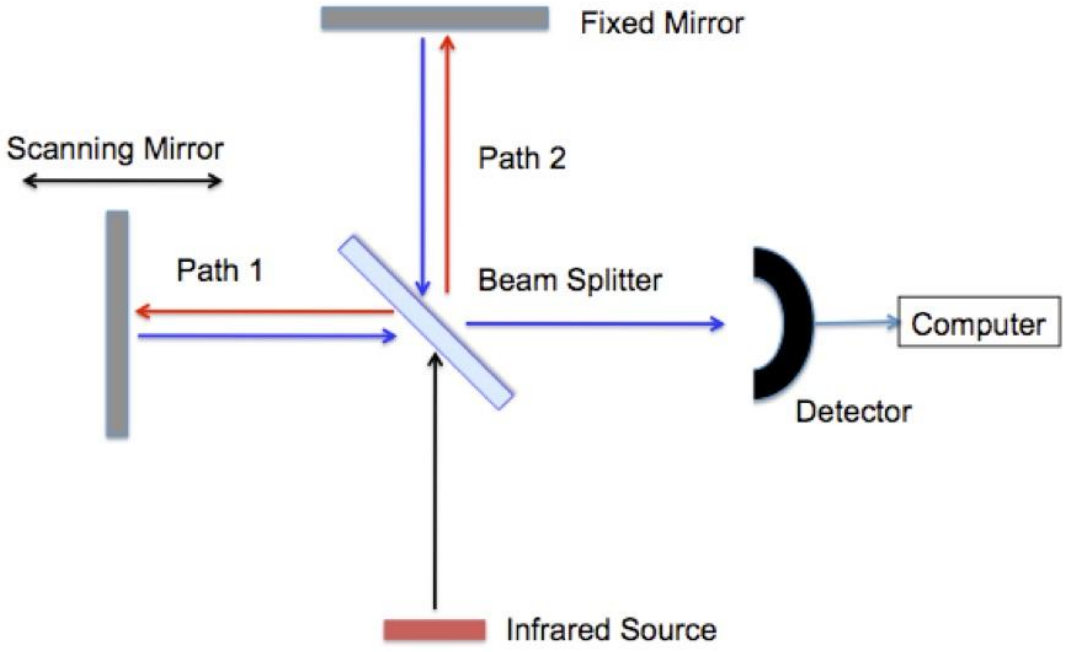

Fig. 2.12 Scheme of the FTIR system [25]

The spectrum measures absorption or transmission intensity versus wave number (cm^{-1}) of the radiation and usually falls in 400–4000 cm^{-1} range. This technique may be used in specular reflection, transmission, diffuse reflectance and attenuated total reflection modes for solid or liquid samples [26].

2.4.11. Ultra Violet-Visible Spectroscopy

UV-visible spectroscopy is a technique based on the absorption of ultraviolet or visible radiation (210-900 nm) by the chemical compound. The electrons are promoted to higher energy levels on irradiation with a known wavelength and regarded as a kind of absorption spectroscopy. Generally, molecules containing either π electrons or non-bonding electrons are

being excited to anti-bonding molecular orbitals. Here, the change in absorbance is monitored with respect to radiation wavelength. It gives rapid quantitative measurements. The scheme given in **Fig. 2.13** denotes a classic UV-visible instrument.

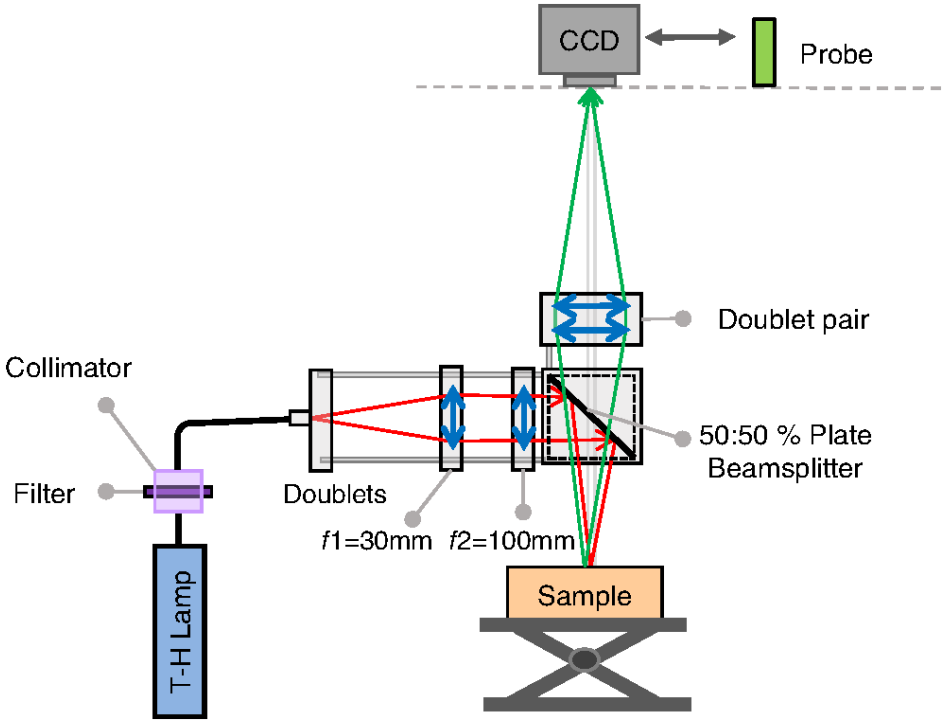

Fig. 2.13 Illustration of DRUV spectrometer [27]

The concentration of a known solute can be quantified from Beer-Lambert law which is stated by the expression,

$$A = \mathrm{Log}_{10}\,(I_0/I) = \varepsilon c L \qquad (Eq.\ 2.7)$$

where, **A** is the absorbance measured, $\mathbf{I_0}$ and **I** are the intensities of the incident and transmitted radiation respectively, **L** is the path length of radiation through the sample (cm), **c** is the concentration of dissolved solute (mol L^{-1}) and **ε** is extinction coefficient (L mol^{-1} cm^{-1}); a constant for each species and wavelength. This technique employed in the diffuse reflectance mode helps to investigate the local environment of atomic sites [28].

2.4.12. Inductively Coupled Plasma Mass Spectrometry (ICP-MS)

ICP-MS is developed for the detection and quantification of elements in the trace levels in any given sample. It is a highly potent and extremely sensitive analysis method even used to distinguish between isotopes. The basic principle of this spectrometry is atomic absorption and atomic emission. During the analysis the elements are ionized and are detected with the

mass spectrometer sorted by their respective mass. The ionization of elements is performed with inductively coupled plasma which is energized with the electromagnetic coil by inductively heating the gas [29]. **Fig. 2.14** denotes the diagram of ICP-MS.

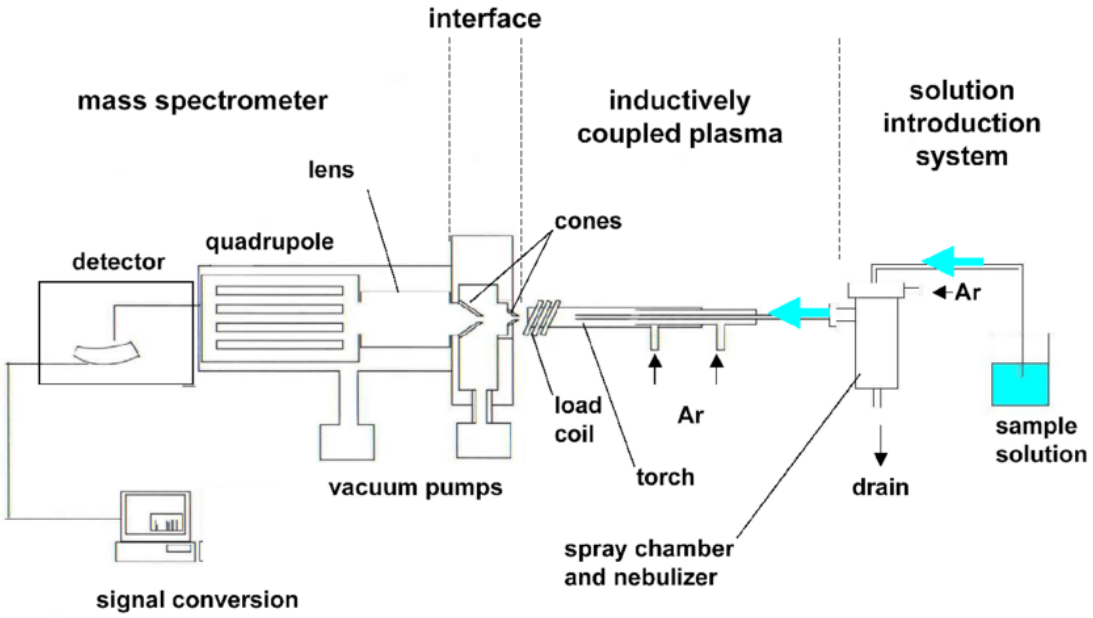

Fig. 2.14 Schematic of ICP mass spectrometer [30]

2.4.13. Fixed Bed Reactor (FBR)

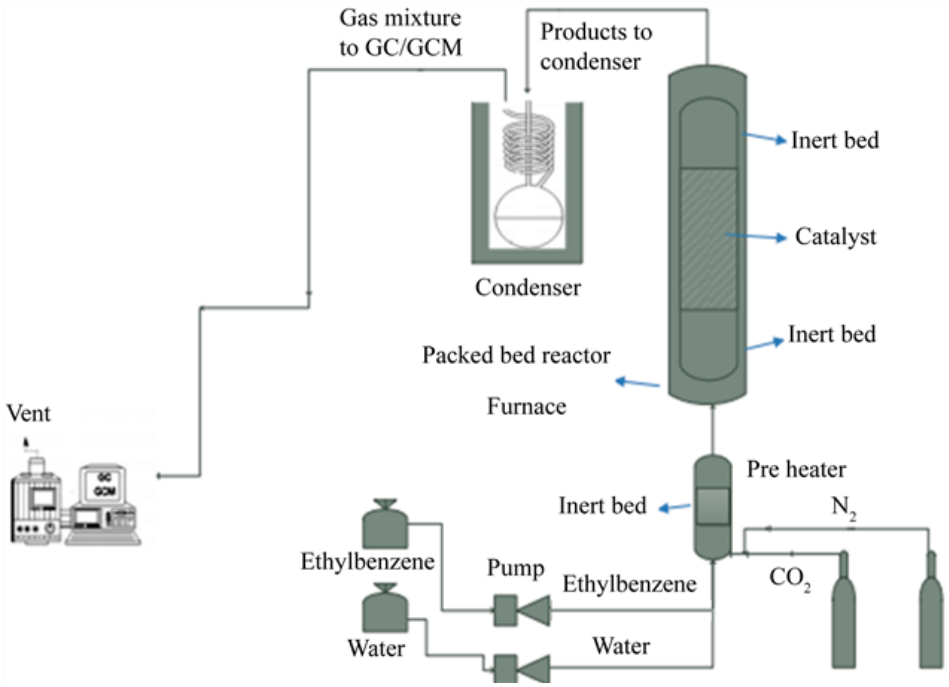

Fig. 2.15 Experimental set up of FBR [31]

A fixed bed reactor system is a simple reactor design where solid catalyst pellets are packed as a bed and loaded inside a cylindrical tube. The empty space of the container can be filled with some inert material. Further, the reactor tube is heated in a furnace with the help of heating coils. The reactants are fed through the valves in to the catalyst bed. The complete experimental scheme of FBR for the ethylbenzene DH is shown in **Fig. 2.15**. This kind of reactor may be designed for different capacities. During the experiment, the rate of the reaction and pressure drop at the catalyst bed must be balanced.

Fig. 2.16 FBR system engaged for the study

FBR is simple, flexible and easy to scale up. Nevertheless, high cost, low heat transfer, development of hotspots and low effectiveness factor are a few drawbacks of this type. The productivity of FBR may be improved by coupling with multiple reactors. It is utilized for the large scale industrial production of necessary chemicals and intermediates [32]. The continuous flow fixed bed reactor system used for the current work is given in **Fig. 2.16**.

2.4.14. Gas Chromatography (GC)

Gas chromatography is vitally important for identifying, separating and quantifying compounds even from a complex mixture. It is a chromatographic method where gas is used

as the mobile phase and solid or liquid as the stationary phase. The instrument diagram is presented in **Fig. 2.17** which mainly consists of three components viz. injection port, column and detector. The mixture is introduced at the injector after combining with the carrier gas (mobile phase) and passes through the column containing a suitable stationary phase. The separation happen in this column kept inside an oven and finally the detector converts the signals into chromatogram.

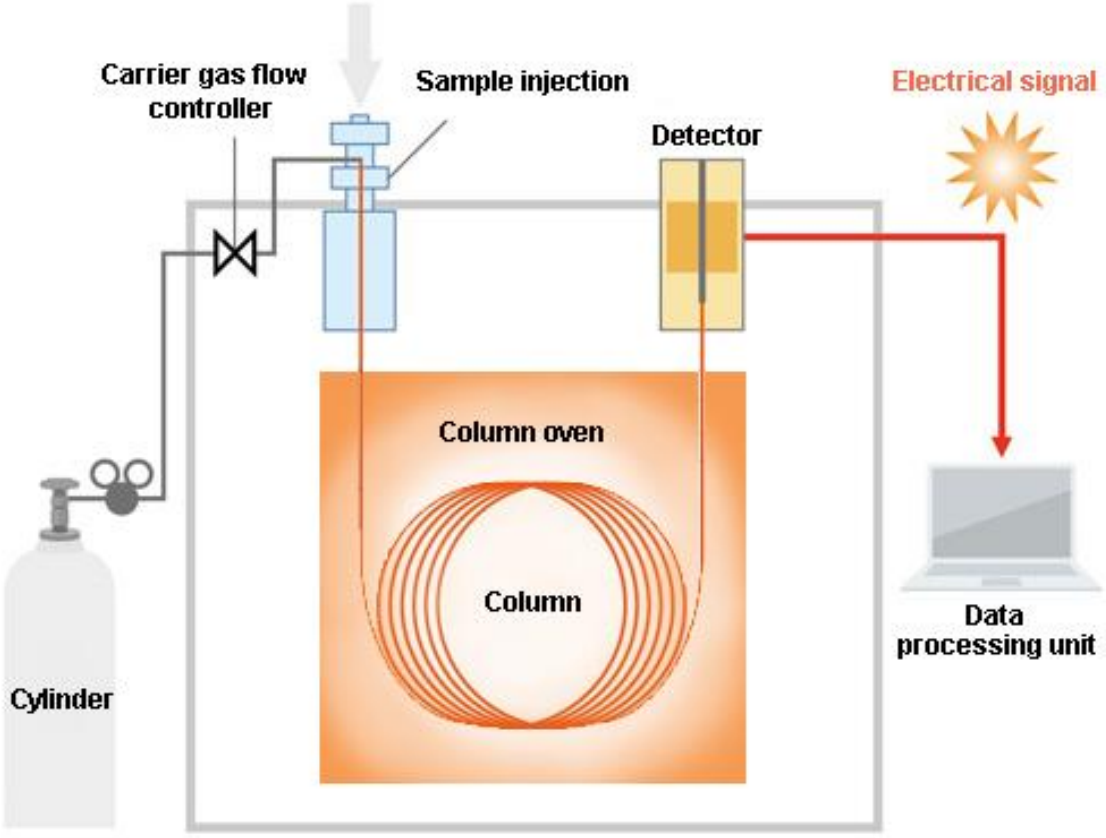

Fig. 2.17 GC system configuration [33]

GC column is selected according to the mixture to be analyzed. Thermal conductivity detector (TCD) measures the thermal conductivity of the component gas using the Wheatstone bridge principle as well as flame ionization detector (FID) where compound ionizing and detection occur; are the primary type of detectors employed. The separation by GC depends on the vapor pressure, boiling point and polarity of the component. However, a conventional GC suffers from long analysis times. In addition, compound either having boiling point above 400 °C or easily decomposing nature cannot be analyzed through this technique [34].

2.5. Instrument configuration

In this section, the instrument configuration of the above characterization methods employed for the present work is given in concise. The detailed procedure for the sample analysis is also mentioned in the respective parts.

2.5.1. Material crystallinity

Crystalline phases of the synthesized materials were identified by powder X-ray diffraction analysis in PANalytical X'pert Pro dual goniometer diffractometer. The data were collected with a step of 0.008° (2θ) and a scan rate of 0.5 ° min^{-1} at room temperature. Cu Kα (1.5418 Å) radiation was applied with Ni filter, and the data was obtained using a flat holder in Bragg-Brentango geometry.

2.5.2. Textural properties

Nitrogen adsorption-desorption isotherms data were collected from Quantachrome Quadrasorb SI (USA) using the Brunauer-Emmett-Teller (BET) model. The textural properties of the materials were determined by N_2 physisorption at –196 °C after degassing at 300 °C. The data corresponding to the relative pressure of P/P_0=0.05–0.3 was taken to calculate BET surface area.

2.5.3. Catalyst morphology

A dual-beam scanning electron microscope FEI company made and Quanta 200 3D model operated at 30 kV was used to collect scanning electron microscopy images. High-resolution transmission electron spectroscopy study was performed in JEM2100 multipurpose instrument operated at 300 kV. The sample is prepared by dispersing the powder in isopropyl alcohol followed by drop casting on carbon-copper mesh (200 μm size) and silicon wafer respectively for TEM and SEM study. The non-conducting samples are gold coated prior to SEM imaging.

2.5.4. Thermal properties

Temperature programmed experiments were carried out in a Micromeritics Autocem II 2920 chemisorption analyzer (USA). In a single TPR analysis, 0.05 g catalyst was pre-treated at 400 °C inside the furnace coupled with the instrument with 30 cm^3 min^{-1} of 10 % O_2/He controlled by Brooks make mass flow controllers. Then, reduced with 5 % H_2/Ar at 30 cm^3

min^{-1} flow rate while ramping the sample temperature from 50 to 1000 °C at 10 °C min^{-1}. Hydrogen consumption was quantified using thermal conductivity detector.

Acidity and basicity of the materials are determined in the same model instrument. In typical TPD study, the samples were degassed at 400 °C under Helium at 30 cm^3 min^{-1} flow before each run. Afterwards, sample temperature was brought down to 50 °C to adsorb the respective probe molecule viz. 10 % NH_3/He or 10 % CO_2/He (30 cm^3 min^{-1}) for the acidic and basic site evaluation respectively in separate analysis. The desorbed gas was analyzed from 100 to 1000 °C with 10 °C min^{-1} ramp rate. The quantification is made from the resulting TPD profiles.

Coke deposition over the spent catalyst was determined with the help of the Perkin Elmer instrument. TG analysis was performed under the air atmosphere and the carbon combustion temperature was taken from the exothermic event in DTA.

2.5.5. Spectroscopic studies

X-ray photoelectron spectra were acquired using Thermo Scientific K-Alpha+ using micro-focused and monochromated Al Kα radiation with energy 1486.6 eV. Pelletized material was taken for the surface analysis. Horiba JY LabRAMHR800 Raman spectrometer coupled with a microscope in a reflectance mode under 628 nm excitation wavelength was used to record Raman spectra of the catalyst pellets. UV-visible spectra of powder samples were collected under diffuse reflectance mode in Shimadzu spectrophotometer (model UV 2550) with spectral grade $BaSO_4$ as reference material.

Fourier transform infrared spectra were collected using CO as probe molecule over the fine powder catalyst in the range 500–4000 cm^{-1}. Nicolet iS50 Analytical FTIR spectrometer (Thermo Fisher Scientific) instrument is connected with KBr window. The quantification of elements was estimated by Microwave plasma atomic emission spectroscopy on 4100 MP-AES spectrometer from Agilent Technologies. All samples were prepared into a dilute solution after digesting in aqua-regia.

2.6. Catalytic activity study

The general description of the catalytic activity test is given as follows. The oxidative as well as non-oxidative DH of C_4 hydrocarbons were studied in a continuous flow mode fixed bed reactor system operated at the atmospheric pressure. During a particular catalytic run, a definite amount (0.3–0.6 g) of catalyst was sieved into 1.2 mm to 1.7 mm grain sized pellets.

Later, it was loaded in the middle of reactor tube made of Inconel (nickel-chromium based alloy material) with 8×11×480 mm (ID×OD×length) dimensions. The catalyst bed was formed between quartz wool, and the empty space was filled with thermally stable ceramic beads. Afterwards, the reactor tube was heated to the desired temperature by two furnace zones with heating coils. The catalyst bed temperature was continuously monitored using a K type thermocouple inserted inside a thermowell. The reactant gas mixture was fed into the catalyst bed using 5890E series Brook's make mass flow controllers. The reaction parameters were different for the selected reactions. Further details of the individual reactions are illustrated in **Table 2.7** given below.

Table 2.7 Description of reaction parameters

Reaction	**ODH of n-butane**		**ODH of 1-butene**		**DH of isobutane**
Catalyst system	**xBMO**	**yV5BMO**	**Bismuth ferrites**[b]	**CF**[c]	**Fe-alumina**
Catalyst weight (g)	0.5	0.5	0.5	0.6	0.3
Temperature (°C)	350–550	400–550	350–500	200–300	400–600
Feed ratio	O_2/C_4=1	O_2/C_4=1	O_2/C_4=1	Ar/C_4=5	Ar/C_4=1
GHSV (h^{-1})[a]	600	3000	3000	3000	400

[a]Balanced with Ar.
[b]Effect of steam is studied in a different experiment with C_4: O_2: H_2O: Ar=5:5:25:90 feed.
[c]Catalyst regeneration is performed at Ar/O_2=5.

2.7. Quantification of reaction products

The reaction products were evaluated with the help of Thermo Scientific Trace 1110 gas chromatography coupled with both FID outfitted with Alumina plot column and TCD equipped with Porapak Q and Molecular sieve columns. Analysis was made in each 30 min interval of time. The chromatogram was analyzed using the Chromcard software. Each component in the gaseous mixture was quantified by comparing with the authentic calibration gas mixture. The reaction data was taken for tabulation at the end of 4 h for each reaction. The conversion of n-butane and selectivity for C_4 olefins were determined based on carbon balance [35].

Conversion is defined as the fraction of reactant transformed and C_4 conversion can be generally given by the relation,

$$\mathbf{C_4H_x\ Conversion\ (\%) = \frac{C_4H_x\ (in) - C_4H_x\ (out)}{C_4H_x\ (in)}} \qquad \textit{(Eq. 2.8)}$$

Here, **x** can be 8 or 10 depending on the reactant hydrocarbon. Selectivity for each hydrocarbon is determined as,

$$\mathbf{C_yH_z\ Selectivity\ (\%)} = \frac{\mathbf{C_yH_z\ (Products)}}{\mathbf{Total\ products}} \qquad \textit{(Eq. 2.9)}$$

Here, **y** and **z** will vary for C_1-C_4 products. Another factor involved in the reaction parameter is space velocity which is the ratio of flow rate to the size of the reactor. Hence, gas hourly space velocity (GHSV) is defined as the volume of feed as gas per volume of the reactor or its content of catalyst [36]. **Table 2.7** represents GHSV selected for the reactions under study.

References

[1] T.N. Pham, L. Zhang, D. Shi, M.R. Komarneni, M.P. Ruiz, D.E. Resasco, J. Faria, ChemCatChem 8 (2016) 3611–3620.

[2] J.T. Han, Y.H. Huang, X.J. Wu, C.L. Wu, W. Wei, B. Peng, W. Huang, J.B. Goodenough, Adv. Mater. 18 (2006) 2145–2148.

[3] M.O. Mazan, A. Craievich, E.B. Halac, M.C.A. Fantini, D.G. Lamas, S.A. Larrondo, Ceramics International 41 (2015) 13721–13730.

[4] B. Yan, Y. Gao, B. Wang, X. Fan, F. Alam, J. Li, T. Jiang, ChemCatChem. 9 (2017) 4480–4483.

[5] Q. Yuan, A.X. Yin, C. Luo, L.D. Sun, Y.W. Zhang, W.T. Duan, H.C. Liu, C.H. Yan, J. Am.Chem.Soc. 130 (2008) 3465–3472.

[6] https://www.xtal.iqfr.csic.es/Cristalografia/index-en.html

[7] B. Toby, R. Harlow, M. Holomany, Powder Diffraction 5 (1990) 2–7.

[8] K.V. Kumar, S. Gadipelli, B. Wood, K.A. Ramisetty, A.A. Stewart, C.A. Howard, D.J.L. Brett, F.R. Reinoso, J. Mater. Chem. A 7 (2019) 10104–10137.

[9] G. Ertl, H. Knözinger, J. Weitkamp (Eds.), Handbook of Heterogeneous Catalysis; VCH, Weinheim: 1997.

[10] https://www.liberaldictionary.com/scanning-electron-microscope/

[11] D.E. Newbury, N.W.M. Ritchie, J. Anal. At. Spectrom. 28 (2013) 973–988.

[12] https://www.thermofisher.com/blog/microscopy/edx-analysis-with-sem-how-does-it-work/

[13] http://www.hk-phy.org/atomic_world/tem/tem02_e.html

[14] B. Fultz, J. Howe, Transmission Electron Microscopy and Diffractometry of Materials; Springer: 2007.

[15] M.E. Brown, Introduction to thermal analysis: Techniques and application; second edition, Springer: 2007.

[16] M.S.H. Akash, K. Rehman, Thermo Gravimetric Analysis. In: Essentials of Pharmaceutical Analysis; Springer: 2020.

[17] https://www.micromeritics.com/Product-Showcase/AutoChem-II-2920.aspx

[18] https://www.micromeritics.com/Repository/Files/appnote120.pdf

[19] https://www.micromeritics.com/Repository/Files/Autochem%20II%202920%20technique%20TPD.pdf

[20] C.V. Raman, K.S. Krishnan, Nature 121, (1928) 501–502.

[21] https://www.edinst.com/blog/what-is-raman-spectroscopy/

[22] M.J. Baker, C.S. Hughes, A. Katherine, Raman spectroscopy; Morgan and Claypool Publishers: 2016, Chapter 3, Pages 1–13.

[23] https://en.wikipedia.org/wiki/File:XPS_CC_Roland_Siegbert.svg

[24] P.G. Zambonin, E. Desimoni, X-Ray Photoelectron Spectroscopy: Principles, Instrumentation, Data Processing and Molten Salt Applications. In: Mamantov G., Marassi R. (eds) Molten Salt Chemistry. NATO ASI Series (Series C: Mathematical and Physical Sciences), vol. 202. Springer: 1987.

[25] https://chem.libretexts.org/Courses/Howard_University/Howard%3A_Physical_Chemistry_Laboratory/14._Fourier_Transform_Infrared_Spectroscopy_(FTIR)

[26] M.A. Mohamed, J. Jaafar, A.F. Ismail, M.H.D. Othman, M.A. Rahman, Chapter 1 - Fourier Transform Infrared (FTIR) Spectroscopy, Editor(s): Nidal Hilal, Ahmad Fauzi Ismail, Takeshi Matsuura, Darren Oatley-Radcliffe, Membrane Characterization, Elsevier: 2017, Pages 3–29.

[27] V. Sorgato, M. Berger, C. Emain, C.V. Bizet, J.M. Dinten, G.B. Heckly, A.P. Chrétien, J. Biomed. Opt. 21 (2016) 065003.

[28] G. Gauglitz, T. Vo-Dinh, Handbook of Spectroscopy, WILEY-VCH Verlag, Weinheim: 2003.

[29] S. Greenfield, J. Anal. At. Spectrom. 9 (1994) 565–592.

[30] G.R. Allen, Jr. A colloidal nanoparticle form of indium tin oxide: system development and characterization, 2009.

[31] E. Sadeghi, M.S. Oskoui, M. Khatamian, A.H. Ghassemi, MRC 5 (2016) 75–83.

[32] X. Wang, M. Economides, Chapter 7 - Gas-To-Liquids (GTL), Editor(s): Xiuli Wang, Michael Economides, Advanced Natural Gas Engineering, Gulf Publishing Company: 2009, Pages 243–287.

[33] https://www.shimadzu.com/an/gc/support/fundamentals/gc.html

[34] E. Stauffer, J.A. Dolan, R. Newman, Chapter 8 - Gas Chromatography and Gas Chromatography–Mass Spectrometry, Editor(s): Eric Stauffer, Julia A. Dolan, Reta Newman, Fire Debris Analysis, Academic Press: 2008, Pages 235–293.

[35] S. Park, Y. Lee, G. Kim, S. Hwang Korean J. Chem. Eng. 33 (2016) 3417–3424.

[36] V.G. Jenson, G.V. Jeffreys, Mathematical methods in chemical engineering. 2nd edn. Academic press, 6, (1977).

Chapter-3

Enhanced Catalytic Activity of Boron-Containing MgO on Vanadium Loading for the Oxidative Dehydrogenation of n-Butane

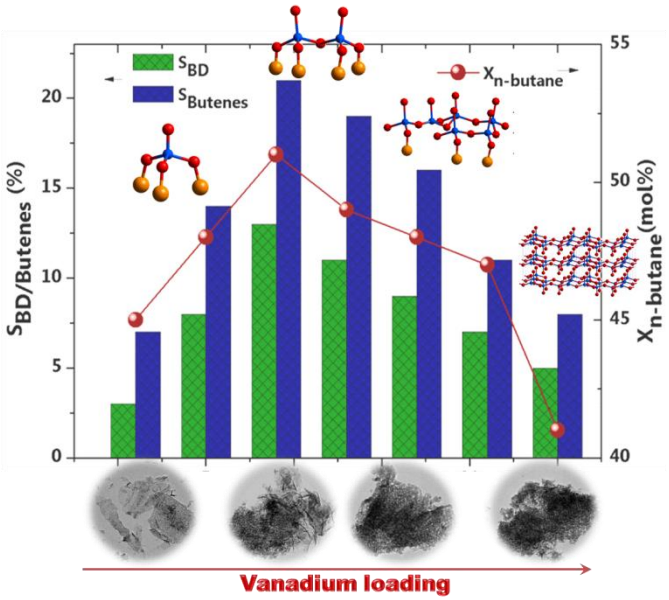

Highlights

- Vanadium loaded boron containing MgO catalysts are synthesized and the oxidative dehydrogenation of n-butane (ODHnB) to 1, 3-butadiene is studied with molecular oxygen as oxidant

- Catalyst compositions as well as reaction parameters are varied for maximum productivity

- Vanadium addition improved the activity and found selective in monomeric as well as oligomeric forms

- V^{4+}/V^{5+} ratio and acidic-basic sites are crucial to define the catalyst performance

- Boron helps for VO_x site isolation and the best catalyst is sturdy over 150 h at the optimized reaction conditions

3.1. Oxidative dehydrogenation of n-butane

Polymers play an essential role in the everyday life of human beings as a starting precursor for almost all essential materials. Monomers are the basic unit of a polymer and among them; 1, 3-butadiene (BD) is one of the most important chemical commodities. It is a valuable petrochemical product as well as a key monomer for the fabrication of synthetic rubber and for the manufacture a wide variety of industrially useful chemicals [1, 2]. The on-purpose synthesis strategy of BD is the industrially implemented catalytic dehydrogenation (DH) of n-butane and/or n-butenes, namely; Philips process and Houdry Catadiene process respectively [3]. Even though these processes provide a high selectivity towards the desired olefin, [4] the endothermicity of DH (*Eq. 3.1*) demands elevated operational temperatures of 550–700 °C which causes rapid catalyst deactivation due to coke formation. Employment of steam [5] or the regeneration cycles can improve catalyst lifetime, which might increase the unit operational cost [6]. This scenario leads the research interest to uncover alternative methods for DH with minimum capital cost and energy efficiency for industrial realization.

$$C_4H_{10} \leftrightarrow C_4H_6 + 2H_2;\ \Delta H_r = +107\ \text{kJ/mol} \qquad \textit{(Eq. 3.1)}$$

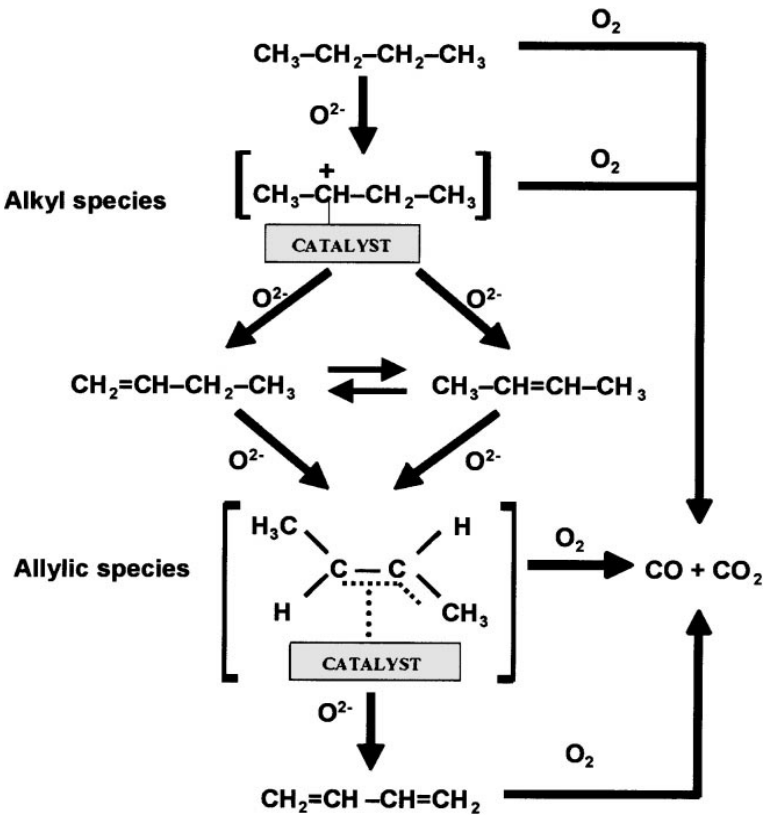

Scheme 3.1 Plausible reaction pathway of ODBnB [7]

In the past decades, oxidative dehydrogenation of n-butane (ODHnB) has been attracted enormous attention as an alternative route to normal non-oxidative dehydrogenation reaction owing to its exothermic nature (*Eq. 3.2*). Hence, the process becomes thermodynamically favourable at lower workable temperatures with proper control over the equilibrium. The presence of oxidant and the formation of stable water molecule during the reaction can retard the coke formation to a certain extent and increases the catalyst life span [8]. The reaction pathway and possible product formation are depicted in **Scheme 3.1**.

$$C_4H_{10} + {}^1/_2O_2 \rightarrow C_4H_6 + 2H_2O;\ \Delta H_r = -132\ \text{kJ/mol} \qquad \textit{(Eq. 3.2)}$$

A substantial amount of work has been done until now, while the development of an appropriate ODHnB catalyst for the successful commercial implanting remain challenging due to the possible formation of over oxidation products at vigorous reaction environment [9]. Hence, the catalyst should be tailored with suitable properties to immediately desorb the formed products from the stream before any runaway reactions [3].

3.2. Background of the work

The ODH catalysts should be selected depending on the nature of the reactant alkane. Many transition metal based materials are engaged taking advantage of their redox nature. Molybdenum and vanadium based systems are well established for the ODH of alkanes. Extensive studies were accomplished on vanadium-based catalytic systems for ODHnB to BD [10–12]. It is widely accepted that, dispersion as well as the structure of vanadia species over the support are the essential parameters to define the activity for ODHnB [9, 13].

Setnicka *et. al.* have studied supported VO_x catalysts on HMS and recognized the formation of four different types of surface vanadia species (**Fig. 3.1**): tetrahedrally coordinated highly dispersed monomeric units (type I), one-dimensional oligomeric units with distorted tetrahedral coordination (type II), octahedrally coordinated two-dimensional polymeric units (type III) and three-dimensional V_2O_5 bulk crystallites (type IV) [9]. Among these various types, the major active species for a particular reaction is determined by the nature and interaction of vanadium with the support. Highly dispersed vanadia species are found most active and selective for ODHnB, and hence type I, II, and III are much desired to achieve the best yield of BD. VO_x species with more than four oxygen are more active but less selective than VO_4 in tetrahedral coordination. Isolated tetrahedral species are more selective but less active than V–O–V bridged V sites. Moreover the reduction of V^{5+} to V^{3+} as well as V^{5+} to

V^{4+} can also play an important role in the mechanism. Following the reduction $V^{5+} \rightarrow V^{4+}$; C–H activation by homolytic scission can occur over VO_x supported catalysts [14]. At a well-dispersed level, VO_x units can selectively activate C–H bonds limiting the cracking-combustion reactions by taking advantage of their geometric and electronic structure, which is easily tuneable with the support and temperature.

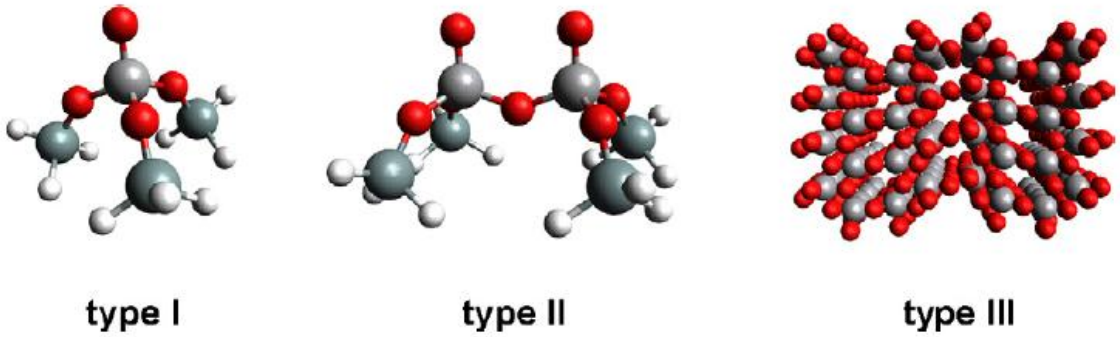

Fig. 3.1 Different types of surface VO_x species [9]

The textural properties and acidic, basic nature of the catalyst support plays an indispensable part in the activity performance via appropriately dispersing vanadia on the surface [15, 16]. Hence, MgO support protrudes among other systems since the basic butenes can easily desorb from the basic support suppressing consecutive over oxidation and ultimately improving BD selectivity. Moreover, the acidic nature of vanadia can accelerate maximum dispersion on MgO support. Considering all these aspects, V/MgO can be the right candidate for ODHnB and reported by Chaar *et. al.* [17]. Furthermore, $Mg_4V_2B_2O_x$ catalyst composition exhibited very high selectivity to butenes at 500 °C providing structural site isolation of vanadia. The recent studies in boron-based catalysts proved that Brønsted acidic property of BO_4 sites [18] could primarily increase the catalytic activity for alkane DH [19].

Apart from the previous studies, here we report a different citrate gel combustion method for the *in situ* addition of boron in MgO, followed by the wet impregnation of vanadium. Further, the effect of boron addition and vanadium loading on the catalytic activity towards BD synthesis is investigated via ODH of n-butane in the presence of molecular oxygen as an oxidant. Our main aim is to emphasize the synthetic strategy to develop a finely dispersed material by varying the catalyst compositions. Further, the performance is correlated to the material properties combing various analysis techniques like powder X-ray diffraction,

nitrogen physisorption, temperature-programmed study, spectroscopy, and microscopic methods.

3.3. Results and discussion

The catalysts were synthesized by combustion followed by wet impregnation of vanadium and broadly discussed in the **Section 2.3.1**. Further, the activity for ODHnB was studied and correlated to the material properties in this part.

3.3.1. Catalytic activity study

All synthesized catalysts were tested for the ODHnB reaction to study the effect of boron and vanadium composition in a continuous flow mode fixed bed reactor using molecular oxygen as the oxidant (refer **Section 2.6** and **2.7**). Different reaction parameters like on set temperature, alkane to oxidant ratio are varied to investigate their individual role in the final product yield. *Caution must be taken during the reaction since the reaction feed consists of a combustible gas mixture of n-butane and oxygen operating at high temperatures.* The reaction data was collected for tabulation at the end of 4 h for each run. Negligible coke formation was observed on the catalyst bed and is quantified post reaction.

3.3.1.1. Effect of boron content in xBMO

The BMO catalysts prepared by sol-gel combustion are subjected for ODHnB at 450 °C with n-butane to oxygen ratio as one making a total feed flow of 600 h^{-1}. **Fig. 3.2a** reveals that activity is observed even for the least boron-containing catalyst with minor selectivity towards butenes ($S_{butenes}$). The conversion of n-butane ($X_{n\text{-}butane}$) increases to a maximum of 15 % with the boron content up to 5BMO. After that, it decreases, making a parabolic activity trend with the boron loading. BD selectivity (S_{BD}) also followed a similar behavior; however, the value remained constant after 10BMO.

Additionally, a steady rise in the selectivity of butenes is found while increasing the boron content. These observations indicate that an optimum amount of boron can selectively navigate the formation of BD from butenes through the second dehydrogenation step. Furthermore, high boron content can favor the first dehydrogenation of n-butane to butenes. For the 5BMO sample, 8 % BD selectivity, as well as 10 % butenes selectivity, are summarized from the reaction results at 46 % n-butane conversion. Hence, the catalyst composition is optimized as 5BMO under the given reaction conditions.

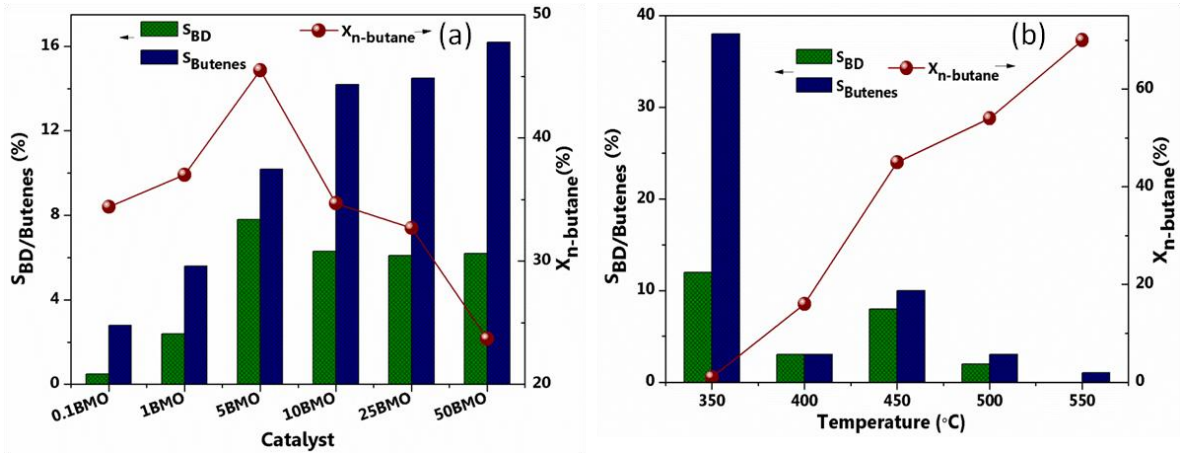

Fig. 3.2 Effect of (a) boron loading on MgO at 450 °C and (b) temperature over 5BMO. *Reaction conditions: 500 mg catalyst, O_2/C_4=1, 600 h^{-1} GHSV with respect to total feed.*

3.3.1.2. Effect of reaction temperature over 5BMO

Afterward, 5BMO catalyst is investigated to find the reaction temperature, which gives the highest yield of BD. The onset temperature is varied from 350 to 550 °C in different runs under the feed flow; O_2/C_4=1 at 600 h^{-1} GHSV. The data obtained is graphically represented in **Fig. 3.2b**. Though, maximum BD yield is quantified at 350 °C, the reactant conversion is almost zero and could not be considered for further studies. It is obvious to observe an increase in n-butane conversion with the reaction temperature. At 550 °C, butene formation is not detected due to the cracking process either to lower hydrocarbons, carbon oxides, or to coke. The highest selectivity for BD and butenes is obtained as 8 and 10 % respectively for 5BMO at 450 °C; and therefore 450 °C is regarded as the optimized reaction temperature.

3.3.1.3. Effect of vanadium loading in yV5BMO

To improve the butenes' yield, vanadium was loaded in different amounts on 5BMO, the optimized composition from the previous experiment. The catalyst performance of various VBMO catalysts is executed at 550 °C with O_2/C_4=1 with Ar balance together making a total GHSV of 3000 h^{-1}. The results are displayed in **Fig. 3.3a**, and there is a significant increase in the n-butane conversion as well as the yield of C_4-ODH products with vanadium loading upto 9V5BMO. At higher vanadium loading, the values gradually decrease. It may be observed that the catalytic activity falls in a parabolic pattern with the addition of vanadium. From this study, the role of vanadium is regarded as to improve the overall activity of ODHnB reaction; but, a specific catalyst composition is decisive. Here, 9V5BMO gives the highest results among the catalysts studied, and the values are 51 % n-butane conversion with 13 % as well as 22 % selectivity towards BD and butenes, respectively. Therefore, 9V5BMO is considered

as the optimum catalyst composition for the system under study. The reduction in the activity, as well as product selectivity of higher vanadium-containing materials, could be attributed to the polymerization of VO_x species on the surface, [20] which is broadly discussed in the **Section 3.3.2**.

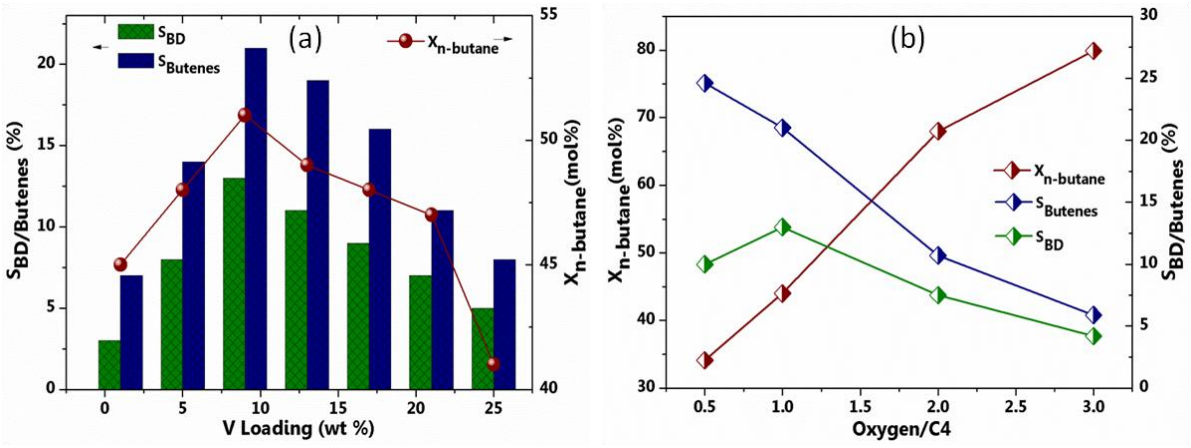

Fig. 3.3 Effect of (a) vanadium loading on 5BMO at O_2/C_4 =1 and (b) O_2 to C_4 ratio over 9V5BMO.
Reaction conditions: 500 mg catalyst, 550 °C, 3000 h^{-1} GHSV with respect to total feed, Ar balance.

3.3.1.4. Effect of O_2 to C_4 ratio over 9V5BMO

The effect of feed composition is studied by conducting the reaction over 9V5BMO catalyst with different oxygen to n-butane ratio ranging from 0.5–3.0 while keeping other parameters constant as 550 °C and GHSV making up to 3000 h^{-1} with argon gas. The data represented in **Fig. 3.3b** shows that plenty of oxygen in the reaction mixture drastically amplifies the conversion of n-butane reaching the maximum; 80 % at O_2/C_4=3.0. However, the ODHnB product yield is sharply reduced with oxidant to n-butane ratio. Extra molecular oxygen available during the reaction mainly leads to combustion products. The reaction is selective under lean oxygen partial pressures, and the highest yield is found at O_2/C_4=1 and thus selected for further studies. The peak result is depicted as 51 % n-butane conversion and 13 % BD selectivity under the specified conditions.

3.3.1.5. Effect of reaction temperature over 9V5BMO

The operating temperature is a vital factor influencing any catalytic reaction. From the earlier study, the material composition, as well as reactant feed ratio, are chosen as 9V5BMO as well as O_2/C_4=1 at 3000 h^{-1} GHSV. Further, the temperature onset is varied stepwise from 400 to 550 °C in a regular interval of 50 °C, and the results are summarized in **Fig. 3.4a**. An entirely

different activity trend is observed for 9V5BMO compared to 5BMO discussed in the S**ection 3.3.1.2**. As expected, the conversion of n-butane is steeply increased up to 500 °C, although, after that, it is independent of reaction temperature. Butenes' selectivity falls in an inverse parabolic trend with the temperature, as shown in the graph. The selectivity of BD is gradually improved to 13 %, with the reaction temperature giving the maximum performance at 550 °C. These observations match well with the reported literature that typically, vanadium based catalysts are active for ODH at high temperatures [7, 9, 21].

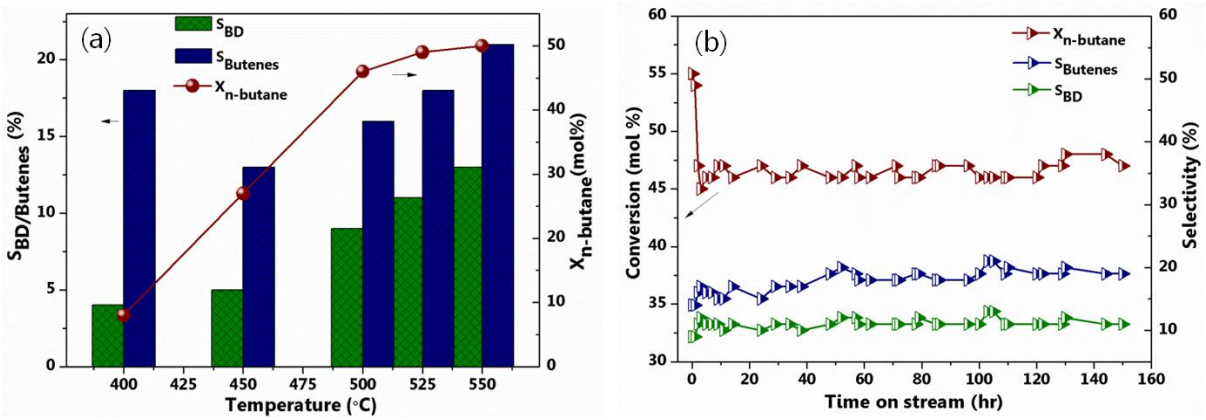

Fig. 3.4 (a) Effect of reaction temperature over 9V5BMO and (b) on stream study over 9V5BMO at 550 °C.
Reaction conditions: 500 mg catalyst, O_2/C_4=1, 3000 h^{-1} GHSV with respect to total feed, Ar balance.

3.3.1.6. On stream study

Finally, a separate experiment is conducted to test the stability of the best catalyst. Towards this purpose, ODHnB is continuously run over 9V5BMO catalysts at the optimized reaction parameters such as 550 °C, O_2/C_4=1, and 3000 h^{-1} GHSV as depicted in **Fig. 3.4b**. Initially, there is a 55 % conversion of n-butane, which falls to 48 % after the induction period. This is reflected as an improvement in C_4 alkenes' selectivity. After the second hour, the activity performance of 9V5BMO remains constant for 150 h under the set reaction conditions. The best ODHnB activity is observed as 48 % n-butane conversion with 13 % and 22 % selectivity towards BD and butenes, respectively. Even though the product yield achieved is lower than the reported vanadia based catalysts, [7, 22] this work has significance in terms of steady catalytic activity over 150 h. The reasons behind the stable activity of this catalyst composition will be explained in the following discussion.

3.3.2. Catalyst characterization

This section establishes the relation between the catalytic activity results and the physico-chemical properties (see S**ection 2.5**) of materials with the help of reported literatures.

3.3.2.1. Material crystallinity

Crystalline phases of the powder samples are identified from PXRD analysis. The diffraction patterns of xBMO calcined at 550 °C for 12 h are given in **Fig. 3.5a**. For the samples containing boron up to 10 wt %, mainly five diffraction peaks observed at 36.7, 42.8, 62.2, 74.7 and 78.6 ° representing the (111), (200), (220), (311) and (222) planes of periclase MgO phase respectively which are matching well with the JCPDS card no. 43-1022. No other phase segregation is visible in these materials. The diffractogram of 0.1BMO clearly shows well crystalline features of MgO, while the crystallinity decreases when increasing the boron content. This is reflected as a gradual enhancement in the full width at half maximum (FWHM) of the principal peak at 42.8 ° as observed from **Fig. 3.5a**. This indicates boron incorporation into the MgO crystal lattice at lower loadings. Also, Pham *et. al.* have analyzed (111) crystal plane of the periclase MgO phase and found that B^{3+} can occupy either the trigonal or tetrahedral position of MgO [23]. Even at higher boron loaded samples, such as; 25BMO and 50BMO, no reflections for either boron oxides or magnesium borates are present. The broad peaks might correspond to an amorphous or nanomaterial formed during the material synthesis. Further characterization of xBMO is beyond the scope of this work.

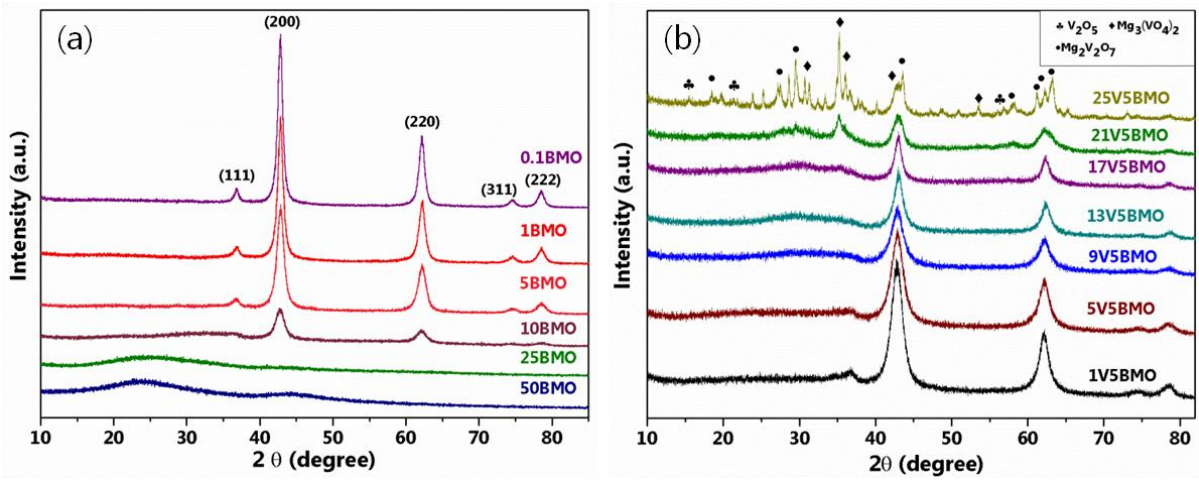

Fig. 3.5 PXRD patterns of fresh (a) xBMO and (b) yV5BMO samples

They are shown in **Fig. 3.5b**, which is the wide-angle XRD patterns of vanadium loaded 5BMO catalysts generally represented as yV5BMO. Similar to xBMO, at lower vanadium contents, the crystalline features of periclase MgO are present. At lower loadings, the

synthesized catalysts do not contain V_2O_5 polycrystallites because polymerization happens only at a high concentration of vanadia species. Beyond 17 wt % of V, segregation and separation of other peaks are predominantly seen. In the 25V5BMO catalyst, several small peaks are observed, indicating mixed crystalline phases of magnesium orthovanadate ($Mg_3(VO_4)_2$), magnesium pyrovanadate ($Mg_2V_2O_7$) and small amount of bulk V_2O_5. Previous studies on vanadium doped MgO depict the active phase as Mg orthovanadate [24]. This could be due to the highly dispersed and isolated monomeric vanadia species, which serves as the intense catalytic center for ODHnB as reported by Setnicka *et. al.* [9]. On the other hand, it is reported that Mg pyrovanadate is nonselective for this reaction [25]. Furthermore, Mg metavanadate (MgV_2O_6) is not present in this pattern. The optimized catalyst 9V5BMO also contain highly dispersed $Mg_3(VO_4)_2$ phase unidentified in PXRD, but the Raman spectrum of the catalyst given in **Fig. 3.13a** confirms this active phase. Nonselective phases in the catalysts at higher vanadium loading make them less active for the reaction. Similar to the studies by Karakoulia *et. al.* [26]. And Liu *et. al.* [27], in the present work also V_2O_5 crystallites are detected at vanadium loadings more significant than 17 wt %. In summary, $Mg_3(VO_4)_2$ phase is critical for the highest activity of 9V5BMO. But, further material characterization should be made to find other reasons.

3.3.2.2. Textural properties

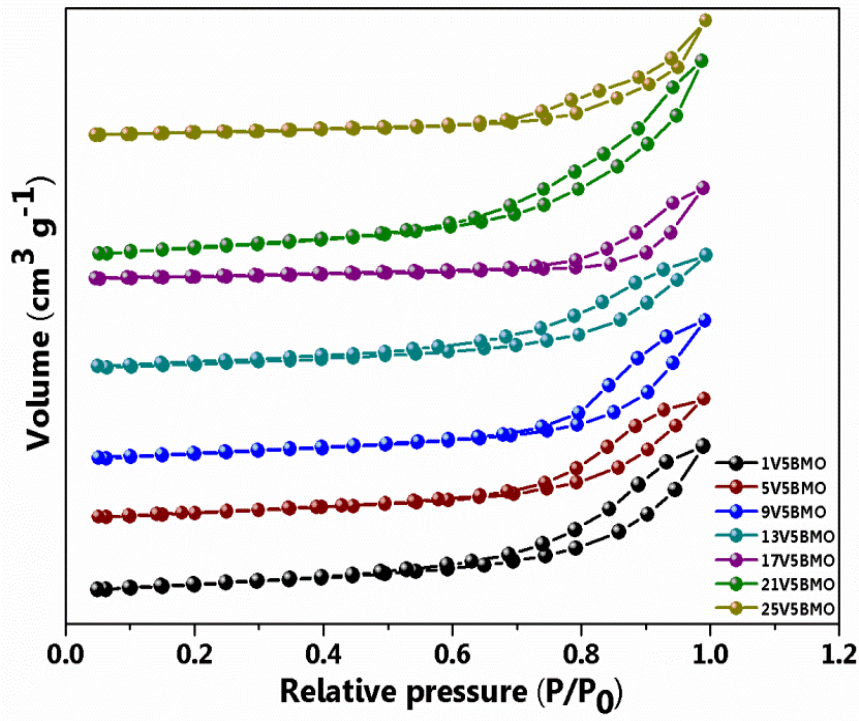

Fig. 3.6 N_2-sorption isotherms of calcined yV5BMO materials

Textural properties of the catalysts synthesized via combustion followed by impregnation are analyzed by nitrogen sorption study. The adsorption-desorption isotherms of these materials represented in **Fig. 3.6** revealed type IV isotherms with H1 hysteresis loop typical of mesoporous structure. **Table 3.1** shows the catalyst compositions and surface areas (S_{BET}) of the sintered catalysts calculated by the BET analysis method. Sample without vanadium exhibited 66 m^2 g^{-1} BET surface area. After loading vanadium, the value increases to 118 m^2 g^{-1} for 1V5BMO. The optimized catalyst, 9V5BMO, has a considerable surface area of 117 m^2 g^{-1}.

Table 3.1 Physicochemical properties of the catalysts

Catalyst	**S_{BET}[a] (m^2 g^{-1})**	**H_2 consumption[b] (mmol g^{-1})**	**T_{max}[c] (°C)**	**CO_2 desorbed[d] (mmol g^{-1})**	**NH_3 desorbed[d] (mmol g^{-1})**	**Coke deposition[e] (%)**
5BMO	66	-	-	1.326	1.308	-
1V5BMO	118	0.27	656	1.649	2.125	8
5V5BMO	111	0.72	573	1.508	1.914	4
9V5BMO	117	1.68	590	1.425	2.151	3
13V5BMO	90	2.25	643	0.983	1.41	1
17V5BMO	85	2.91	679	1.149	1.553	5
21V5BMO	83	3.47	702	0.866	1.203	4
25V5BMO	51	4.39	607	1.34	0.917	3

[a]Specific surface area determined by the BET method.
[b]Quantified from H_2-TPR data.
[c]The first temperature of maxima in TPR profile.
[d]Total consumption quantified from CO_2/NH_3 TPD results.
[e]Calculated by TG/DTA analysis under air atmosphere.

From the BET results of other samples given in **Table 3.1**, it appears that the surface area reduces with vanadium loading. This behavior may be attributed to the deposition of vanadia species on the pores, which will cause pore blockage, and ultimately S_{BET} will be decreased [28]. The polymerization of VO_x occurring at higher vanadium loadings can also cover the support surface. Surprisingly, the decrease in surface area is relatively gradual. The lowest S_{BET} for 25V5BMO might be credited due to the segregation of multi phases of magnesium vanadates and minor amount of bulk vanadia crystals, as evidenced by PXRD data. This could be one of the reasons for the least activity of this particular catalyst for ODHnB. Therefore, catalytic performance can be directly related to the total surface area of the catalyst systems.

3.3.2.3. Catalyst morphology

Morphology and surface topology of the best catalyst are investigated with microscopic techniques viz. TEM and SEM. The representative TEM images of the 9V5BMO catalyst are given in **Fig. 3.7**. The fresh catalyst (**Fig. 3.7a**) exhibits a porous structure supporting the mesoporous character evidenced by N_2-sorption isotherm. The electron diffraction pattern given in the inset shows the crystalline nature of the material in accordance with the PXRD pattern. Even after the reaction, the catalyst maintains its porosity, as seen from **Fig. 3.7b**. The lattice fringes measure 0.2 nm width characteristic of the periclase MgO (200) crystal plane.

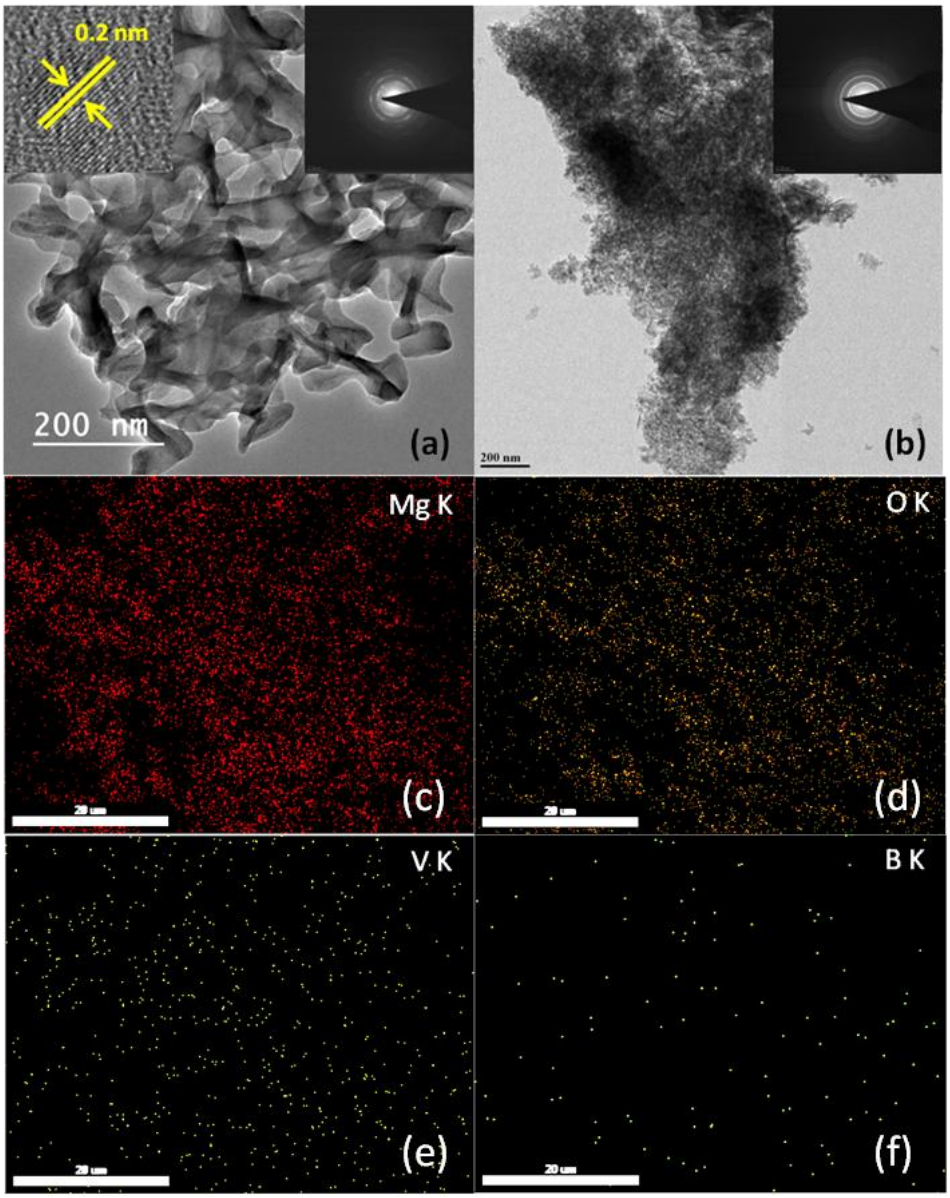

Fig. 3.7 (a, b) HR-TEM and (c-f) elemental mapping images of 9V5BMO

SEM image given in **Fig. 3.8** doesn't demonstrate any particular morphology. A collective analysis of the EDX spectrum depicted in **Fig. 3.8** and the elemental mapping images represented in **Fig. 3.7c-f** shows the presence of elements viz; B, V, Mg, and O. Accordingly, 9V5BMO catalyst illustrates excellent dispersion of all elements as well as high material purity. Also, the fine spreading of homogenous vanadia is deduced over 5BMO support. This property of the optimized catalyst will also largely contribute to enhance C_4 olefins yield.

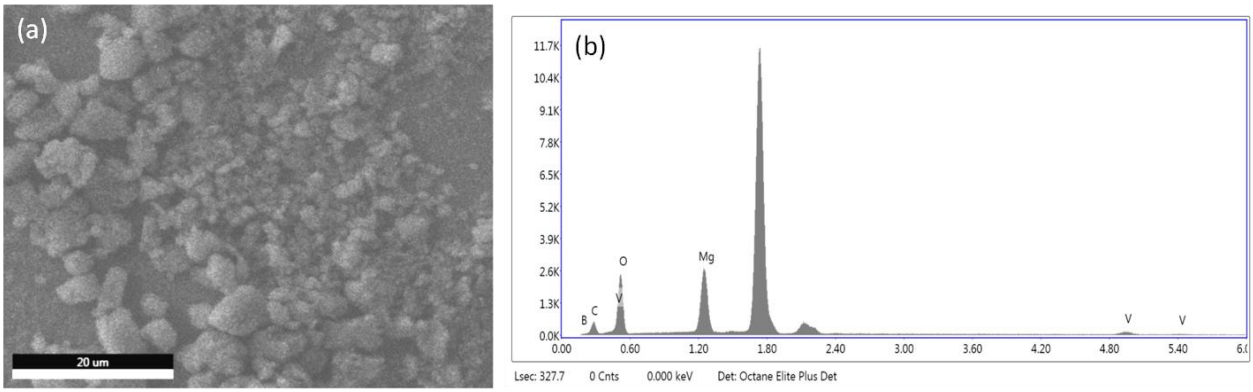

Fig. 3.8 (a) SEM and (b) EDX spectra of 9V5BMO

3.3.2.4. DR UV-visible spectroscopy

Ultraviolet-visible spectroscopy in the diffuse reflectance mode often used to study the nature of vanadia species and its local coordination. It also provides information about the oxidation states of vanadium. The spectra recorded for all samples are shown in **Fig. 3.9a**. It may be noted that BMgO supports do not exhibit any peak in the spectra. The absorption bands usually represent the ligands to metal charge transfer transition (LMCT), $O \rightarrow V^{5+,}$ and d-d transition [29]. The characteristic d-d transition identified for V^{4+} is weak, which means vanadium mostly exists in the +5 oxidation state. No peaks are observed above 500 nm, which deduces that the absorption band corresponds to inactive V_2O_5 bulk oxide with octahedral coordination is absent. The signals in the range of 200–300 nm belong to tetrahedrally coordinated VO_x species [30]. Followed by that, at around 350 nm, a combination of monomeric as well as oligomeric vanadia tetrahedral units are present. Above 350 nm, the presence of either tetrahedral oligomeric vanadia or bulk like octahedral species is confirmed.

From the spectra, it is obvious to see a high concentration of vanadia monomeric and oligomeric units for the 9V5BMO catalyst, which can contribute to the selective formation of C_4 olefins. Accordingly, it may be concluded that the polymerization of vanadia is proved from DR UV analysis supporting H_2-TPR results discussed in the S**ection 3.3.2.6**.

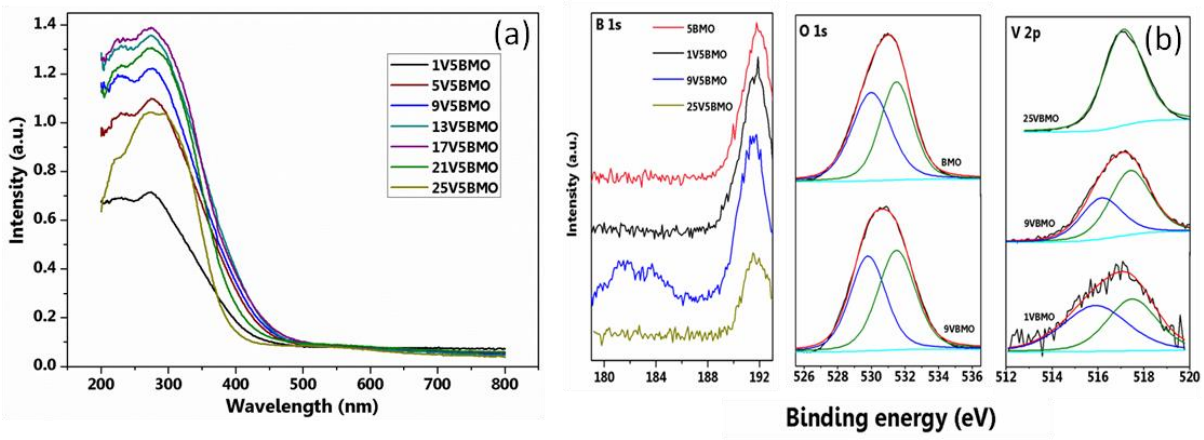

Fig. 3.9 (a) DR UV-Visible spectra of yV5BMO catalysts and (b) XPS spectra of B 1s, O 1s, V 2p core levels of different catalysts.

3.3.2.5. XPS study

The surface atomic composition of the fresh catalysts is determined by XPS analysis. The spectra of B 1s, O 1s, and V 2p core levels are shown in **Fig. 3.9b**. Boron exists in the +3 oxidation state in the studied catalytic systems, as revealed from the spectra. The function of boron might be providing structural site isolation of the active vanadium species [31]. XPS spectra of O 1s and V 2p are deconvoluted using XPSPeak41 software by taking C 1s of contaminant carbon to correct any charge induced binding energy (BE) shifts. V 2p is separated into two peaks corresponding to +4 and +5 at 516.2 and 517.4 eV, respectively. However, 25V5BMO demonstrated a single peak attributed to V^{5+} only.

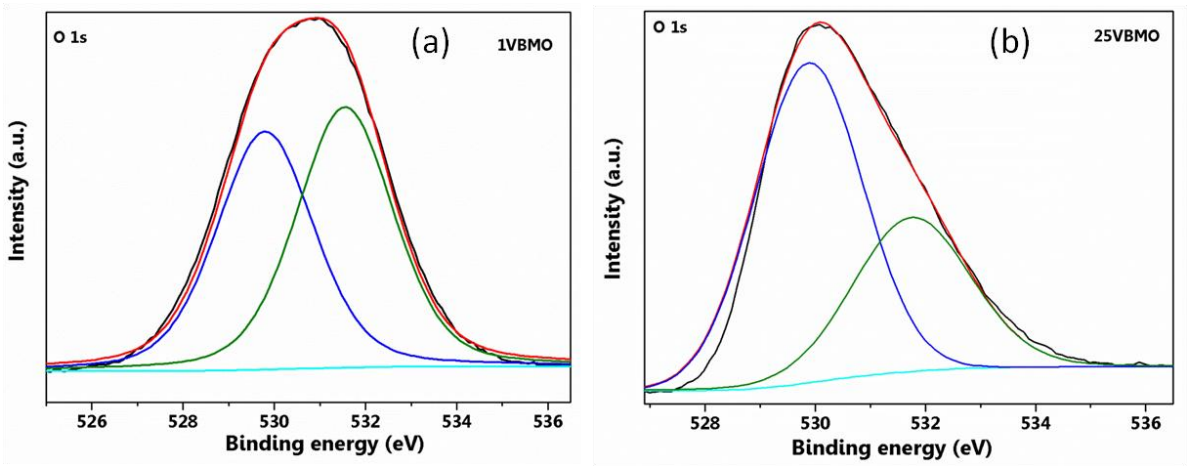

Fig. 3.10 Deconvoluted O 1s XPS spectra of (a) 1V5BMO and (b) 25V5BMO

O 1s give two different peaks after peak deconvolution, as represented in **Fig. 3.9b** and **Fig. 3.10**. The lattice oxygens on the material surface show peak around 529.6 eV. At 531 eV, the contribution from the hydroxyl species and the surface adsorbed oxygens are identified [32].

The amount of both lattice, as well as adsorbed oxygen species, are quantified from the spectra and given in **Table 3.2**. The optimized composition 9V5BMO contains 47.6 % of lattice oxygen along with V^{4+}/V^{5+} ratio, 0.7 appropriate for ODHnB. Jian *et. al.* proved that selective oxidative of alkane over the VPO catalyst needs proper V^{4+}/V^{5+} balance, which plays a vital role in defining the final alkene yield [33]. This result may be applicable for the current reaction also. Apart from this, V^{5+} is essential for C–H activation [14].

Table 3.2 The surface atomic composition of the catalysts in percentage

Catalyst	O_{latt}	O_{ads}	V^{4+}	V^{5+}
5BMO	51.7	48.3	-	-
1V5BMO	47.7	52.3	53.5	46.5
9V5BMO	47.6	52.4	42.8	57.2
25V5BMO	65.8	34.2	-	100

Meanwhile, 25V5BMO holds 100 % V^{5+} due to a complex mixture of different phases formed via the highest extent of polymerization of VO_x units, as observed from XRD and TPR. The surface will be covered entirely with bulk vanadia. However, the absence of any V^{4+} ion reflects in the lowest selectivity for ODH butenes [24]. The polymerization phenomena will reduce the active monomeric vanadia species and hence gives low BD productivity at higher loadings.

3.3.2.6. Catalyst reducibility

Temperature programmed reduction technique is used to analyze the redox character of the materials and also to distinguish different types of vanadia species dispersed on the surface. The plotted TPR profiles are presented in **Fig. 3.11a**, and the additional results obtained from the patterns are summarized in **Table 3.1**. MgO support does not exhibit any reduction peak in the studied temperature range. From the table, it is clear that hydrogen consumption linearly increases with the vanadium loading and reaches maximum for 25V5BMO. The temperature corresponding to the first maxima; T_{max} of each catalyst is also given in **Table 3.1**. A proper reduction peak is not identified in the 1V5BMO sample owing to the least vanadium content. The peak observed at 573 °C for 5V5BMO contributes to the reduction of highly dispersed monomeric vanadia species with tetrahedral like coordination [34]. Further, T_{max} is shifted to a higher temperature region with an increase in vanadium content. For the catalyst containing 21% V, T_{max} is at 702 °C, signifying the gradual formation of polymeric vanadia units probably in the octahedral coordination [34]. This result is in good agreement with the DR UV spectra interpretations (**Section 3.2.2.4**).

A thorough analysis of UV-visible, as well as TPR results, can indicate that the low-temperature reduction peak might represent both monomeric and oligomeric tetrahedral like VO_x species [34]. Hence, the catalysts with less vanadium are much prone to reduction than other catalysts, which make it a better candidate for ODHnB reaction. Among the materials with low vanadium, 9V5BMO exhibits two well-separated peaks attributing to the reduction of isolated V^{5+} in distorted tetrahedral VO_x and isolated V^{5+} in $Mg_3(VO_4)_2$ [9]. Comparatively higher activity of this material might be due to the sufficient amount of easily reducible vanadia dispersed over the surface.

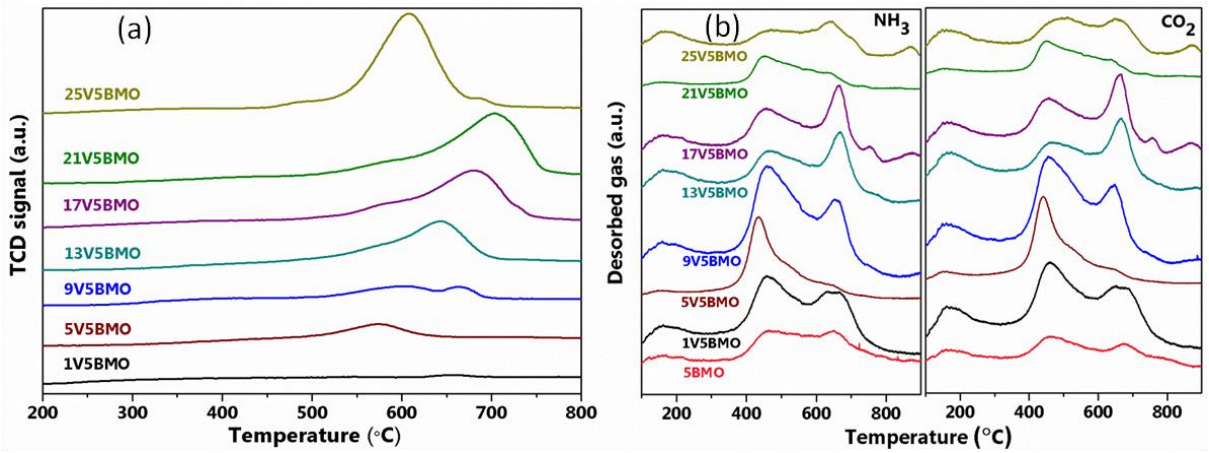

Fig. 3.11 (a) H_2-TPR and (b) NH_3/CO_2 TPD profiles of yV5BMO catalysts

3.3.2.7. Acid-base properties

The acidic-basic nature of the catalysts greatly influences the selectivity of BD and the C_4 olefin distribution. Therefore, to explain the acidic and basic nature of the catalysts, all the calcined catalyst samples were subjected to temperature-programmed desorption studies using NH_3 and CO_2 as probe molecules. The final plots are shown in **Fig. 3.11b**, and the quantified values are given in **Table 3.1**. The presence of the weak, medium, and strong acidic-basic sites are visible in the TPD profiles at the temperature region around 200, 450, and 700 °C, respectively. Vanadium incorporation increases the acidic nature while slightly reduces the basic character, as depicted in **Table 3.1** and the TPD profiles.

Basicity is a significant factor in determining the desorption of formed olefins from the catalyst surface [3]. In addition, a proper balance between acidity and basicity is crucial for the activation of n-butane during the ODH process [35]. The TPD results show that an increase in vanadium content has steadily increased the number of medium acid-base sites up to 9V5BMO catalyst. At higher vanadium loadings, the strong acid-base character is

prominent which is unfavourable for the reaction. The highest catalytic activity of 9V5BMO might be because of the optimum amount of medium acidic and basic sites. An appropriate balance between acid-base properties makes the easy desorption of the desired products from the active sites [36]. This will further reduce the formation of cracked products and so the selectivity of required products will be improved. Hence, coking can also be reduced to a great extent.

3.3.2.8. Spent catalyst analysis

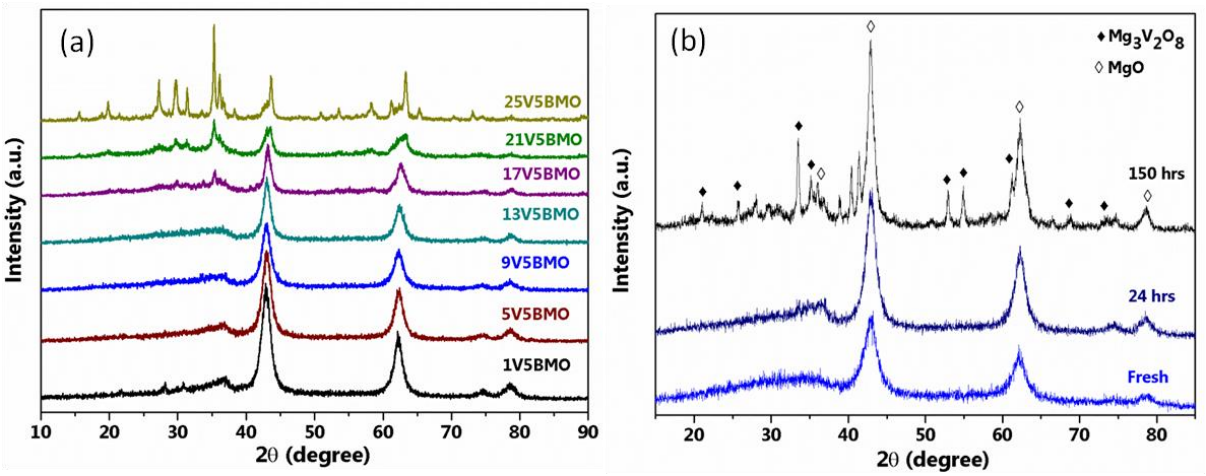

Fig. 3.12 PXRD patterns of (a) spent yV5BMO catalysts and (b) 9V5BMO after ODHnB for different reaction time.

The characterization of the spent catalysts can provide valuable information regarding the stability of the crystalline structure and the state of vanadia species. For this purpose, the materials after the ODH reaction at 550 °C are subjected to detailed analysis. The crystalline state of the spent catalysts is analyzed with PXRD, and the patterns are shown in **Fig. 3.12a**. A thorough analysis of the diffractograms reveals the separation of various Mg vanadate phases at lower and higher vanadium loadings. Hence, it may be deduced that these systems fail to retain the structural properties after the high-temperature ODH reaction. However, 9V5BMO maintains the structural stability even under the harsh reaction conditions. Further, spent catalyst was removed from the reactor bed after 24 and 150 h of on stream study in different experiments and analyzed with PXRD. The results given in **Fig. 3.12b** depict that the pattern is the same after 24 h reaction. However, $Mg_3(VO_4)_2$ phase is separated from the MgO lattice while the catalyst was still active for the ODHnB reaction, as illustrated in the 150 h TOS analysis (**Fig. 3.4b**). This observation proves the active phase as magnesium orthovanadate, $Mg_3(VO_4)_2$.

Table 3.3 ICP-AES analysis of fresh and spent 9V5BMO

Sample	V content (wt %)
9V5BMO Fresh	8.2
9V5BMO after 24 h	7.7
9V5BMO after 150 h	6.6

Conversely, the catalytically active magnesium orthovanadate phase is identified in the fresh 9V5BMO also from the Raman analysis. Further, Raman spectra of the fresh, as well as spent catalysts are presented in **Fig. 3.13a**. Both catalysts comprise the $Mg_3(VO_4)_2$ phase, and the structural features are intact even after the high-temperature ODH reaction at 550 °C. Thus, Raman analysis substantiated the conclusions derived from PXRD of the used catalyst.

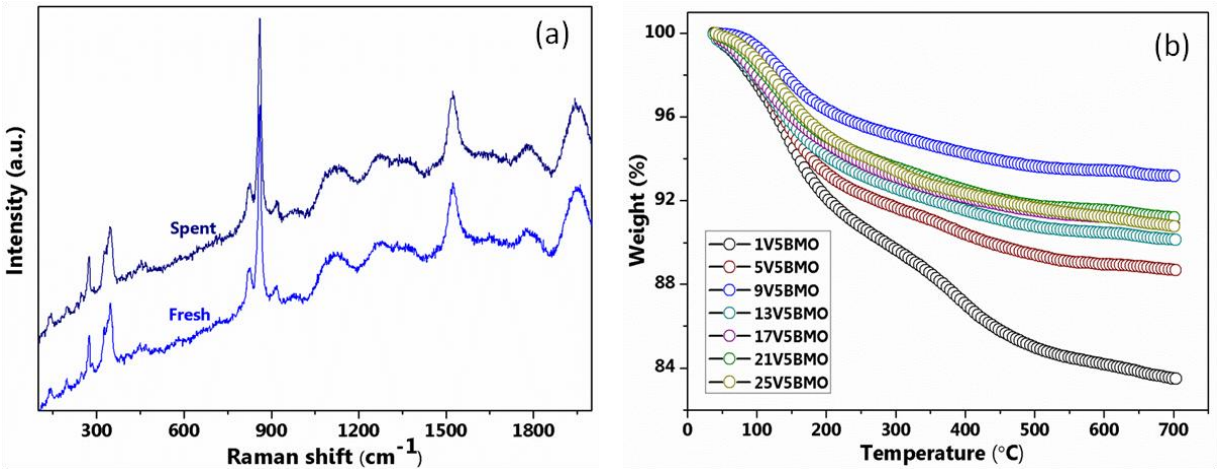

Fig. 3.13 (a) Raman spectra of fresh and spent 9V5BMO; (b) thermograms of all spent yV5BMO catalysts.

Further, the catalysts after 24 h and 150 h reaction are analyzed with ICP-AES. The values tabulated in **Table 3.3** shows that slight amount of vanadium leaching occurs during the reaction. Coke formation and deposition are common during the ODHnB high-temperature reaction, and the strength may fluctuate depending on the catalyst system employed and reaction circumstances. Here, all yV5BMO spent catalysts after the reaction at 550 °C are investigated with thermogravimetry in the air atmosphere, and the thermograms are represented in **Fig. 3.13b**. Coke deposition on the surface is quantified for each catalyst at around 350 °C, and the results are tabulated in **Table 3.1**. As shown in the table, the least carbon deposits are found over 9V5BMO, indicating minimum C–C cracking reactions over this catalyst compared to other compositions. Therefore, it may be summarized that other

catalyst compositions are much prone to give the undesired products under the optimized reaction parameters reducing the final C_4 olefin yield.

3.4. Conclusions

A series of vanadium loaded boron-containing MgO materials prepared by coupling combustion as well as wet impregnation methods. The catalyst composition and reaction parameters are varied to achieve maximum ODH butenes selectivity. The optimized catalyst gave appreciable and stable BD selectivity over 150 h in the on-stream analysis. An appropriate number of acid-base sites and suitable V^{4+}/V^{5+} ratio are beneficial for the reaction. Boron helps to increase the dispersion of the active monomeric and oligomeric tetrahedral vanadia units over the basic MgO support. This increase in the dispersion can enhance the easy desorption of the products and improve the olefin yield. In summary, this work discovers the synergy between the metallic and non-metallic systems co-existing in a catalyst through a different approach towards the synthesis strategy for the ODHnB reaction.

References

[1] W.C. White, Chem. Biol. Interact. 166 (2007) 10–14.

[2] S. Matar, M.J. Mirbach, H.A. Tayim, Catalysis in Petrochemical Processes; Kluwer Academic Publishers: Dordrecht, 1989.

[3] J.H. Park, H. Noh, J.W. Park, Appl. Catal. A Gen. 431 (2012) 137–143.

[4] L.M. Madeira, M.F. Portela, Catal. Rev. 44 (2002) 247–286.

[5] J.J.H.B. Sattler, J. Ruiz-Martinez, E. Santillan-Jimenez, B.M. Weckhuysen, Chem. Rev. 114 (2014) 10613–10653.

[6] G. Mitran, T. Cacciaguerra, S. Loridant, D. Tichit, I.-C. Marcu, Appl. Catal. A Gen. 417–418 (2012) 153–162.

[7] J.M.L. Nieto, P. Concepción, A. Dejoz, F. Melo, H. Knözinger, M.I Vázquez, Catal. Today 61 (2000) 361–367.

[8] X. Wang, G. Zhou, Z. Chen, W. Jiang, H. Zhou, Microporous Mesoporous Mater. 223 (2016) 261–267.

[9] M. Setnička, R. Bulánek, L. Čapek, P. Čičmanec, J. Mol. Catal. A Chem. 344 (2011) 1–10.

[10] T. Blasco, A. Galli, J.M. López Nieto, F. Trifiró, J. Catal. 169 (1997) 203–211.

[11] J. McGregor, Z. Huang, G. Shiko, L.F. Gladden, R.S. Stein, M.J. Duer, Z. Wu, P.C. Stair, S. Rugmini, S.D. Jackson, Catal. Today. 142 (2009) 143–151.

[12] Z. Strassberger, E. V Ramos-Fernandez, A. Boonstra, R. Jorna, S. Tanase, G. Rothenberg, Dalt. Trans. 42 (2013) 5546–5553.

[13] S.B. Bukallah, A. Bumajdad, K.M.S. Khalil, M.I. Zaki, Appl. Surf. Sci. 256 (2010) 6179–6185.

[14] O.O. James, S. Mandal, N. Alele, B. Chowdhury, S. Maity, Fuel Process. Technol. 149 (2016) 239–255.

[15] P. Concepción, A. Galli, J.M.L. Nieto, A. Dejoz, M.I. Vazquez, Top. Catal. 3 (1996) 451–460.

[16] A. Corrna, J.M.L. Nieto, N. Parades, A. Dejoz, I. Vazquez, Oxidative dehydrogenation of propane and n-butane on V-Mg based catalysts, in: V.C. Corberán, S.V.B.T.-S. in S.S. and C. Bellón (Eds.), New Dev. Sel. Oxid. II, Elsevier, 1994: pp. 113–123.

[17] M.A. Chaar, D. Patel, M.C. Kung, H.H. Kung, J. Catal. 105 (1987) 483–498.

[18] S. Sato, M. Kuroki, T. Sodesawa, F. Nozaki, G.E. Maciel, J. Mol. Catal. A Chem. 104 (1995) 171–177.

[19] M. Dixit, P. Kostetskyy, G. Mpourmpakis, ACS Catal. 8 (2018) 11570–11578.

[20] T. Williams, J. Beltramini, G.Q. Lu, Microporous Mesoporous Mater. 88 (2006) 91–100.

[21] N. Madaan, R. Haufe, N.R. Shiju, G. Rothenberg, Top. Catal. 57 (2014) 1400–1406.

[22] M. Setnička, P. Čičmanec, R. Bulánek, A. Zukal, J. Pastva, Catal. Today. 204 (2013) 132–139.

[23] T.N. Pham, L. Zhang, D. Shi, M.R. Komarneni, M.P. Ruiz, D.E. Resasco, J. Faria, ChemCatChem. 8 (2016) 3611–3620.

[24] C. Téllez, M. Abon, J.A. Dalmon, C. Mirodatos, J. Santamaría, J. Catal. 195 (2000) 113–124.

[25] M.C. Kung, H.H. Kung, J. Catal. 134 (1992) 668–677.

[26] S.A. Karakoulia, K.S. Triantafyllidis, A.A. Lemonidou, Microporous Mesoporous Mater. 110 (2008) 157–166.

[27] W. Liu, S.Y. Lai, H. Dai, S. Wang, H. Sun, C.T. Au, Catal. Letters. 113 (2007) 147–154.

[28] L. Čapek, J. Adam, T. Grygar, R. Bulánek, L. Vradman, G. Košová-Kučerová, P. Čičmanec, P. Knotek, Appl. Catal. A Gen. 342 (2008) 99–106.

[29] D.E. Keller, T. Visser, F. Soulimani, D.C. Koningsberger, B.M. Weckhuysen, Vib. Spectrosc. 43 (2007) 140–151.

[30] R. Bulánek, L. Čapek, M. Setnička, P. Čičmanec, J. Phys. Chem. C. 115 (2011) 12430–12438.

[31] D.L. Stern, J.N. Michaels, L. DeCaul, R.K. Grasselli, Appl. Catal. A Gen. 153 (1997) 21–30.

[32] C. Wang, J.-G. Chen, T. Xing, Z.-T. Liu, Z.-W. Liu, J. Jiang, J. Lu, Ind. Eng. Chem. Res. 54 (2015) 3602–3610.

[33] J. Jian, K. You, X. Duan, H. Gao, Q. Luo, R. Deng, P. Liu, Q. Ai, H. Luo, Chem. Commun. 52 (2016) 3320–3323.

[34] S. Ahmed, F. Rahman, A.M.J. Al-Amer, E.M. Al-Mutairi, U. Baduruthamal, K. Alam, React. Kinet. Mech. Catal. 105 (2012) 483–493.

[35] P. Concepción, J.M. López Nieto, J. Pérez-Pariente, Catal. Letters. 19 (1993) 333–337.

[36] L.M. Madeira, R.M. Martín-Aranda, F.J. Maldonado-Hódar, J.L.G. Fierro, M.F. Portela, J. Catal. 169 (1997) 469–479.

Chapter-4

Oxidative Dehydrogenation of 1-Butene

Buta-1, 3-diene (BD) is one of the most important chemical commodities. It is a precursor for the manufacture of many synthetic chemicals. A large number of polymers like styrene-butadiene rubber (SBR), acrylonitrile-butadiene rubber (ABS), polybutadiene, etc can be produced from BD as well [1]. Thus, it contributes substantially to assure the global demand of synthetic rubbers; especially for the production of tires. The synthesis of BD mainly comprises three methods: steam cracking of naphtha, catalytic dehydrogenation (DH) as well as oxidative dehydrogenation (ODH) of n-butane and butenes [2]. Nearly 98 % of the global demand for BD is achieved by the extraction of C_4 raffinates from naphtha through catalytic steam cracking. However the high operating temperature, as well as separation processes makes this method expensive and, also, the overall yield of BD will be very low. Although, catalytic DH can give a better yield, rapid catalyst deactivation, and endothermicity (*Eq. 4.1*) of the process are big challenges.

$$C_4H_8 \leftrightarrow C_4H_6 + H_2; \Delta H_r = +107 \text{ kJ/mol} \qquad \textit{(Eq. 4.1)}$$

Meanwhile, the annual demand for BD is increasing [3] and expected to incessantly increase in the future. In consequence, ODH of n-butane and butenes has been practiced as a promising energy-efficient method in the presence of an oxidant which oxidizes detached hydrogen to a stable water molecule. A high BD yield can be achieved via this independent single unit method and has attracted remarkable attention. The exothermicity of the process (*Eq. 4.2*) can perform subsequent coke removal and allows control over the existing equilibria. Moreover, the reaction can be operated at lower temperatures compared to naphtha, steam cracking and DH methods [4]. The presence of oxidants will reinforce catalyst life time too. Besides, the limited availability of crude oil and the recent discovery of shale gas resources have switched the feedstock from naphtha to gases.

$$C_4H_8 + {}^1/_2O_2 \rightarrow C_4H_6 + H_2O; \Delta H_r = -132.1 \text{ kJ/mol} \qquad \textit{(Eq. 4.2)}$$

Among n-butane and 1-butene, the latter will be better as a feedstock starting material owing to its higher reactivity. Furthermore, it is inexpensive and largely abundant in methanol as well as the biomass industry. Hence ODH of 1-butene (ODH1B) has acquired much more attention owing to its significant advantages over the other existing processes for BD

production. The general route of ODH1B reaction with the major possible products formation is represented in **Scheme 4.1**.

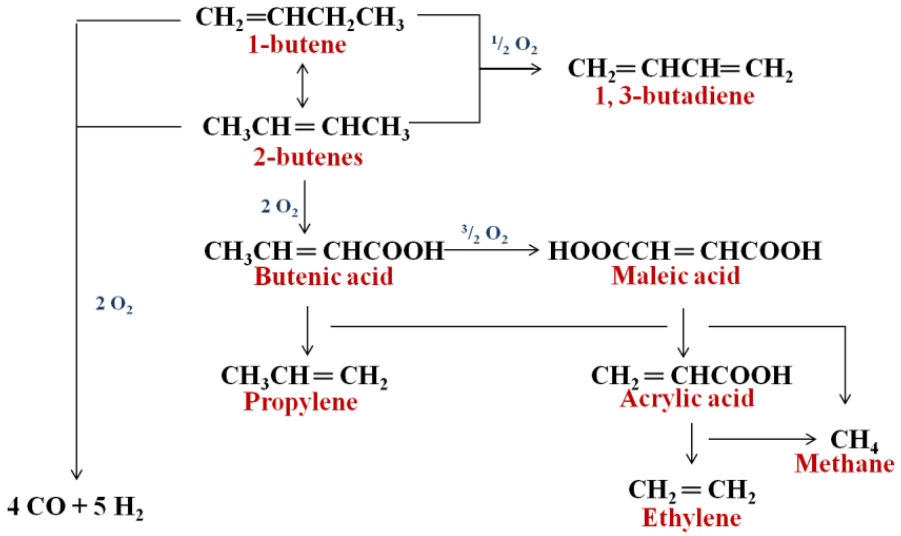

Scheme 4.1 Possible reaction pathway of ODH1B

The ODH of alkanes was proposed to progress by Mars van Krevelen (MVK) mechanism [5] which mainly consists of some elementary steps. Alkane will be adsorbed on the catalyst surface and the α–hydrogen will be removed to form an allylic intermediate. Later, the lattice oxygen will react with the allylic intermediate to form desired products. Afterward the reduced catalyst will be re-oxidized under an external supply of oxidant [6]. Accordingly, the lattice oxygens play a vital role in the MVK mechanism as selective oxidizing agents to improve the production of BD [7]. **Scheme 4.2** denotes a simple representation of MVK mechanism for ODH1B on the catalyst surface.

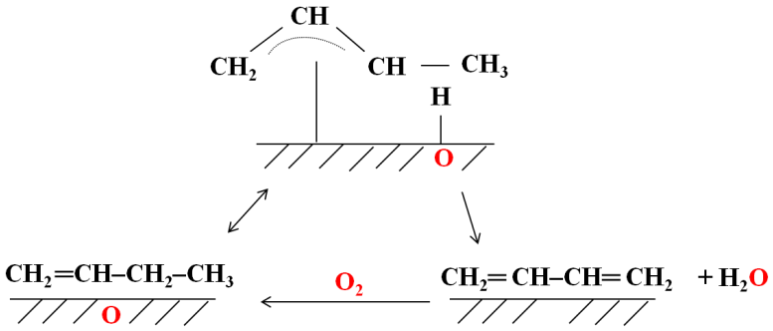

Scheme 4.2 MVK mechanism for ODH1B

The nature of a catalyst and its activity for a particular reaction can be modified by changing the support, adding promoter, etc. For ODH1B, the catalyst should be tailored to suppress

hydrocarbon combustion without lowering C–H activation energy. At higher oxygen partial pressure, total oxidation of 1-butene may occur as given in *Eq. 4.3* and *Eq. 4.4*. In this instance, a metal oxide catalytic system can be an appropriate candidate with an effective redox cycle capacity for MVK mechanism.

$$C_4H_8 + 6O_2 \rightarrow 4CO_2 + 4H_2O;\ \Delta H_r = -2540\ kJ/mol \qquad (Eq.\ 4.3)$$

$$C_4H_8 + 4O_2 \rightarrow 4CO + 4H_2O;\ \Delta H_r = -2540\ kJ/mol \qquad (Eq.\ 4.4)$$

In particular, a transition metal that can exist in multiple oxidation states could contribute to this redox cycle, and also the mobility, as well as the capacity of the lattice oxygens, greatly depends upon the nature of the metal cation. A wide variety of metal oxide-based catalysts has been employed for the ODH1B including bismuth molybdates, [8] ferrites, [9] zinc aluminates, [10] and vanadium-containing catalysts [11]. Multi-component bismuth molybdates composed of transition, inner transition metals, or non-metals were broadly investigated to improve the catalytic performance towards ODH [8, 12–14]. The catalytic activity of these materials was affected by oxygen mobility, oxygen capacity, and the crystalline phase composition [15, 16]. However, the design of a suitable catalyst with appropriate oxygen species active and stable for ODH1B is a pivotal challenge.

Depending upon the catalyst system employed, this chapter is further divided into two parts.

A. *Influence of transition metal addition in bismuth ferrite on the oxidative dehydrogenation of 1-butene*
B. *Utilizing the oxygen carrier property of cerium iron mixed oxide for the low temperature synthesis of 1, 3-butadiene from 1-butene*

References

[1] W.C. White, Chem. Biol. Interact. 166 (2007) 10–14.

[2] E. Hong, J.H. Park, C.H. Shin, Catal. Surv. from Asia 20 (2016) 23–33.

[3] (CMAI) Chemical Marketing Associates, Inc., Completes 2011 World Butadiene Analysis, 2011.

[4] L.M. Madeira, M.F. Portela, Catal. Rev. 44 (2002) 247–286.

[5] P. Mars, D.W. van Krevelen, Chem. Eng. Sci. 3 (1954) 41–59.

[6] E. Grootendorst, Y. Verbeek, V. Ponec, J. Catal. 157 (1995) 706–712.

[7] R.K. Grasselli, Top. Catal. 21 (2002) 79–88.

[8] J.H. Park, C.H. Shin, Appl. Catal. A Gen. 495 (2015) 1–7.

[9] H. Lee, J.C. Jung, H. Kim, Y.M. Chung, T.J. Kim, S.J. Lee, S.H. Oh, Y.S. Kim, I.K. Song, Catal. Letters 122 (2008) 281–286.

[10] H. Lee, J.C. Jung, I.K. Song, Catal. Letters 133 (2009) 321–327.

[11] M.A. Pepera, J.L. Callahan, M.J. Desmond, E.C. Milberger, P.R. Blum, N.J. Bremer, J. Am. Chem. Soc. 107 (1985) 4883–4892.

[12] C. Wan, D. Cheng, F. Chen, X. Zhan, Chem. Eng. Sci. 135 (2015) 553–558.

[13] J.H. Park, H. Noh, J.W. Park, K. Row, K.D. Jung, C.-H. Shin, Appl. Catal. A Gen. 431–432 (2012) 137–143.

[14] J.C. Jung, H. Lee, H. Kim, Y.M. Chung, T.J. Kim, S.J. Lee, S.H. Oh, Y.S. Kim, I.K. Song, Catal. Commun. 9 (2008) 1676–1680.

[15] A.P. Vieira Soares, L.D. Dimitrov, M.C.R.A. de Oliveira, L. Hilaire, M.F. Portela, R.K. Grasselli, Appl. Catal. A Gen. 253 (2003) 191–200.

[16] J.C. Jung, H. Lee, H. Kim, Y.M. Chung, T.J. Kim, S.J. Lee, S.H. Oh, Y.S. Kim, I.K. Song, J. Mol. Catal. A Chem. 271 (2007) 261–265.

Chapter-4A

Influence of Transition Metal Addition in Bismuth Ferrite on the Oxidative Dehydrogenation of 1-Butene

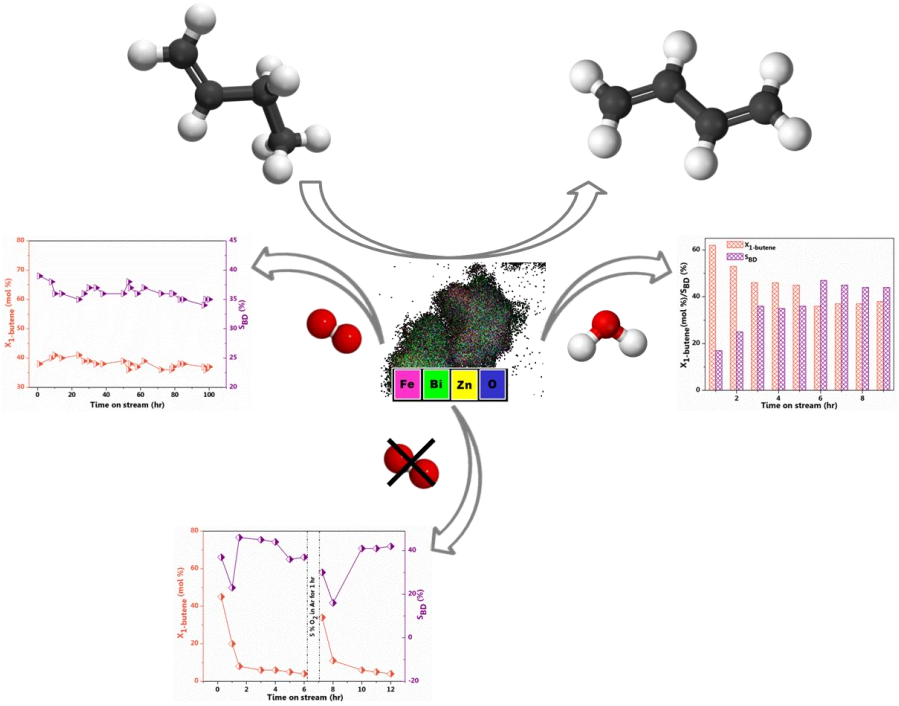

Highlights

- Transition metal (Cu, Ni, Zn, Co, Mn, Cr) doped bismuth ferrites are synthesized by simple scalable method and employed for the oxidative dehydrogenation of 1-butene (ODH1B) to 1, 3-butadiene with molecular oxygen as oxidant
- Catalyst composition as well as reaction parameters are tuned and optimized to achieve maximum product yield
- PXRD study showed that the materials exist in distorted perovskite structure
- Zinc doped catalyst gave the highest yield and the best catalyst found stable over 100 h of time on stream
- Lattice oxygens drive the reaction for a few hours and the presence of steam enhanced selectivity

4A.1. Background of the work

Bismuth molybdates are the extensively studied oxide system for the ODH1B reaction. Many transition metals have been employed to enhance the oxygen mobility of bismuth molybdates [1-3]. Bismuth functions as the component responsible for the C–H activation process [3]. Meanwhile, bismuth ferrites constitute a large family of sillenite and perovskite-type materials. Consequently, they receive distinguished consideration due to its fascinating properties. Although the synthesis of phase pure $BiFeO_3$ (BF) is very difficult and always accompanies with the impurities such as $Bi_2Fe_4O_9$, Bi_2O_3, and $Bi_{25}FeO_{39}$ [4, 5]. This arises due to the incomplete reaction by the volatile nature of some of the reactants.

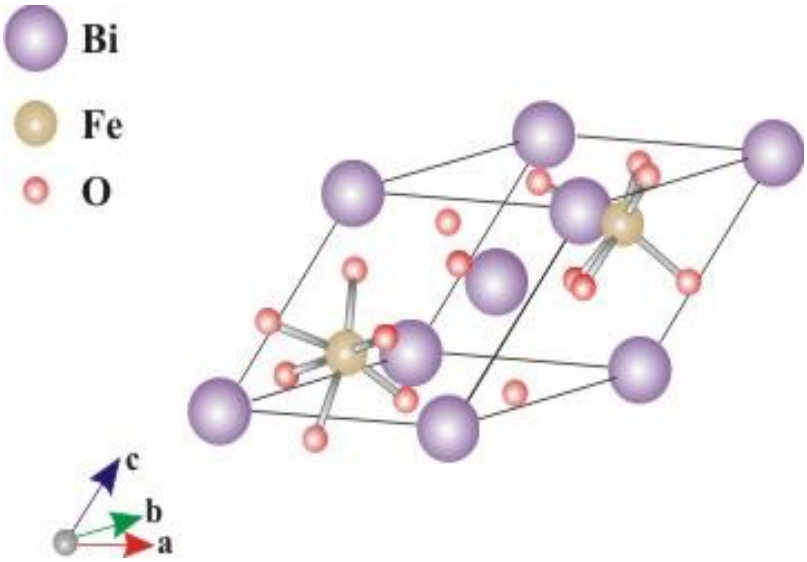

Fig. 4A.1 Distorted perovskite structure of $BiFeO_3$

Bismuth ferrites mainly fall under the structured oxides called perovskites with general formula ABO_3 where A is a 12 fold coordinated cation and B cation is 6 fold coordinated with oxygen anions [6]. At room temperature, Fe^{3+} ions are in the distorted oxygen octahedra while Bi^{3+} occupying dodecahedral positions moved near to one of the Fe^{3+} ions because of the lone pair effect and hence BF exists in the distorted rhombohedral perovskite structure. In the perovskite unit cell, Bi^{3+} and Fe^{3+} occupy in eight and six-fold coordination respectively [7]. **Fig. 4A.1** represents the unit cell structure of BF in the distorted perovskite structure. These multiferroic materials have widespread applications as spintronics, sensors, photovoltaics, compact storage devices, etc [8, 9]. Apart from these, they function as good oxidation catalysts also [10]. The previous studies have proved that the abstraction of α-hydrogen for 1-butene and the formation of the allylic intermediate is the rate-determining

step in ferrite catalysts (**Scheme 4A.1**). Moreover, the addition of metal cations to ferrite catalysts can improve the catalytic properties.

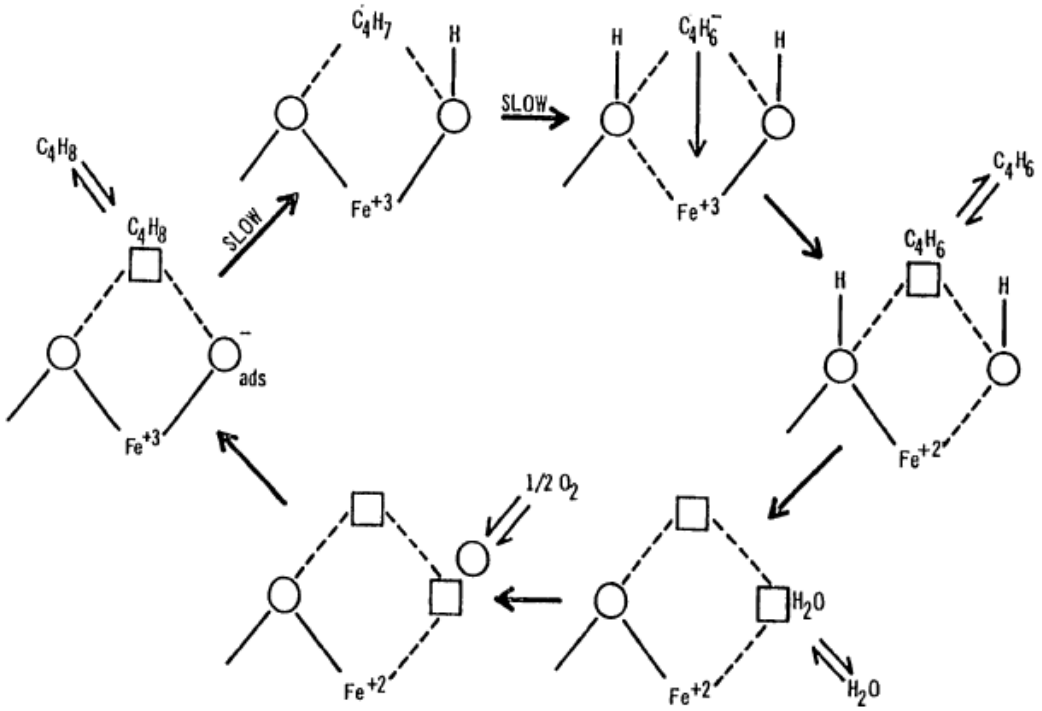

Scheme 4A.1 Proposed ODH1B mechanism over ferrites [11]

The co-substitution in BF at Bi^{3+} and Fe^{3+} cationic sites were performed by many research groups. Structural, electrical, and optical properties of BF were observed to influence by doping with rare earth metal cations like La^{3+}, Eu^{3+} and Er^{3+} synthesized via microwave-assisted solution combustion method [12]. It has been observed that the doping of Gd^{3+} at the A site enhanced the photocatalytic degradation of Rhodamine B [13]. In addition, the doping of Sn^{4+} improved the electromagnetic properties of BF material [14]. The simultaneous doping of these two has substantially improved the photocatalytic activity [15]. Kung *et. al.* observed that zinc oxide can increase the selectivity when added along with haematite for 1-butene to BD reaction [16]. Among various spinel metal ferrite systems studied, $ZnFe_2O_4$ was best active mainly because of the high surface acidity. Furthermore, the density of selective oxidation sites is more than unselective combustion sites [17].

Meanwhile, the irreversible reduction of Fe^{3+} to Fe^{2+} in the spinel structure can cause catalyst deactivation of ferrites which may be avoided by the addition of promoters [11]. Conversely, bismuth ferrites including in the perovskite system can be active for ODH1B. The mechanistic steps involved in the ODH process over a ferrite system are represented in **Scheme 4A.1**. Accordingly, C–H activation is the slow rate determining route and Fe^{2+}/Fe^{3+}

redox couple is crucial. Hydrothermal, coprecipitation, sol-gel, thermal decomposition, and molten salt techniques have been employed for doped BF synthesis while the hydrothermal method can produce this oxide with different morphology by carefully tuning the conditions [18].

In the current study, ODH1B over various transition metal-doped bismuth ferrites systems were tested for the first time. The present study mainly aims to explicate the effect of different promoters in the given structured metal oxide for the catalytic performance of 1-butene conversion to BD. We investigated the properties of different transition metal-doped bismuth ferrites ($M1_xBi_{1-x}FeO_3$ and $BiM2_xFe_{1-x}O_3$; where M1=Cu, Ni, Zn and M2=Co, Mn, Cr respectively) and the catalytic activity of these materials for ODH1B. These catalysts were characterized for phase identification and purity using PXRD; oxygen species were quantified with XPS and TPR studies. TEM, N_2 sorption, and SEM analysis provided the textural properties of the synthesized materials. Post reaction characterization of the catalysts was also conducted to examine the changes occurred during the reaction.

4A.2. Results and discussion

Various perovskite catalysts are prepared by coprecipitation and the experimental procedure for the catalyst synthesis is elaborated in the previous chapter (see **Section 2.3.2**). The below given part discussed the important results obtained from the study.

4A.2.1. Catalytic activity study

A systematic study of catalytic properties of the materials for ODH1B to BD is carried out in a continuous flow fixed bed reactor at varying reaction conditions (refer **Section 2.6** and **2.7**). *Caution must be taken due to the exothermic nature of the reaction which is practiced in the presence of combustble hydrocarbon and oxygen mixture operated at high temperatures*. The reaction proceeded through side processes also; viz 1-butene isomerization to 2-butenes, cracking to C_1-C_3 hydrocarbons, and combustion to CO_x along with the selective ODH to BD. The catalyst composition is optimized by separately doping different metals at A as well as B sites and also by varying the amount of metal doping. The temperature for the highest activity is determined and taken forward for further studies. Steam is employed to see any enhancement in the BD selectivity. The role of lattice oxygen is also analyzed using the best catalyst composition. Finally, the stability of the material is tested with the optimized catalyst at optimized reaction conditions.

4A.2.1.1. Effect of cation doping

ODH1B over BF is performed at 400 °C with 3000 h^{-1} GHSV where O_2/C_4 ratio is taken as one. Transition metal cation is doped at the "A" and "B" sites of distorted perovskite bismuth ferrite and conducted the reaction to investigate any effect on catalytic activity. Conversion of 1-butene ($X_{1\text{-butene}}$) and selectivity for BD (S_{BD}) are compared with BF for both batches of materials in **Fig. 4A.2 a** and **b** respectively. 0.1 mol % of Ni (BNiF), Cu (BCuF), and Zn (BZnF) are doped at the "A" site, and among all; BZnF exhibited the highest activity with 37 % conversion and 38 % BD selectivity. Even though conversions were good, selectivity was lower for BNiF and BCuF. A detailed analysis of the activity results showed that doping in BF has considerably enhanced the conversion of 1-butene; while it does not follow this trend in the selectivity of BD.

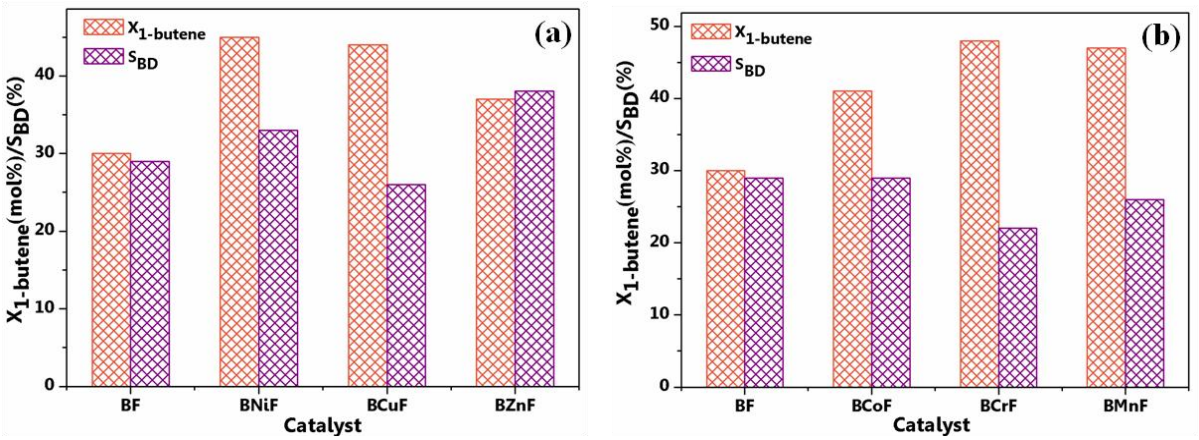

Fig. 4A.2 Effect of cation doping in (a) "A" and (b) "B" site of BF on ODH1B.

Reaction conditions: *500 mg catalyst, 400 °C, O_2/C_4=1, balance Ar and 3000 h^{-1} GHSV with respect to total feed.*

Similarly, the effect of cation doping at the "B" site is also evaluated at the same reaction conditions. Co, Cr, and Mn are doped with 0.1 mol% at Bi^{3+} site and the catalytic activity performance is depicted in **Fig. 4A.2b**. Significant enhancement in conversion is noticed in this case also, after the cation doping. Surprisingly, BD selectivity do not improved in any of these doped catalysts but, it is decreased for BCoF, BCrF, and BMnF compared to BF. The activity of these studied catalysts is reduced in the order: BZnF>BNiF>BCoF>BF>BMnF>BCuF>BCrF. Hence, BZnF is selected as the best catalyst. Although, the yield obtained for the catalysts used in this study is lower than bismuth molybdates; it provides the consequences of transition metal doping in the presently discussed system.

4A.2.1.2. Effect of Zn doping

Catalyst composition has a crucial role in the activity performance of any reaction. BZnF has shown the highest activity for ODH1B at 400 °C with O_2/C_4=1 and GHSV making upto 3000 h^{-1} with Ar. Further, the amount of zinc is varied as 0.05, 0.1 and 0.2 mol% to optimize the effect of doping under the same reaction parameters (**Fig. 4A.3a**). At the lowest and highest Zn doping, i.e; for BZn0.05F and BZn0.2F conversion slightly improves; while S_{BD} is low. It is clear from the activity data that $Bi_{0.9}Zn_{0.1}FeO_3$ (BZn0.1F) exhibits the best conversion for 1-butene as 37 % with 38 % BD selectivity.

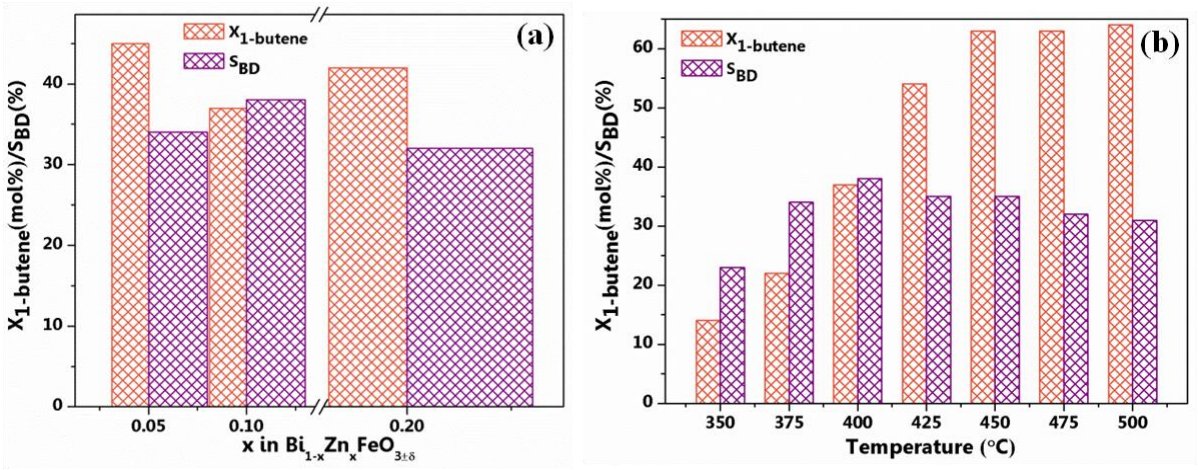

Fig. 4A.3 Effect of (a) Zn doping in BF at 400 °C and (b) temperature over BZn0.1F on ODH1B.
Reaction conditions: *500 mg catalyst, O_2/C_4=1, balance Ar and 3000 h^{-1} GHSV with respect to total feed.*

4A.2.1.3. Effect of reaction temperature

The temperature of a reaction is one of the most important parameters directly affecting the catalytic activity. Hence to determine the optimum operating temperature, BZn0.1F catalyst is further evaluated from 350 to 500 °C with stepwise increment of 25 °C. O_2/C_4 ratio is kept one with balance Ar under 3000 h^{-1} GHSV concerning the total feed. The activity results are depicted in **Fig. 4A.3b**. At 350 °C, the lowest S_{BD} is observed and the product distribution shows that isomerization of 1-butene happens at this temperature. As expected, $X_{1\text{-butene}}$ drastically increases with temperature up to 450 °C where S_{BD} is 34 %. Further, the increase in temperature negligibly improved the conversion. However, the correlation of BD selectivity with reaction temperature exhibited a volcano-shaped curve which suggests that moderate temperature is suitable for ODH1B. At higher temperatures, the possibility of coke formation, as well as combustion, will be more which will lead to low selectivity towards the

desired product. The best result is observed at 400 °C as 37 % conversion for 1-butene and 38 % selectivity towards BD. Thus, 400 °C is chosen as the optimized temperature for further studies.

4A.2.1.4. Effect of steam

Most of the reported works have been employed steam in the reactant feed to improve the activity of the catalysts inspired by the commercial practice. To examine the effect of steam on the catalytic performance; BZ0.1F is chosen as a model catalyst and the reaction is executed under the optimized operating conditions. Reactant feed in a fixed composition, i.e; C_4:O_2:steam:Ar= 5:5:25:90 is supplied in to the catalyst bed at 400 °C. **Fig. 4A.4a** shows the activity performance of BZ0.1F as a function of reaction time. Initially, there was a 63 % conversion with 18 % BD selectivity. After 5 h, a stable activity is achieved and $X_{1\text{-butene}}$ was 39 % with 43 % S_{BD}. Interestingly, the catalytic activity is improved in the presence of steam. A maximum selectivity for the preferred product indicated that the undesired reactions have been decreased with a minimum selectivity for combustion products. Meanwhile, the reaction data obtained in the previous sections concludes no steam is requisite for maximum conversion of 1-butene.

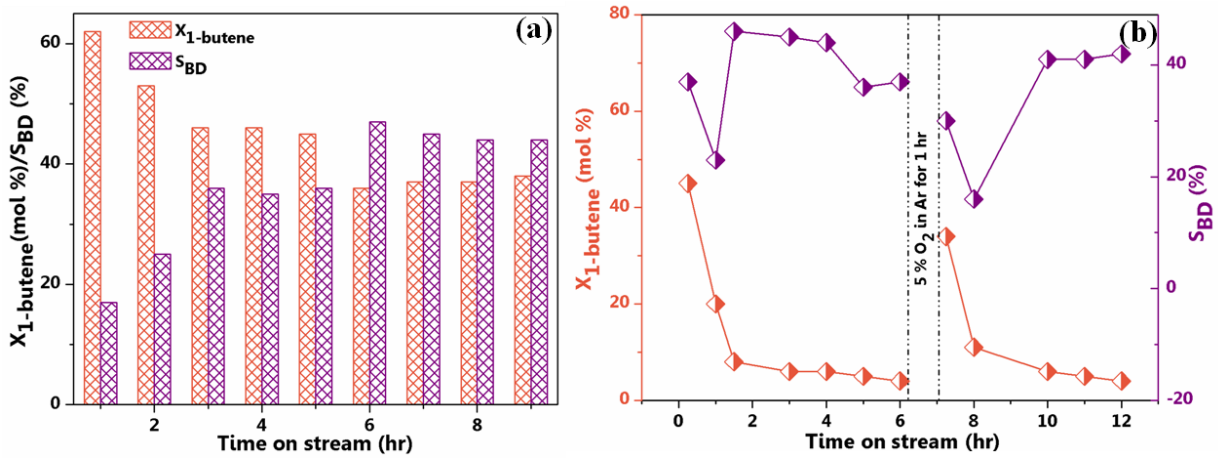

Fig. 4A.4 Effect of (a) steam at C_4:O_2:steam:Ar= 5:5:25:90 and (b) lattice oxygen with 5 %1B in Ar for ODH1B.
Reaction conditions: *BZ0.1F, 500 mg catalyst, 400 °C, 3000 h^{-1} GHSV with respect to total feed.*

The existing literatures proved that steam can preferably block the active site for CO_2 generation and function as a heat sink for hindering hot spots during the reaction. Furthermore, steam plays vital role in decreasing contact time, lowering partial pressure, and regenerating active sites on the catalyst surface. Jung *et. al.* employed steam in the reaction

mixture to improve BD yield over bismuth molybdates [19]. Another study proved that the addition of water vapor has promoted acetic acid formation from 1-butene suppressing the total oxidation reactions [20]. In conflict ODH reaction is suppressed at higher temperatures in the presence of steam [21, 22]. However, a huge quantity of steam is not thermodynamically favorable for the ODH reaction.

4A.2.1.5. Effect of lattice oxygen

Perovskites are structured oxides with plenty of labile oxygen. It is reported that ODH1B follows MVK mechanism where the lattice oxygens directly react with 1-butene and the gaseous oxygens will make up the vacancy created on the catalyst surface. Accordingly, the available oxygens of BF could be utilized for the non-oxidative DH of 1-butene. The reaction is conducted with 5 % 1-butene in Ar to make a total GHSV of 3000 h^{-1} at 400 °C for 12 h of time on stream (TOS) as represented in **Fig. 4A.4b**. Initial conversion of 44 % and 38 % BD selectivity is observed and the activity has been dropped within 6 h with the consumption of lattice oxygens. Then, the catalyst bed is reoxidised for 1 h with 5 % molecular oxygen in Ar to fill the vacancies. Later, the feed is again switched to the reactant mixture for a second cycle after flushing the catalyst surface with pure Ar for one hour to remove any loosely bound molecular oxygens. The reaction results observed are in accordance with the trends of the previous reports for the ODH of propane, ethane, and ethylbenzene [23–25]. Surprisingly, the same trend in catalytic activity is followed in the second cycle also with a considerable decrease from the initial conversion as well as selectivity. This could be due to the decreased chemisorbed oxygen on the catalyst in the second cycle; which can also contribute to 1-butene conversion.

4A.2.1.6. Long term stability test

To appraise the stability of BZ0.1F catalyst, a long term activity evaluation is performed for 100 h of time on stream study under the optimized reaction parameters. Wherein, 37 % 1-butene conversion, as well as 38 % S_{BD}, is retained for ODH1B as outlined in **Fig. 4A.5**. Throughout the reaction, conversion is maintained with a slight decrease in the selectivity during 100 h of reaction. However, BZ0.1F was established stable at the given reaction conditions from the long term stability experiment. Hence it can be concluded that the catalyst is sturdy with an appreciable performance which make it economically executable. The slight drop in selectivity may be due to the bismuth ferrite impurity phases $Bi_2Fe_4O_9$, Bi_2O_3, and $Bi_{25}FeO_{39}$ separated under the reaction conditions [4, 5].

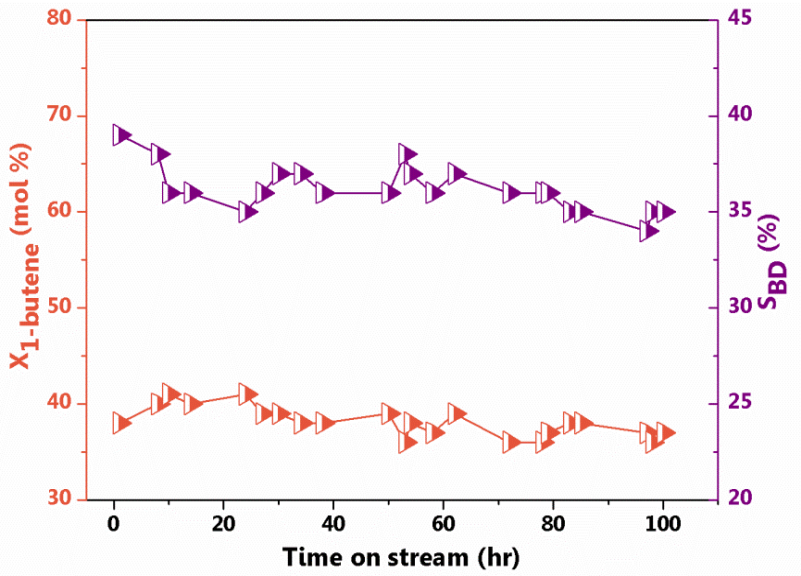

Fig. 4A.5 Long term stability test of BZ0.1F for ODH1B over 100 h

Reaction conditions: *500 mg catalyst, 400 °C, O_2/C_4 =1, balance Ar and 3000 h^{-1} GHSV with respect to total feed.*

4A.2.2. Characterization of the catalysts

Analysis of the material properties are further done with appropriate instrumentation techniques (given in **Section 2.5**) and interpreted to correlate with the activity results.

4A.2.2.1. Crystallinity of the materials

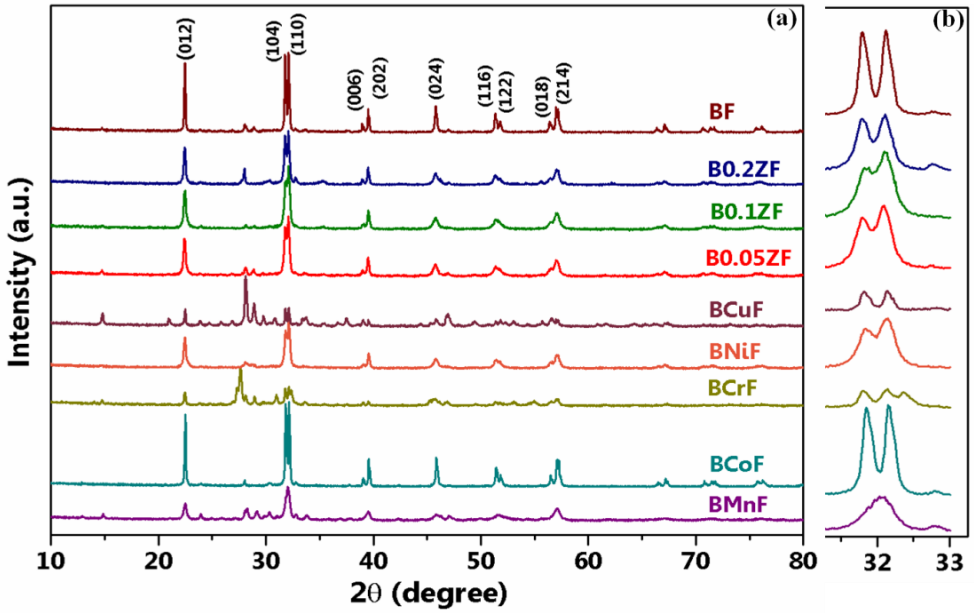

Fig. 4A.6 PXRD patterns of the (a) as-synthesized materials and (b) enlarged view of (104) and (110) planes.

The crystalline phases of the synthesized materials sintered at 550 °C are analyzed from PXRD patterns shown in **Fig. 4A.6a**. The structure of different transition metal-doped bismuth ferrites are compared with pristine BF. All peaks are indexed with JCPDS card no: 71-2494 existing in a hexagonal system with distorted rhombohedral perovskite structure of $BiFeO_3$ [7]. The synthesis of single-phase pure $BiFeO_3$ in perovskite structure is difficult and always accompanied by the impurity oxides due to the kinetics of formation and possible volatilization of the reactants as reported by many researchers [26]. **Fig. 4A.6a** depicts secondary phases like Bi_6O_7, $Bi_2Fe_4O_9$, and $Bi_{25}FeO_{39}$ as impurities [27, 28]. The diffraction patterns of BCuF, BCrF, and BMnF showed secondary impurity peaks. **Fig. 4A.6b** exhibits doublet peak corresponds to (104) and (110) planes. Except in BCoF, these peaks are merging to singlet showing the effect of doping the foreign transition metal cation due to the ionic radii difference between the host and guest species [29]. A shift of this merged peak also indicates the phase transformation from rhombohedral to orthorhombic with the co-doping of transition metals [30]. Hence, doping has significantly affected the crystal structure of pristine BF. A slight shift in the main peak for (110) plane (2θ=32 °) is observed towards higher 2θ value for BCoF, BNiF, and BCuF which might be due to the unit cell contraction arise from the substitution of smaller radii cation. This phenomenon may also cause a decrease in the interplanar distance [31, 32]. In contrast, the peak at (110) plane has considerably shifted to a lower diffraction angle for BMnF because of the higher ionic radii of Mn^{2+}.

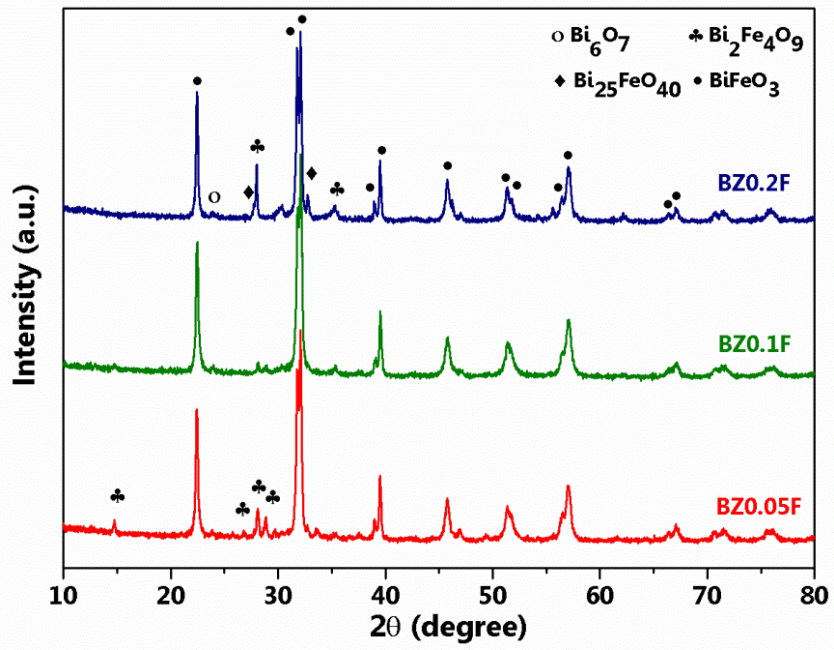

Fig. 4A.7 PXRD patterns of zinc doped bismuth ferrite catalysts

The crystallite size of the materials is tabulated in **Table 4A.1**; calculated using Debye-Sherrer formula $D=k\lambda/\beta\cos\theta$ where D is the average crystallite size, k is the dimensionless constant with a value 0.9, λ is the wavelength of X-ray source (1.54178 Å), θ is Bragg angle of the diffraction peak and β is the structural broadening. The mean crystallite size of the material exhibited large value due to its high crystallinity. Notably, the optimized catalyst showed a minimum D value of 35.3 nm represents the formation of small crystallites.

Table 4A.1 Textural and structural properties of the as-synthesized materials

Catalyst	S_{BET}[a] (m^2/g)	Pore volume[a] (cm^3/g)	Average pore diameter[a] (nm)	Average crystallite size[b] (nm)
BF	3	0.023	4.3	56.4
B0.05ZF	6	0.026	3.1	47.0
B0.1ZF	6	0.021	3.1	35.3
B0.2ZF	18	0.056	3.4	40.3
BCuF	8	0.036	3.1	65.1
BNiF	11	0.027	3.4	36.8
BCrF	12	0.052	3.1	49.8
BCoF	5	0.027	3.4	60.5
BMnF	11	0.054	3.1	26.5

[a]Data obtained from BET analysis.
[b]Calculated using Scherrer formula for the (111) crystal plane.

The stability of a perovskite structure can be expressed with Goldschmidt's tolerance factor defined with the equation as,

$$t = (r_A + r_O) / \sqrt{2}\,(r_B + r_O) \qquad \textit{(Eq. 4A.1)}$$

where, r_A, r_B, and r_O are the average radius of A, B cations, and O^{2-} respectively. When t value is less than 1, Fe–O bonds will be compressed inducing lattice distortion in Bi–O bonds. To reduce this lattice stress rotation of oxygen octahedra will take place which leads to the evolution of the lower symmetric orthorhombic phase by suppressing the rhombohedral phase [33, 34]. Hence, a smaller tolerance factor specifies more aggressive distortion of Fe–O in the octahedral site [35]. In the case of doped bismuth ferrites, the effective ionic radius should be included for the calculation of t as, $r_{A(eff)} = r_A(1-x) + r_M(x)$ where M is the metal-doped at A site [36].

The powder diffraction analysis of Zn doped BF materials (BZnF) represented in **Fig. 4A.7** revealed that minimum impurity phases are present in BZ0.1F and evidences perfect doping of zinc in the crystal lattice; which might be one of the reasons for its highest activity.

Therefore, it may be concluded that the crystal structure influences the activity of the material for ODH1B to some extent.

4A.2.2.2. N_2-sorption analysis

Fig. 4A.8 represents the nitrogen adsorption-desorption isotherms of all synthesized catalysts. The textural properties of the materials including surface area (S_{BET}), pore volume, and average pore size are given in **Table 4A.1**. All samples have low surface area values characteristic of perovskite oxides [37]. BET isotherms exhibited typical of type IV with the initial region close to type II [15]. Capillary condensation was also observed from the hysteresis loop and the materials have mesoporous structure. The average pore size of doped materials is almost the same but lower than that of fresh BF. The doped BF materials exhibited larger surface area than the un-doped BF sample, which could be contributed to the increased activity. B0.2ZF showed the highest surface area; probably due to the largest separation of the impurity phase.

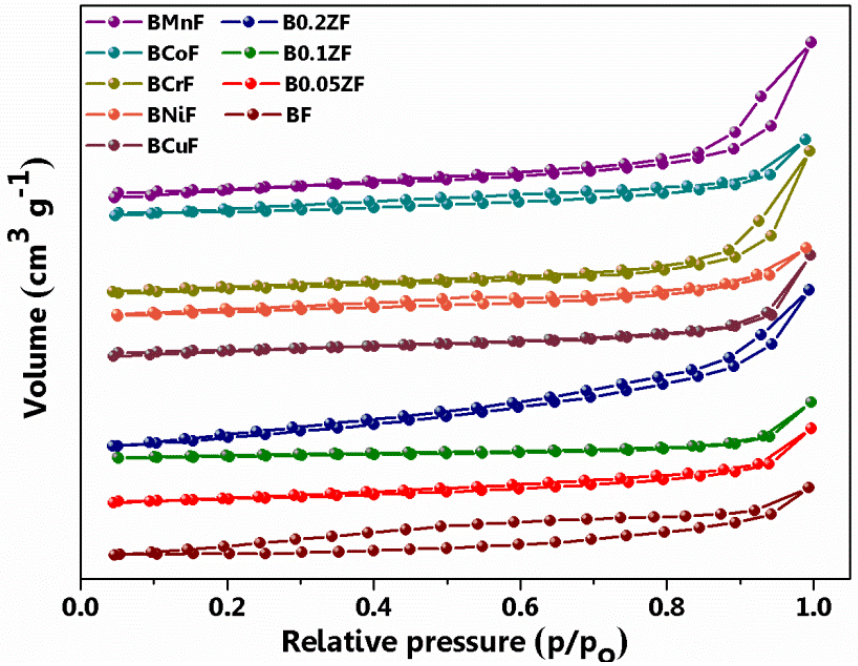

Fig. 4A.8 N_2-sorption isotherms of the as-synthesized materials

4A.2.2.3. Catalyst morphology

Surface morphology of the highly active catalyst; BZ0.1F is studied with TEM, SEM, and elemental mapping analysis. The HRTEM micrographs of as-synthesized BZ0.1F catalysts are presented in **Fig. 4A.9a** and **b**. Irregular nanocrystals of mean particle size 13.1 nm are visible which is lower than the crystallite size calculated from Scherrer equation. An

agglomerated plate-like structure with well-developed lattice fringes are seen in **Fig. 4A.9b** having widths; 0.5 and 0.29 nm which can be correlated to (012) and (110) planes respectively. The perfect doping of Zn into the pristine BF crystal lattice slightly increased fringe widths from the original 0.395 and 0.279 nm for the $BiFeO_3$ phase. These values are in consistent with the interplanar distance (d) calculated from PXRD using Bragg's equation; $n\lambda=2d\sin\theta$, where, n is the order of diffraction, λ is the wavelength of CuKα radiation (1.54178 Å) and θ is the angle of diffraction. Selected area electron diffraction (SAED) pattern of sharp bright spots and well-defined periodicity shown in the inset proved high crystallinity of the sample complementing PXRD results.

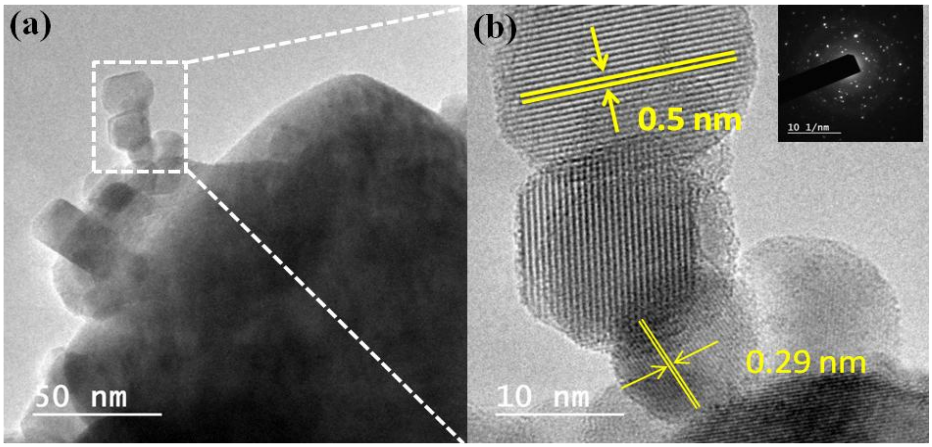

Fig. 4A.9 HRTEM images of fresh BZ0.1F

The SEM images of fresh BZ0.1F (**Fig. 4A.10a**) showed an aggregated spherical morphology accompanied by porous nature which is preserved even after the reaction (**Fig. 4A.10b**).

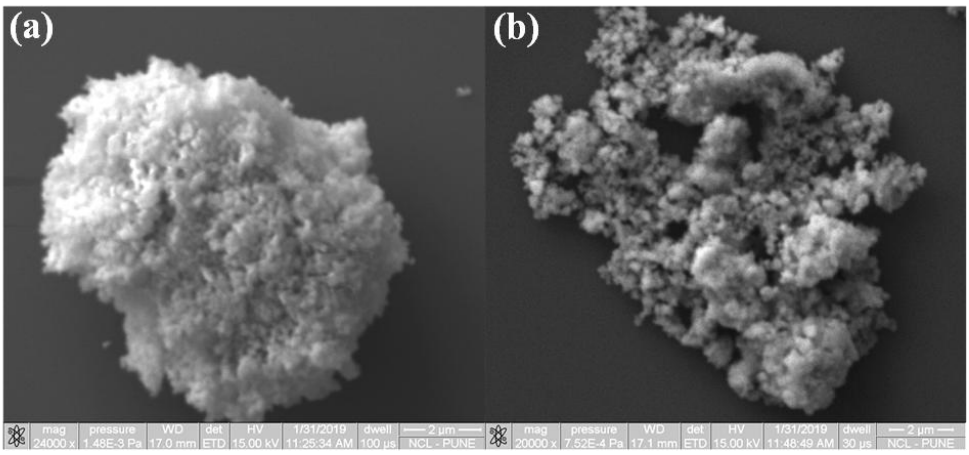

Fig. 4A.10 SEM images of (a) fresh and (b) spent BZ0.1F

Elemental mapping images of pristine BZ0.1F are shown in **Fig. 4A.11**. All elements are detected and are assigned different colors for better understanding. Form the images an excellent dispersion is observed for the optimized catalyst.

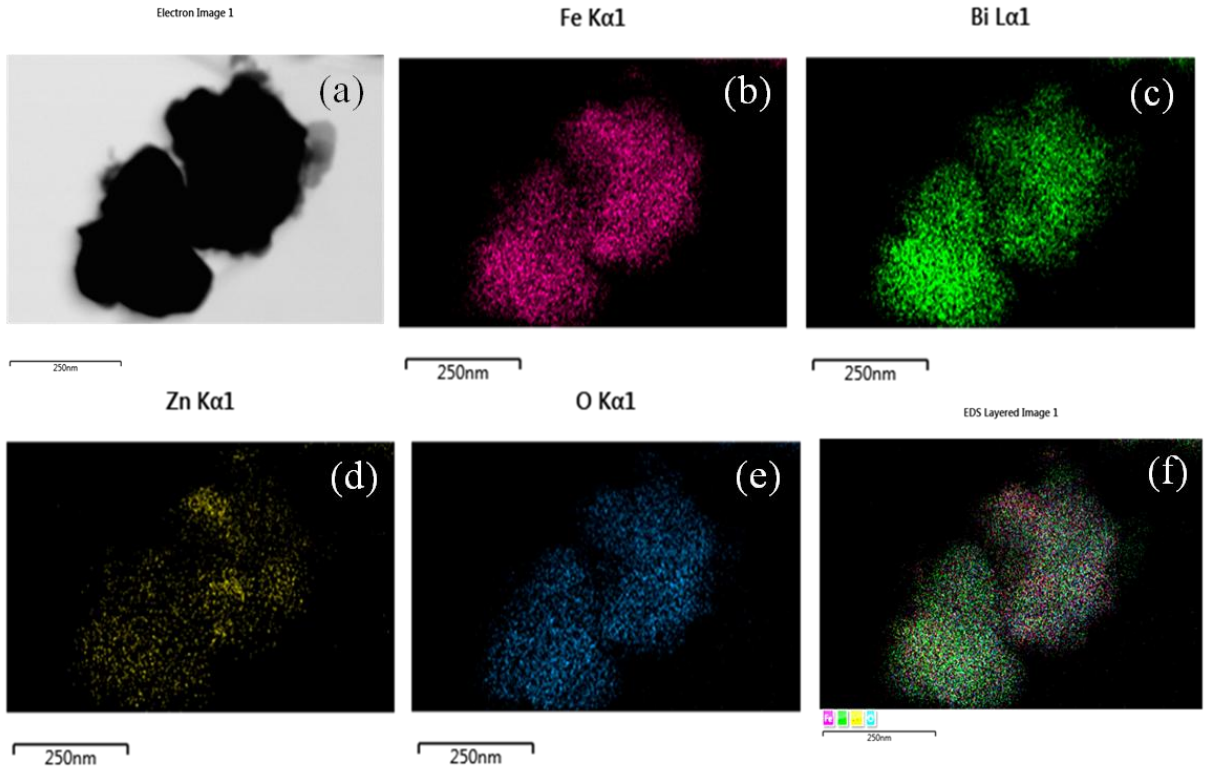

Fig. 4A.11 Elemental mapping images of fresh BZ0.1F. (b) Fe-Pink, (c) Bi-green, (d) Zn-yellow, (e) O-Blue and (f) overlay image.

4A.2.2.4. Reduction properties

Reducibility of the catalysts is one of the most significant properties of materials in ODH reaction and demonstrated using H_2-TPR. Reduction properties of zinc doped BF materials are compared with pristine BF in the TPR profiles given in **Fig. 4A.12**. Two reduction peaks are reported for pristine ZnO at 465 and 800 °C for Zn^{2+} to Zn^0 and sublimation [38, 39]. Besides, pure Fe_2O_3 in the haematite phase consumes hydrogen in three steps occurring at different temperatures. At 348 °C, the transition of Fe_2O_3 to Fe_3O_4 will happen followed by Fe_3O_4 to FeO transition at 621 °C. Further, FeO will be reduced to metallic Fe above 800 °C [40]. Usually, fresh Bi_2O_3 exhibits two reduction peaks at 446 and 628 °C corresponding to the reduction of surface and bulk oxygen species [41].

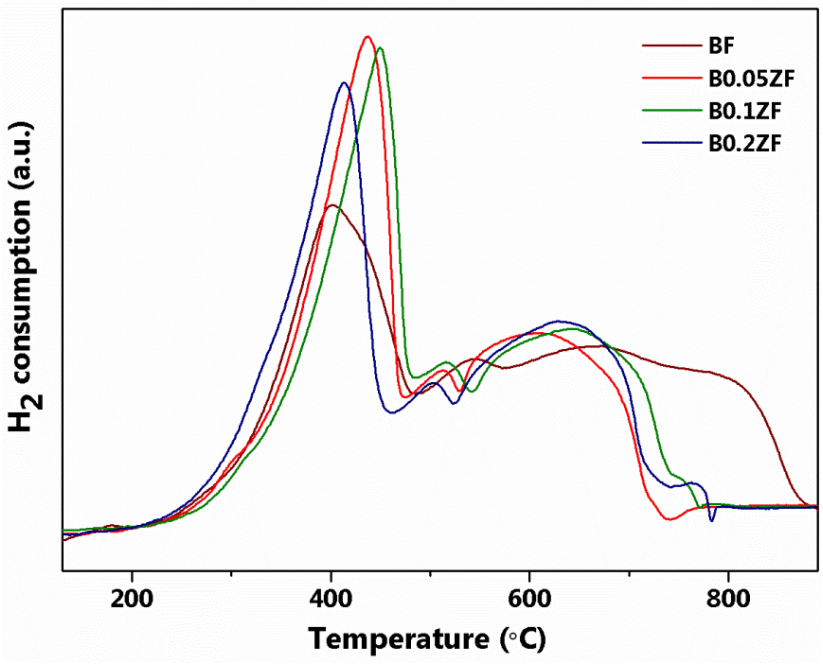

Fig. 4A.12 H_2-TPR profiles of BZnF catalysts

It can be perceived from the TPR results that the reduction properties of the materials are increased after doping Zn at low temperatures; while the bulk reduction around 550 and 800 °C is declined to around 500 and 600 °C respectively [42]. The addition of zinc as a dispersed impurity may generate more defects by incorporating Bi–Zn–F bonds which causes a considerable change in the reduction behaviour and contribute towards the activity. Total H_2 consumption for the Zn doped samples is slightly reduced to ~12 mmol g^{-1} compared to BF (14.5 mmol g^{-1}). A small difference in the reduction temperature is also observed. Hence, TPR results supported fine dispersion of zinc within the BF structure. The optimized BZ0.1F is exhibited maximum H_2 consumption and the main reduction peak falls at the highest temperature at 448.8 °C as illustrated in **Table 4A.2**.

Table 4A.2 Thermal and surface properties of BZnF materials

Catalyst	H_2 consumption[a] (mmol g^{-1})	T_{max}[b] (°C)	Amount of lattice oxygen[c] (%)	Coke deposition[d] (wt %)
BF	14.5	401.2	45.2	1.0
B0.05ZF	12	437.4	27.5	1.9
B0.1ZF	12.1	448.8	35.1	1.3
B0.2ZF	11.9	411.4	30.6	0.9

[a]Calculated by H_2-TPR.
[b]Temperature of the first maxima in the H_2-TPR profile.
[c]Calculated from XPS.
[d]Quantified from TG analysis under air atmosphere.

4A.2.2.5. XPS study

The nature and composition of a catalyst surface are very important in heterogeneous catalysis and hence, the XPS study becomes highly crucial. Bi 4f, Fe 2p, Zn 2p as well as O 1s core-level spectra are analyzed using XPS for pristine BF and BZnF as shown in **Fig. 4A.13**. Binding energy (BE) value of 284.8 eV was assigned to adventitious carbon and all peaks are corrected with respect to this value. Drastic changes in the surface atomic composition are observed in all spectra after successive Zn doping to pure BF.

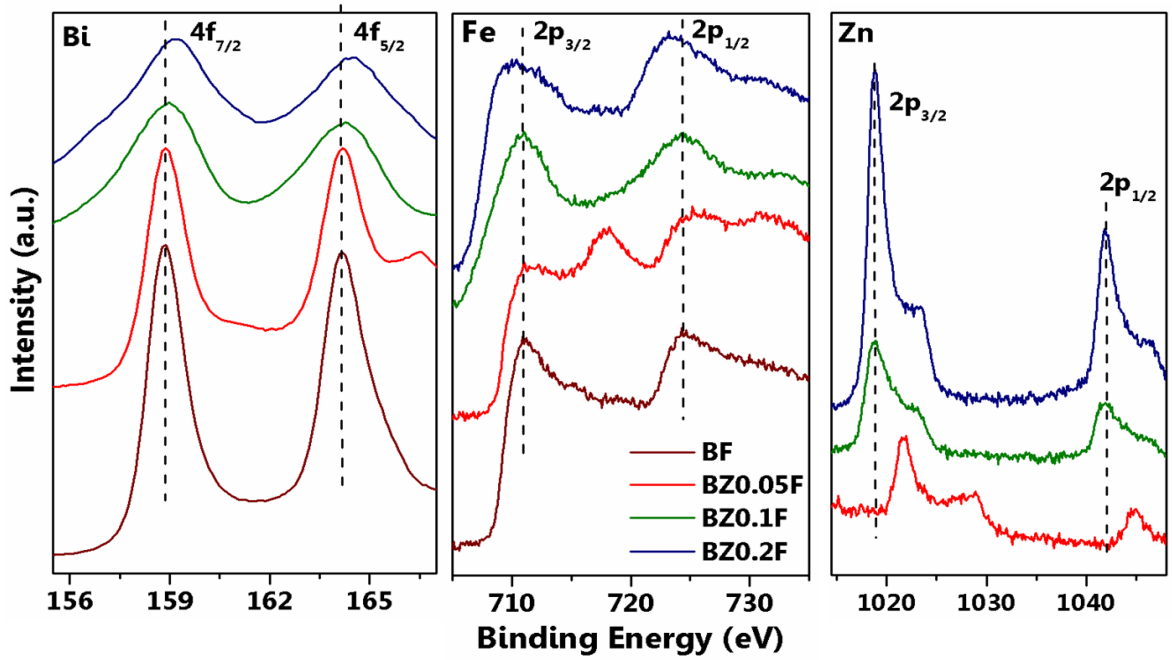

Fig. 4A.13 Bi 4f, Fe 2p and Zn 2p XPS core-level spectra of BZnF catalysts

A thorough analysis of Bi 4f spectra proved that Bi exists predominantly in Bi^{3+} state in pure BF with BE values 158.8 and 164.2 eV corresponding to $4f_{7/2}$ and $4f_{5/2}$ respectively. After Zn doping, these peaks are shifted to 159.3 and 164.5 eV for both B0.1ZF and B0.2ZF. This represents Bi in +3 oxidation state with a peak separation of 5.2 eV related to spin-orbit coupling [43]. The gradual shift of the main peaks corresponding to Bi towards higher BE with zinc addition shows the proper doping of Zn in Bi site [44]. The O 1s spectra of all samples are deconvoluted using XPSpeak41 software into four signature peaks (**Fig. 4A.14**). The figure shows that XPS peaks of O 1s spectra are shifted to lower BE which could be due to the changes in crystallinity with Zn addition [45] and supported from PXRD results (**Table 4A.1**). Metallic Bi do not observed in any of these samples. The addition of zinc can increase the bond energy of Bi–O in the BZnF catalysts which is reflected in the H_2-TPR where the T_{max} is shifted to a higher temperature for B0.1ZF sample (**Fig. 4A.12**). The observed BE at 710.9 and 724.4 eV

are attributed to Fe $2p_{3/2}$ and Fe $2p_{1/2}$ respectively emerging from the spin-orbit interaction. A satellite peak is also observed at 718.0 eV. Furthermore, the metal exists in both Fe^{2+} and Fe^{3+} oxidation state [46]. At the highest Zn doping (BZ0.2F) a binding energy shift is observed due to the presence of a small amount of zinc ferrite. The characteristic peaks for Zn^{2+} are observed at 1021.5 and 1044.7 eV for $2p_{3/2}$ and $2p_{1/2}$ respectively [47].

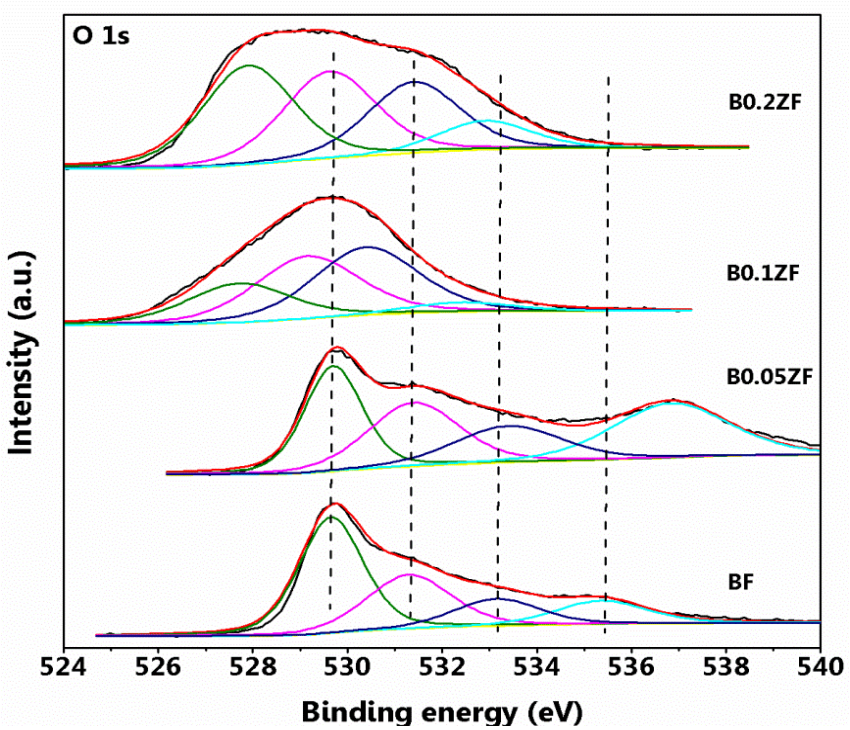

Fig. 4A.14 Deconvoluted XPS spectra of O 1s core level

Fig. 4A.14 denotes peak positioned at 529.6 eV corresponding to the lattice Fe–O oxygens. The Bi–O oxygens are appearing at around 531.4 eV [48]. Hydroxyl and carbonate species adsorbed on the surface exhibited a peak at higher BE values near 533 eV [49]. At 535 eV adsorbed water molecules are detected [50]. A shift in BE towards lower value was observed for the BZ0.1F sample, which implies the highest electronic interaction after Zn doping. The quantification of lattice oxygen species on the surface is shown in **Table 4A.2**. Lattice oxygens are believed to assist MVK mechanism for the production of BD from 1-butene. BZ0.1F holds the highest amount of lattice oxygens among other BZnF catalysts. Even pristine BF consists of 45.2 % lattice oxygens; the high amount of chemisorbed oxygens present in this catalyst can cause undesired reactions. This observation is reflected in the activity performance (refer **Section 4A.2.1.2**) also with very good $X_{1\text{-butene}}$ while low S_{BD} over BF. Hence it can be confirmed that the addition of Zn can make the reaction more selective. Minimal chemisorbed oxygens (5.2 %) in BZ0.1F also supports this prediction.

4A.2.2.6. Spent catalyst analysis

Analysis of the catalyst after the reaction for any structural and textural changes can provide hints for the processes occurred during the reaction. PXRD pattern of the spent catalyst is taken after 100 h of TOS study and compared with that of freshly calcined catalyst as given in **Fig. 4A.15a**. The spent catalyst exhibited no phase transition; with a slight increase in the full width at half maximum (FWHM) value. This observation proved that the catalyst is intact and structurally stable even after the reaction.

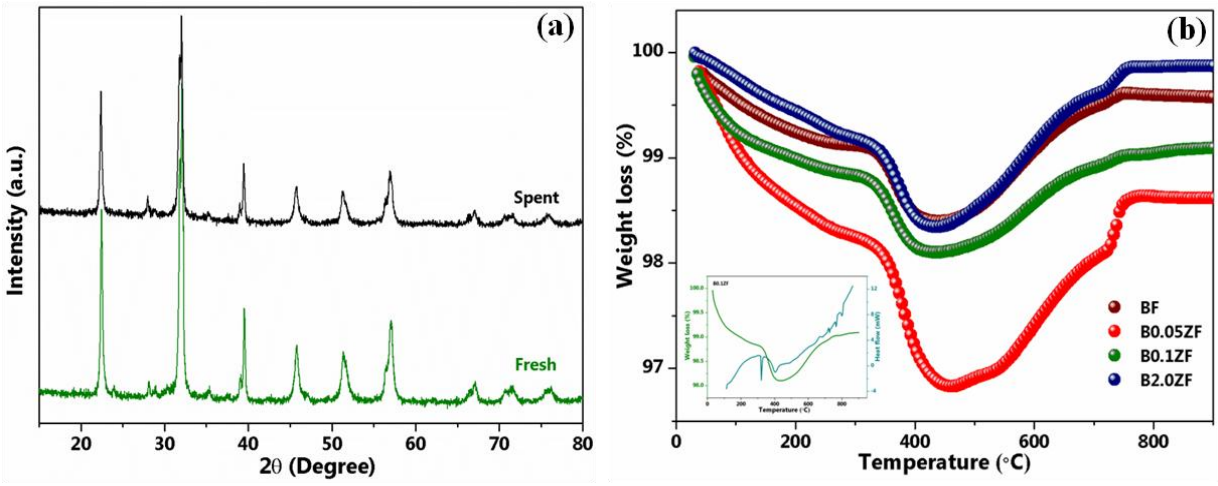

Fig. 4A.15 (a) PXRD of fresh and spent BZ0.1F (b) thermograms of spent BZnF catalysts

Thermogravimetric analysis is conducted to quantify coke deposited on different BZnF catalysts during the reaction. Weight loss is calculated at 350 °C from the thermograms of the materials shown in **Fig. 4A.15b**. The temperature of weight loss is selected in accordance with the exothermic reaction for carbon burning as detected from DTA given in the inset. The amount of coke deposited is displayed in **Table 4A.2**. All catalysts showed negligible coke deposition on the surface even after the reaction at 500 °C. After 400 °C, weight gain is observed for all samples which might be due to the phase transformation to either bismuth or iron rich phases.

4A.3. Conclusions

In this study, a series of first row transition metals doped bismuth ferrite catalysts were synthesized adopting a coprecipitation method to study ODH1B to BD. The structural,morphological, thermal, and spectroscopic properties of the materials have been rigorously inspected with various physic-chemical characterization techniques. The proper doping of zinc in BZ0.1F and a proper amount of lattice oxygens contributed towards the

highest activity. The labile lattice oxygen can direct the reaction only for a few hours while steam can considerably improve the BD selectivity. This a first study to investigate the metal doping effect in bismuth ferrite for the ODH reaction. In summary, this work provides a stable novel perovskite like catalytic system for the activation of lower hydrocarbons.

References

[1] P.A. Batist, J.F.H. Bouwens, G.C.A. Schuit, J. Catal. 25 (1972) 1–11.

[2] P. Forzatti, P.L. Villa, N. Ferlazzo, D. Jones, J. Catal. 76 (1982) 188–207.

[3] T.S.R.P. Rao, K.R. Krishnamurthy, J. Catal. 95 (1985) 209–219.

[4] M.I. Morozov, N.A. Lomanova, V. V Gusarov, Russ. J. Gen. Chem. 73 (2003) 1676–1680.

[5] M. Valant, A.-K. Axelsson, N. Alford, Chem. Mater. 19 (2007) 5431–5436.

[6] J. Zhu, A. Thomas, Appl. Catal. B Environ. 92 (2009) 225–233.

[7] P. Fischer, M. Polomska, I. Sosnowska, M. Szymanski, J. Phys. C Solid State Phys. 13 (1980) 1931–1940.

[8] N.A. Spaldin, S.W. Cheong, R. Ramesh, Phys. Today 63 (2010) 38.

[9] G. Catalan, J.F. Scott, Adv. Mater. 21 (2009) 2463–2485.

[10] T.J. Park, G.C. Papaefthymiou, A.R. Moodenbaugh, Y. Mao, S.S. Wong, J. Mater. Chem. 15 (2005) 2099–2105.

[11] E. Hong, J.H. Park, C.H. Shin, Catal. Surv. from Asia 20 (2016) 23–33.

[12] A. Wrzesinska, A. Khort, I. Bobowska, A. Busiakiewicz, A. Wypych-Puszkarz, J. Nanomater. 2019 (2019) 5394325.

[13] R. Guo, L. Fang, W. Dong, F. Zheng, M. Shen, J. Phys. Chem. C 114 (2010) 21390–21396.

[14] M. Sobhan, Q. Xu, J. Zhao, A. Franklin, Y. Hu, J.S. Tse, P. Wu, EPL Europhysics Lett. 111 (2015) 18005.

[15] S. Irfan, S. Rizwan, Y. Shen, L. Li, Asfandiyar, S. Butt, C.-W. Nan, Sci. Rep. 7 (2017) 42493.

[16] H.H. Kung, M.C. Kung, B.L. Yang, J. Catal. 69 (1981) 506–510.

[17] H.H. Kung, M.C. Kung, in: D.D. Eley, H. Pines, P.B.B.T.A. in C. Weisz (Eds.), Academic Press, 1985, pp. 159–198.

[18] J.T. Han, Y.H. Huang, X.J. Wu, C.L. Wu, W. Wei, B. Peng, W. Huang, J.B. Goodenough, Adv. Mater. 18 (2006) 2145–2148.

[19] J.C. Jung, H. Kim, Y.S. Kim, Y.M. Chung, T.J. Kim, S.J. Lee, S.H. Oh, I.K. Song, Appl. Catal. A Gen. 317 (2007) 244–249.

[20] W.Y. Suprun, D.P. Sabde, H.K. Schädlich, B. Kubias, H. Papp, Appl. Catal. A Gen. 289 (2005) 66–73.

[21] A.A. Lemonidou, G.J. Tjatjopoulos, I.A. Vasalos, Catal. Today 45 (1998) 65–71.

[22] J.M. López Nieto, A. Dejoz, M.I. Vazquez, W. O'Leary, J. Cunningham, Catal. Today 40 (1998) 215–228.

[23] S. Sugiyama, T. Hashimoto, Y. Tanabe, N. Shigemoto, H. Hayashi, J. Mol. Catal. A Chem. 227 (2005) 255–261.

[24] A. Dinse, R. Schomäcker, A.T. Bell, Phys. Chem. Chem. Phys. 11 (2009) 6119–6124.

[25] K. Saito, K. Okuda, N. Ikenaga, T. Miyake, T. Suzuki, J. Phys. Chem. A 114 (2010) 3845–3854.

[26] I. Sosnowska, W. Schäfer, W. Kockelmann, K.H. Andersen, I.O. Troyanchuk, Appl. Phys. A 74 (2002) s1040–s1042.

[27] J. Yang, X. Li, J. Zhou, Y. Tang, Y. Zhang, Y. Li, J. Alloys Compd. 509 (2011) 9271–9277.

[28] G. Rojas-George, J. Silva, R. Castañeda, D. Lardizábal, O.A. Graeve, L. Fuentes, A. Reyes-Rojas, Mater. Chem. Phys. 146 (2014) 73–81.

[29] S. Godara, N. Sinha, B. Kumar, Mater. Lett. 136 (2014) 441–444.

[30] G.L. Song, G.J. Ma, J. Su, T.X. Wang, H.Y. Yang, F.G. Chang, Ceram. Int. 40 (2014) 3579–3587.

[31] V. Verma, J. Alloys Compd. 641 (2015) 205–209.

[32] S. Irfan, L. Li, A.S. Saleemi, C.W. Nan, J. Mater. Chem. A 5 (2017) 11143–11151.

[33] X. Zhang, Y. Sui, X. Wang, Y. Wang, Z. Wang, J. Alloys Compd. 507 (2010) 157–161.

[34] F. Huang, Z. Wang, X. Lu, J. Zhang, K. Min, W. Lin, R. Ti, T. Xu, J. He, C. Yue, J. Zhu, Sci. Rep. 3 (2013) 2907.

[35] Y. Zhang, Y. Wang, J. Qi, Y. Tian, M. Sun, J. Zhang, T. Hu, M. Wei, Y. Liu, J. Yang, Nanomaterials 8 (2018) 711.

[36] M.A. Ahmed, E. Dhahri, S.I. El-Dek, M.S. Ayoub, Solid State Sci. 20 (2013) 23–28.

[37] R.J.H. Voorhoeve, D.W. Johnson, J.P. Remeika, P.K. Gallagher, Science (80-.). 195 (1977) 827 LP – 833.

[38] O.W. Perez-Lopez, A.C. Farias, N.R. Marcilio, J.M.C. Bueno, Mater. Res. Bull. 40 (2005) 2089–2099.

[39] J.M.C. Bueno, M. Gazzano, M.G. Coelho, A. Vaccari, Appl. Catal. A Gen. 103 (1993) 69–78.

[40] A. Khan, P.G. Smirniotis, J. Mol. Catal. A Chem. 280 (2008) 43–51.

[41] Y. Xie, C. Zhang, D. Wang, J. Lu, Y. Wang, J. Wang, L. Zhang, R. Zhang, New J. Chem. 43 (2019) 15368–15374.

[42] M.F. Luo, Z.Y. Hou, X.X. Yuan, X.M. Zheng, Catal. Letters 50 (1998) 205–209.

[43] H. Guan, X. Zhang, Y. Xie, J. Phys. Chem. C 118 (2014) 27170–27174.

[44] S. Chauhan, M. Kumar, S. Chhoker, S.C. Katyal, M. Singh, RSC Adv. 6 (2016) 43080–43090.

[45] A. Aytimur, İ. Uslu, Ş. Durmuşoğlu, A. Akdemir, Ceram. Int. 40 (2014) 12899–12903.

[46] X. Wang, M. Zhang, P. Tian, W.S. Chin, C.M. Zhang, Appl. Surf. Sci. 321 (2014) 144–149.

[47] M. Srivastava, S.K. Alla, S.S. Meena, N. Gupta, R.K. Mandal, N.K. Prasad, New J. Chem. 42 (2018) 7144–7153.

[48] A. Mukherjee, S. Chakrabarty, N. Kumari, W.N. Su, S. Basu, ACS Omega 3 (2018) 5946–5957.

[49] J.C. Wang, J. Ren, H.C. Yao, L. Zhang, J.S. Wang, S.Q. Zang, L.-F. Han, Z.J. Li, J. Hazard. Mater. 311 (2016) 11–19.

[50] K. Sutthiumporn, S. Kawi, Int. J. Hydrogen Energy 36 (2011) 14435–14446.

Chapter-4B

Utilizing the Oxygen Carrier Property of Cerium Iron Oxide for the Low-Temperature Synthesis of 1, 3-Butadiene from 1-Butene

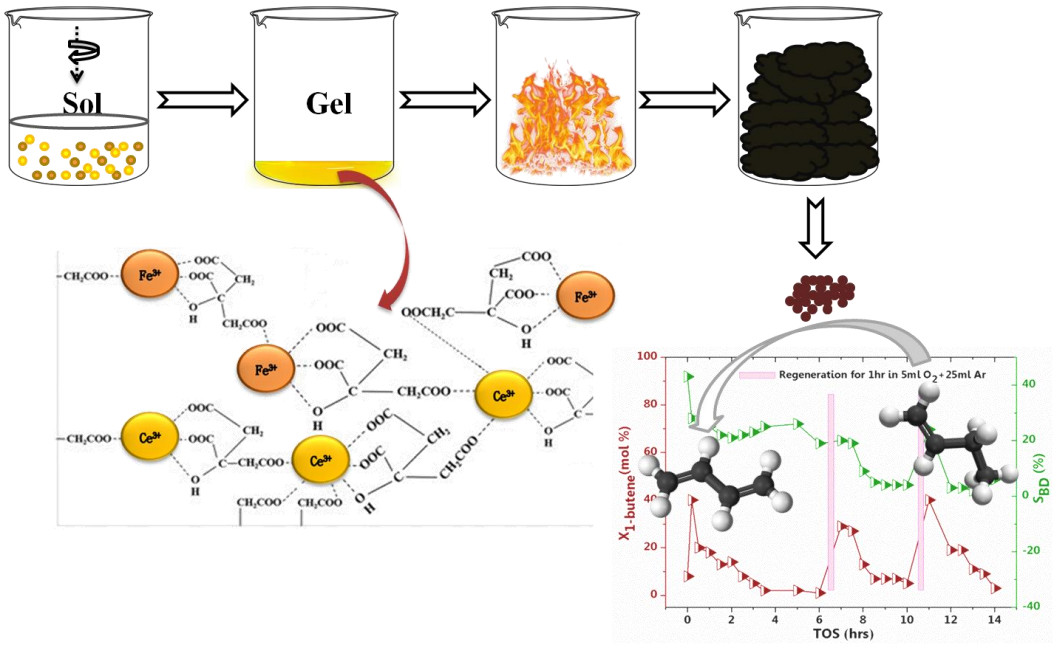

Highlights

- Cerium iron mixed oxide is synthesized by citrate gel combustion and employed for the dehydrogenation of 1-butene in an oxygen free atmosphere
- Oxygen carrier property of the catalyst is utilized for the low temperature synthesis of 1, 3-butadiene
- H_2-TPR, XPS and oxygen uptake studies evidenced the abundance of replaceable labile oxygens in the material
- The activity is decreased through consuming the lattice oxygen and restored after catalyst re-oxidation exploiting Ce^{3+}/Ce^{4+} and Fe^{2+}/Fe^{3+} redox centers

4B.1. Background of the work

Over the past decades, CeO_2 in the fluorite structure has become the most attractive oxide and well known for its excellent oxygen storage capacity (OSC) over a wide range of temperatures owing to its ability to switch between Ce^{3+} and Ce^{4+} [1]. This peculiar property of ceria has been utilized in numerous applications such as threeway catalysts (TWCs), photocatalysis, solid oxide fuel cells, UV rays blockers, oxygen sensors, low-temperature water gas shift (WGS) reactions, water purification, and ceramic materials etc [2–4]. Pure ceria is thermally unstable and undergoes sintering rapidly at high temperatures; therefore not recommended as a catalyst. The addition of trivalent, as well as a smaller sized ion in CeO_2, can lower the activation energy for oxygen migration and enhance the OSC respectively; due to the distortion of the lattice which can create more oxygen vacancies [5]. Furthermore, Pr^{3+} and Tb^{3+} in CeO_2 lattice substantially improved the oxygen migration [6].

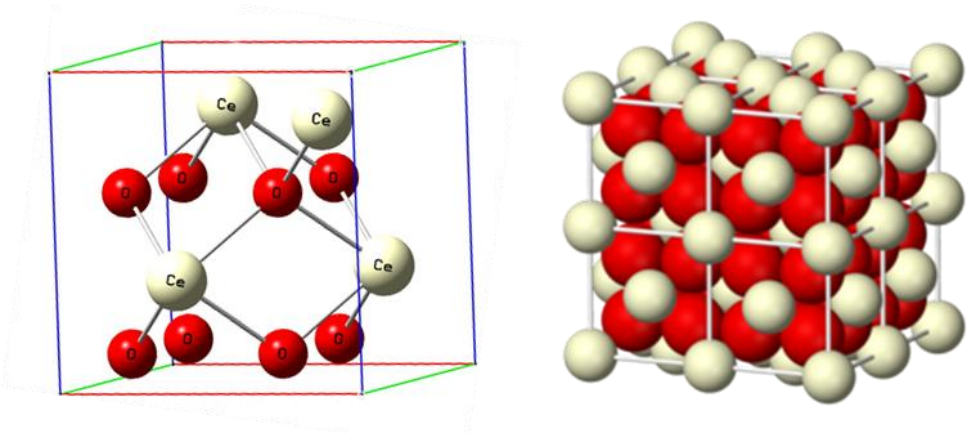

Fig. 4B.1 Cubic (fluorite) structure of ceria

As a cheaper and the most abundant metal in the earth's crust, Fe is likely to be an appropriate candidate for incorporation in ceria lattice. The ionic radius of Fe^{3+} in six coordination (0.68 Å) is much lower than Ce^{4+} in its eight coordination (1.11 Å) [7]. Moreover, a large number of iron-based catalysts; especially ferrites are reported for the ODH of n-butenes [8]. Still, dissolving Fe in ceria lattice remains a challenging task. Though, there are reports where the synthesis of $Ce_{1-x}Fe_xO_{2\pm\delta}$ has been achieved by precipitation, sol-gel, micro emulsion, and hydrothermal methods [9]. It has been believed that the sharing of oxygen in Ce–O–Fe linkage is the main reason for its significant catalytic performance. Meanwhile, the oxygen storage properties of ceria can be improved by the synergy achieved by the combination of Ce^{3+}/Ce^{4+} and Fe^{2+}/Fe^{3+} redox centres. Preetam *et. al.* have studied a wide range of transition and inner transition metals substituted in CeO_2 lattice and Ce_{1-}

$_xFe_xO_{2\pm\delta}$ was found to contain more labile oxygens [10]. This enhanced OSC property was originated from the oxygen sub lattice distortion during Fe substitution [1]. Consequently, iron modified cerium oxide was proposed to have improved textural properties along with the excellent oxygen release capacities [5, 11]. This ability was extensively employed for selective and total oxidation reactions [5, 12–16]. Moreover, these materials can serve as good oxygen carriers too [17, 18].

An ideal ODH catalyst should suppress the combustion of 1-butene without lowering the C–H bond activation energy. Also, the rate-determining step of ODH at temperatures lower than 350 °C mainly depends upon the re-oxidation of the catalyst as well as product desorption from the catalyst surface [19]. According to the existing literature, Ce and Fe could form a solid solution up to 30 mol% Fe when synthesized by conventional precipitation methods [20]; however it will depend upon the synthesis method. Mazan *et. al.* could successfully synthesize nanocrystalline cerium iron oxide by citrate synthesis method with excellent OSC properties [4]. Furthermore, CO_2 was used for the reduction and reoxidation of ceria by employing Fe as the promoter for the ODH of ethylbenzene [5].
Most of the studies have reported ODH1B in the presence of oxygen, air, or CO_2 as oxidants. Employing molecular oxygen may increase the total oxidation products and results in a low BD yield. Some researchers have availed lattice oxygen for ODH1B to inhibit complete oxidation. Kiyokawa *et. al.* have reported that copper ferrite supported on activated carbon could be used repeatedly for ODH by subsequent re-oxidation with molecular oxygen [21]. A type of chemical looping method is also discussed by Keller *et. al.* where releasing and restoring of oxygen species were carried out in two different reactors while circulating the oxygen carrier [22]. Moreover, the reaction is believed to proceed through MVK mechanism where lattice oxygens take a vital role.

The oxygen activation and electron transfer on the catalyst surface are depicted by *Eq. 4B.1, 2* and *3*. Accordingly, nucleophilic O^{2-} species is responsible for the selective oxidation to desired products; while others will lead to combustion reaction [8].

$$O_{2\,(ads)} + e^- \rightarrow O_2^-{}_{(ads)} \qquad \textit{(Eq. 4B.1)}$$

$$O_2^-{}_{(ads)} + e^- \rightarrow 2O^-{}_{(ads)} \qquad \textit{(Eq. 4B.2)}$$

$$O^-{}_{(ads)} + e^- \rightarrow O^{2-}{}_{(lattice)} \qquad \textit{(Eq. 4B.3)}$$

The work reported here is discussed about the synthesis of cerium iron oxide catalyst by a simple citrate gel combustion method. Here, the operating temperature of ODH of 1-butene to BD is considerably reduced by utilizing the oxygen carrier property of the catalyst for the MVK mechanism through which the reaction is known to proceed. The catalyst properties are investigated and the utilization of lattice oxygen is screened by XPS analysis, temperature-programmed methods, and oxygen uptake studies at the reaction temperature. Herein, we report experimental proof for the MVK mechanism occurring during the ODH reaction at significantly low temperature.

4B.2. Results and discussion

Cerium iron oxide is prepared by citrate gel combustion as explained in **Section 2.3.3**. The reaction and material characterization are illustrated in this part.

4B.2.1. Catalytic activity study

The experimental methods of ODH1B in FBR and the product analysis in GC are discussed in **Section 2.6** and **2.7**. The scheme of reaction over the ceria iron oxygen carrier is depicted in **Fig. 4B.2**. Main products observed were minor quantities of n-butane, 2-butenes, propane, propene, ethane, ethene, methane, carbon oxides and water.

4B.2.1.1. Effect of reaction temperature

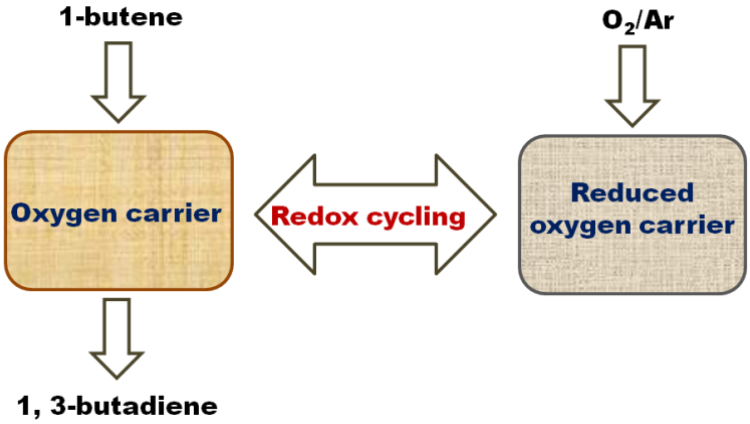

Fig. 4B.2 Method of repeated ODH1B

To determine the best operating temperature, ODH of 1-butene using the lattice oxygen is carried out over CF in the temperature range 200–300 ºC with the flow rate C_4:Ar=1:5 at 3000 h^{-1} GHSV concerning the total feed. The effect of reaction temperature on the conversion of 1-butene ($X_{1\text{-butene}}$) and the selectivity of BD (S_{BD}) is depicted in **Fig. 4B.3a**. Reaction products are analyzed in every 10 minutes and the catalyst is regenerated for

another 10 minutes under O_2: Ar=1:5 at 3000 h^{-1} GHSV. Initially, the catalyst demonstrated 75% 1-butene conversion at 200 ºC with 12 % selectivity for BD which might be due to the maximum availability of lattice and chemisorbed oxygen in the fresh catalyst. Later, the catalyst bed is re-oxidized at 200 ºC followed by increasing temperature to 225 ºC under argon gas flow. Subsequently, the reactant feed; C_4:Ar=1:5 at 3000 h^{-1} GHSV is introduced into the reactor and the product analysis is done after 10 minutes of reaction. This simultaneous ODH and re-oxidation processes are continued at the reaction temperatures viz; 250, 275, and 300 ºC under the above-mentioned feed. Pure argon is flushed through the catalyst bed after regeneration to remove any loosely adsorbed oxygen. Interestingly at 225 ºC, the $X_{1\text{-butene}}$ is reduced to 10 % while S_{BD} is increased. Upon further increasing the reaction temperature, the catalytic performance of the catalyst is gradually improved and the highest activity is achieved at 275 ºC with S_{BD} 28% and 40% 1-butene conversion. Henceforth, 275 ºC is considered as the optimized reaction temperature for further studies.

4B.2.1.2. Catalyst stability during repeated ODH

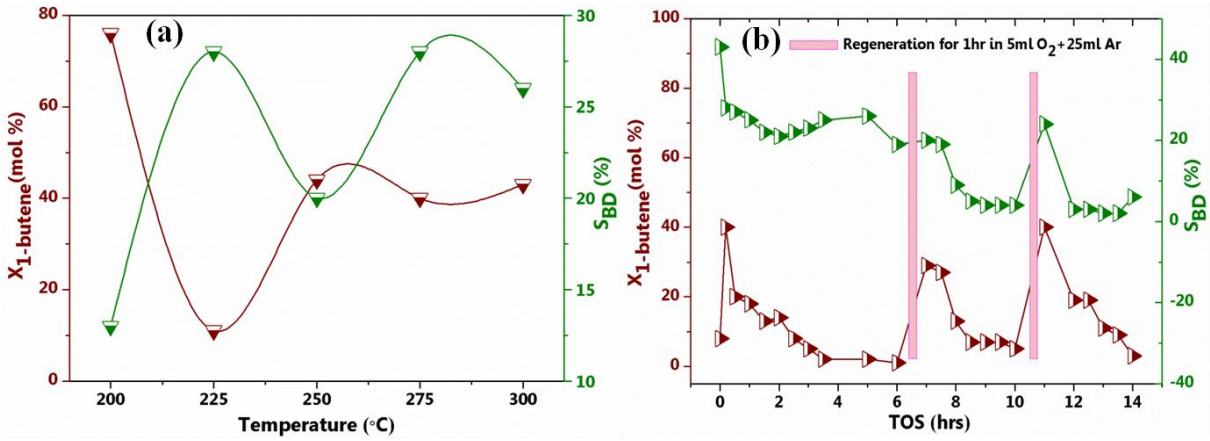

Fig. 4B.3 ODH of 1-butene over CF (a) at different temperatures with catalyst regeneration and (b) TOS study at 275 ºC.

Reaction conditions: 600 mg catalyst, C_4:Ar=1:5, GHSV=3000 $h^{-1}$with respect to total feed.

As 275 ºC is found as the optimum temperature for the reaction, both the time on stream (TOS) study and the maintenance of activity over repeated ODH is studied at this reaction temperature with C_4:Ar feed flow in 1:5 at 3000 h^{-1} GHSV with respect to the total feed. The activity results are shown in **Fig. 4B.3b**. The first cycle is started from zero hour where the conversion of 1-butene is negligible with the highest selectivity for BD. After 10 minutes, the conversion is increased to a maximum value of 40 %; and the selectivity is observed as 28 %. The catalytic activity has been gradually decreased to nearly zero conversion and 20 % S_{BD}

over 6 h of TOS. Further, regeneration is carried out for one hour under O_2 to Ar feed mixture in 1:5 ratio making 3000 h^{-1} total GHSV. Any loosely adsorbed oxygen molecules are removed while flushing the catalyst bed under pure Ar for another one h.

Afterwards, the second reaction cycle is continued while introducing 5 mL 1-butene along with 25 mL Ar in the feed generating the initial reaction feed. The activity is regained with a 10 % decrease in conversion and selectivity. The reaction is continued for another 4 h until the activity becomes stable and negligible. A second regeneration process is carried out followed by the third reaction cycle for another 4 h. During the three reaction cycles, the overall activity is observed to decrease over the TOS study. The loss of lattice oxygen is replenished by molecular oxygen feed and the conversion as well as BD selectivity is restored in the third cycle. Whereas, an appreciable decrease in activity in the second cycle might be due to some changes happened on the catalyst surface explained with the help of XPS studies.

4B.2.2. Catalyst characterization

The fresh catalyst (CF), the catalyst after 6 h of TOS study (CFt), and the catalyst after re-oxidation process (CFr) are collected from different experiments and analyzed for the properties to duly study ODH process. Since lattice oxygens are believed to involve in the reaction, its nature and quantification are made with XPS, TPR, and O_2 chemisorption studies. Further description of the instruments is given in **Section 2.5**.

4B.2.2.1. Material crystallinity

To investigate the structural and chemical changes happened after the ODH reaction and re-oxidation, all samples are analyzed with various techniques. The PXRD patterns of the synthesized $CeFeO_{2\pm\delta}$ (CF) is compared with ceria and iron oxide synthesized via the same combustion method as shown in **Fig. 4B.4a**. Pure ceria exhibited reflections mainly from cubic fluorite phase (JCPDS number:34-0394) with typical planes (111), (200), (220), (311), (222), (400), (331) and (420) corresponding to the diffraction angles 28.59, 33.06, 47.52, 56.39, 59.12, 69.49, 76.71 and 79.23 ° respectively [23]. For iron oxide, the α-Fe_2O_3 hematite (hexagonal) phase is identified with the available database (JCPDS card no. 39-1346) [24]. Although in the freshly prepared catalyst, any reflection corresponds to the hematite phase is not observed. This implies either the absence of crystalline iron species or the substitution of Fe into the ceria lattice. A shift in the peaks to higher 2θ values is observed for CF, CFt, and CFr compared to ceria which might be because of the modification of lattice parameters after substituting Fe cation into CeO_2 lattice [25]. The increase in FWHM of the peaks of CF

compared to pure ceria might be due to the incorporation of Fe^{3+} in the ceria lattice site owing to the smaller ionic radii of the former (Ce^{4+}=0.97, Ce^{3+}=1.43 and Fe^{3+}=0.68 Å). Furthermore, it may also indicate the lower degree of crystallinity or smaller crystallite size [26]. The absence of any cerium ferrite phase nullified the possibility of the formation of perovskite kind of solid solution. Moreover, atom scattering factor of the heavier Ce cations is higher than that of the Fe cations which result in an increased relative high intensity than the α-Fe_2O_3 peaks [27].

Table 4B.1 Physicochemical properties of the samples

Sample code	**S_{BET}[a] (m^2g^{-1})**	**V_p[a] (cm^3g^{-1})**	**D[b] (nm)**	**Lattice constant[c] (nm)**	**O_2 uptake[d] ($mmolg^{-1}$)**	**H_2 Consumption[e] ($mmolg^{-1}$)**
CeO_2	33	0.054	19.04	0.5403	0.67	8.21
Fe_2O_3	15	0.024	45.59	-	0.23	26.31
CF (fresh)	21	0.046	3.99	0.5373	0.51	12.94
CFt (after TOS)	40	0.077	3.81	0.5372	0.68	10.84
CFr (after regeneration)	35	0.074	3.78	0.5373	0.23	14.21

[a]Specific surface area (S_{BET}) and pore volume (V_p) from BET method.
[b]Average crystallite size calculated using Scherrer formula for the (111) crystal plane.
[c]Derived from XRD for the (111) crystal plane.
[d]Calculated by O_2 pulse chemisorptions @ 275 °C.
[e]Total H_2 consumption quantified from H_2-TPR.

Meanwhile, the spent catalyst after the time on stream study (CFt) and the regenerated catalyst after the reaction (CFr) are analyzed for any structural change during the reaction. Both CFt and CFr have retained the structural properties. The crystallite structure was not much altered during the regeneration under molecular oxygen. The lattice parameters for cubic ceria and the other considered solid materials are calculated from the high intense (111) plane in the XRD patterns and tabulated in **Table 4B.1**.

The mean crystallite size is calculated by using Scherrer equation, $D=k\lambda/\beta\cos\theta$; where k is the shape factor ~0.9, λ is the wavelength of Cu Kα radiation equal to 0.15 nm, β is the structural broadening and θ is the diffraction angle of the main peak for ceria at (111) plane. It should be worth to mention that the mixed oxide CF exhibited lower cell parameter (0.5370) than pure ceria (0.5403) as given in **Table 4B.1** which is also observed as a shift in the main peak might be due to the contraction in unit cell proving the substitution of small-sized Fe^{3+} in ceria lattice [25]. While in the case of CFt and CFr hardly any change in the cell

parameter is observed suggesting stability in the crystal structure even after ODH and regeneration processes.

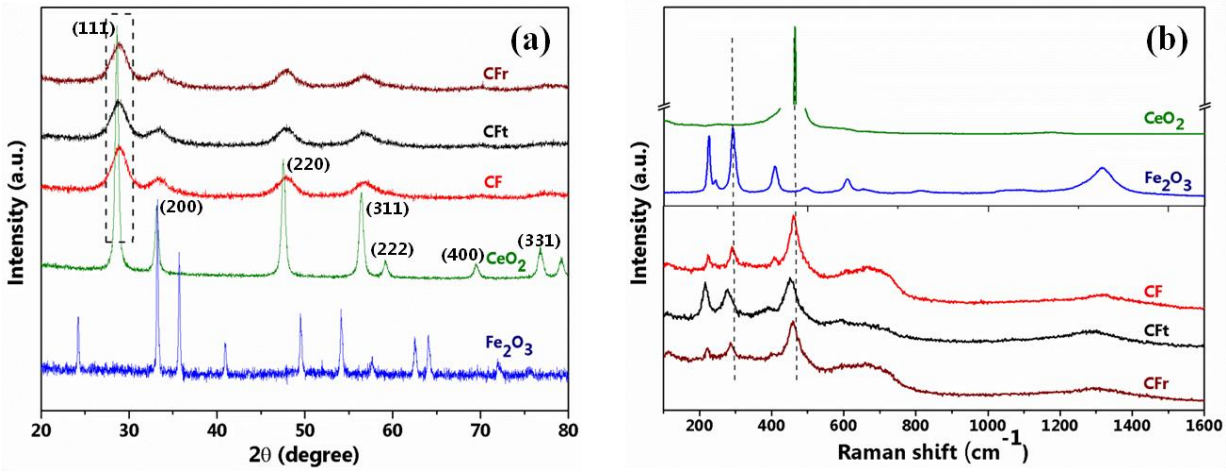

Fig. 4B.4 (a) PXRD patterns and (b) Raman spectra of the samples

4B.2.2.2. Raman spectroscopy

To acquire more structural information, Raman spectroscopy is availed for CF, CFt, CFr, pure CeO_2, and Fe_2O_3 samples and represented in **Fig. 4B.4b**. The high intense peak at 460 cm^{-1} in pure CeO_2 is assigned for the symmetric breathing F_{2g} mode of oxygen atoms around Ce^{4+} ions in the cubic fluorite structure. Moreover, the weak second-order peak observed at 260 and a shoulder band at 590 cm^{-1} are originated from the transverse mode vibration and lattice oxygen vacancy respectively [28]. The main peak is drastically diminished after incorporating Fe which might be due to the reduction in the crystallite size of CeO_2. A similar tendency is observed by Laguna *et. al.* in their study that Fe will considerably interact with the oxygen vacancy bands of ceria [25]. Meanwhile, α-Fe_2O_3 exhibited A_{1g} bands at 222 and 491 cm^{-1}; and E_{1g} bands at 240, 288, 404, and 604 cm^{-1} respectively.

Furthermore, Raman peaks at 662, 816, 1104 and 1320 cm^{-1} for hematite rarely reported by the researchers are also observed [27]. A small shift from the main peak at 463 cm^{-1} could be due to the formation of defects related to the substitution of Fe in ceria lattice [29]. The peaks corresponding to hematite structure is retained in the mixed oxide CF while it is shifted to lower wave numbers after 6 h of reaction as seen in CFt. However, followed by the re-oxidation step, all the peaks are moving back to the initial state proving the structural rearrangement happening within the crystalline solid. The results obtained from Raman are in good agreement with XRD data.

4B.2.2.3. N_2 physisorption

N_2 adsorption-desorption isotherms and pore size distributions of CF compared with CeO_2 and Fe_2O_3 samples are given in **Fig. 4B.5**. The surface area (S_{BET}) and average pore volumes (V_p) of the samples obtained from the BET isotherms are tabulated in **Table 4B.1**. All the materials exhibited low surface area and it is observed that the pore volumes have increased after the reaction and regeneration. The adsorption-desorption isotherm of CF is typical type IV with a hysteresis loop on the range of 0.4–0.99 according to IUPAC classification. A small increase in the surface area and pore volume for CFt and CFr might be because of the surface modification that occurred during the redox process.

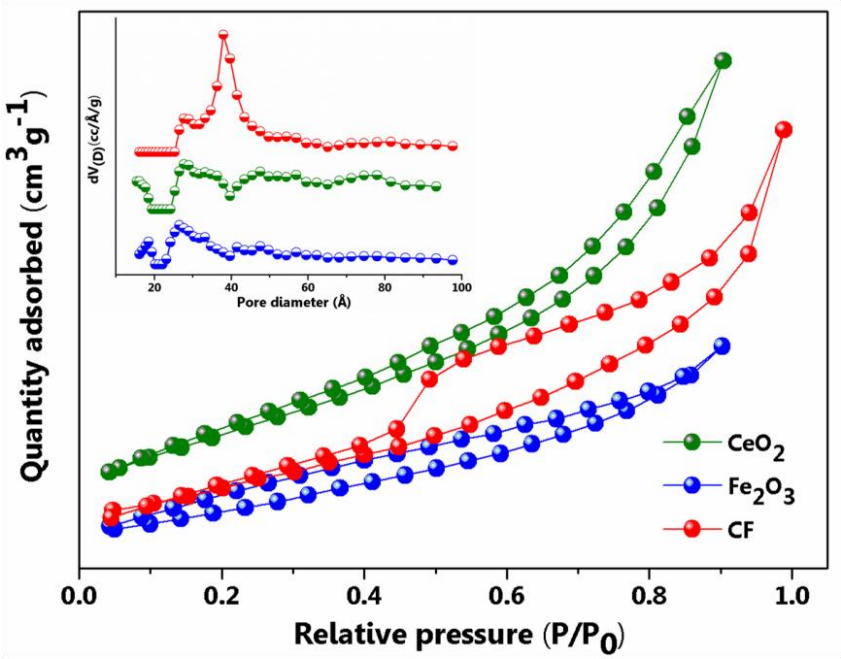

Fig. 4B.5 BET isotherms of calcined CF, CeO_2 and Fe_2O_3; pore size distribution is given on inset.

4B.2.2.4. Morphology of the catalyst

The SEM image and elemental mapping of the as-synthesized CF sample are respectively shown in **Fig. 4B.6a** and **b-d**. SEM micrograph doesn't depict any particular morphology while the mapping clearly revealed the fine dispersion of the metals over the catalyst surface. TEM images, as well as the SAED pattern of the fresh catalyst, are also shown in **Fig. 4B.6e** and **f**. The (111) crystal surface is identified and a decrease in the lattice distance is observed at 29 ° 0.262 nm) for CF compared to that of pure ceria (0.312 nm). This observation could be explained as the ionic radii difference between Fe^{3+} and Ce^{3+}/Ce^{4+} and the preference of the former ion to occupy in ceria lattice. The above observations are in good agreement with

the result obtained from PXRD [30]. Moreover, the substitution of Fe in ceria can reduce the interplanar distance also with lattice contraction [5]. The electron diffraction pattern is typical of a nanocrystalline material which is also evidenced as broad diffraction peaks in PXRD.

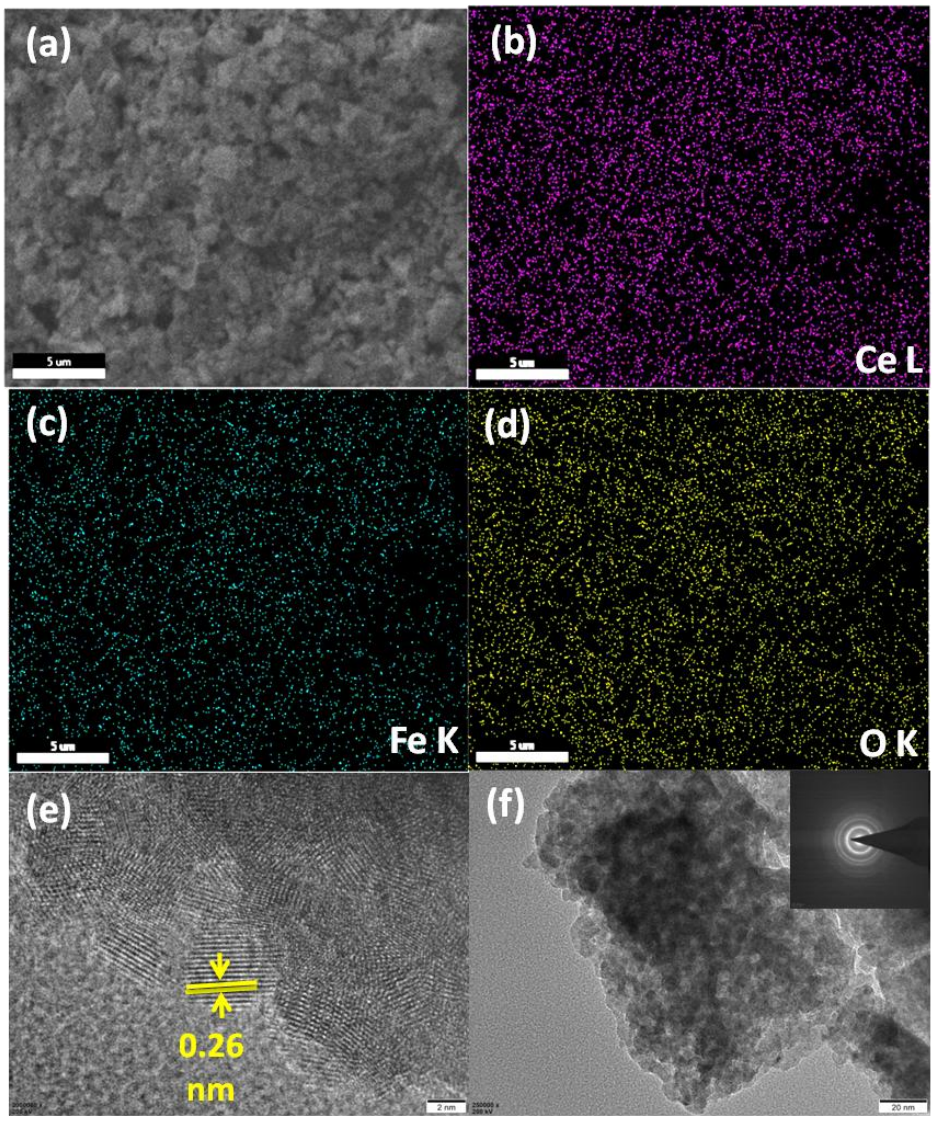

Fig. 4B.6 (a) SEM image, (b-d) elemental mapping and (e, f) HRTEM images of pure CF. SAED pattern is given on inset.

4B.2.2.5. XPS analysis

XPS analysis is performed to investigate the surface compositions and changes in oxidation states of the catalysts. **Fig. 4B.7** shows the XPS spectra of Ce 3d (a) and Fe 2p (b) of CF, CFt, and CFr compared with that of pure CeO_2 and Fe_2O_3 to study any structural changes occurred during the experiments. The binding energy scale is corrected by using the adventitious carbon (284.8 eV) of each sample. Ce 3d spectrum of pure CeO_2 is originated by multiple peaks labelled u and v which represents the $3d_{3/2}$ and $3d_{5/2}$ spin-orbit components

respectively. The peaks correspond to Ce^{3+} ($3d^{10}$ $4f^{1}$) will be appeared at u_0, u', v_0 and v' due to the fewer defects in ceria; while u, u", u"', v, v" and v"' are associated with Ce^{4+} The major peaks are observed at BE ca 882.1, 887.8, 898.1, 900.6, 903.6, 906.6 and 916.3 [31]. Further analysis of the spectrum revealed that the 4+ oxidation state is dominating in pure ceria. Even after the incorporation of iron oxide, the fresh catalyst CF maintained predominantly Ce^{4+}. After the reaction, the surface of the oxygen carrier is reduced by 1-butene. Therefore the oxidation state of Ce^{4+} will change to Ce^{3+} in CFt. Eventually, the surface is re-oxidised again to Ce^{4+} by the external supply of molecular oxygen in the regeneration step as shown in the Ce 3d spectrum for CFr [11].

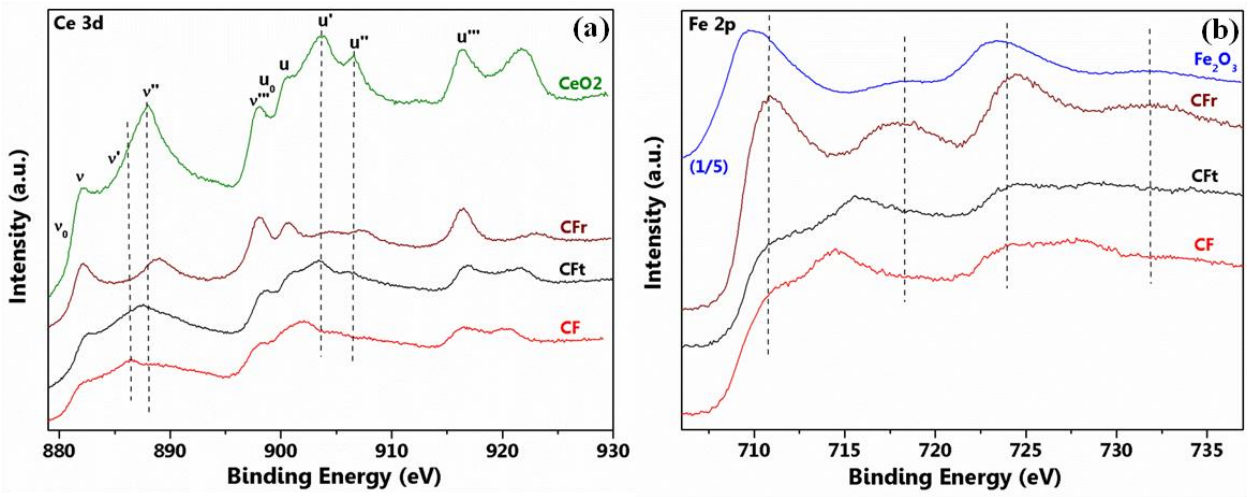

Fig. 4B.7 XPS spectra of (a) Ce 3d and (b) Fe 2p core levels of the materials

The characteristic peaks for $Fe2p_{3/2}$ and $Fe2p_{1/2}$ are observed at 710.8 and 724.1 eV respectively (**Fig. 4B.7**) with the corresponding satellite peaks at 718.3 and 731.9 eV [16]. Fe exists in both 2+ and 3+ oxidation states. The shift in binding energy values might be due to the electronic interaction of iron and cerium core levels. The oxygen species present on the surface are varied with the samples and are reflected in the XPS spectra as depicted in **Fig. 4B.8**. O 1s spectrum of Fe_2O_3 showed typical peak for lattice oxygen at higher binding energy than other samples revealing the high reducibility of the material. This is detected in the TPR profile also. For other ceria containing samples, the main peak at 529.4 eV can be assigned to the lattice oxygen whereas a shoulder detected at 531.1 eV is treated as chemisorbed oxygen species [32]. A peak observed at 533 eV can be due to the surface hydroxyl groups and carbonate impurities [31].

Meanwhile, the adsorbed water moieties are also observed at the highest BE 534.9 eV [33]. The peak shift observed in CFt to higher BE suggest that the labile lattice oxygens from the lattice have been consumed during the reaction and more surface defects are created. Moreover, XRD and Raman patterns of CF, as well as CFr, are similar which implies the possible migration of Fe species during the reduction/re-oxidation cycles [11]. At higher BE values absorbed oxygen/water molecules are detected [34].

Table 4B.2 Surface composition of different oxygen species

Sample	**O_{latt} (%)**	**O_{ads} (%)**	**O_{latt}/ O_{ads}**
CF	20.5	69.5	0.295
CFt	29.2	43.8	0.667
CFr	40.4	48.6	0.831

The distribution of various surface oxygen species is quantified and listed in **Table 4B.2**. The chemisorbed oxygens are denoted as O_{ads} mainly contributing from the electrophilic O^- and O^{2-} at higher and lower BEs respectively. The high-temperature treatment could remove these species substantially which is reflected as an increase in the amount of lattice oxygen [33]. These species will also contribute to the conversion of 1-butene to selectively forming combustion products. This is observed in **Fig. 4B.3a** with 80 % 1-butene conversion at 200 °C. Therefore, it may be concluded that the catalyst exhibit excellent oxygen carrier property due to the synergy achieved by the combination of Ce^{3+}/Ce^{4+} and Fe^{2+}/Fe^{3+} redox centres and is evidenced from the XPS results.

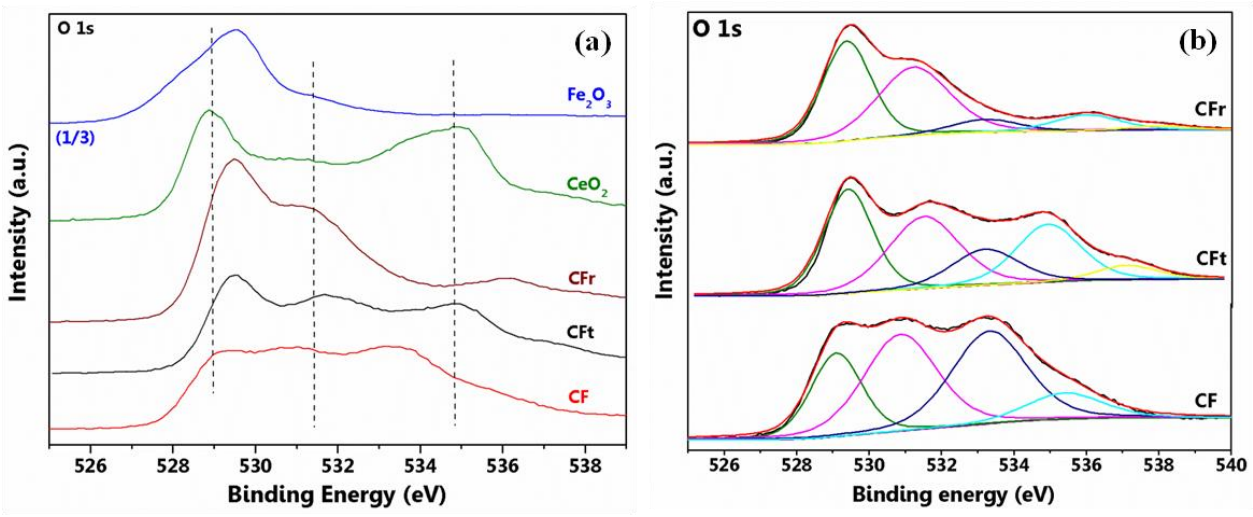

Fig. 4B.8 (a) O1s XPS spectra of all samples and (b) deconvoluted O 1s XPS spectra of CFr, CFt and CF.

4B.2.2.6. H_2-TPR study

XPS is a surface analysis technique and hence to quantify the lattice oxygens in bulk, H_2-TPR of the samples is conducted. Also, it is observed that the lattice oxygens are participating in ODH reaction which makes the study of redox properties of the oxides significant. The TPR profiles of CF, CFt, and CFr are compared with that of pure CeO_2 and Fe_2O_3 in **Fig. 4B.9**. The reduction of pure Fe_2O_3 is believed to occur in two steps. At low temperature, Fe_2O_3 (hematite) will be reduced to Fe_3O_4 (magnetite) which appears at around 382 °C. Further reduction of Fe_3O_4 to FeO and FeO to Fe^0 happens above 500 °C in the TPR profile [35]. In the case of CeO_2, the low-temperature reduction peak is attributed to the reduction of surface CeO_2 covered by surface capping oxygen, and the reduction peak observed at high temperature is credited to bulk CeO_2.

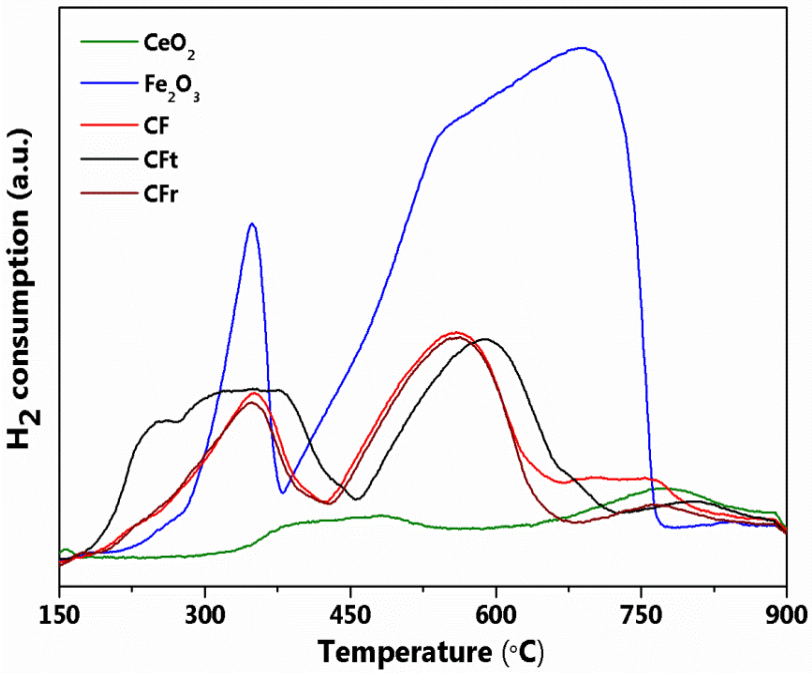

Fig. 4B.9 H_2-TPR profiles of the samples

The surface lattice as well as the bulk oxygen of ceria will be reduced at around 470 and 800 °C respectively [36]. The incorporation of iron in the ceria lattice increases the mobility of surface lattice oxygen and shift the reduction peaks to lower temperatures with a considerable decrease in hydrogen consumption. This might be due to the synergistic interaction between ceria and iron oxide. The high dispersion of Fe ions in the ceria matrix as evidenced by PXRD could form surface Fe–O–Ce species and is attributed to synergism. Henceforth, the

enhanced reducibility improves the redox properties of CF and is reflected in the catalytic activity [16].

4B.2.2.7. O_2-pulse chemisorption

The labile oxygens available for the reaction have to be quantified to study the redox mechanism in detail. In favour of this, the amount of oxygen adsorbed at the optimized reaction temperature i.e; 275 °C is calculated with the oxygen pulse chemisorption experiment (**Fig. 4B.10**) and the values are displayed in **Table 4B.1**. The strength of oxygen storage capacity (OSC) will be in the order CFt≈CeO_2>CF>CFr=Fe_2O_3. Thus, CFt contains more oxygen vacancies which prove that lattice oxygen is consumed for the conversion of 1-butene to BD in the TOS study. During re-oxidation, these vacancies will be restored and hence least oxygen uptake was observed for CFr.

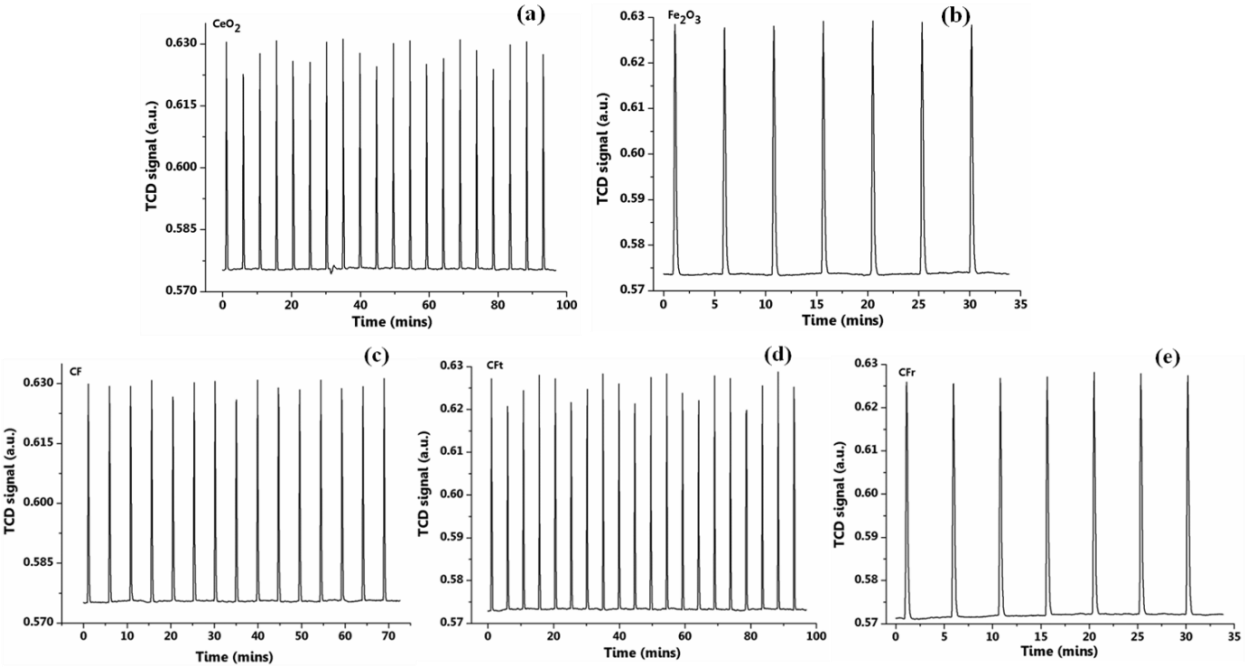

Fig 4B.10 O_2-uptake pulses of (a) CeO_2 (b) Fe_2O_3 (c) CF (d) CFt and (e) CFr at 275 °C

It could be concluded from the combined results of TPR and oxygen pulse studies that more selective surface and bulk oxygen species are available in cerium iron mixed oxide than pure ceria which can contribute towards the catalytic activity [5]. It is observed from the TOS study that 1-butene DH is decreased over 6 h mainly because the labile oxygens are consumed during the reaction. These vacancies could be later regenerated with external molecular oxygen supply. Apart from this, total H_2 consumption for CF is 12.94 mmolg^{-1}and the value decreases to 10.84 mmolg^{-1} for CFt which indicates that the catalyst surface is

reduced during the DH reaction. This observation is in good agreement with the XPS results also. Following this, the reduction peak is shifted to 586 °C for CFt when compared with CF (558 °C). After the catalyst is treated with oxygen, the reduction peak is restored to 558 °C for CFr. Considering all these observations, it can be concluded that the CF mixed oxide serves as an excellent oxygen carrier with replaceable lattice oxygens and regenerable redox properties.

4B.2.2.8. *in situ* FTIR spectroscopy

CO-FTIR spectra peformed *in situ* can provide evidences for the lattice oxygen utilization. Two different experiments are conducted to support the oxygen carrier property of the synthesized material. In the first experiment, interaction of CO with the catalyst is carried out at different temperatures from 50–275 °C and illustrated in **Fig. 4B.11a**. The bands at 1298 and 1778 cm^{-1} correspond to the carbonate species adsorbed on the surface. The peak around 2100 cm^{-1} represents the surface physical adsorption of CO [32]. Gaseous CO_2 is observed at about 2112 cm^{-1}. The enhancement in the CO oxidation reaction with the increase in temperature is reflected in the intensity of the second band. From the spectra, it is evident that CO can adsorb to Fe^{2+} as well as Fe^{3+} at 2100 and 2200 cm^{-1} respectively. XPS results also revealed the presence of these iron species on the surface. The results demonstrate that CO can react with the lattice oxygen even at 50 °C. This is because of the excellent CO oxidation property of ceria based catalyst systems even at low temperatures reported in the literature [14, 37].

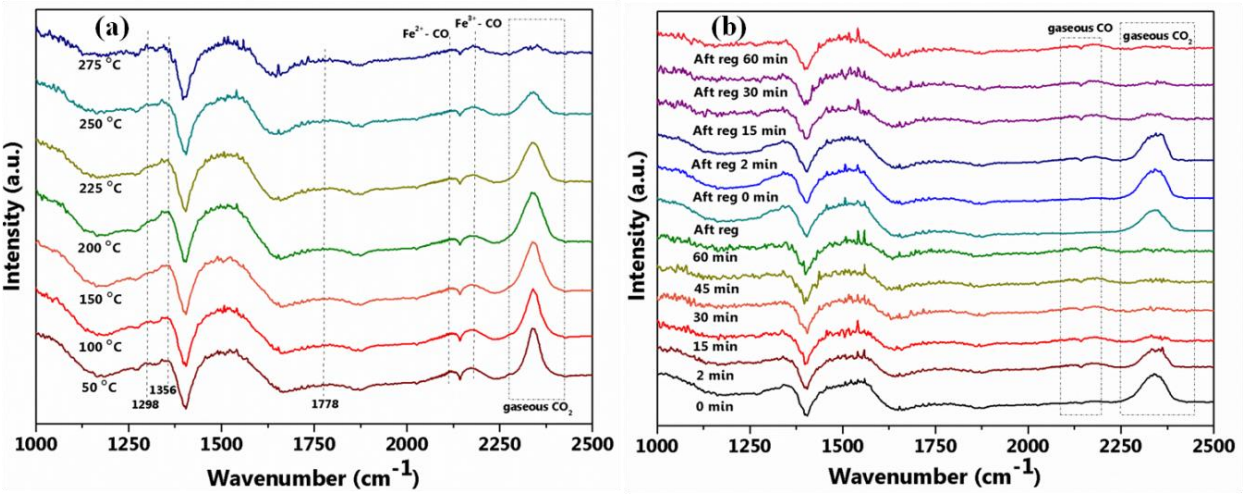

Fig. 4B.11 *in situ* CO-FTIR spectra of CF at (a) different temperatures and (b) 275 °C

Similarly, **Fig. 4B.11b** shows the second experiment where the utilization of lattice oxygens is studied at the optimized reaction temperature viz; 275 °C. Gaseous CO_2 formation is identified immediately after the exposure to CO and is continuously observed up to 45 minutes. After the regeneration process with 5 % oxygen in nitrogen, the surface is flushed with pure nitrogen to remove any loosely bound molecular oxygen. Then, the second step of CO-FTIR is started and the formation of CO_2 is detected. After a few minutes, the peak corresponding to CO_2 becomes weak with the appearance of CO peak. These experiments further confirm the efficient utilization of lattice oxygen and the replenishing of the vacancies created in the cerium iron mixed oxide.

In another study, soon after the pre-treatment of the fresh catalyst with nitrogen for one hour, *in situ* FTIR is performed using 1-butene as a probe molecule at 275 °C. The spectra are recorded up to 4 h at different time intervals and represented in **Fig. 4B.12**. When the reactant molecule 1-butene is introduced into the chamber containing the fresh catalyst, typical bands correspond to the alkene were immediately emerged due to the adsorption of 1-butene on CF. Distinctive C═C stretching vibration is observed at 1660 cm^{-1}. The symmetric and asymmetric vibration modes of $–CH_2$ can be assigned to the bands evolved at 2856 and 2934 cm^{-1}. Bands observed at 1257 and 1305 cm^{-1} could be raised from C–H scissoring [38]. The increasing features at 1588, 3000, 3090, and 3110 cm^{-1} indicate the formation of BD [39].

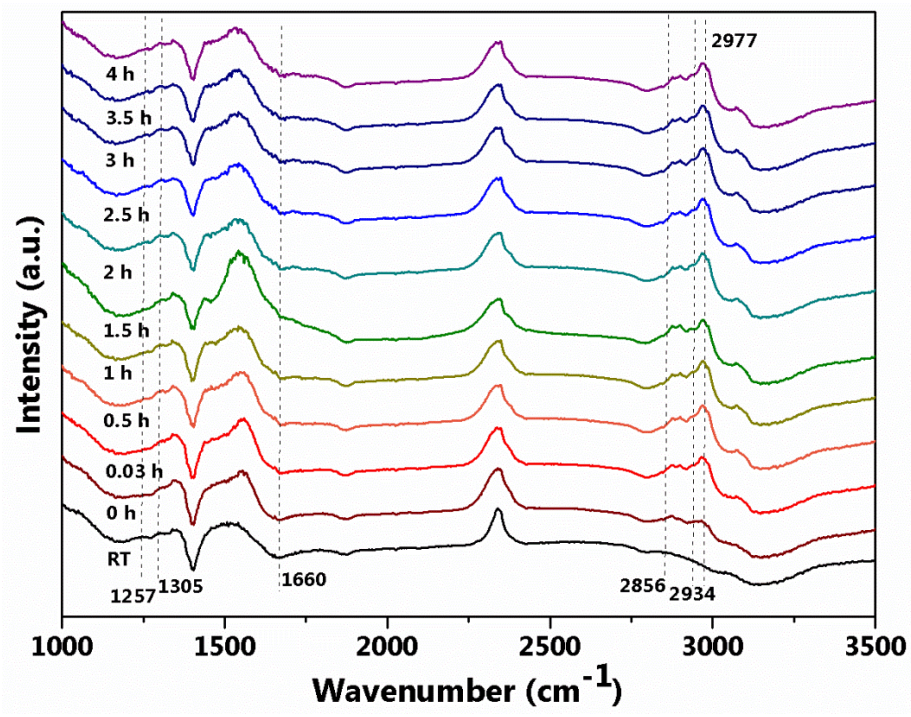

Fig. 4B.12 *in situ* FTIR of CF with 1-butene as probe molecule

The experiment is continued for 4 h and the formation of BD was steady throughout the analysis. Compared to the CO oxidation reaction, 1-butene conversion to BD happens very slowly with the utilization of lattice oxygen. This observation is supported by the disappearance of the CO_2 band after 45 minutes in the *in situ* CO-FTIR spectra. It might be because of the better oxidation activity of CO than 1-butene. Nevertheless, *in situ* 1-butene DH supports the previous results retrieved from other characterization techniques.

4B.3. Conclusions

The present work could successfully incorporate Fe in ceria lattice which improved the textural properties and oxidation properties by lowering the activation energy for oxygen migration. XPS, PXRD, and HRTEM results are evidenced for this and were correlated with the catalytic activity measurements. Since ODH is known to proceed through the Mars van Krevelen mechanism by consuming the lattice oxygen from the catalyst, the oxygen carrier property of the synthesized oxide has been effectively utilized for BD synthesis. It is achieved at a lower temperature over CeFe oxide which is not reported in the literature so far up to our knowledge. During the reaction, the catalyst surface is reduced and the vacancies are replenished with molecular oxygen. In conclusion, this work utilized the oxygen carrier property of a simple cerium iron mixed oxide for the low-temperature ODH of 1-butene in a continuous flow fixed bed reactor resulting in an appreciable yield of BD and experimentally demonstrated MVK mechanism. Also, a substantial reduction in the reaction temperature diminishes the operating cost and makes BD synthesis more inexpensive. Moreover, steam was not used in the present work which has added advantage over the existing methods. The outcomes of this study give new insights to the ODH of the 1-butene process as energy-efficient and economically viable for the production of BD by considerably bringing down the operating temperature.

References

[1] A. Gupta, A. Kumar, U.V. Waghmare, M.S. Hegde, Chem. Mater. 21 (2009) 4880–4891.

[2] C. Sun, H. Li, L. Chen, Energ. Environ. Sci. 5 (2012) 8475–8505.

[3] A.K.P. Mann, Z. Wu, F.C. Calaza, S.H. Overbury, ACS Catal. 4 (2014) 2437–2448. A.D. Mayernick, M.J. Janik, J. Phys. Chem. C 112 (2008) 14955–14964.

[4] O.M. Mariano, F.C. Aldo, B.H. Emilia, C.A.F. Marcia, G.L. Diego, A.L. Susana, Ceram. Int. 41(2015)13721–13730.

[5] Q. Wang, X. Li, W. Li, J. Feng, Catal. Commun. 50 (2014) 21–24.

[6] A. Trovarelli, Comments Inorg. Chem. 20 (1999) 263–284.

[7] R.D. Shannon,C.T.Prewitt, Acta Crystallogr. B 25 (1969) 925–946.

[8] E. Hong, J.H. Park, C.H. Shin, Catal. Surv. Asia 20 (2016) 23–33.

[9] A.C. Avinash, H. Kim, RSC Adv. 6 (2016) 88859–88867.

[10] P. Singh, M.S. Hegde, J. Solid State Chem. 181 (2008) 3248–3256.

[11] K. Li, H. Wang, Y. Wei, D. Yan, Appl. Catal. B Environ. 97 (2010) 361–372.

[12] K. Z. Li, H. Wang, Y.G. Wei, D.X. Yan, J. Phys. Chem. C 113 (2009) 15288–15297.

[13] G. Neri, A. Pistone, C. Milone, S. Galvagno, Appl. Catal. B Environ. 38 (2002) 321–329.

[14] H. Laguna, M.A. Centeno, M. Boutonnet, J.A. Odriozola, Appl. Catal. B Environ. 106 (2011) 621–629.

[15] A.S. Reddy, C.Y. Chen, C.C. Chen, S.H. Chien, C.J. Lin, K.H. Lind, C.L. Chene, S.C. Chang, J. Mol. Catal. A Chem. 318 (2010) 60–67.

[16] Z. Zhang, D. Han, S. Wei, Y. Zhang, J. Catal. 276 (2010) 16–23.

[17] S. Takenaka, K. Nomura, N. Hanaizumi, K. Otsuka, Appl. Catal. A Gen. 282 (2005) 333–341.

[18] O. Nakayama, N. Ikenaga, T. Miyake, E. Yagasaki, T. Suzuki, Catal. Today 138 (2008) 141–146.

[19] H.H. Kung, M.C. Kung, Adv. Catal. 33 (1985) 159-198. T. Uda, T.T. Lin, G.W. Keulks, J. Catal. 62 (1980) 26–34.

[20] H. Bao, X. Chen, J. Fang, Z. Jiang, W. Huang, Catal. Lett. 125 (2008) 160–167.

[21] T. Kiyokawa, N. Ikenaga, Appl. Catal. A Gen. 536 (2017) 97–103.

[22] M. Keller, D.P. Anderson, H. Leion, T. Mattisson, Appl. Catal. A Gen. 550 (2018) 105–112.

[23] M.E. Khan, M.M. Khan, M.H. Cho, Sci. Rep. 7 (2017) 5928–5945.

[24] R. Wahab, F.K.A. Abdulaziz, Al-Khedhairy, RSC Adv. 8 (2018) 24750–24759.

[25] O.H. Laguna, F.R. Sarria, M.A. Centeno, J.A. Odriozola, J. Catal. 276 (2010) 360–370.

[26] G. Kimmel, D. Dayan, Snyder, R. L.; Fiala, J.; Bunge, H. J., In IUCR Monographs on Crystallography; Eds.; Oxford Science Publications: 1999.

[27] F.J. Perez-Alonso, M.L. Granados, M. Ojeda, T. Herranz, S. Rojas, P. Terreros, J.L.G. Fierro, M. Gracia, J.R. Gancedo, J. Phys. Chem. B 110 (2006) 23870–23880.

[28] Z. Zhang, D. Han, S. Wei, Y. Zhang, J. Catal. 276 (2010) 16-23. J.R. McBride, K.C. Hass, B.D. Poindexter, W.H. Weber, J. Appl. Phys. 76 (1994) 2435–2441.

[29] G. Cheng, T. Kou, J. Zhang, C. Si, H. Gao, Z. Zhang, Nanomater. Energy 38 (2017) 155–166.

[30] G. Li, R.L.S. Jr., H. Inomata, J. Am. Chem. Soc. 123 (2001) 11091–11092.

[31] A.K. Venugopal, A.T. Venugopalan, P. Kaliyappan, T. Raja, Green Chem. 15 (2013) 3259–3267.

[32] X. Hou, J. Qian, L. Li, F. Wang, B. Li, F. He, M. Fan, Z. Tong, L. Dong, L. Dong, Ind. Eng. Chem. Res. 57 (2018) 16675–16683.

[33] J.C. Wang, J. Ren, H.C. Yao, L. Zhang, J.S. Wang, S.Q. Zang, L.F. Han, Z.J. Li, J. Hazard. Mater. 311 (2016) 11–19.

[34] K. Sutthiumporn, S. Kawi, Int. J. Hydrogen Energ. 36 (2011) 14435–14446.

[35] M. Kurian, C. Kunjachan, A. Sreevalsan, Chem. Eng. 308 (2017) 67–77.

[36] E. Rocchini, A. Trovarelli, J. Llorca, G.W. Graham, W.H. Weber, M. Maciejewski,A. Baiker, J. Catal. 194 (2000) 461–478.

[37] S. Zhao, F. Chen, S. Duan, B. Shao, T. Li, H. Tang, Q. Lin, J. Zhang, L. Li, J. Huang, N. Bion, W. Liu, H. Sun, A.Q. Wang, M. Haruta, B. Qiao, J. Li, J. Liu, T. Zhang, Nature commun.10 (2019) 3824.

[38] A. Valcarcel, A. Clotet, J.M. Ricart, F. Delbecq, P. Sautet, Surf. Sci. 549 (2004) 121–133.

[39] R.W. Wenig, G.L. Schrader, J. Phys. Chem. 91 (1987) 1911–1918.

Chapter-5

Selective Dehydrogenation of Isobutane to Isobutene over Promoted Mesoporous Fe-Alumina Catalysts

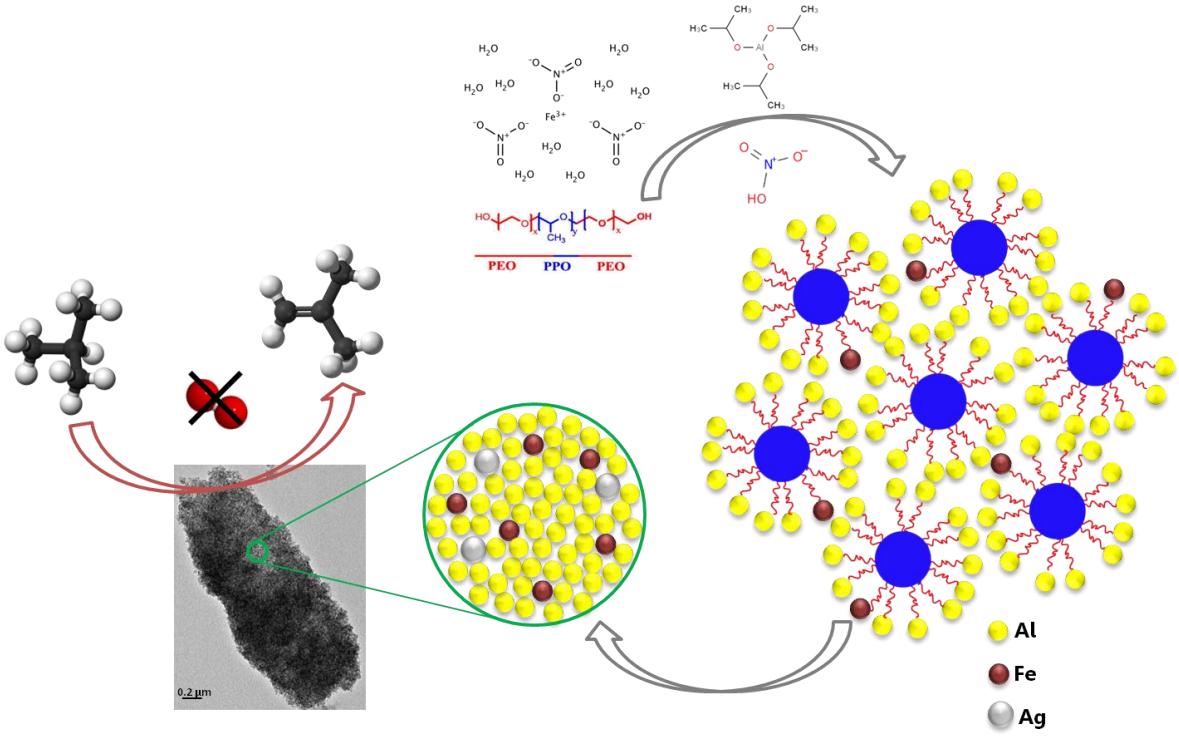

Highlights

- Promoted mesoporous iron doped alumina catalysts are synthesized and studied for the high temperature dehydrogenation of isobutane to isobutene
- PXRD, Raman and TEM studies revealed proper doping of Fe in alumina matrix
- Silver promoted catalyst exhibited the highest isobutene yield under the studied reaction conditions
- The catalytic activity is slightly declined over 60 h of stability test due to particle agglomeration as well as carbon nanotubes formation

5.1. Selective dehydrogenation of isobutane

The demand for light alkenes is increasing since the last century mainly because of the application in polymer industry. They are the fundamental precursor for synthetic rubber [1]. Among them, isobutene has a significant role as the intermediate for high octane oxygenates production. The presence of highly reactive double bond in isobutene is utilized for the conversion to a large number of reaction intermediates like methyl *tert*-butyl ether (MTBE), ethyl *tert*-butyl ether (ETBE), methacrylates etc [2]. The worldwide demand of isobutylene is predicted to increase in the nearest future as depicted in **Fig. 5.1**. Current production of isobutene is achieved by conventional steam cracking and fluid catalytic cracking of naphtha along with ethene and propene as main products [3]. However, the final yield of isobutene is low in these processes and hence the direct dehydrogenation (DH) of isobutane acquires a significant role.

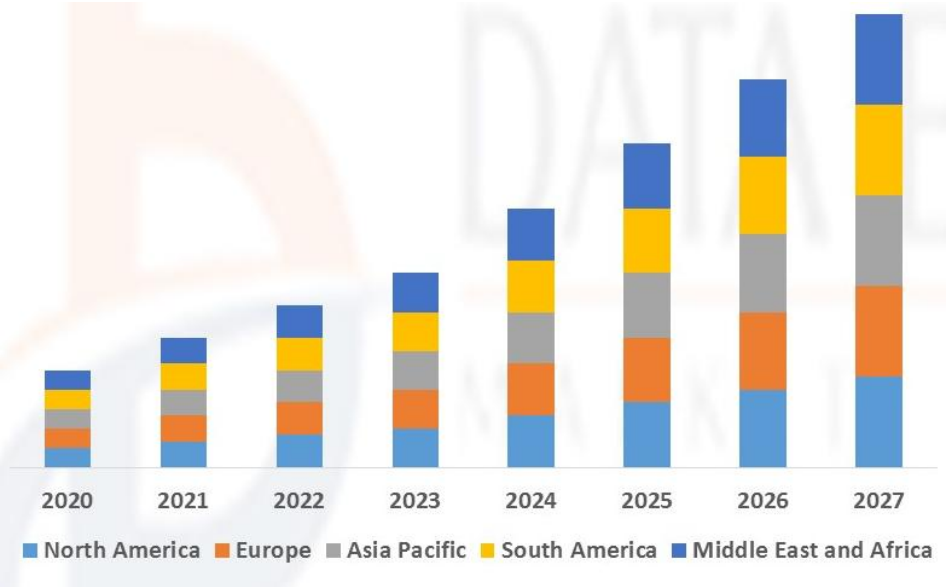

Fig. 5.1 Global isobutene market size [4]

Dehydrogenation of isobutane (DHisoB) has attracted wide industrial attention for the bulk synthesis of isobutene. Usually, Pt and Cr based catalysts are employed for this purpose. Even though these systems are giving reasonable product yield, the toxicity as well as related environmental problems has to be taken into consideration [5]. Therefore, researchers aim to develop a safe and cost effective catalyst for the selective DH reaction.

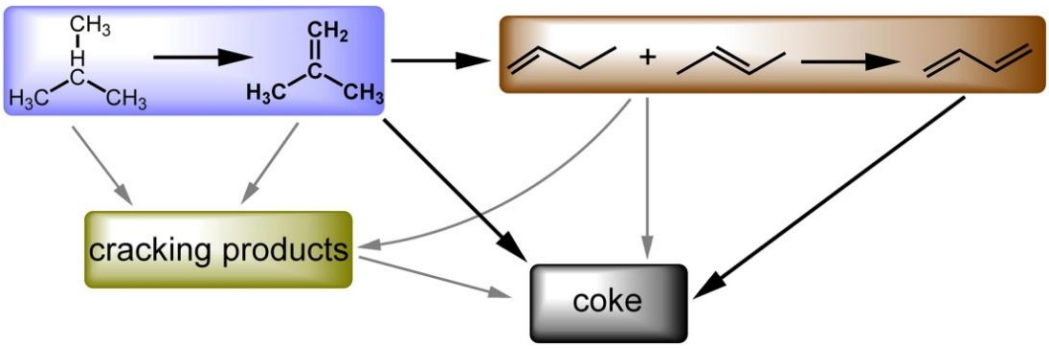

Scheme 5.1 Product distribution in DHisoB [6]

General pathway of DHisoB is represented in **Scheme 5.1**. The reaction gives multiple side products and so reduces the selectivity towards isobutene. The endothermicity of the reaction (*Eq. 5.1*) demands higher operating temperature which increases the chances of coke formation.

$$i\text{–}C_4H_{10} \leftrightarrow i\text{–}C_4H_8 + H_2;\ \Delta H = +117\ \text{kJ mol}^{-1} \qquad (Eq.\ 5.1)$$

Hence, designing suitable catalyst for the selective conversion of isobutane to isobutene is a big challenge in heterogeneous catalysis. More detailed information about isobutene is given in **Section 1.7**.

5.2. Background of the work

Catalyst support has a significant role in defining the performance. Especially, for a DH reaction, the support should be thermally stable to survive the rigorous reaction conditions. Moreover, the limited acidity can evade undesired C–C cracking and alkane isomerization reactions. High surface area and uniform pore size distribution of the support will enhance homogeneous metal dispersion [7, 8]. While considering all these aspects, the non-reducible metal oxide; alumina will be an excellent candidate for the DH reaction owing to its high thermal stability as well as mechanical strength. Moreover, the state of art drawn from the existing literature evinced alumina as the most preferred support for DHisoB including industrial applications [6, 9-10]. Meanwhile, the commercialized catalysts have been modified to overcome the current difficulties and improve activity by adding different metal oxides as active components [11, 12]. Recently, Uwe *et. al.* have proved that bare alumina itself is active for the reaction with a 30 % yield for isobutene due to the coordinatively unsaturated Al sites on the surface [13]. The supported VO_x, GaO_x, and MoO_x materials on alumina have improved the conversion and selectivity for DHisoB [8].

Alumina is acidic and hence it should be modified to restrain the acidity. Researchers have successfully attempted to reduce the acidic properties of alumina by combining with ZnO and MgO which has improved the dehydrogenation activity and catalyst stability [14]. The addition of alkali metals can also contribute to this by selectively poisoning the acidic sites and hindering the coke formation [15, 16]. Shingo *et. al.* have established that the addition of a small amount of iron can improve the activity, selectivity, and stability of Pt/Al_2O_3 catalyst for the dehydrogenation of isobutane. NH_3-TPD studies have proved a considerable reduction in strong acid sites after Fe addition [10] which is in good agreement with the studies of Kania *et. al.* [17]. These strong acidic sites prompt alkene hydrogenolysis and decrease isobutene selectivity [18]. Apart from these, iron oxide-containing activated carbon also served as a good catalyst for the dehydrogenation of C_4–C_5 hydrocarbons [19].

Inspired by these described observations, here we illustrated the synthesis of chromium free mesoporous iron alumina catalytic systems. To solve the above-discussed problems, the catalyst is separately modified with an alkali metal, phosphorous as well as noble metal via dry impregnation method. The synthesized materials are characterized for their topology, morphology and chemical properties by an array of instrumentation techniques including PXRD, N_2 physisorption analysis, SEM, TEM, Raman spectroscopy, XPS, H_2-TPR, NH_3-TPD and TGA. The materials displayed promising catalytic activity towards the non-oxidative DH of isobutane.

5.3. Results and discussion

Mesoporous alumina based catalysts are synthesized by soft template method followed by dry impregnation as elaborated in **Section 2.3.4**. The reaction results and the catalyst characterization are briefly discussed here.

5.3.1. Catalytic activity study

The catalytic activity of the mesoporous alumina catalysts are measured in a conventional fixed bed reactor as described in **Section 2.6**. The effect of different promoters as well as reaction parameters like temperature on the activity performance is investigated through different experiments. Effluents are identified in GC (refer **Section 2.7**) and the major components were n-butane, 2-butenes, butadiene, propene, propane, ethene, ethane, methane as well as hydrogen. No carbon oxides were observed. Coke deposition is also detected near the catalyst bed at the end of each experiment.

5.3.1.1. Effect of promoters

It is a normal practice to utilize catalyst promoters on an existing catalyst to improve the product yield. Therefore, the effect of different promoters on the selective DH of isobutane to isobutene is analyzed at 600 °C. All experiments are conducted at 400 h^{-1} GHSV concerning isobutane and argon mixture taken in 1:1 ratio and the results are depicted in **Fig. 5.2a**. For the comparison study, the reaction is carried out over MesoAl also. Interestingly, as can be seen, the bare support exhibited appreciable activity under the given reaction conditions with the highest selectivity towards total dehydrogenated products (S_{TDP}) which include isobutene, 1-butene, 2-butenes, propene, and ethene. However, the final conversion and selectivity for isobutene (S_{isoB}) are negligible. The incorporation of Fe simultaneously decreased S_{TDP} and increased isobutane conversion. It can be realized from the activity performance given in **Fig. 5.2a** that the addition of a small amount of promoters noticeably affects the DH reaction pattern at 600 °C. Potassium promoted catalyst (KMesoFeAl) showed very good selectivity towards the reaction while conversion was comparatively low. Conversely, the acid-treated material (PMesoFeAl) was less selective for isobutene with a better isobutane conversion. Surprisingly, the noble metal promoted AgMesoFeAl displayed the highest activity at the studied reaction parameters. Isobutane conversion achieved was 36 % with 32 % selectivity towards isobutene. It is important to highlight the appreciable S_{TDP} over the same catalyst.

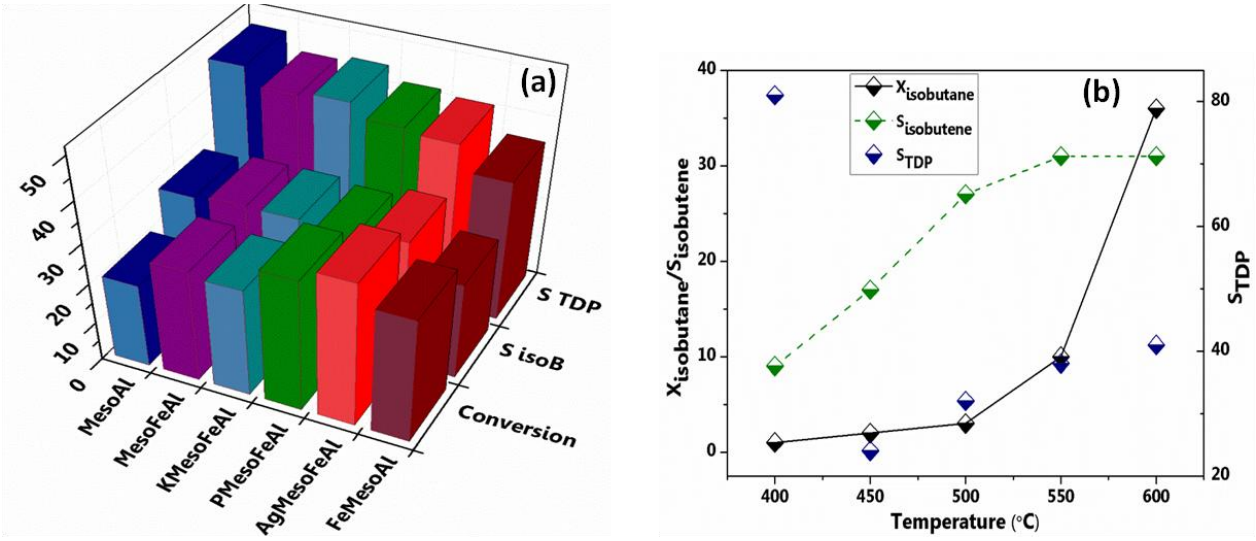

Fig. 5.2 (a) DHisoB over different catalysts at 600 °C and (b) effect of reaction temperature on catalytic activity over AgMesoFeAl.

Reaction conditions: 300 mg catalyst, i–C_4/Ar=1, GHSV=400 h^{-1} with respect to total feed.

To investigate the effect of synthesis strategy adopted for Fe incorporation in MesoAl support on the reaction, FeMesoAl is prepared by dry impregnation method.Further, the activity

performance of this catalyst is compared with the *in situ* prepared MesoFeAl catalyst. The activity results represented in **Fig. 5.2a** clearly illustrate that FeMesoAl shows the least selectivity towards the DH process among all. The reason for this observation is analyzed with the material properties and explained in the respective sections. It may be interpreted in terms of the amount of coke deposited on the surface which is quantified from TG analysis. From the above results, AgMesoFeAl is selected as the optimized catalyst for further analysis.

5.3.1.2. Influence of reaction temperature

Fig. 5.2b shows isobutane conversion and isobutene selectivity as a function of reaction temperature over the AgMesoFeAl catalyst. At 400 °C, isobutane conversion was insignificant with the least isobutene selectivity through the formation highest S_{TDP}. The main process occurred at this temperature would be isomerization of the formed alkene. On further increasing the reaction temperature up to 500 °C made a very slight improvement in conversion accompanied by the steady increase in product selectivity. After 500 °C a sharp increase in reactant conversion is observed. Contrastively, selectivity is slowly increased with temperature and remained constant after 550 °C. **Fig. 5.2b** illustrates 36 % isobutane is converted with 32 % selectivity towards isobutene at 600 °C. The formation of other alkenes is also in line with isobutene selectivity pattern when plotted against temperature. At higher temperatures, the formed isobutene might further cracked into lighter hydrocarbons. Finally, coke is formed which will be deposited on the catalyst surface blocking the active sites. Post characterization of the spent catalysts supports this observation. This activity trend may also be correlated to the particle size distribution over the alumina support.

5.3.1.3. On-stream performance of the catalyst

The stability of a catalyst under the reaction conditions has great significance once approaching commercialization. Hence, the time on stream study of the best catalyst is executed at optimized reaction temperature; 600 °C. **Fig. 5.3** further depicts the long term performance of AgMesoFeAl and it is perceived that at an early time on stream, the conversion is 30 % with high selectivity for DH reaction. Gradually, isobutane conversion improves over 4 h of reaction time and correspondingly the selectivity for isobutene decreases. The highest performance is achieved as 32 % isobutene selectivity and 36 % conversion of isobutane under the studied conditions. After 4 h, the catalytic activity decreases to 30 % conversion as well as 30 % selectivity over the analysis time. Afterwards,

this activity remained constant after 10 h. Followed by this initial phase, nearly stable activity is maintained up to 60 h.

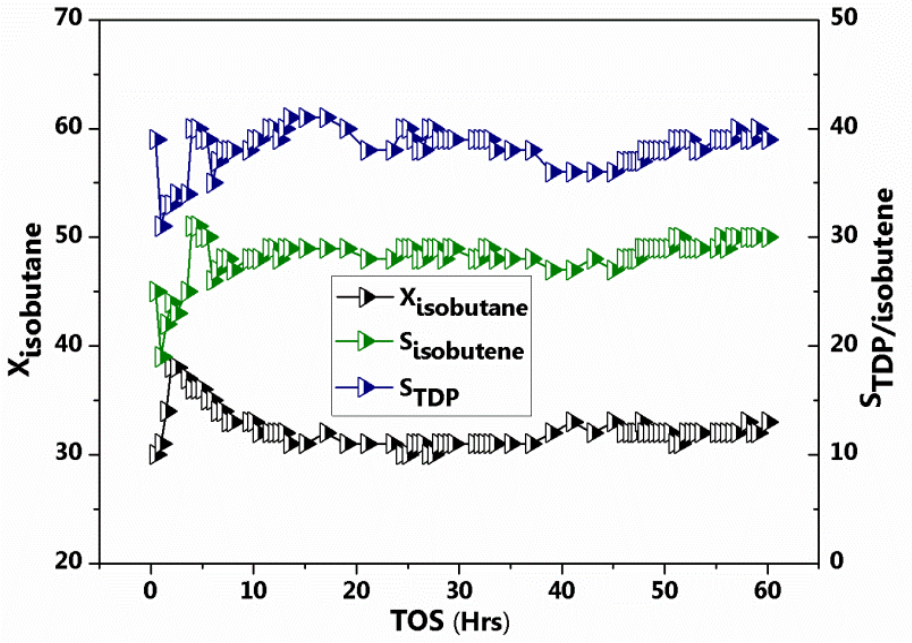

Fig. 5.3 Time on-stream performance of AgMesoFeAl for DHisoB
Reaction conditions: 300 mg catalyst, 600 °C, i–C_4/Ar=1, GHSV=400 h^{-1} with respect to total feed.

The main significance of the present work is the maintenance of overall product yields over 60 h under the drastic reaction conditions. Additionally, here DH is practiced with a low space velocity. Major reasons for the decrease in activity after 10 h and the maintenance of isobutene yield will be explained in the material characterization section based on the particle distribution and carbon deposition on the catalyst.

5.3.2. Material characterization

All synthesized mesoporous alumina catalysts are well studied for the structural, textural properties and surface morphology to establish the correlation between activity and material characteristics. The instrumental description is explained in **Section 2.5**.

5.3.2.1. Textural properties

Textural features of the calcined promoted catalysts and pure MesoAl support are depicted in **Fig. 5.4**. Total BET surface area (S_{BET}), pore volume (V_p), and average pore-size values were calculated and presented in **Table 5.1**. According to the IUPAC classification system, the N_2-sorption isotherms given in **Fig. 5.4a** indicate type IV isotherms with H1 hysteresis loop typical of mesoporous materials. However, FeMesoAl possesses slight features of the H_2 loop

with wide pore size distribution. These are characteristic of bottlenecked pores [20]. A close analysis of isotherms of the promoted catalysts proves that even after the impregnation process, the materials retained mesoporosity. Pore size distribution curves derived from the N_2-desorption process shown in **Fig. 5.4b** also supports the presence of mesopores. Additionally, it may be mentioned here that small pores are unfavourable for the migration of coke deposited from the active sites towards the acidic sites [21].

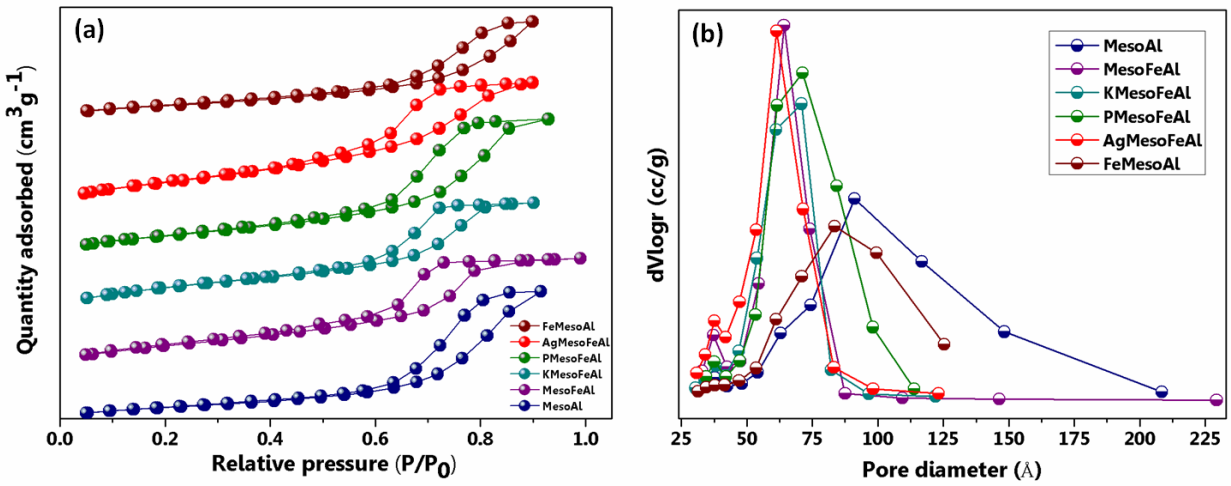

Fig. 5.4 (a) N_2-adsorption-desorption isotherms and (b) pore size distributions of as-synthesized samples.

Table 5.1 Textural and chemical properties of the mesoporous alumina catalysts

Catalyst	**S_{BET}[a] (m^2 g^{-1})**	**V_p[a] (cc g^{-1})**	**D_p[a] (Å)**	**Acidic amount[b] (mmol g^{-1})**	**H_2 consumption[c] (mmol g^{-1})**	**Coke deposition[d] (%)**
MesoAl	162	0.407	100.1	0.02	0.23	7.2
MesoFeAl	259	0.378	58.3	0.34	0.86	16.2
KMesoFeAl	301	0.388	51.6	0.21	0.06	15.9
PMesoFeAl	247	0.459	74.4	0.25	0.14	12
AgMesoFeAl	287	0.424	59.1	0.32	1.49	12.7
FeMesoAl	153	0.32	83.4	0.07	2.21	26.6
AgMesoFeAl-TOS	-	-	-	-	-	14.4

[a]Calculated from N_2-sorption isotherms.
[b]Determined from NH_3-TPD results.
[c]Quantified from H_2-TPR data.
[d]Measured by TGA in presence of air.

All mesoporous materials exhibited an appreciable specific surface area. Surprisingly, the total surface area of MesoAl increases after Fe doping. However, iron impregnation on mesoporous alumina support may block the pores of FeMesoAl sample in the rich presence

of iron oxide resulting in a slight reduction in surface area from 162 to 153 m^2 g^{-1} [22]. The average pore diameter (D_p) considerably decreases in the synthesized catalysts compared to the pristine support MesoAl due to the entering of the active metal species into the pore channels. The uniform mesoporous structure and noticeably large pore volume of these materials can significantly contribute to catalytic activity. AgMesoFeAl has a remarkable surface area with optimum pore dimensions compared to other samples which make this catalyst a perfect applicant for the non-oxidative DH reaction.

5.3.2.2. Structural properties

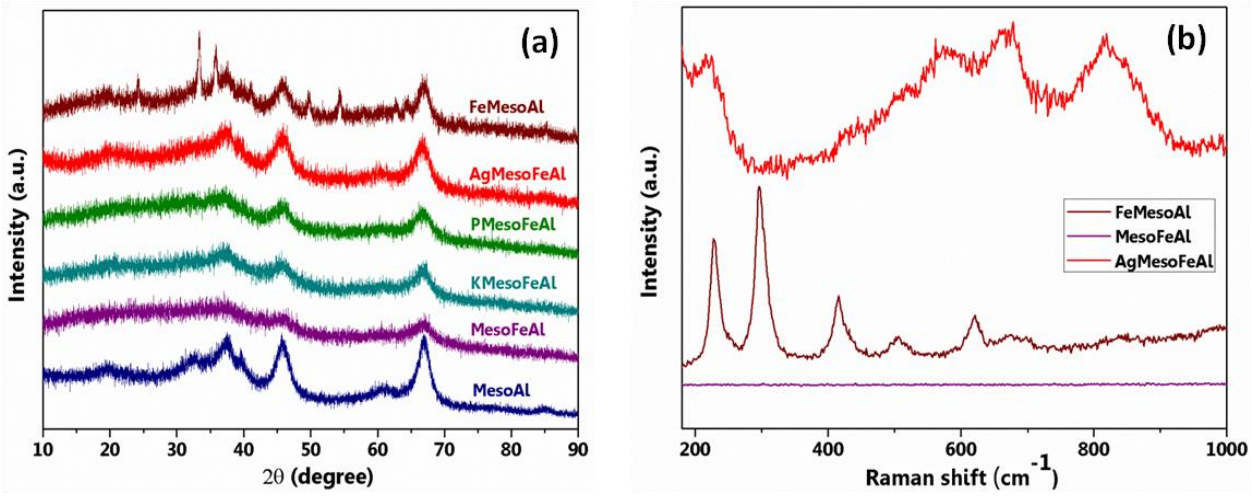

Fig. 5.5 (a) X-ray diffraction patterns and (b) Raman spectra of the materials

Fig. 5.5a presents the diffractograms of the synthesized mesoporous alumina-based catalysts. The diffraction pattern of all samples indicated the formation of γ-Al_2O_3 phase with JCPDS card no. 10-0425. The reflections observed at 31.9, 37, 39.5, 45.9, 60.5 and 67 ° are attributed to the diffraction planes (220), (311), (222), (400), (440) and (511) respectively [23]. For MesoFeAl, no peak linked to iron is found suggesting high dispersion of Fe during the *in situ* synthesis and the formed iron oxide domains are too small to be detected. However, Fe is indeed detected in XPS and elemental mapping analysis. Moreover, Kobayashi *et. al.* reported that at low content; Fe_2O_3 can form a solid solution with γ-Al_2O_3 [10]. Although, the iron impregnated sample FeMesoAl exhibited peaks at 2θ values 24.3, 33.3, 35.9, 41.1, 49.6, 54.3, 57.6, 57.9, 62.7, and 64.4 ° corresponding to α-Fe_2O_3 phase (JCPDS card no. 33-0664). This observation stipulates that only diminutive amount of Fe is doped in the alumina framework and also iron oxide species are poorly dispersed on mesoporous alumina support due to the *ex situ* synthesis method. The excess amount of Fe would oxidize in the air during the calcination process to form iron oxide and separately crystallizes on the surface.

When promoters are added in the MesoFeAl sample, the corresponding peaks are not identified due to the high dispersion of those species on the alumina matrix. Except in FeMesoAl, a small shift in the diffraction angle to lower 2θ values is noticed in all solids compared to the pristine support MesoAl. This could be because of the changes occurred in the lattice parameters which might arise from the proper doping of elements into the aluminium site [24]. The difference in ionic radii of Fe^{3+} (0.645 Å) and Al^{3+} (0.535 Å) might cause the broadening of γ-Al_2O_3 reflections. Compared to other materials, AgMesoFeAl best resembled in crystalline structural features with MesoAl proving the perfect incorporation of Fe and Ag and could be a reason for the observed highest activity. No silver oxide peaks are found in this sample, because of the very small size and greater dispersion in the MesoFeAl matrix. Hence, it can be concluded that stable phases of Fe_2O_3 and Al_2O_3 are formed in the studied catalysts after sintering at high calcination temperature.

Further examination of the structural and crystalline properties to support PXRD results is conducted with Raman analysis of the annealed samples. **Fig. 5.5b** shows the Raman spectra of FeMesoAl, MesoFeAl, and AgMesoFeAl samples. FeMesoAl revealed peaks at 228 as well as 504; and 247, 297, 416, as well as 620 cm^{-1} corresponding to A_{1g} and E_g modes of α-Fe_2O_3 respectively. Additionally, some rare Raman peaks reported by a few researchers for the hematite phase are also identified at 669 and 836 cm^{-1} [25]. Surprisingly, MesoFeAl does not exhibit a single peak attributing to iron oxide demonstrating either high dispersion of Fe in alumina matrix or undetectable in Raman analysis. This observation further supports PXRD and HRTEM studies.

5.3.2.3. Catalyst morphology

Material morphology and proper dispersion of the elements contribute to a great extent towards the catalytic performance. Hence, the optimized catalyst is analyzed with TEM, and the images collected were shown in this section. The bare support, MesoAl is shown in **Fig. 5.6a**. The TEM results (**Fig. 5.6** and **5.7**) exhibited a mesoporous structure supporting the data obtained from BET analysis. A sheet-like morphology is visible for the fresh AgMesoFeAl catalyst (**Fig. 5.7a**) with evenly distributed metal nanoparticles. High-resolution TEM analysis provided well-resolved lattice fringes with 0.2 nm spacing characteristic of the interplanar distance of (104) plane of the α-Fe_2O_3 phase. The SAED pattern of this sample with concentric rings and bright spots represented typical of a nanocrystalline material with an average particle size measured 5.6 nm.

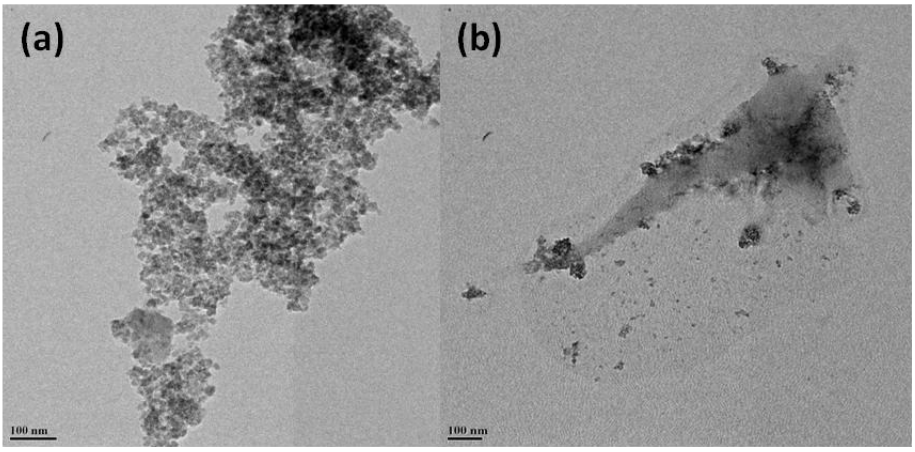

Fig. 5.6 TEM images of (a) MesoAl and (b) FeMesoAl

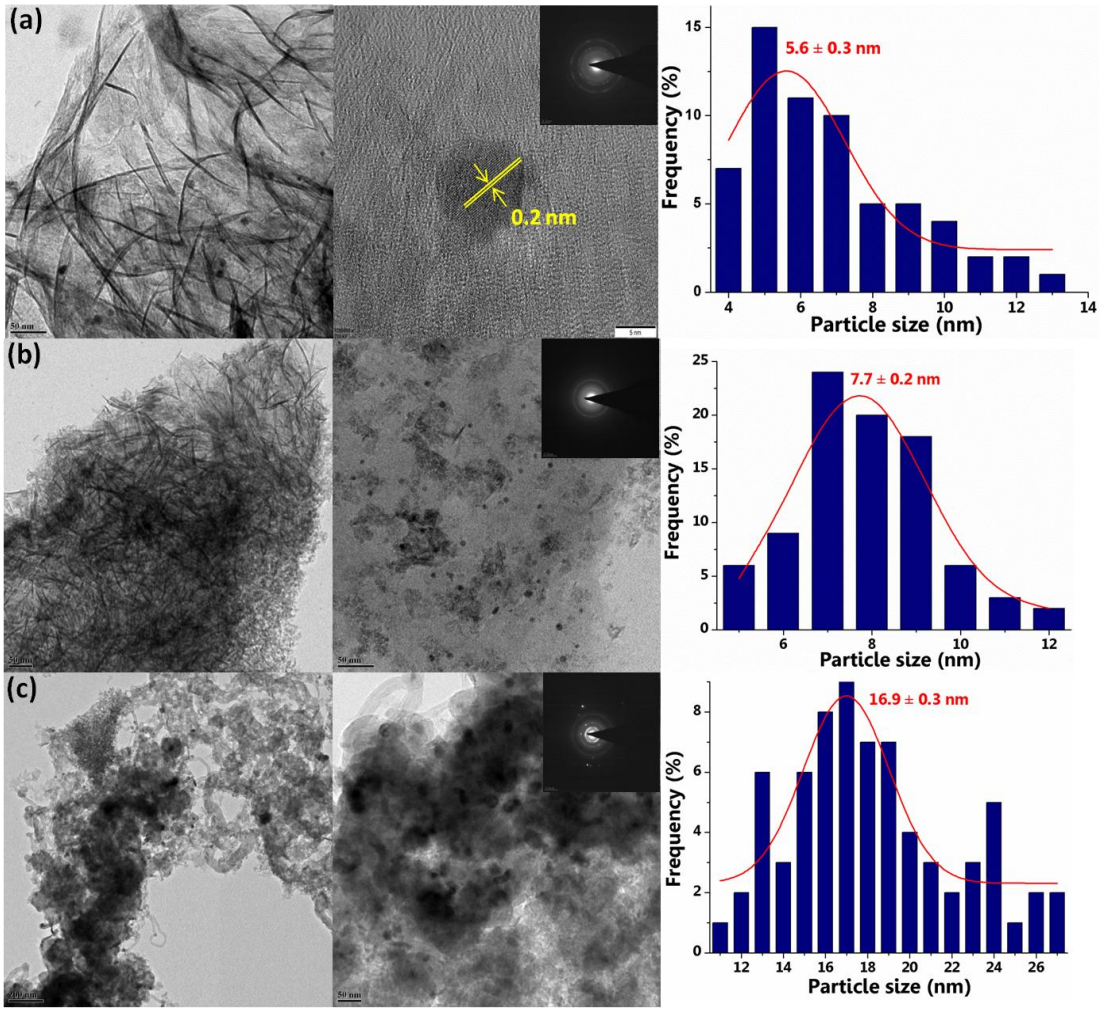

Fig. 5.7 TEM images, SAED pattern and particle size distribution of (a) AgMesoFeAl- Fresh, (b) AgMesoFeAl- after 6 h and (c) AgMesoFeAl- after TOS study.

Agglomeration and small clusters of iron oxide particles on the surface were observed in FeMesoAl as represented in **Fig. 5.6b** demonstrating poor dispersion of the material proving the PXRD results. This could be due to the different synthesis strategies adopted for this material. Therefore, all other catalysts are superior to FeMesoAl in the studied selective DH

reaction. On the other hand, AgMesoFeAl exhibited better dispersion of metal nanoparticles which can contribute to catalytic activity. Elemental mapping of fresh AgMesoFeAl as a respect for its best catalytic properties is performed using HRTEM and the results are shown in **Fig. 5.8**. The images revealed uniform distribution of the elements over the surface and can be correlated to the corresponding PXRD studies.

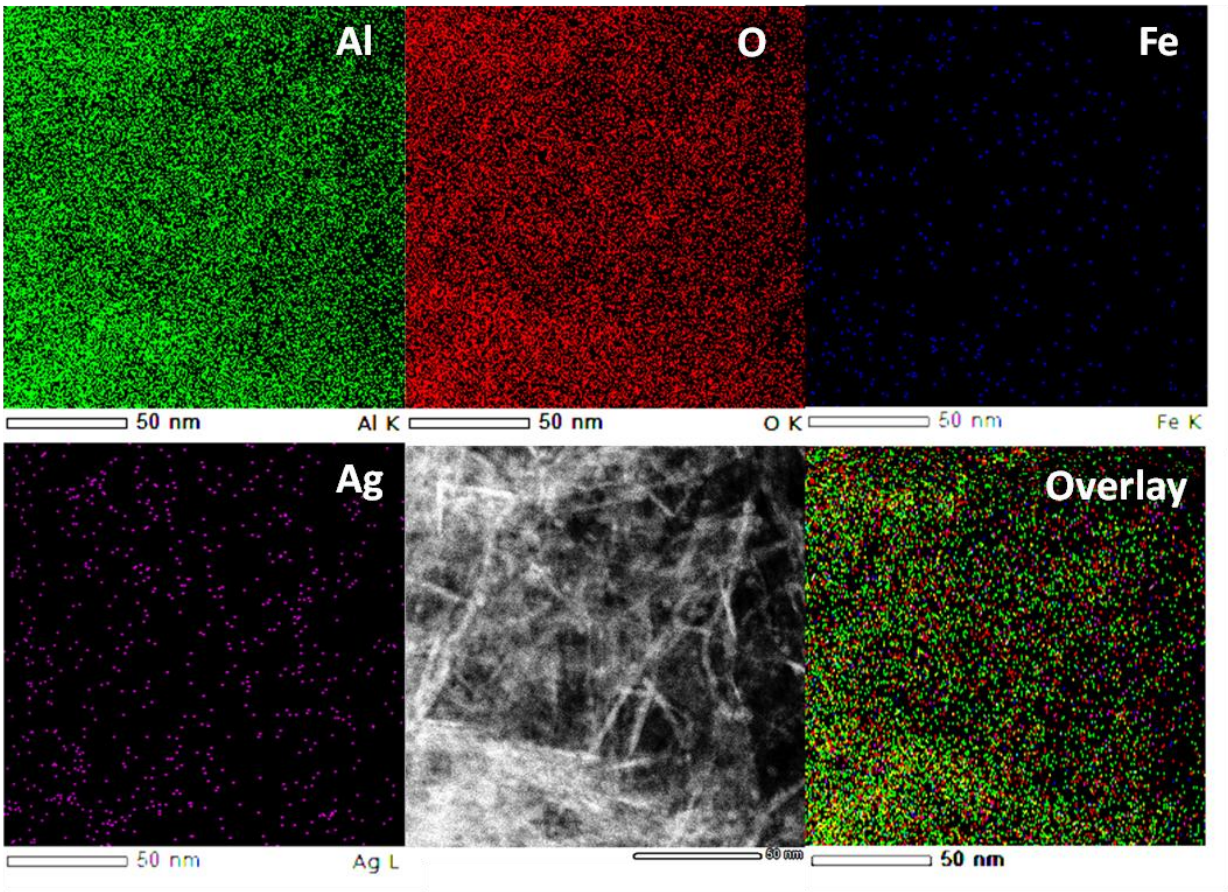

Fig. 5.8 HR-TEM mapping images of fresh AgMesoFeAl

SEM analysis is used to determine the surface morphology of the catalyst and it do not exhibited any particular morphology as represented in **Fig. 5.9**. The particle shape remained the same before and after the non-oxidative DH reaction. The EDX data also confirms the presence of all elements in the catalyst. No elements other than Ag, Fe, Al, and O are present which signify very good purity of the sample. Therefore, the proper dispersion of active metal species on the mesoporous alumina matrix can facilitate the DH activity. These observations declare the proper incorporation of Fe in alumina consistent with PXRD analysis.

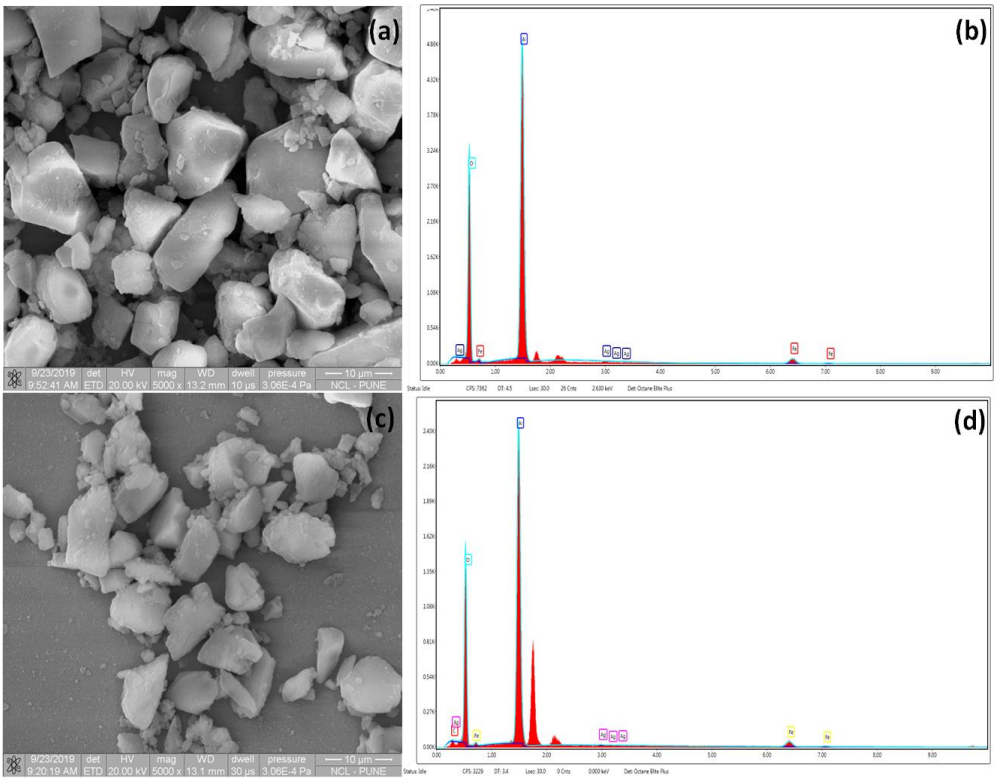

Fig. 5.9 (a, c) SEM images and (b, d) EDX spectra of fresh and spent AgMesoFeAl respectively.

5.3.2.4. Acidic properties

Acid basic properties of the materials are crucial in defining the catalytic activity. In view of this, temperature-programmed desorption experiments are conducted with NH_3 as probe molecule to measure the amount of acid sites present in the catalysts. The uptake of NH_3 is propotional to this value. The TPD profiles are given in **Fig. 5.10a** and the acidity values measured are represented in **Table 5.1**. According to the existing works from the literature, the samples exhibit two major peaks at around 150 and 450 °C corresponding to NH_3 desorbed from the weak and medium Lewis acidic sites respectively [26]. It is observed from the TPD profile and the acidic strength values given in **Table 5.1** that bare support MesoAl (0.02 mmol/g) and FeMesoAl (0.07 mmol/g) are least acidic in nature. Iron doping to MesoAl has considerably improved the acidity to 0.34 mmol/g.

As reported by Carvalho *et. al.*, strong acid sites cause hydrogenolysis of alkenes [18] which are absent in the studied materials. Isobutane mainly activates on the acidic centres promoting the conversion. On the other hand, desorption of isobutene may inhibit at the medium and strong acidic centres which can promote the cracking reactions [21]. The *in situ* Fe-doped catalysts show a comparable amount of medium acidic sites which matches well with the

activity trend proving the role of catalyst acidity. The ratio between the number of active metal sites to the number of acidic sites has a great role in defining catalytic performance. AgMesoFeAl might have the optimum amount of acidic sites among all which can contribute to its highest activity for DH reaction.

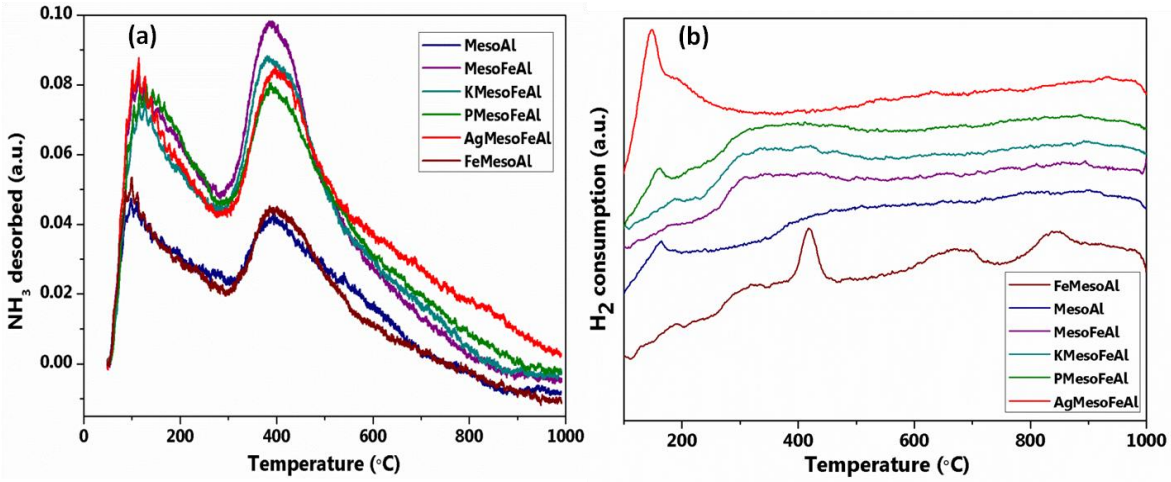

Fig. 5.10 (a) NH_3-TPD and (b) H_2-TPR profiles of the calcined catalysts

5.3.2.5. Reducibility of the catalysts

The redox properties of the catalysts are another factor affecting the catalyst performance. Therefore, the synthesized materials are measured with H_2 probed temperature-programmed reduction analysis. Under the reducing atmosphere, the amount of consumed hydrogen for all sintered catalysts is quantified from the TPR profiles given in **Fig. 5.10b** and tabulated in **Table 5.1**. AgMesoFeAl exhibited the highest H_2 consumption among the promoted catalysts (1.49 mmol/g); due to the additional reduction of silver oxide which occurs at low temperatures. Except in FeMesoAl, no other materials demonstrate reduction peaks correspond to the iron oxides proving the high dispersion of these species on alumina. On the contrary, the sample FeMesoAl is reduced in different steps as $Fe_2O_3 \rightarrow Fe_3O_4 \rightarrow FeO \rightarrow Fe$ [27, 28]. The peak broadening is detected due to the multistep reduction. Easily reducible silver oxides make AgMesoFeAl favourable for high-temperature dehydrogenation.

5.3.2.6. XPS study

To understand the surface species involved, XPS analysis is conducted *ex situ* for the fresh and spent catalysts and the results are represented in the given figures. All spectra are BE shifted by carbon correction using the C 1s core level value of adventitious carbon on the surface as 284.8 eV. Spectra recorded for Ag 3d (**Fig. 5.11a**) exhibited main peaks at 367.8

and 373.7 eV constitute for $3d_{5/2}$ and $3d_{3/2}$ of Ag_2O in Ag^+ state [29]. The presence of AgO cannot be rejected or confirmed owing to its high instability under ultra-high vacuum [30]. Al 2p spectra given in **Fig. 5.12a** contained $2p_{3/2}$ peak at 74.5 eV assigned to Al^{3+} in mesoporous alumina [31]. XPS peak appeared at 78 eV is attributed to anhydride Al_2O_3 [32]. The doping of metal into alumina lattice can affect the chemical states of Al and O and the binding energy values may be changed [33].

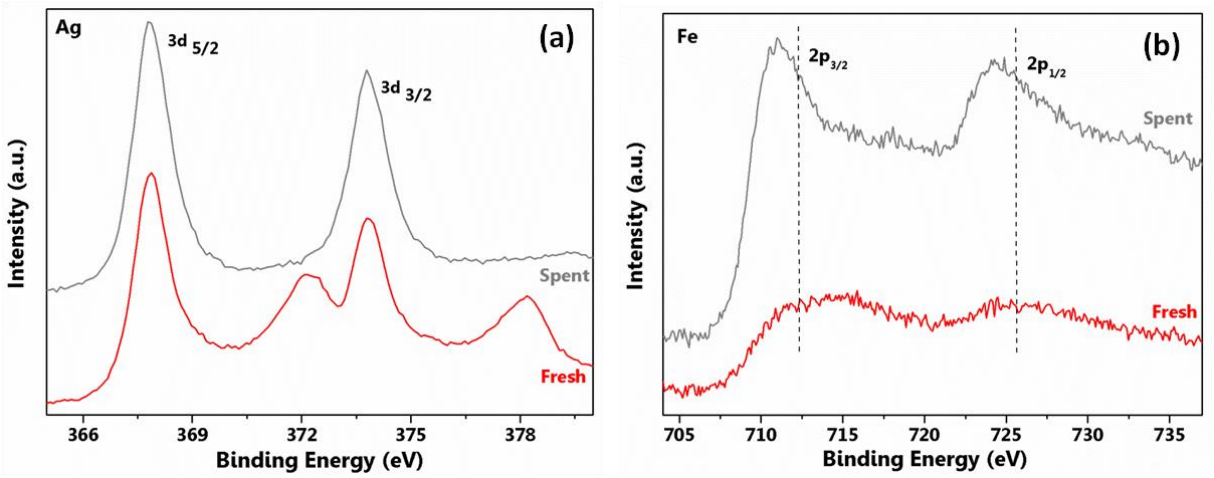

Fig. 5.11 XPS spectra of (a) Ag 3d and (b) Fe 2p core levels

O 1s level XPS spectra recorded is shown in **Fig. 5.12b** for the samples before and after reactions. A major broad peak at lower BE value 530 eV represents the lattice oxygen collectively contributed from all metals. The surface Al–O species will be present at around 531.4 eV. Subsurface O species form silver may also contribute towards this peak [34]. The isolated –OH groups give rise to a peak at 532.7 eV [35]. It is well known that any chemisorbed oxygen species like water molecules appear at higher BE. These values fall in slightly higher regions compared to the reported data. A close inspection of Fe 2p core-level spectra of fresh AgMesoFeAl in **Fig. 5.11b** hints the presence of $2p_{3/2}$ at BE 712 eV accompanied by satellite peak located at 720 eV [36]. A small peak shift observed indicate that the catalyst surface is reduced after the reaction.

Silver oxide can be reduced to metallic silver under the high-temperature DH atmosphere in the presence of isobutane. Probably the Ag^0 would drive the reaction. But no peaks correspond to Ag metal were detected in XPS may be due to its high susceptibility for atmospheric oxidation. Interestingly, phenomena called voltage induced differential charging happen in the core level spectra of the studied samples. Consequently, distortion of emission

peaks and shift of the measured position of the peaks corresponding to the core levels occurs. This is usually observed on the non-uniformly conducting sample surface [37].

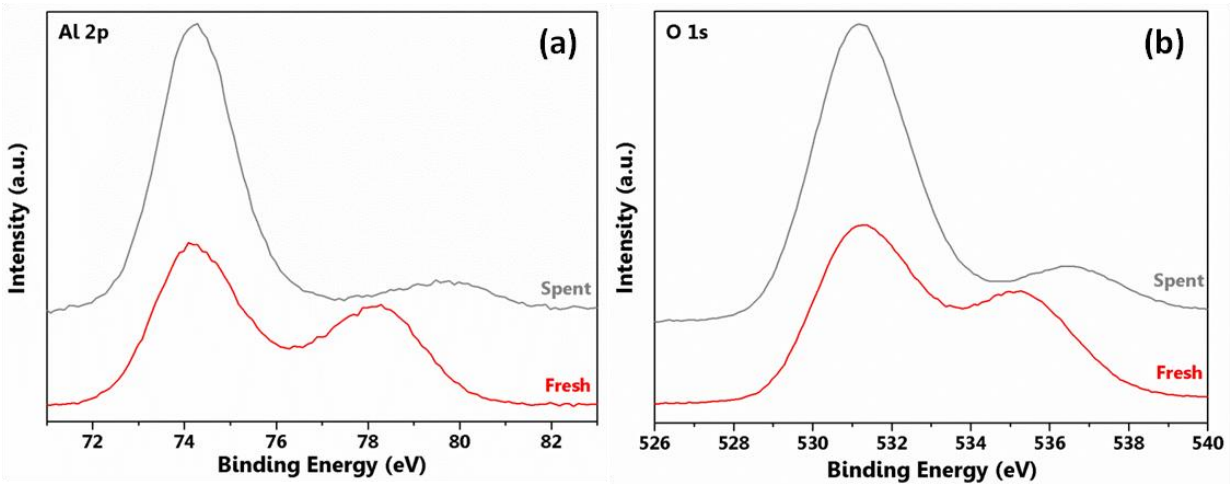

Fig. 5.12 XPS spectra of (a) Al 2p and (b) O 1s core levels

5.3.2.7. Post reaction analysis

Post reaction analysis of the catalysts was carried out to discover the structural and chemical changes occurred during the high-temperature isobutene synthesis. The X-ray diffraction patterns of all catalysts after the reaction are collected and given in **Fig. 5.13a**. The crystallinity of the samples remained intact even after the reaction at 600 °C. Crystalline phases are analyzed after 6 as well as 60 h of DHisoB at the optimized reaction parameters and presented in **Fig. 5.13b**.

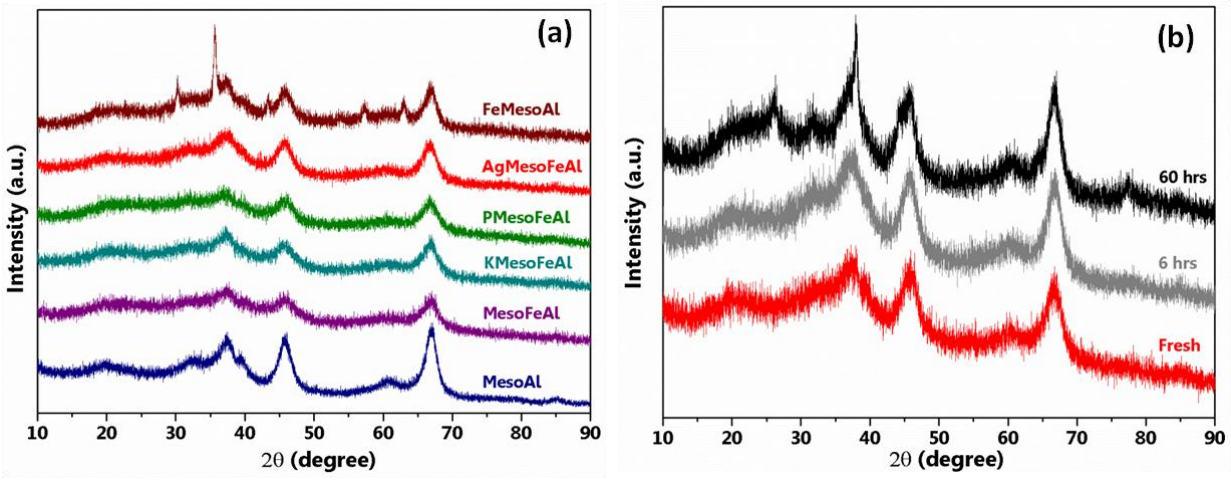

Fig. 5.13 PXRD patterns of the spent catalysts

TEM images of spent AgMesoFeAl catalyst are recorded to study the changes occurred in the catalyst morphology. The material retained sheet-like structure and the mesoporous structure even after 6 h of dehydrogenation reaction at 600 °C with a small increment in particle size to

7.7 nm as depicted in **Fig. 5.7b**. Also, slightly bigger particles are observed in the TEM image. However, after 60 h of TOS study more agglomerated metal particles are seen in **Fig. 5.7c** and the average particle size is increased to 16.9 nm. The SAED pattern given in the inset corroborated the separation of crystalline metal oxides and is also distinctly perceived from the XRD pattern of the AgMesoFeAl-TOS sample presented in **Fig. 5.13**. Moreover, thermogravimetric analysis in presence of air quantified 14.4 % coke deposition on the catalyst after on-stream analysis (T**able 5.1**) which is observed as carbon nanotubes in the TEM images depicted in **Fig. 5.7c**. Close analysis of the TEM images illustrates some of the active metal particles are entrapped in the nanotubes which would also be a reason for the activity decrease. A Raman spectrum of this sample shown in **Fig. 5.14a** is confirmed the formation of both sp^2 and sp^3 hybridized carbon formed during the high-temperature DH process. This coke formation mainly leads to slight deactivation of AgMesoFeAl over the 60 h of stability test. However, the material maintained mesoporosity throughout the reaction.

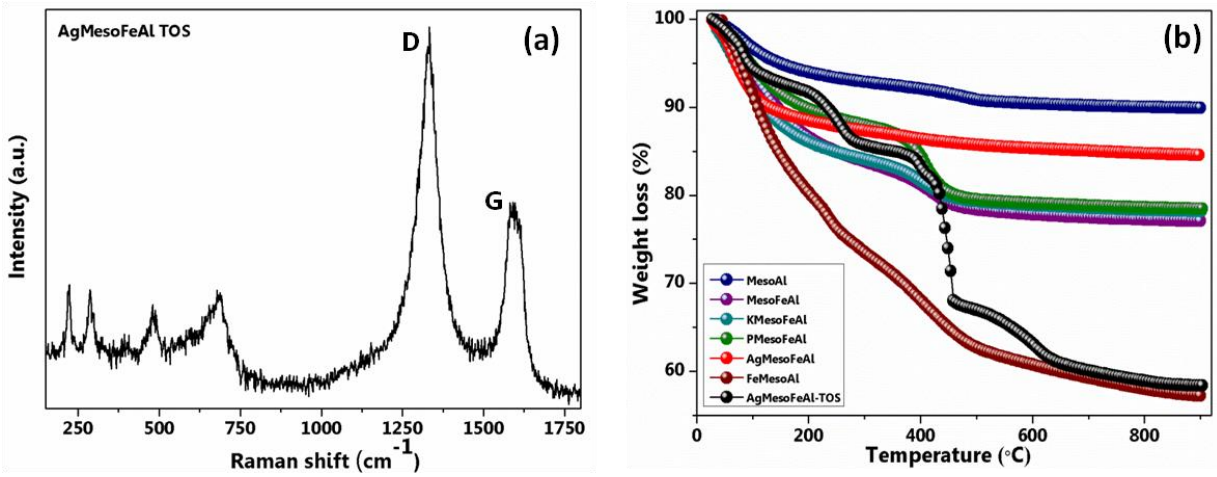

Fig. 5.14 (a) Raman spectra of AgMesoFeAl-TOS and (b) thermograms of spent catalysts

Coke formation is one of the chief concerns involved in DHisoB at high temperatures. The type of coke formed and the blocking of active sites after coke deposition can cause severe catalyst deactivation. Hence, AgMesoFeAl spent catalyst after 60 h of on stream study is investigated with Raman spectroscopy to study the nature of coke. The spectrum is given in **Fig. 5.14a** proved the presence of D and G bands at 1330 and 1590 cm^{-1} respectively attributed to the disordered and pristine graphene bands [38]. In addition to this, peaks correspond to Fe_2O_3 are also emerged which were not visible in the fresh catalyst. These observations could be correlated to PXRD and TEM results evidencing phase separation as well as carbon deposition happening on the catalyst surface which leads to the deactivation on the catalyst during TOS analysis.

Since, carbon formation is observed as the main reason for catalyst deactivation; the quantification of coke deposited over the spent catalyst becomes inevitable. Therefore, thermogravimetric analysis is carried out for all spent catalyst after the reaction and depicted in **Fig. 5.14b**. The thermogram of AgMesoFeAl-TOS after on stream DHisoB reaction is also represented. The amount of coke for each spent catalyst is quantified at 300 °C and tabulated in **Table 5.1**. The pristine support MesoAl exhibited least coke deposition which might be due to the less C–C cracking reactions occurred during DH reaction. The table clearly shows PMesoFeAl (12 %), as well as AgMesoFeAl (12.7 %) materials; have lower coke compared to other promoted catalysts. Highest C–C cracking occurred on FeMesoAl (26.6 % coke) which is more than AgMesoFeAl after 60 h TOS study (14.4 %) and MesoFeAl (16.2 %).

These observations illustrated the importance of *in situ* Fe doping in alumina and Ag promotion of the materials. The results obtained from TG analysis could be directly correlated to the DHisoB reaction trend. FeMesoAl exhibited very low isobutene yield due to the cracking of formed alkene under severe reaction conditions. Therefore, maximum carbon deposition is calculated for this sample. Additionally, sometimes carbon deposition can also contribute to maintaining the alkene selectivity through deactivating the extreme active sites [39]. This can also be positively connected to the reaction results where the activity is maintained on the carbon nanotubes in TOS study.

5.4. Conclusions

In summary, mesoporous alumina-based catalysts synthesized by the sol-gel method along with the material characterization correlated to their activity performance for non-oxidative DH delivered essential insights to the synthesis of isobutene. The overall yield of isobutene over these catalysts was improved after promoting the selected chemical species. The proper doping of iron in the alumina matrix and the optimum surface acidity are viewed as the chief properties to inhibit cracking reactions and thus affecting isobutene selectivity. The optimized catalyst was proven to have the best doping of iron oxide with the highest dispersion of active metal species. The catalyst surface was reduced after the reaction. Particle agglomeration followed by carbon nanotube development has occurred over the continuous gas phase high-temperature dehydrogenation reaction and isobutene formation is slightly hindered. To conclude, Ag promoted catalyst present appreciable activity and can be a promising catalyst for the DHisoB.

References

[1] H. Zhao, H. Song, L. Xu, L. Chou, Appl. Catal. A Gen. 456 (2013) 188–196.

[2] M.A. Centeno, M. Debois, P. Grange, J. Catal. 192 (2000) 296–306.

[3] O.O. James, S. Mandal, N. Alele, B. Chowdhury, S. Maity, Fuel Process. Technol. 149 (2016) 239–255.

[4] https://www.databridgemarketresearch.com/reports/global-isobutene-market

[5] Randy D. Cortright, Josephine M. Hill, James A. Dumesic Catal. Today 55 (2000) 213–223.

[6] U. Rodemerck, S. Sokolov, M. Stoyanova, U. Bentrup, D. Linke, E. V Kondratenko, J. Catal. 338 (2016) 174–183.

[7] Y. Zhang, Y. Zhou, J. Shi, S. Zhou, X. Sheng, Z. Zhang, S. Xiang, J. Mol. Catal. A: Chem. 381 (2014) 138–147.

[8] J.J.H.B. Sattler, J. Ruiz-Martinez, E. Santillan-Jimenez, B.M. Weckhuysen, Chem. Rev. 114 (2014) 10613–10653.

[9] G.J. Siri, M.L. Casella, G.F. Santori, O.A. Ferretti, Ind. Eng. Chem. Res. 36 (1997) 4821–4826.

[10] S. Kobayashi, S. Kaneko, M. Ohshima, H. Kurokawa, H. Miura, Appl. Catal. A Gen. 417–418 (2012) 306–312.

[11] Y. Fu, H. Ma, Z. Wang, W. Zhu, T. Wu, G. Wang, J. Mol. Catal. A Chem. 221 (2004) 163–168.

[12] A.N. Matveyeva, N.A. Zaitseva, P. Mäki-Arvela, A. Aho, A.K. Bachina, S.P. Fedorov, D.Y. Murzin, N.A. Pakhomov, Ind. Eng. Chem. Res. 57 (2018) 927–938.

[13] U. Rodemerck, E. V Kondratenko, T. Otroshchenko, D. Linke, Chem. Commun. 52 (2016) 12222–12225.

[14] H. Armendáriz, A. Guzmán, J.A. Toledo, M.E. Llanos, A. Vázquez, G. Aguilar-Ríos, Appl. Catal. A Gen. 211 (2001) 69–80.

[15] M.L. Casella, G.J. Siri, G.F. Santori, O.A. Ferretti, M.M. Ramírez-Corredores, Langmuir. 16 (2000) 5639–5643.

[16] S.R. de Miguel, S.A. Bocanegra, I.M.J. Vilella, A. Guerrero-Ruiz, O.A. Scelza, Catal. Letters. 119 (2007) 5–15.

[17] W. Kania, K. Jurczyk, Appl. Catal. 34 (1987) 1–12.

[18] L.S. Carvalho, C.L. Pieck, M.C. Rangel, N.S. Fígoli, C.R. Vera, J.M. Parera, Appl. Catal. A Gen. 269 (2004) 105–116.

[19] A.L. Jones, Solon, R.M. Benslay, Northfield, Ohio, assignors to The Standard Oil Company, Cleve Land, Ohio, Dehydrogenation of hydrocarbons employing a catalyst of iron oxide-containing activated carbon, US3647910A, 1972.

[20] S. Tan, B. Hu, W.-G. Kim, S.H. Pang, J.S. Moore, Y. Liu, R.S. Dixit, J.G. Pendergast, D.S. Sholl, S. Nair, C.W. Jones, ACS Catal. 6 (2016) 5673–5683.

[21] S. Luo, N. Wu, B. Zhou, S. He, J. Qiu, C. Sun, J. Fuel Chem. Technol. 41 (2013) 1481–1487.

[22] X. Zhang, G. Dou, Z. Wang, L. Li, Y. Wang, H. Wang, Z. Hao, J. Hazard. Mater. 260 (2013) 104–111.

[23] W.-Z. Li, L. Kovarik, D. Mei, J. Liu, Y. Wang, C.H.F. Peden, Nat. Commun. 4 (2013) 2481.

[24] W. Zhao, X. Zheng, S. Liang, X. Zheng, L. Shen, F. Liu, Y. Cao, Z. Wei, L. Jiang, Green Chem. 20 (2018) 4645–4654.

[25] F.J. Pérez-Alonso, M.L. Granados, M. Ojeda, T. Herranz, S. Rojas, P. Terreros, J.L.G. Fierro, M. Gracia, J.R. Gancedo, J. Phys. Chem. B. 110 (2006) 23870–23880.

[26] J. Sun, R.A.L. Baylon, C. Liu, D. Mei, K.J. Martin, P. Venkitasubramanian, Y. Wang, J. Am. Chem. Soc. 138 (2016) 507–517.

[27] P. Michorczyk, P. Kuśtrowski, L. Chmielarz, J. Ogonowski, React. Kinet. Catal. Lett. 82 (2004) 121–130.

[28] G. Munteanu, L. Ilieva, D. Andreeva, Thermochim. Acta. 291 (1997) 171–177.

[29] T.C. Kaspar, T. Droubay, S.A. Chambers, P.S. Bagus, J. Phys. Chem. C. 114 (2010) 21562–21571.

[30] D. Lützenkirchen-Hecht, H.-H. Strehblow, Surf. Interface Anal. 41 (2009) 820–829.

[31] J.S. Lee, H.S. Kim, N.-K. Park, T.J. Lee, M. Kang, Chem. Eng. J. 230 (2013) 351–360.

[32] A. Barrera, F. Tzompantzi, J. Campa-Molina, J.E. Casillas, R. Pérez-Hernández, S. Ulloa-Godinez, C. Velásquez, J. Arenas-Alatorre, RSC Adv. 8 (2018) 3108–3119.

[33] X. Zhang, B. Deng, T. Sun, W. Li, C. Duan, Nanoscale Res. Lett. 12 (2017) 392.

[34] A.I. Boronin, V.I. Bukhityarov, A.L. Vishnevskii, G.K. Boreskov, V.I. Savchenko, Surf. Sci. 201 (1988) 195–210.

[35] I. Lorite, M.S. Martín-González, J.J. Romero, M.A. García, J.L.G. Fierro, J.F. Fernández, Ceram. Int. 38 (2012) 1427–1434.

[36] A. Miyakoshi, A. Ueno, M. Ichikawa, Appl. Catal. A Gen. 219 (2001) 249–258.

[37] S.L. Bergman, G.S. Sahasrabudhe, H. Ji, R.J. Cava, S.L. Bernasek, Chem. Mater. 29

(2017) 4162–4166.

[38] Z. Zhao, Y. Dai, J. Mater. Chem. A. 2 (2014) 13442–13451.

[39] Y. Zhang, Y. Zhou, L. Wan, M. Xue, Y. Duan, X. Liu, Fuel Process. Technol. 92 (2011) 1632–1638.

Chapter-6

Summary and Conclusions

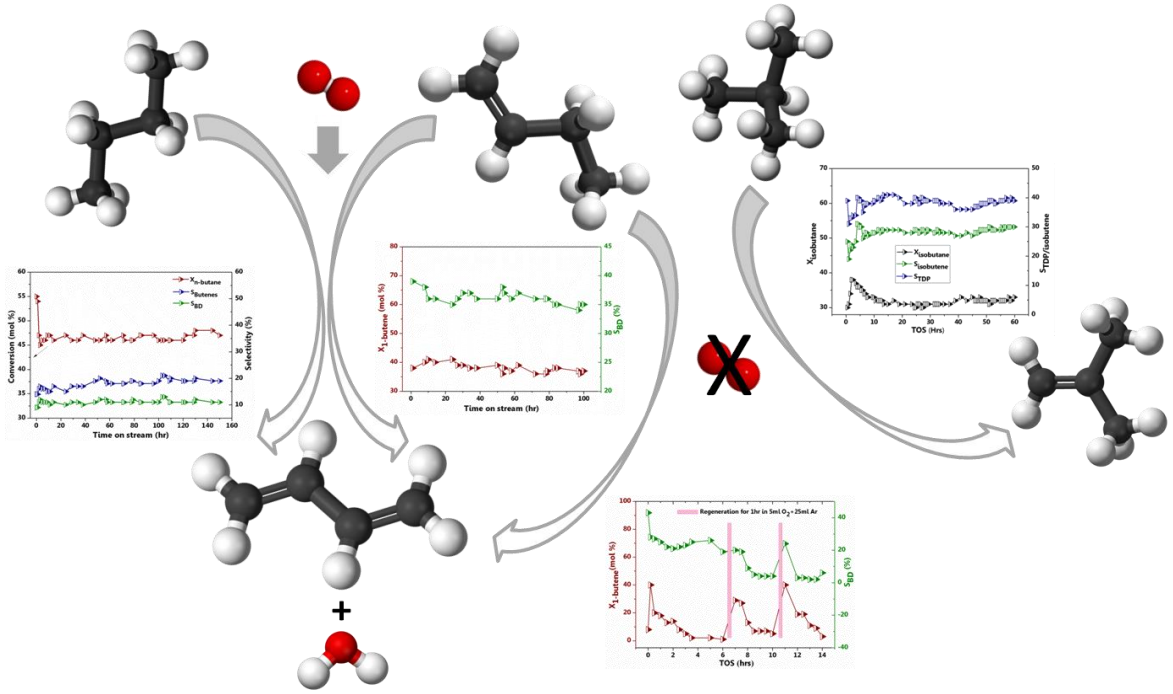

Reaction	**ODH of n-butane**		**ODH of 1-butene**		**DH of isobutane**
Catalyst system	**xBMO; x = 0.1, 1, 5, 10, 25 and 50**	**yV5BMO; y = 1, 5, 9, 13, 17, 21 and 25**	**$M1_xBi_{1-x}FeO_3$ and $BiM2_xFe_{1-x}O_3$; M1=Cu, Ni, Zn M2=Co, Mn, Cr**	**$CeFeO_x$**	**Fe-mesoporous alumina (promoted with K, P, Ag)**

6.1. Summary of the thesis

This chapter summarizes the complete details of the research work covered for this thesis. The background of the scientific problem, various experimental measures executed towards the solution and the key results achieved from the study are briefly delivered. The thesis has undertaken three different reactions for the lab-scale production of industrially important monomers such as n-butenes, BD and isobutene using particular catalyst systems. The concise summary of each chapter is given.

***Chapter 1**: Introduction*

The basic definition of catalyst and heterogeneous catalysis are stated in the introduction part. The importance of selective activation of alkanes particularly C_4 hydrocarbons is analyzed through past and present industrial trends. The market size and worldwide demand of C_4 olefins such as; BD and isobutene are quoted from the industry reports. It is elaborated that the existing production methods should shift to more cost-effective and secure process like ODH. The scientific characteristics of this method are widely discussed citing previous literatures. A thorough study of the research background allows concluding the selection criteria of perfect catalysts for the selective conversion of C_4 hydrocarbons.

***Chapter 2**: Catalyst synthesis and characterization*

The basic norms furnished from the literature survey are followed to design suitable catalytic systems. The synthesis approach for V-Mg-B oxides, bismuth ferrites, Ce-Fe oxide and mesoporous alumina are broadly explained and listed in this chapter. The theory and instrumental configuration for the characterization techniques like PXRD, BET analysis, microscopy, spectroscopy, thermal methods etc., are briefly described. Reactor specifications and analysis methodology adopted are also elaborated.

***Chapter 3**: Enhanced catalytic activity of boron-containing MgO on vanadium loading for the oxidative dehydrogenation of n-butane*

In this chapter, ODH of n-butane to BD was investigated over B-containing MgO systems synthesized by citrate gel combustion method and the catalyst composition was optimized. Further, vanadium was loaded through wet impregnation over this optimized catalyst to improve BD selectivity. The best catalyst composition was screened, and the reaction conditions were varied to maximize the desired product yield. A combined study of PXRD, Raman spectroscopy, UV-DRS and H_2-TPR results proved magnesium orthovanadate as the

active phase for ODH of n-butane. Boron functioned for the active site isolation of the vanadia species which will facilitate better dispersion tetrahedral vanadia. XPS analysis demonstrated that the proper balance of V^{4+} and V^{5+} is necessary to improve the selectivity towards BD. The best catalyst composition was displayed an optimum population acidic-basic sites in molecule probed thermal desorption studies. Post reaction evaluation of the catalysts showed stable activity even after 150 h of continuous-time on stream reaction with appreciable yield.

Chapter 4

A brief introduction on the ODH of 1-butene and the economic importance of BD is discussed. Chapter 4 is divided into two parts depending on the catalyst system employed.

A. *Influence of transition metal addition in bismuth ferrite on the oxidative dehydrogenation of 1-butene*

A comparatively better starting molecule such as 1-butene was used to synthesize BD by the ODH process using bismuth ferrite based catalysts. Various catalysts were prepared by the coprecipitation method by doping different transition metals such as Ni, Cu, Cr, Mn, Zn and Co on bismuth ferrite. PXRD revealed the materials exist in a distorted perovskite structure. Among all, zinc-containing bismuth ferrite exhibited the highest activity for 1-butane ODH at 400 °C owing to its structural retaining ability in the rhombohedral phase. The amount of zinc was optimized and the catalyst was sturdy under reaction conditions over 100 h. Employing steam into the reaction feed has considerably improved BD selectivity. The optimized catalyst composition contained the maximum amount of lattice oxygen crucial for the reaction mechanism as quantified with XPS and the lattice oxygen was observed to solely drive the reaction for a couple of hours under DH condition.

B. *Utilizing the oxygen carrier property of cerium iron mixed oxide for the low-temperature synthesis of 1, 3-butadiene from 1-butene*

To further reduce the working temperature for BD synthesis from 1-butene, the cerium-iron mixed oxide was synthesized through the citrate sol-gel combustion method. The material was proved to have oxygen carrier property by oxygen uptake analysis. H_2-TPR demonstrated that the redox properties of the material were improved in the Ce-Fe mixed oxide compared to the corresponding pure single metal oxides. Restorable oxygen vacancies helped to maintain the catalytic activity over three reaction cycles after replenishing with

oxygen as proved from XPS and *in situ* CO-FTIR studies. The synthesized catalyst gave better BD yield than the reported catalysts for the low-temperature ODH of 1-butene.

***Chapter 5**: Selective dehydrogenation of isobutane to isobutene over promoted mesoporous Fe-alumina catalysts*

Isobutene (2-methylpropene) is one of the important C_4 olefin extensively used for the synthesis of various oxygenates and butyl rubber. The increasing demand for isobutene persists the researchers to uncover alternative methods other than conventional catalytic cracking methods that deliver low product yield. Dehydrogenation of isobutane is well exploited in this regard especially over Pt and chromium-based catalytic systems. Considering the cost-effectiveness and environmental impacts of these catalysts, a better promising *in situ* Fe loaded mesoporous alumina catalyst was synthesized by utilizing a soft template method followed by dry impregnation of P, K and Ag as promoters. Promoters have substantially improved isobutane conversion while easily reducible Ag promoted Mesoporous Fe-alumina catalyst exhibited slightly better isobutene selectivity than other promoted materials. Dry impregnated Fe on mesoporous alumina showed the lowest surface area and also the poorly dispersed iron oxide increased unwanted cracking reactions subsequently retarding catalyst lifetime.

6.2. Conclusions

C_4 hydrocarbons are potential precursors for the manufacture of a large number of organic chemicals and serve as the building blocks of the synthetic rubber industry. However, the activation of these hydrocarbons which comprises indirect or multistep reaction routes is a big challenge. The currently existing dehydrogenation and steam cracking processes suffer from many disadvantages which brought the ODH process as an alternative method. Still, many factors could affect this process like the nature of catalysts, reactor type, reaction parameters, etc. These variables may be properly tuned to achieve maximum olefin selectivity. Hence, the catalyst should be designed to overcome the drawbacks of existing materials.

6.3. Scientific contribution

The current thesis work has been contributed to the research community with new heterogeneous catalytic systems for the dehydrogenation of n-butane, 1-butene, and isobutane

under oxidative as well as non-oxidative reaction conditions with considerable activity. The studied reactions are significant considering the commercial importance of the end products in synthetic and polymer chemical industries. In conclusion, a catalyst system should be modified to attain suitable physicochemical properties for the activation of a particular substrate for a specific reaction. The information coined from the former studies is applied to improve the efficiency of the catalysts to achieve reasonable productivity. The current work was thriving to realize the selected reactions under relatively cost-effective conditions than the industrially executed processes.

6.4. Future perspectives

The attractiveness of C_4 dehydrogenation process rests mostly in the difference between the cost of the feedstock and the sale price of the olefin being produced. To make the industrial process economically interesting, it is worthwhile to increase the conversion per pass at the point of maximum selectivity of the required product. It will make recycling and downstream processing inexpensive. A capable catalyst employed in a suitable reactor configuration might be discovered providing a high yield of desired product through the activation of C_4 hydrocarbons. The key results of the current studies also specify that the ODH reaction can be made eco-benign and more profitable engaging CO_2 as the oxidant.

6.5. Outlooks of the work

The major advantages of ODH reactions over the existing processes drive that to employ in industries. However, the problems of ODH method and the catalytic systems have also to be considered. Even though some of the reported catalysts are giving better C_4 olefin yield than the manufacturing process, these techniques are inadequate to convince industrialists. The energy loss and environmental issues happening during C_4 hydrocarbon activation have to be contemplated. The design of a catalyst to avoid the side reactions with more selectivity towards C_4 olefins is a big challenge. More research may be implemented to elucidate the mechanism of C–H activation and the nature of active sites for the process.

Publications

- ❒ Ashok Kumar V, **Aswathy T V**, Periyasamy K, T Raja, Oxidative dehydrogenation of ethyl benzene to styrene over hydrotalcite derived cerium containing mixed metal oxides. *Green Chem*., 2013, 15, 3259–3267.
- ❒ Sanjay S Negi, **Aswathy T V**, T Raja, A. P. Singh, C S. Gopinath, A green chemistry approach to styrene from ethylbenzene and air on $Mn_xTi_{1-x}O_2$ catalyst. *RSC Adv*., 2014, 4, 57087–57097.
- ❒ Periyasamy K, **Aswathy T V**, Ashok kumar V, Manikandan M, Shukla R, A K. Tyagi, T Raja, An efficient robust fluorite $CeZrO_{4-\delta}$ oxide catalyst for the eco-benign synthesis of Styrene. *RSC Adv*., 2015, 5, 3619–3626.
- ❒ Prabu K, Prabu M, Ashok Kumar V, **Aswathy T V**, W.V.Y.S Sandilya, C S. Gopinath, T Raja, Effective and selective oxidation of 2-butanol over Mn supported catalyst systems. *Appl. Catal. A Gen.*, 2016, 525, 237–246.
- ❒ T Raja, Ashok Kumar V, **Aswathy T V**, M Prabu, Novel improved process for conversion of alkanes to alkenes, WO 2018/087777 A1 dated; 17/05/2018.
- ❒ Ashok Kumar V, **Aswathy T V**, T Raja, Exploring the influence of transition metal incorporation on the performance of cerium vanadates in 1-butene oxidative dehydrogenation. *Nano Prog*., 2019, 1, 22–29.
- ❒ Prabu K, Pranjal G, **Aswathy T V**, T Raja, A highly efficient and reusable Ru-NaY catalyst for the base free oxidation of 5-Hydroxymethylfurfural to 2, 5-Furandicarboxylic acid. *Catal. Today*, 2020 in press.

- ❒ **Aswathy T V**, Prabu K, T Raja, Promoted mesoporous Fe-alumina catalysts for the non-oxidative dehydrogenation of isobutane. (Under review in *Catal. Commun.*).
- ❒ **Aswathy T V**, Ashok Kumar V, Prabu K, T Raja, Enhanced catalytic activity of boron containing MgO on vanadium loading for the oxidative dehydrogenation of n-butane. (Communicated to *Appl. Catal. A Gen.*).
- ❒ **Aswathy T V**, Prabu K, Pranjal G, T Raja, Utilizing the oxygen carrier property of cerium iron oxide for the low-temperature synthesis of 1, 3-butadiene from 1-butene. (Communicated to *Catal. Lett.*).
- ❒ **Aswathy T V**, Prabu K, T Raja, Investigation on transition metals doped bismuth ferrites for the production of 1, 3-butadiene. (Manuscript ready to communicate).

Conferences

- Participant, **CATSYMP 21**, CSIR-IICT, Hyderabad, *2012*.
- Participant, **2nd National Workshop on Materials Chemistry (CAT-MAT)**, BARC, Mumbai, *2013*.
- Participant, **16th National Workshop on Catalysis for Sustainable Development**, CSIR-NEERI, Nagpur, *2014*.
- Poster presenter, "Oxidative dehydrogenation of n-butane over cobalt and gallium containing mixed metal oxides", **National Science Day**, CSIR-NCL, Pune, *2016*.
- Poster presenter, "Catalytic activity of Co/TiO_2 for oxidative dehydrogenation of n-butane to butenes", **National Science Day**, CSIR-NCL, Pune, *2017*.
- Poster presenter, "Catalytic activity of Co/TiO_2 for oxidative dehydrogenation of n-butane to butenes", **CATSYMP 23**, PPISR, Bengaluru, *2018*.
- Poster presenter, "Catalytic activity of Co/TiO_2 for oxidative dehydrogenation of n-butane to butenes", **National Science Day**, CSIR-NCL, Pune, *2018*.
- Poster presenter, "Low temperature oxidative dehydrogenation of 1-butene with lattice oxygen of cerium iron mixed oxide", **National Science Day**, CSIR-NCL, Pune, *2019*.
- Oral presenter, "Catalytic synthesis of 1, 3-butadiene from n-butane and 1-butene", **Student's Annual Conference**, CSIR-NCL, Pune, *2019*.
- Poster presenter, "Low temperature oxidative dehydrogenation of 1-butene with lattice oxygen of cerium iron mixed oxide", **International Conference on Recent Trends in Catalysis (RTC2020)**, NITC, Kozhikode, *2020*.